Theory of Kondo Effect in Nanoscale Systems
and
Studies of III-V Diluted Magnetic Semiconductors

A thesis presented
by

Gregory Alan Fiete

to
The Department of Physics
in partial fulfillment of the requirements
for the degree of
Doctor of Philosophy
in the subject of

Physics

Harvard University
Cambridge, Massachusetts
June 2003

For my mother and late father

Abstract

Theory of Kondo Effect in Nanoscale Systems

and

Studies of III-V Diluted Magnetic Semiconductors

Gregory Alan Fiete

Thesis Advisor: Prof. E. J. Heller

Committee Members: Prof. B. I. Halperin and Prof. C. M. Marcus

In this thesis, we study the interplay of local magnetic moments and quantum particles (electrons or holes) in two qualitatively different systems. The first half of this thesis describes our efforts to understand a new generation of low temperature Scanning Tunneling Microscope (STM) experiments that probe Kondo physics at the single impurity level through the local density of states. We develop a scattering theory of electrons in the surface states of the noble metals (such as Cu(111)) that gives exceptional quantitative agreement with recent "quantum mirage" experiments in quantum corrals. We then study the Kondo physics generated by a small nanometer size ferromagnetic particle in electrical contact with a metallic host and delineate a number of important regimes and situations that are experimentally accessible. The second of these projects bears directly on recent STM experiments of Co nanoparticles on single-wall metallic nanotubes.

In much of the remainder of the thesis we describe work relating to magnetic impurities in the diluted ferromagnetic semiconductor $Ga_{1-x}Mn_xAs$. On both the insulating and metallic side of the transition (occurring for $x \approx 0.03$), we study the effects of the strong spin-orbit coupling in the valence bands of GaAs on the Mn-Mn interactions. In the insulating limit we derive an effective Hamiltonian describing spin 3/2 polarons hopping between the Mn sites and coupled to the Mn spins. We study the model in meanfield theory at zero temperature and find a strong disorder-induced magnetic anisotropy which plays an important role in the physics. In the metallic limit, we compute the effective RKKY interaction between two Mn spins within the spherical approximation. In Monte Carlo calculations we find a number disorder-dependent features of the magnetization, susceptibility and Curie temperature consistent with experiment but not captured in other models.

In the final chapter we discuss the problem of quantum decoherence in modern semiclassical language. In particular, using the classical mechanics which underlies any semiclassical approach, we attempt to present an intuitive and general theory of quantum decoherence. We place an emphasis on the types of processes that lead to the loss of quantum properties when a particle interacts with environmental degrees of freedom. We show that “dephasing” (randomization of the phase of the particle) almost always contributes to decoherence, but trajectory changes also play an important role and cannot be neglected in general.

Contents

List of Figures

Acknowledgments

First of all, I would like to thank my advisor, Rick Heller, for giving me all the opportunities I needed while a graduate student to develop as a scientist. He was always supportive, approachable and generous. He gave me a great deal of freedom to work on many different problems with many different collaborators. For this I am very grateful. In our work together, he was always full of insight and routinely amazed me with his physical intuition. He is a man of great character and depth.

I would like to thank Bert Halperin for taking me under his wing for a year or so at a critical stage in my graduate study to begin research on many-body problems in condensed matter physics. It was an opening chapter for me on what has become my primary research direction. His impressive ability to cut away peripheral issues to get to the essence of a complicated problem greatly inspired me. Without question, I consider our collaboration together one my most important experiences as a graduate student. I appreciate and respect his frankness and integrity in all matters.

I would like to thank Charlie Marcus for being on my committee, for access to his experiments and for physics discussions. I benefitted a great deal from a course he ran on mesoscopic physics and from his entire group through many discussions and collaborations. His group is constantly putting out work at the very forefront of mesoscopics research and it has really enhanced the condensed matter environment here at Harvard.

A special thanks to Gergely Zaránd with whom I spent more time during my thesis research than anyone. He is an exceptional scientist and I learned a tremendous amount from him about all the nitty-gritty details of research from, as he often said, “doing the calculation”, to formatting figures. I am grateful to have had the opportunity to work with him on a variety of topics from the Kondo problem to ferromagnetic semiconductors, here at Harvard, in Argonne National Labs and later in the Technical University Budapest.

I would like to thank the Kavli Institute for Theoretical Physics in Santa Barbara, California, the Technical University Budapest, Hungary and Argonne National Laboratory, Illinois for their hospitality and financial support where parts of this thesis were done. I would also like to thank ITAMP and NSF for financial support for thesis work and NSF and NATO for financial support to attend conferences.

I would like to thank Boldizsár Jankó, Kedar Damle, Yuval Oreg, Jesse Hersch, Hari Manoharan, Chris Lutz and Don Eigler for our collaborations together; Jacek Furdyna, Alex Johnson and Teri Odom for many discussions on their experiments. Stephan Kehrein for discussions on Kondo effect, Arne Brataas for discussions on spintronics and Troy Van Voorhis for discussions on semiclassical methods; I thank Rob Parrott, Scot Shaw and Adam Lupu-Sax for help on countless computer issues and Ian Affleck, Axel Andre, Leon Balents, Alex Barnett, Ryan Barnett, Diego Vaz Bevilaqua, Bill Bies, Miriam Blaauboer, Anton Burkov, Antonio Castro-Neto, Amit Chattopadhyay, Henry Chen, Doron Cohen, Jan-Hein Cremers, Eugene Demler, Henry Ehrenreich, Matthew Fisher, Leonid Glazman, Denis Gorokov, Andreas Heinrich, Mike Hermele, Walter Hofstetter, Jian Huang, Yoseph Imry, Barbara Jones, Allison Kalben, Lev Kaplan, Karyn Le Hur, Natasha Lepore, Brian LeRoy, Anna Lopatnikova, Sheng Li, David Lubensky, Amulya Madhav, Neepa Maitra, Luca

Marinelli, Akakii Melikidze, Areez Mody, Martin Naraschewski, Arun Paramakenti, Andrey Pashin, Misha Pustilnik, Jiang Qian, Gil Refael, David Reichman, Subir Sachdev, Jen Schwarz, Pascal Simon, Todd Squires, Ady Stern, Manny Tannenbaum, Steve Tomsovic, Mark Topinka, Yaroslav Tserkovnyak, Orsi Újsághy, Jay Vaishnaw, Jiri Vanicek, Vincenzo Vitelli, Jan von Delft, Olivia White, Fred Zawadowski and Lukasz Zielinksi for many physics discussions.

I would like to thank my High School physics teacher, James McPhee, for introducing me to the subject of physics. He taught me my first two years of physics and spent much time with me after hours when I wanted to learn more. His enthusiasm for the subject, excellent grasp of the material and ability to reduce it all to very intuitive ideas, and superior teaching skills have obviously influenced the course of my life. He is a great friend and mentor.

I would like to thank all of the many good friends Ila and I made in graduate school for their support and friendship. We had such a good time with our friends from the physics department, from the dorms and from Dudley House during all the various trips and outings we made.

I would like to thank Mummy-Babuji for their love and support. Babuji is one of the greatest men I know. He excels in all areas of life and has been a wonderful and inspiring example of how hard work, discipline and dedication to family can make a real difference in everyone's life around him. He has shown by example the merits and rewards of an academic life. Mummy has been the glue that keeps the family together. She works so hard to make sure we are all happy, well fed and loved. She is responsible for much of the success of her children (original and new) and is full of wisdom.

I would like to thank Mom and Dad for their love, support and all of the opportunities they gave me early in life. My father passed away before he or I knew I had any interest in physics or mathematics, but his kind nature has no doubt influenced my personal life. Mom was always there to help set me on the right path when I was younger and was my constant "training companion" whether it was BMX, weightlifting or triathlon. Mom and Dad both gave me the chance to pursue what now seems like any dream I had. Without their encouragement and support I would not be here writing this.

I would like to thank Brian, Anoop and Bhabhiji for their love. It is wonderful to have such a great family to spend the good times and the bad times with. I am very proud of Brian, especially, for how well he has done in his own endeavors. Anoop has always provided excellent advice on many important matters and we have had many good times together pursuing the pleasure of the palate. "Bobiji" has always made me feel at home during our trips to NY.

Finally, and most of all, I would like to thank Ila for everything. I am the luckiest man alive to have her as my wife. She is my closest advisor, companion, cheerleader and source of joy. She constantly thinks of me before herself and has always done everything she can to make life as good for us as possible. She has balanced me and strengthened my weaknesses considerably. I could not dream up a more wonderful partner. Sharing is love.

Citations to Previously Published Work

Much of this thesis has been previously published or is available on the Los Alamos server (http://xxx.lanl.gov):

- "Scattering Theory of Kondo Mirages and Observation of Single Kondo Atom Phase Shift", G. A. Fiete, J. S. Hersch, E. J. Heller, H. C. Manoharan, C. P. Lutz and D. M. Eigler, *Phys. Rev. Lett.* **86**, 2392 (2001).
- "Kondo Effect and STM spectra through Ferromagnetic Nanoclusters", G. A. Fiete, G. Zaránd, B. I. Halperin and Y. Oreg, *Phys. Rev. B* **66**, 024431 (2002).
- "Theory of Quantum Corrals and Quantum Mirages", G. A. Fiete and E. J. Heller, To appear in *Rev. Mod. Phys.* (cond-mat/0211607).
- "Effective Hamiltonian for $\mathrm{Ga}_{1-x}\mathrm{Mn}_x\mathrm{As}$ in the Dilute Limit", G. A. Fiete, G. Zaránd and K. Damle, Submitted to *Phys. Rev. Lett.* (cond-mat/0212074).
- "Semiclassical Theory of Coherence and Decoherence", G.A. Fiete and E. J. Heller, To appear in *Phys. Rev. A* (quant-ph/0211184).

Chapter 1

Introduction

1.1 Problems Investigated

This thesis is primarily concerned with quantum condensed matter systems. The entire thesis deals, in some form or the other, with the interaction of a particle (usually an electron or hole) with some spatially localized degree of freedom (often a magnetic impurity). In particular, we study the behavior of systems with magnetic impurities in 2 limits: (1) The limit in which the number of magnetic impurities is much smaller than the number of itinerant electrons or holes. This is the single-impurity limit where the impurity can be thought of as a perturbation to the Fermi sea. One of the most interesting physical situations that occurs in this limit is the Kondo effect. The Kondo effect is an old and well-studied problem, but here we address new STM experiments that provide a direct probe of the local density of states around a Kondo impurity. Since these new experiments are in nanoscale systems, interesting new finite-size effects appear that need explanation. (2) The opposite limit is the limit of few itinerant carriers per magnetic impurity. This is the regime of the ferromagnetic semiconductor $Ga_{1-x}Mn_xAs$. In this limit, the Mn ions can no longer be treated as a perturbation on a Fermi sea and interactions between magnetic impurities can be appreciable, resulting in a ferromagnetic state. We study this material in the limits of very small Mn concentration ($x \approx 0.01$, insulating regime) and small Mn concentration ($x \approx 0.05$, metallic regime) using a combination of analytical and numerical techniques (mean field and Monte Carlo).

All of the effects described above that we study depend on *coherent* quantum particles. The last chapter of this thesis is an investigation of quantum coherence itself.

1.2 Outline of Thesis

In chapter 2 we begin with a discussion of scattering theory and the STM. We emphasize the importance of surface states for the physics associated with the quantum corrals that we later discuss. We outline the essential ingredients of the theory of STM measurement. We review the differences between topographic (constant current) and spectroscopic (constant tip height) measurements, what they probe and how to calculate the STM signal in terms of the substrate physics. We then show how scattering theory can be used for metals with surface states to calculate the dominant contribution to the local density of states, which the STM measures. Finally, we tie everything together to discuss the calculation of the STM signal in and around quantum corrals.

In chapter 3 we discuss the two most commonly used models to describe the physics of a local moment in a metallic host: (1) The Anderson Model and (2) The Kondo Model. Since a local moment is required to generate a Kondo effect, it is important for the chapters that follow to understand the basic physics of local moments in metals. The Anderson model is perhaps the simplest model to study the conditions under which a local moment forms when a magnetic impurity is placed in a metallic host. The Kondo Model is simply a special case of the more general Anderson Model. The Kondo Model is valid in the local moment regime of the Anderson Model and can be derived from the latter in second order perturbation theory.

In chapter 4 we apply the results of chapter 2 and chapter 3 to develop a theory for the “quantum mirage”. We discuss both the theory for the original elliptical corrals as well as unpublished “Kondo Lattice” STM experiments. Our theory is based on an s-wave phase shift that takes into account the Kondo resonance at the Fermi energy and incoherent scattering at the substrate adatoms. For both experimental situations the agreement between theory and experiment is excellent. This suggests that understanding the “Kondo Lattice” experiments does not require anything beyond single impurity Kondo physics. We conclude this chapter with a discussion of recent results, developments and outstanding questions on both the theoretical and experimental side.

In chapter 5 we round out our discussion of Kondo effect in nanoscale systems with a discussion of the Kondo effect generated by a ferromagnetic *nanocluster* in contact with a metallic host. Compared to the Anderson Model, there are essentially two new ingredients: (1) There is more than one relevant "local" level on the nanocluster and (2) the nanocluster may have a diameter comparable to the Fermi wavelength making an s-wave scattering approximation very unrealistic. Using a modified Anderson Model, we derive an effective Kondo Hamiltonian whose coupling constant is generally a matrix (due to its finite spatial size) rather than a number, as is the case for the familiar Kondo Hamiltonian. The coupling constant depends on the many details of the problem such as the nanocluster-host tunneling matrix elements, the Coulomb charging energy of the cluster and the spin-dependent density of states of the cluster. In contrast to the Anderson model, it is possible to have *ferromagnetic* cluster spin-conduction electron coupling. We also use our theory to calculate the spectrum of a ferromagnetic nanocluster coupled to a metallic substrate and we find that a large asymmetry for positive and negative tip biases can result, consistent with what is often seen in experiment. To conclude this chapter we estimate the Kondo temperature of a ferromagnetic nanocluster and find that it is exponentially suppressed with increasing cluster size.

In chapter 6 we give an introduction to the second part of the thesis which deals with the diluted magnetic semiconductor (DMS) $\mathrm{Ga}_{1-x}\mathrm{Mn}_x\mathrm{As}$, which is of interest because of its possible use in a "spintronic" device. When Mn substitutes for Ga in a GaAs host, local moments are added as well as holes. The local Mn moments are the source of the magnetism and the holes are the source of the Mn-Mn spin interaction, which happens to be ferromagnetic on average for a specific range of x and temperatures1. As a function of the doping concentration, x, the material under goes two zero temperature transitions: (1) A metal-insulator transition and (2) A ferromagnetic to paramagnetic quantum phase transition. The value of x for both transitions is approximately the same and is around $x \approx 0.03$. Because magnetic impurities are generally insoluble in semiconductors, it has been quite difficult to create materials that are both magnetic and semiconducting. Nonequilibrium molecular beam epitaxy is required to fabricate the samples and the physical characteristics of the material such as hole concentration, magnetization, resistivity and the Curie temperature all depend very strongly on the post-growth annealing protocol. We discuss common theoretical approaches to both the dilute and the metallic doping limits.

In chapter 7 we derive an effective Hamiltonian for $\mathrm{Ga}_{1-x}\mathrm{Mn}_x\mathrm{As}$ in the dilute limit ($x \approx 0.01$) which describes spin 3/2 polarons hopping from Mn site to Mn site. We begin by first solving the problem of a bound hole to Mn in a GaAs host. This is done with a variational calculation that includes the strong spin-orbit effect of the GaAs host and the effective spin-orbit coupling of the Baldereschi-Lipari “spherical approximation”. Using the wavefunctions from the single-impurity variational solution, we study the problem of a hole hopping between two Mn centers in the GaAs host. We compute the parameters of an effective tight-binding Hamiltonian for this problem from the single-impurity wavefunctions. Because of the effective spin-orbit coupling, the hopping parameters turn out to have strong angular dependence. We then generalize the hole hopping to an arbitrary number of centers. We also include a coupling of the Mn spin to the spin density of the bound hole at the Mn site and the effects of on-site hole-hole interactions to obtain a final Hamiltonian. We conclude the chapter by studying the effective Hamiltonian in the mean field approximation (spin orientations and spin density at the Mn sites are computed self-consistently). We find that because of the strong effective spin-orbit coupling, the random positions of the Mn generates a strong anisotropy in the orientation of the net magnetization. In our final calculation of the chapter, we demonstrate that for parameters reasonable for GaAs, there is a well formed impurity band at $x = 0.01$ with delocalized states present *before* the impurity band has merged with the valence band. Many of the more technical details of the calculations in this chapter have been relegated to the appendixes.

In chapter 8 we turn to a study of $\mathrm{Ga}_{1-x}\mathrm{Mn}_x\mathrm{As}$ in the metallic limit ($x \approx 0.05$). We take as a starting point a valence band partially filled with holes. We then calculate the RKKY kernel of Mn-Mn interactions by integrating out the heavy and light hole sectors to obtain an expression for the interaction of two Mn spins a distance R away from each other. Because of the effective spin-orbit coupling in the spherical approximation, the energy depends not only on the relative spin orientations (as it does without the effective spin-orbit coupling) but also on the orientations of the spins relative to the axis joining them. Using this interaction kernel as an input to Monte Carlo calculations (treating the Mn spin as a classical variable) we compute the temperature dependence of the magnetization, the susceptibility and the Curie temperature. We also compute the distribution of angles between individual Mn spins and the net magnetization of the sample. This measures the degree of non-collinear magnetism. We study the effects of hole concentration and Mn positional disorder on these quantities.

In chapter 9 we round out the thesis by discussing an issue central to all the previous chapters–quantum coherence. We present a semiclassical theory of coherence and decoherence. Our approach is based on modern semiclassical methods (coherent state wavepackets) which avoid many of the singularities inherent in a more traditional Van Vleck propagator approach. Because all semiclassical methods are ultimately based on classical dynamics, our approach can provide a more intuitive physical picture of the mechanisms that lead to quantum decoherence. We study the relative role of phase randomization or "dephasing" and trajectory changes in decoherence and find that decoherence can not generally be described as "dephasing". Strong system-bath interactions always lead to rapid decoherence, so we investigate the perturbative regime in detail using a density matrix (and therefore basis independent) formulation.

Chapter 2

Scattering Theory and the STM

2.1 The Importance of Surface States

The beautiful standing wave patterns observed in STM corral experiments[1, 2, 3, 4] result from the presence of Shockly surface states[1] on the metallic substrate. These are the same surface states responsible for the standing wave patterns observed near a step edge[6]. Surface states are the result of a particular crystallographic cut of the material, usually a noble metal, which places the Fermi energy in a band gap for electrons propagating normal to the surface. The surface states of Cu(111), Au(111) and Ag(111) are commonly used in STM experiments. In the direction normal to the surface (and in a range of angles around the normal), Bloch states are forbidden at the Fermi energy. However, solutions to the Schrödinger equation exist with exponentially decaying amplitude into both the bulk material and the vacuum. For such solutions electrons are still free to move in the plane of the surface and form

---

[1] For more details and experimental results for several materials see [5].

a type of two dimensional electron gas (2DEG) there. Often, the surface state band is only partially filled, giving a low density on the surface, and a nearly quadratic dispersion relation with a constant effective mass.

The scattering theory that we develop for quantum corrals in Sec. 2.3 is based on these free two dimensional surface state electrons. We will see that although the quantum corrals are two dimensional systems in many respects, there are some important ways in which the underlying bulk material makes its presence felt. This is especially true with the quantum mirage experiments where the bulk electrons play an important role in the formation of the Kondo resonance[7].

Before we leave our brief discussion of surface states it is important to give some typical numerical values of important quantities such as the wavelength of electrons in the surface states, λ, the effective mass of surface state electrons, m^*, and density of states of the surface state electrons, ϱ_{surf}. These three quantities are all related through the dispersion relation

$$E_{\text{surf}}(k) - E_F = E_0 + \frac{\hbar^2 k^2}{2m^*} \, , \tag{2.1}$$

where $\varrho_{\text{surf}} = \frac{m^*}{\pi \hbar^2}$ includes both spin up and spin down electrons. In the case of Cu(111), Au(111) and Ag(111) the surface state band minimum, E_0, is very close to the Fermi energy. Typical values are fractions of an eV below the Fermi energy[5], E_F, where E_F is typically 5-10 eV. For Cu(111), $E_0 \approx -450$ meV and $m^* = 0.38 m_e$ with m_e the mass of the free electron. The surface state electron density of Cu(111) is $n \approx 7 \times 10^{13}\,\text{cm}^{-2}$ which corresponds to approximately one surface state electron per 12 Å × 12 Å square.

There are three important physical consequences of small E_0. The first is that it makes the dispersion relation quadratic and *isotropic* (in the plane of the surface) to a very good approximation. An isotropic dispersion relation is very convenient for the application of scattering theory because one does not need to know the orientation of the underlying crystal lattice. Secondly, a small E_0 makes the filling of the surface state band rather low compared to bulk bands, which in turn makes the typical wavelength of the surface state electron, $\lambda_F = \frac{2\pi}{k_F}$, very large compared the lattice spacing and the size of atomic impurities on the surface. For Cu(111), $\lambda_F = 29.5$ Å. Since λ_F is much larger than the underlying Cu(111) lattice spacing, the standing wave patterns are easy to separate from atomic scale charge density variations and since λ_F is large compared to the surface adatoms, we can make an s-wave approximation in the scattering theory. Thirdly, a small E_0 makes the electron filling small so the density of surface states is small compared to bulk states at the same energy. This has implications for the microscopic details of the Kondo effect from a magnetic impurity like Co on the Cu(111) surface. We will return to this point in Chapter 4.1. We now turn to the STM measurement.

2.2 STM Theory: Topographic Images and Spectroscopic Measurement

In this section we briefly review the physics of the tunneling measurement. The basic tunneling geometry and energy diagram is shown in Fig. 2.1. The STM tip usually sits a few Å above the surface. The STM data can be taken in two ways: (i)

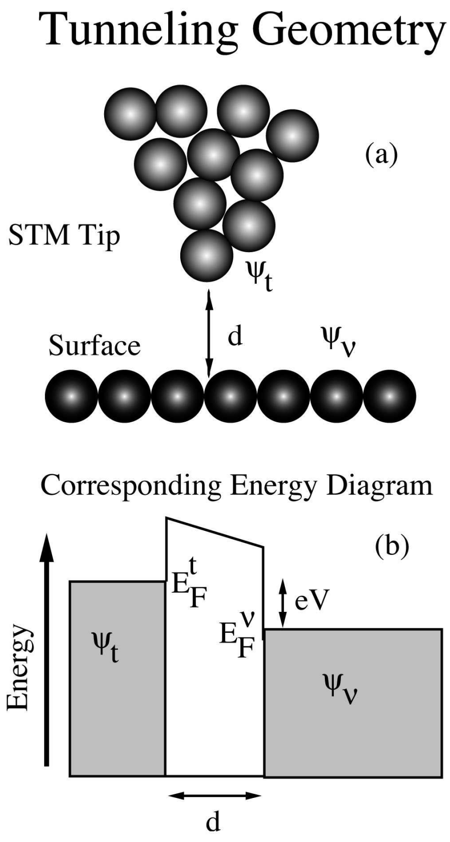

Figure 2.1: (a) Schematic of the STM tip above the substrate. The STM tip states are labelled by ψ_t and the eigenstates of the substrate are labelled by ψ_ν. The current is exponentially sensitive to the tip-surface distance, d. (b) Energy diagram of the tunneling process. Electrons must tunnel across a vacuum barrier of thickness d from occupied states of the tip to unoccupied states of the surface (energies $E_F^\nu < \epsilon < E_F^t$). The total current, Eq. (2.5), is given by sum of all such processes while the conductance, Eq. (2.6), just measures the tunneling rate for electrons at a particular energy in this window.

A feedback loop can be used to control the height of the tip above the surface so that the total tunneling current is kept constant as the tip is scanned over the surface. This is called a "topographic" image and, as we will soon see, at each point it is a measure of the *energy-integrated* local density of surface states. (ii) In the second type of measurement the feedback loop is opened so that the tip height is kept roughly constant with respect to the surface and the voltage is swept to measure the local spectroscopy at the tip position.

Tunneling measurements of quantum corrals are typically done at small voltage biases, $V < 0.3$ Volts, and low temperatures, $T < 70$ K. In such a situation perturbation theory can be applied to compute the tunneling current in terms of the unperturbed tip states and surface states. According to Fermi's Golden Rule, the current at position $\mathbf{r}$ and STM bias voltage V is[8, 9]

$$I(\mathbf{r}) = \frac{2\pi e}{\hbar} \sum_{t,\nu} |M_{t,\nu}(\mathbf{r})|^2 f(\epsilon_t) \left(1 - f(\epsilon_\nu)\right) \delta(\epsilon_t + eV - \epsilon_\nu) \ , \tag{2.2}$$

where e is the charge of the electron, t (ν) labels the tip (surface) states, f is the Fermi function and $M_{t,\nu}(\mathbf{r})$ is the matrix element from the tip state t to the surface state ν at position $\mathbf{r}$. The expression, Eq. (2.2), has a simple physical interpretation. It says that the tunneling current is proportional to the square of the matrix element connecting the various tip states to the various surface states times a factor which gives the probability of an occupied tip state and an empty surface state. The delta function enforces energy conservation. Finally all tip states and surface states are summed over. When the tip is treated as a point source, $|M_{t,\nu}(\mathbf{r})|^2 \propto |\psi_\nu(\mathbf{r})|^2$[8], where $\psi_\nu(\mathbf{r})$ are the eigenfunctions of the surface. Assuming also that the temperature is low enough to replace the Fermi functions by step functions, using the relation $\int d\omega \delta(\epsilon_t + eV - \omega)\delta(\omega - \epsilon_\nu) = \delta(\epsilon_t + eV - \epsilon_\nu)$ and converting the sum over tip states to an integral, we obtain

$$I(\mathbf{r}) \propto \int_0^{eV} \varrho_t(\epsilon) \mathrm{LDOS}(\mathbf{r}, \epsilon) d\epsilon \ , \tag{2.3}$$

where $\varrho_t(\epsilon)$ is the density of states of the tip and

$$\mathrm{LDOS}(\mathbf{r},\epsilon) = \sum_\nu |\psi_\nu(\mathbf{r})|^2 \delta(\epsilon - E_\nu) \ . \tag{2.4}$$

Usually the density of states of the tip is assumed constant so it can be pulled out of the integral,

$$I(\mathbf{r}) \propto \int_0^{eV} \mathrm{LDOS}(\mathbf{r},\epsilon) d\epsilon \ , \tag{2.5}$$

and

$$\frac{dI}{dV}(\mathbf{r},\epsilon) \propto \mathrm{LDOS}(\mathbf{r},\epsilon) \ . \tag{2.6}$$

The last three equations above, Eqs. (2.4), (2.5) and (2.6) are the most important formulas for the interpretation of the quantum corral experiments. The central quantity to calculate is Eq. (2.4) as the current, Eq. (2.5), and the conductance, Eq. (2.6), depend on it. The LDOS is expressed in terms of the eigenstates, labeled by ν, of the surface. It is through the calculation of these eigenstates from scattering theory that Eq. (2.4) provides the bridge between scattering theory and the tunneling measurement of the STM. We will develop this connection fully in Sec. 2.3. From Eq. (2.5) and Eq. (2.6) it is evident that the STM signal is related to the square of the surface state wavefunctions at a given location. If the wavefunction has large (small) amplitude at a particular location the current and conductance will tend to be larger (smaller) there.

A topographic measurement corresponds to Eq. (2.5) in which a feedback loop is used to modulate the tip height to keep the current constant. This is usually the type of measurement used to produce data like the standing wave patterns in quantum corrals. Typical bias voltages are on the order of 10 meV so that the current at position $\mathbf{r}$ is an integral over approximately 10 meV of energy. In most experiments, the density of states at any given position $\mathbf{r}$ does not vary much over 10 meV. However, in the mirage experiments the Kondo effect actually produces strong variations in the local density of states over 10 meV[3].

In the spectroscopic measurement the STM tip-surface distance is held fixed by turning off the feedback loop. The voltage is swept (at a given position) to reveal the energy dependence of the LDOS, Eq. (2.6). This is the type of measurement that reveals the energies and widths of resonances in quantum corrals which appear as peaks in a plot of dI/dV vs. V. The Kondo resonance at a Kondo impurity also has a strong signature in dI/dV[10, 11, 3]. The quantum mirage is most easily probed in this way[3, 12].

2.3 Scattering Theory for Surface State Electron Density

In this section we develop a scattering theory for the electron density in quantum corrals. In Sec. 2.1 we emphasized the importance of the surfaces states on the (111) surfaces of noble metals and gave the important properties for the development of scattering theory: two dimensional electron states on the surface, isotropic and parabolic dispersion of the energy and long electron wavelength compared to the lattice spacing and the size of the adatoms. We now describe how the quantities of the STM measurement described in Sec. 2.2, namely Eq. (2.4), is obtained from scattering theory. The physical picture to have in mind is of a circularly symmetric electron amplitude emanating from the STM tip into the surface states of the substrate. This amplitude spreads radialey outward from the tip until it encounters a defect (such as an impurity) on the surface or a step edge, at which time it scatters. Part of this amplitude is reflected back to the STM tip (possibly scattering several more times along the way from different impurities) and interferes with the outgoing amplitude leading to fluctuations in the LDOS, and hence the tunneling current, as a function of position. Note that the fluctuations are a result of the *coherent* part of the backscattered amplitude.

Let the Hamiltonian of an electron on the surface be $\hat{H} = \hat{H}_0 + \hat{V}$, where $\hat{H}_0$ is the Hamiltonian describing free propagation in the surface states and $\hat{V}$ accounts for the spatially local and separate potential perturbations due to the impurities on the surface. The amplitude to propagate from point $\mathbf{r}$ to point $\mathbf{r}'$ in time t on the surface is given by the retarded Green's function, $G^{\text{ret}}(\mathbf{r}', \mathbf{r}, t) = -i\theta(t)\langle \mathbf{r}'|e^{-i\hat{H}t/\hbar}|\mathbf{r}\rangle$, where $\theta(t)$ is the step function. The eigenstates of $\hat{H}$ are the scattering eigenstates of the particle in the presence of the potential $\hat{V}$. Inserting a complete set of eigenstates,

$$G^{\text{ret}}(\mathbf{r}', \mathbf{r}, t) = -i\theta(t) \sum_{\nu} \langle \mathbf{r}'|e^{-iE_\nu t/\hbar}|\psi_\nu\rangle\langle\psi_\nu|\mathbf{r}\rangle \ , \tag{2.7}$$

and taking the Fourier transform of this,

$$G^{\text{ret}}(\mathbf{r}', \mathbf{r}, \epsilon) = \sum_{\nu} \frac{\psi_\nu^*(\mathbf{r})\psi_\nu(\mathbf{r}')}{\epsilon - E_\nu + i\delta} \ . \tag{2.8}$$

Here $\psi_\nu(\mathbf{r})$ are the eigenstates of the Hamiltonian $\hat{H}$ and δ is an infinitesimal positive quantity. For the STM measurements, we are interested in the part of the amplitude that back scatters to the tip. Thus, we are interested in $\mathbf{r}' = \mathbf{r}$. The imaginary part of the diagonal amplitude is proportional to the local density of states,

$$\mathrm{LDOS}(\mathbf{r},\epsilon) \equiv -\frac{1}{\pi}\mathrm{Im}\left[G^{\mathrm{ret}}(\mathbf{r},\mathbf{r},\epsilon)\right] = \sum_{\nu} |\psi_{\nu}(\mathbf{r})|^{2}\delta(\epsilon - E_{\nu}) \ . \tag{2.9}$$

What we have established is a relationship between the full Green's function, Eq. (2.8), the scattering eigenstates of the Hamiltonian $\hat{H}$, $\psi_\nu(\mathbf{r})$, and the local density of states. What remains is to develop a method for calculating the Green's function, Eq. (2.8).

We first consider the case where $\hat{V}$ represents a single scatterer. Dyson's equation can be written

$$\hat{G}^{\mathrm{ret}} = \hat{G}_0^{\mathrm{ret}} + \hat{G}_0^{\mathrm{ret}}\hat{V}\hat{G}^{\mathrm{ret}} \ , \tag{2.10}$$

where $\hat{G}^{\mathrm{ret}}$ is the full retarded Green's function and $\hat{G}_0^{\mathrm{ret}}$ is the free retarded Green's function. When $\hat{V}$=0, $\hat{G}^{\mathrm{ret}} = \hat{G}_0^{\mathrm{ret}}$. The $\hat{G}^{\mathrm{ret}}$ on the right hand side of Eq. (2.10) can formally be eliminated by iterating the equation. In operator notation,

$$\begin{aligned} \hat{G}^{\mathrm{ret}} &= \hat{G}_0^{\mathrm{ret}} + \hat{G}_0^{\mathrm{ret}}\hat{V}\hat{G}_0^{\mathrm{ret}} + \hat{G}_0^{\mathrm{ret}}\hat{V}\hat{G}_0^{\mathrm{ret}}\hat{V}\hat{G}_0^{\mathrm{ret}} + \cdots \\ &= \hat{G}_0^{\mathrm{ret}} + \hat{G}_0^{\mathrm{ret}}(\hat{V} + \hat{V}\hat{G}_0^{\mathrm{ret}}\hat{V} + \cdots)\hat{G}_0^{\mathrm{ret}}. \end{aligned} \tag{2.11}$$

The terms in the series have the physical interpretation of a particle that (i) does not scatter at all from the potential, (ii) scatters once and leaves, (iii) scatters once, propagates, scatters again and then leaves (iv...) and so on to infinite order. Truncation of the series at $\hat{V}$, for example, is just the first Born approximation. The terms within parentheses can be grouped into into a single object called the *t-matrix*. The *t-matrix* is defined by

$$\hat{T} = \hat{V} + \hat{V}\hat{G}_0^{\mathrm{ret}}\hat{V} + \cdots \ . \tag{2.12}$$

When the spatial extent of the scattering potential is small compared to the wavelength of the incoming particle, as is the case for adatoms on the Cu(111) surface, the scattering is s-wave (isotropic) because the wavelength of the incident particle is too large to "feel" the spatial structure of the target. In the s-wave approximation, the *t-matrix* takes a particularly simple form in position representation[13, 14]:

$$\begin{aligned} G^{\mathrm{ret}}(\mathbf{r},\mathbf{r}) &= G_0^{\mathrm{ret}}(\mathbf{r},\mathbf{r}) + \\ & \int\int d^2\mathbf{r}' d^2\mathbf{r}'' G_0^{\mathrm{ret}}(\mathbf{r},\mathbf{r}') \\ & \times s\delta(\mathbf{r_0}-\mathbf{r}'')\delta(\mathbf{r_0}-\mathbf{r}')G_0^{\mathrm{ret}}(\mathbf{r}'',\mathbf{r}) \ , \end{aligned} \tag{2.13}$$

where $s(k) = 2i(e^{2i\delta(\epsilon)}-1)$, $\mathbf{r_0}$ is the position of the impurity and $\delta(\epsilon)$ is the energy dependent phase shift in the s-wave orbital channel (which can be computed once $V(r)$ is known or determined directly from experiment). The integral can then be done trivially to yield

$$G^{\mathrm{ret}}(\mathbf{r},\mathbf{r}) = G_0^{\mathrm{ret}}(\mathbf{r},\mathbf{r}) + sG_0^{\mathrm{ret}}(\mathbf{r},\mathbf{r_0})G_0^{\mathrm{ret}}(\mathbf{r_0},\mathbf{r}). \tag{2.14}$$

Note that when $V(r)$ goes to zero, $\delta(\epsilon)$ goes to zero and one obtains $G^{\mathrm{ret}}(\mathbf{r},\mathbf{r}) = G_0^{\mathrm{ret}}(\mathbf{r},\mathbf{r})$. That is, the full Green's function reduces to the free Green's function.

The extention to several scatterers is straightforward. The schematic situation is shown in Fig. 2.2. The new ingredient in the many scatterer case is an extra self-consistency condition on the scattered amplitude. Imposing this self-consistency condition is equivalent to calculating the scattering among all the impurities to infinite order. This is the heart of multiple scattering theory. (The *t-matrix* gives the result of scattering from a single impurity to infinite order.)

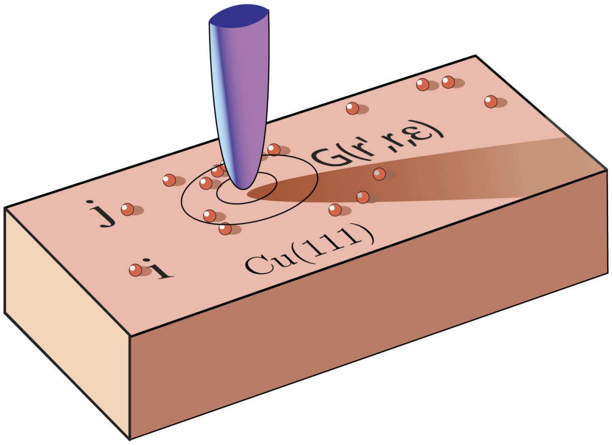

Figure 2.2: Schematic of the scattering geometry of multiple scattering theory. The scattering centers, shown as little beads, are adatoms on the surface of a noble metal such as Cu(111). In the approximation that the STM tip is point-like, a circularly symmetric electron amplitude, $G_0(\mathbf{r}', \mathbf{r}, \epsilon)$, eminates from the tip into the surface states of the metal and encounters the impurities on the surface. Since the wavelength of the electrons in the surface states is much larger than the size of the scatters, one can treat the scatterers as s-wave scatterers and ignore all higher orbital channels. Because the scatterers are far apart compared to their size, we assume that electrons propagate freely between impurities. i and j label different impurities.

In the presence of N scatterers the *t-matrix* equation $\sum_{i=1}^{N} \hat{T}_i \hat{G}_i^{\mathrm{ret}} = \sum_{i=1}^{N} \hat{V}_i \hat{G}^{\mathrm{ret}}$ ($\hat{V}_i$ are nonoverlapping scattering potentials, the $\hat{T}_i$ are the corresponding *t-matricies* for these potentials) generalizes Eq. (2.13) to

$$\begin{aligned} G^{\mathrm{ret}}(\mathbf{r},\mathbf{r}) &= G_0^{\mathrm{ret}}(\mathbf{r},\mathbf{r}) + \sum_{i=1}^{N} \int\int d^2\mathbf{r}' d^2\mathbf{r}'' G_0^{\mathrm{ret}}(\mathbf{r},\mathbf{r}') \\ &\quad \times s_i \delta(\mathbf{r}_i - \mathbf{r}'')\delta(\mathbf{r}_i - \mathbf{r}') G_i^{\mathrm{ret}}(\mathbf{r}'',\mathbf{r}) \\ &= G_0^{\mathrm{ret}}(\mathbf{r},\mathbf{r}) + \sum_{i=1}^{N} s_i G_0^{\mathrm{ret}}(\mathbf{r},\mathbf{r}_i) G_i^{\mathrm{ret}}(\mathbf{r}_i,\mathbf{r}) \ , \end{aligned} \tag{2.15}$$

where the G_i^{ret} are the self-consistently calculated values of the Green's functions at the locations of the scatterers,

$$G_i^{\mathrm{ret}}(\mathbf{r}_i,\mathbf{r}) = G_0^{\mathrm{ret}}(\mathbf{r}_i,\mathbf{r}) + \sum_{j\neq i}^{N} s_i G_0^{\mathrm{ret}}(\mathbf{r}_i,\mathbf{r}_j) G_j^{\mathrm{ret}}(\mathbf{r}_j,\mathbf{r}) \ , \tag{2.16}$$

and

$$s_i(\epsilon) = \frac{4i\hbar^2}{m^*}(e^{2i\delta_i(\epsilon)} - 1) \ , \tag{2.17}$$

for the i^{th} scatterer. The solution of Eq. (2.16) is given by the equation

$$\mathbf{G} = \mathbf{A}^{-1}\mathbf{G_0} \ , \tag{2.18}$$

where $\mathbf{A}$ is an $N \times N$ matrix with elements $\mathbf{A}_{ij} = \delta_{ij} - s_i G_0(\mathbf{r}_i,\mathbf{r}_j)$ containing all the information about the propagation between the impurities and $\mathbf{G_0}$ and $\mathbf{G}$ are N-dimensional column vectors of elements $\mathbf{G_{0i}} = G_0(\mathbf{r}_i,\mathbf{r})$ and $\mathbf{G}_i = G(\mathbf{r}_i,\mathbf{r})$, respectively, containing the information about propagation from the STM tip to the impurities and from the impurities to the STM tip.

The STM signal is then calculated from scattering theory by specifying the s-wave scattering phase shifts $\delta_i(\epsilon)$, the locations $\{\mathbf{r}_i\}$ of the N impurities on the surface and the incident electron amplitude. Given the dispersion relation, Eq. (2.1), the free Green's function, $G_0^{\mathrm{ret}}(\mathbf{r}',\mathbf{r},\epsilon)$, is determined from Eq. (2.8) in the case of $\hat{V}$=0. In two dimensions, the outgoing Green's function from a point source is $G_0^{\mathrm{ret}}(\mathbf{r}',\mathbf{r},\epsilon) = -i\frac{m^*}{2\hbar^2}\left(J_0(k|\mathbf{r}'-\mathbf{r}|) + iY_0(k|\mathbf{r}'-\mathbf{r}|)\right)$ where J_0 (Y_0) is the Bessel function of the first (second) kind. The final step is to solve the system of equations, Eq. (2.15) and Eq. (2.16) by Eq. (2.18) at a particular energy. The solution is then substituted into Eq. (2.9), which directly gives the STM signal through Eqs. (2.5) and (2.6).

The theory just developed applies equally well to electrons or holes near the Fermi energy. Although the STM tip is the source (or sink in the case of positive bias, i.e., the tip has larger voltage) of electrons (or holes), we have not made one correction that in principle is present, namely any residual unscreened potential felt by an electron near the STM tip. In fact the tip itself can be thought of as a source of scattering, causing disturbances to any electron passing under it. However, we have so far not seen any experimental evidence indicating this correction is needed.

2.4 Application to Quantum Corrals

The scattering theory of Sec. 2.3 may be directly applied to quantum corrals. Here we discuss the case of Fe atoms on Cu(111)[2] which do not show a Kondo effect at 4 K. Our goal is to calculate the standing wave patterns and corral spectroscopy of the type first observed by [1]. To do so we pull together the results of Sec. 2.1, 2.2 and 2.3. Since we know the dispersion relation, Eq. (2.1), for the Cu(111) surface as well as the positions of the iron impurities from STM measurements, all that remains to determine the current and conductance at a given position is a determination of the phase shift, $\delta(\epsilon)$, of the Fe atoms. Once $\delta(\epsilon)$ is determined, the LDOS$(\mathbf{r}, \epsilon)$ is determined everywhere by the scattering theory except within 7 Å of an adatom, where there is extra charge density not accounted for in the theory. Electron amplitude from the STM tip is assumed to emanate in a circularly symmetric fashion into the surface states, so we use the outgoing free Green's function, $G_0^{\rm ret}(\mathbf{r}', \mathbf{r}, \epsilon) = -i\frac{m^*}{2\hbar^2}\left(J_0(k|\mathbf{r}' - \mathbf{r}|) + iY_0(k|\mathbf{r}' - \mathbf{r}|)\right)$, as the incident amplitude.

Early measurements[15] of single iron impurities on the surface of Cu(111) pointed to a phase shift near -80^o. However, from Eq. (2.17), it is clear the the Green's function is invariant with respect to a phase shift of π, so the phase shift could equally well have been near $+100^o$. When the scattering theory was applied with a phase shift of $+100^o$ to circular corrals to compute dI/dV, Eq. (2.6), the widths of the resonances were far too narrow compared to experiment, indicating a longer electron confinement than was actually inferred from the broader, measured linewidths. The important insight[2] was that the resonances could be broadened if one allows electron amplitude to be absorbed from the surface states at the Fe impurities. A phase shift of nearly $+100^o$ is quite close to $+90^o$. This leads to

$$s_i(\epsilon) = \frac{4i\hbar^2}{m^*}(e^{2i\delta_i(\epsilon)} - 1) \xrightarrow{\delta=\frac{\pi}{2}} \frac{4i\hbar^2}{m^*}(-2) \; . \tag{2.19}$$

On the other hand, if the Fe atoms are assumed to be maximally absorbing "black dots"[2], $\delta = i\infty$, so that

$$s_i(\epsilon) = \frac{4i\hbar^2}{m^*}(e^{2i\delta_i(\epsilon)} - 1) \xrightarrow{\delta=i\infty} \frac{4i\hbar^2}{m^*}(-1) \; , \tag{2.20}$$

and so that the overall scattering amplitude has the same phase but is reduced by a factor of 2. Thus, the two phase shifts, $\delta = \frac{\pi}{2}$ and $\delta = i\infty$, are equivalent except that the "black dot" approximation, $\delta = i\infty$, leads to an attenuation of the scattered wave and a broadening of corral resonance widths. When $\delta = i\infty$ is used to evaluate the LDOS$(\mathbf{r}, \epsilon)$, at the center of a circular quantum corral the agreement with experiment is excellent. Fig. 2.3 shows a direct comparison between theortical and experimental dI/dV curves for a 88.7 Å diameter, 60-atom circular corral of Fe atoms on the Cu(111) surface. Note that except for the first peak[2] the agreement with experiment is excellent. Both the resonance energies and the widths of the resonances

---

[2] The first peak has been investigated in more detail by [16].

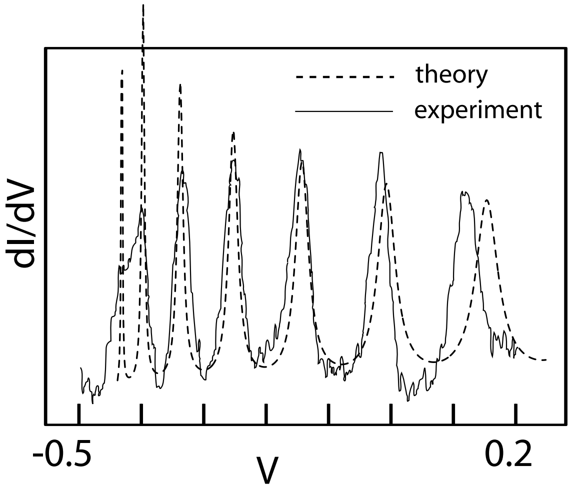

Figure 2.3: Figure courtesy of Rick Heller. The experimental and theoretical voltage dependence of dI/dV, with the tip of the STM located at the center of an 88.7 Å diameter, 60-atom circular corral of Fe atoms on a Cu(111) surface. The experiment has a smooth background removed.

are remarkably alike and scale together except for the highest energy peak[3]. Fig. 2.4 shows a comparison between theory and experiment for a "topographic" image for a cut across the diameter of the same circular corral. Note again the excellent agreement: Every experimental oscillation is quantitatively reproduced by the scattering theory. Finally, the full standing wave patterns for both theory and experiment for a "stadium" shaped quantum corral are shown in Fig. 2.5.

The Fe adatoms can be located only at the available triangular lattice sites in the Cu(111) surface. This lattice allows arcs, ellipses, and other shapes to be only approximated. The locations where one can place atoms can be seen in Fig. 2.6, for

---

[3] The scattering theory can be brought into nearly perfect agreement with even the highest energy peak by allowing for a quartic correction to the parabolic dispersion, Eq. (2.1)[17].

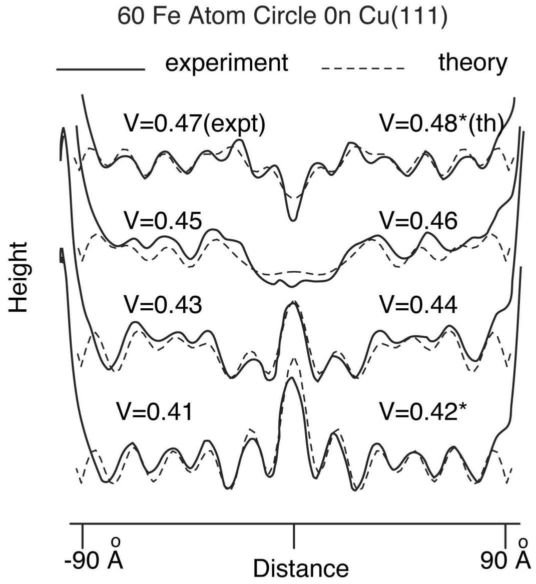

Figure 2.4: Figure courtesy of Rick Heller. The experimental data and theoretical curves for the tip height as a function of position across the diameter of a circular corral (88.7 Å diameter, 60-atoms) for low bias. Various voltages are given; they are measured relative to the bottom of the surface state band.

the case of a 48 atom stadium, where the smooth boundary is drawn for comparison. It is important to put in the correct atomic positions in order to get the best agreement with the experiments. The corral walls, while acting like smooth (although absorbing) bondaries for some purposes, still reveal their roughness and granularity.

We now turn to a physical interpretation of the "black dot" approximation. If electron flux is absorbed at the Fe atoms where does it go? We believe that much of the lost surface state amplitude goes into to the bulk[4]. This idea has been supported by theoretical studies of [18] and [19]. Shortly after the work of [2], [20] developed an elastic scattering theory of quantum corrals. The elastic theory was able to qualitatively reproduce the standing wave patterns inside the corrals but

---

[4] Spin-flip processes at the Fe impurities would also appear as a loss of coherent amplitude.

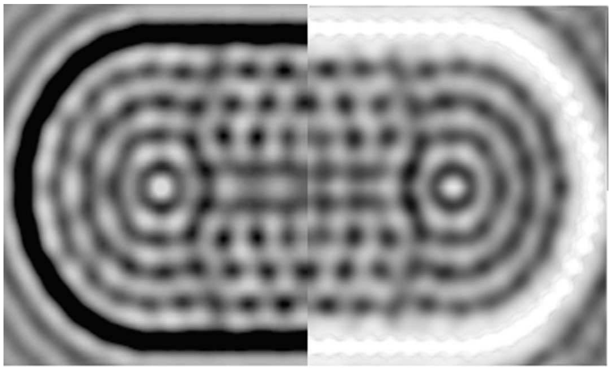

Figure 2.5: Figure courtesy of Rick Heller. Local density of electron states (LDOS) near E_F for a 76 Fe atom "stadium" of dimensions 141 × 285 Å. Right Hand Side: Experiment, bias voltage 0.01 V (ϵ=0.45 eV); Left Hand Side: Theory (ϵ=0.46 eV). The density near the center of the Fe adatoms is not accounted for in the theory and appears black.

does relatively poorly compared to the scattering theory for dI/dV. (See Fig. 3 in [20].) The inelastic scattering theory presented here accounts properly not only for the widths of the resonances in corrals but also gives the height, weight and energy dependence of the resonances and resonance widths much more accurately than the elastic theory of [20]. For this reason we believe that a purely elastic theory which ignores the presence of the bulk states is incorrect. One should also note the possibility of spin flip upon the electron's interaction with the Fe adatom; this would only add to the decoherence of the electron and bring the absorbing s-wave, black dot assumption closer to actuality.

It is important to summarize what we have learned from the application of scattering theory to quantum corrals thus far: (i) Corrals do confine electrons in surface states, but do so rather poorly (resonance widths are broad) because the adatoms tend to couple surface states quite strongly to bulk states. A host

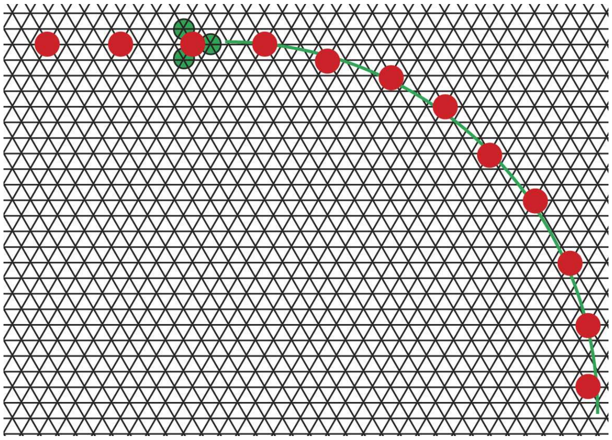

Figure 2.6: Shown is a grid of the underlying lattice of the Cu(111) surface. Adatoms cannot site at exact ellipse positions, but must site on the nearest site of the underlying lattice. When the exact positioning of the adatoms in taken into account, the agreement with experiment is enhanced.

of studies[18, 19, 12, 7, 21] suggest that it is quite generic for adatoms to strongly couple surface states to bulk states. (ii) The standing wave patterns in corrals depend on coherent electron propagation in the surface states to give interference effects. For temperatures below 70 K, the coherence length of surface state electrons on noble metals is hundreds of Angstroms[22], while the corrals typically have maximum dimensions on the order of a hundred Angstroms thus allowing coherent electron propagation across the corrals. (iii) “Particle-in-a-box” models[1] may qualitatively agree with the observed resonance energies of closed structures, but they have no predictive power for resonance widths or standing wave patterns in open structures. Scattering theory works equally well for one atom as for any arbitrary arrangement of any number of atoms (provided the structure is small enough to allow coherent electron propagation across it). (iv) The only place the scattering theory fails to agree with experiment is within 7 Å of an atom. Here the assumptions of the theory break down because the extra charge density at the impurity is not properly accounted for.

One comment is in order on the multiple scattering theory. As simple as it is to invert a matrix of the dimension equalling the total number of atoms to obtain the Green's function, it is still perhaps curious to do a multiple scattering expansion in terms of $0, 1, 2, \ldots$ scattering events. It turns out that this fails for typical configurations, due to the presence of closely spaced pairs, triplets, etc., of atoms. Even though the Q-factor of the cavity, as indicated for example by the line widths of the dI/dV resonances, is only around 2, suggesting about two bounces are important before leakage occurs, the Q-factor and the low order of scattering is an appropriate concept only for walls thought of as smooth scattering units, with the local multiple internal scattering between neighboring atoms included to infinite order.

If one performs a calculation for a plane wave of appropriate wavevector impinging normal to a line of Fe adatoms at the closets experimental Fe atom spacing, one finds that only about 25% of the amplitude is coherently backscatted (also normal to the line), while 25% is transmitted, and 50% is lost to decohering inelastic events.

The scattering theory does not have to confine itself only to atomic surface impurities. The experiments abound with step edges for example, even though one looks for regions as far away as possible from such defects to build corrals. The step edges affect the images, although not so much inside closed corrals, which have enough attenuation at the wall to prevent those paths which begin inside the corral, get out, hit an edge, and come back inside from having any important weight.

Chapter 3

Essentials of Kondo Physics

3.1 The Anderson Model

The Kondo effect[1] is the name given to the low energy response of the Fermi sea of a metal to a magnetic impurity. In the mirage experiments, the magnetic impurity (Co) sat on the surface of Cu(111). The canonical (and simplest) model[2] of a local magnetic moment in a metallic host was given by [27],

$$\begin{aligned} \hat{H}_{\text{Anderson}} = \sum_{k,\sigma} \epsilon_{k\sigma} \hat{n}_{k\sigma} &+ \sum_{\sigma} \epsilon_d \hat{n}_{d\sigma} + U \hat{n}_{d\uparrow} \hat{n}_{d\downarrow} \\ &+ \sum_{k,\sigma} (V \hat{c}^{\dagger}_{k\sigma} \hat{d}_{\sigma} + h.c.) \ . \end{aligned} \tag{3.1}$$

The first term represents the energy of the electrons of the Fermi sea (assumed to be non-interacting), the second term represents the energy of a single localized site (an approximation to the d or f atomic level of an atom), the third term represents an

---

[1] For an overview of Kondo effect and a list of references see [23]. For a brief survey of the Kondo effect in *mesoscopics* see [24] and references therein.

[2] The Anderson model applies to a spin $S = 1/2$ impurity. However, it can be shown[25] that impurities of higher spin can be treated with an effective spin $S = 1/2$ model. For a discussion of the Kondo effect for spin $S > 1/2$ see [26].

on-site repulsion if two electrons try to occupy the localized level, and the last term represents hybridization between the local moment and the conduction electrons. Here $\epsilon_{k\sigma}$ ($\hat{n}_{k\sigma}$) is the energy (number operator) of an electron of the Fermi sea with wavevector k and spin σ and ϵ_d ($\hat{n}_{d\sigma}$) is the spin degenerate energy (number operator, not generally spin degenerate) of an electron in the localized d or f-level with spin σ. Here U represents the charging energy of doubly occupying the localized level. In the fourth term, V is the hopping matrix element connecting the electrons of the Fermi sea to the localized impurity level and vice versa, and $\hat{c}^{\dagger}_{k\sigma}$ ($\hat{d}^{\dagger}_{\sigma}$) is the creation operator for an electron in the state with wavevector k (d or f-level) with spin σ.

In the case $V = 0$, Eq. (3.1) can be solved exactly. The states are just direct products of the local moment states and the Fermi sea. The energy is just the sum of the energy of the Fermi sea and the energy of the electron(s) on the localized level. The energy cost for having one electron on the localized level is ϵ_d and the cost for adding the second is $\epsilon_d + U$. If one considers a small nonzero V, the Hamiltonian is no longer exactly solvable. The singly and doubly occupied states of the local level will be broadened (by an amount that can be estimated by Fermi's Golden Rule, $\Gamma \approx 2\pi V^2 \varrho_0$, where ϱ_0 is the density of states of the Fermi sea at the Fermi energy). For the Kondo problem one particular regime of Eq. (3.1) is of central importance: the case where $\epsilon_d < E_F$ and $\epsilon_d + U > E_F$. This is shown in Fig. 3.1. [27] showed that Eq. (3.1) will lead to local moment formation at low enough temperatures when $\Gamma \approx 2\pi V^2 \varrho_0 \ll |\epsilon_d|$, $\epsilon_d + U$.

The impurity (d-level) density of states in the Anderson model in the local

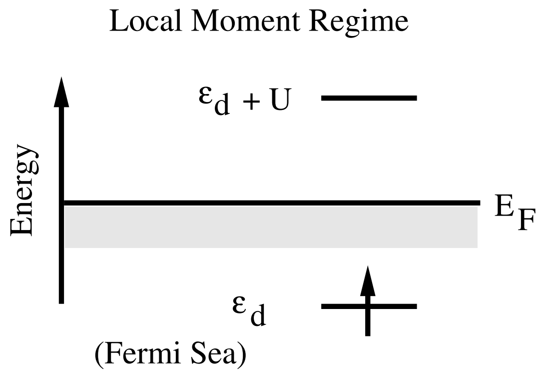

Figure 3.1: Local Moment Regime of the Anderson Model. The Kondo effect occurs when the impurity level energies are situated as shown. The spin degenerate singly occupied level has energy $\epsilon_d < E_F$. The cost for adding the second electron of opposite spin to the impurity level is $\epsilon_d + U > E_F$. Thus, the impurity ground state has only one electron electron on the local level giving it a net spin.

moment regime we have just discussed is shown in Fig. 3.2. The peak in the density of states at zero bias is sometimes referred to as the "Kondo" peak[23]. The Kondo peak always sits near the Fermi energy and corresponds to the formation of the *many-body* Kondo state. It is this peak that shows up in the form of a "Fano resonance" in the dI/dV spectra near (within 10 Å) a Kondo atom on the surface of a metal[10, 11, 3, 25, 28, 29]. Although the Kondo resonance is associated with many-body correlations of the Fermi sea and has no single-particle level analagous to the two spectral peaks corresponding to the bare levels at ϵ_d and $\epsilon_d + U$ in Fig. 3.2, it still *behaves* as a single-particle resonance when it is fully formed at $T \ll T_K$[30, 25, 29]. It is this single-particle like behavior or "local Fermi liquid theory"[30] of the Kondo resonance that allows us to use a single-particle scattering theory for the mirage experiments. The density of states of Fig. 3.2 translates into a strongly energy dependent phase shift for electrons of the Fermi sea near the Fermi energy [23]. For a single impurity

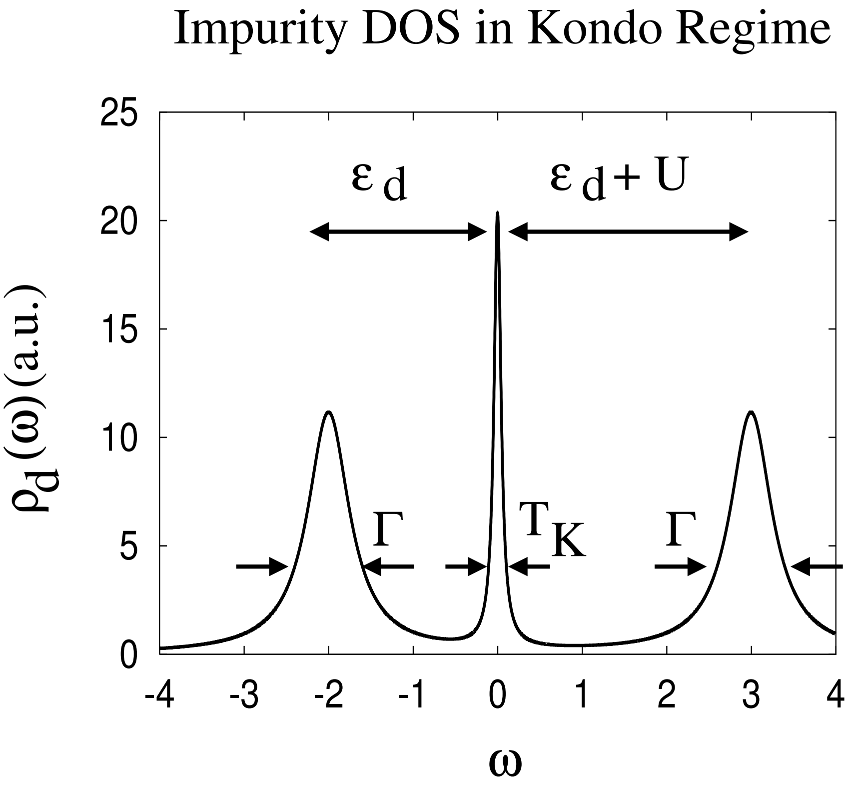

Figure 3.2: Density of States of the Anderson Impurity Model in the Kondo Regime.The figure is not an actual calculation but illustrates the central features of the density of states in the Kondo regime. Both axis are in arbitrary units, but for a real system energy units of eV would not be unrealistic. The broad upper and lower peaks (at energies ϵ_d and $\epsilon_d + U$) have width $\Gamma \approx 2\pi V^2 \varrho_0$. These peaks are due to single-particle energy levels of the impurity. They are broadened by coupling to the Fermi sea. The central peak is a many-body resonance sometimes called the "Kondo peak". It arises from correlations beyond a mean-field calculation such as Hartree-Fock and its width is exponentially small in the coupling parameter $J\varrho_0$, $T_K \sim De^{-\frac{1}{2J\varrho_0}}$.

in a host (or on the surface) the density of states is (to a good approximation) just the sum of the two: $\varrho(\epsilon) = \varrho_0(\epsilon) + \varrho_{\mathrm{imp}}(\epsilon)$. Therefore, the change in the density of states due to the impurity is $\Delta\varrho(\epsilon) \equiv \varrho(\epsilon) - \varrho_0(\epsilon) = \varrho_{\mathrm{imp}}(\epsilon)$. It can be shown to be equal to[23]

$$\Delta\varrho(\epsilon) = \frac{1}{\pi}\frac{\partial\delta(\epsilon)}{\partial\epsilon} \; . \tag{3.2}$$

The resonance at the Fermi energy in Fig. 3.2 can be approximated as a Lorentzian and leads to a $\tan^{-1}$ in the phase shift $\delta(\epsilon)$ of Eq. (2.17) when Eq. (3.2) is integrated over energy. It is highly non-trivial that one can treat a many-body problem like the Kondo effect phenomenolgically with a single-particle theory and a resonant phase shift. It is the single most important reason for the sucess of our approach to the quantum mirage.

3.2 The Kondo Model

The Kondo model is a special limit of the Anderson model, Eq. (3.1), valid in the local moment regime shown in Fig. 3.1. It was used by J. [31] (hence the name) to explain the minimum in the resistivity (as a function of temperature) of metals with magnetic impurities. The Kondo model can be derived by second order perturbation theory in V from the Anderson model[3]. The Kondo Hamiltonian (including a purely potential scattering term that also appears in second order perturbation theory) is

$$\begin{aligned} \hat{H}_{\mathrm{Kondo}} = \sum_{k,\sigma} \epsilon_{k\sigma}\hat{n}_{k\sigma} \quad &+ \quad J\sum_{k,k'} \hat{S}\cdot\hat{c}^{\dagger}_{k\sigma}\frac{\vec{\tau}_{\sigma\sigma'}}{2}\hat{c}_{k'\sigma'} \\ &+ \quad K\sum_{k,k',\sigma} \hat{c}^{\dagger}_{k\sigma}\hat{c}_{k'\sigma} \; , \end{aligned} \tag{3.3}$$

---

[3] This result was first derived by [32].

where the first term is the same as in Eq. (3.1),

$$J \approx V^2 \left(\frac{1}{U + \epsilon_d} - \frac{1}{\epsilon_d} \right) > 0 \,, \tag{3.4}$$

and

$$K \approx -\frac{V^2}{2} \left(\frac{1}{U + \epsilon_d} + \frac{1}{\epsilon_d} \right) . \tag{3.5}$$

Here $\hat{S}$ is the spin operator of the impurity and $\vec{\tau}$ are the Pauli spin matricies. The crucial feature of Eq. (3.3) is that it leads to spin-flip scattering events[4] through terms like $S_x \tau_x + S_y \tau_y = (S_+ \tau_- + S_- \tau_+)/2$. Kondo's explanation of the divergence comes by looking at the effect of the second term of Eq. (3.3) in a second-order perturbative calculation of the *t-matrix*. It turns out that because $S_+ S_- \neq S_- S_+$ one of the sums over the intermediate states of the Fermi sea is cut off at the Fermi surface, leading to a logarithmic divergence in the resistivity[31, 23].

Besides the features of the Kondo problem we have already mentioned, one more result is worthy of note. In order to understand the low energy behavior of many physical systems it is often useful to integrate out the high energy fluctuations and compensate for this by "renormalizing" the parameters of an effective low energy theory. This can be quite complicated in general, but for the Kondo Hamiltonian a particularly simple version known as "poor man's scaling", introduced by[33], can be used to identify the low energy properties[23]. The idea is to look again at the second order contributions to the second term of Eq. (3.3) to the *t-matrix*. The sum

---

[4] These spin-flip scattering events can also be looked at from the point of view of the Anderson model. A spin-flip would occur if, e.g., the intial electron on the local level were spin up, a second spin down electron hopped on in the intermediate state and then finally the original spin up electron hopped off leaving behind the spin down electron on the local level.

over the intermediate states of the conduction electrons contains electrons that are at the band edges. Anderson suggested removing a few states at the band edges and adjusting J so that the scattering amplitude remains invariant (ignoring the potential scattering terms). When this is done a set of "scaling equations" is generated for J which can then be solved. It turns out that a "scaling invariant" appears and it is generally denoted by T_K and referred to as the Kondo temperature:

$$T_K \sim De^{-\frac{1}{2J\varrho_0}} \; . \tag{3.6}$$

The quantity T_K is invariant under a rescaling of J in response to a shrinking of the bandwidth, D. As $D \to 0$, $J \to \infty$, which from the second term of Eq. (3.3) implies that the spin-flip processes are "frozen out" in the low energy theory and the scattering becomes purely potential scattering. As before, ϱ_0 is the density of states of the host at the Fermi energy. The Kondo effect, in this simplest of models, is thus characterized by only one energy scale, T_K. This is the width of the "Kondo peak" that appears in the low temperature density of states of the Anderson model in Fig. 3.2, the width of the Fano resonance[10, 11, 3, 34, 25, 28, 29] and it is also the width of the scattering resonance[12], from Eq. (3.2), of the Co atoms (for experimental temperatures lower than T_K when the Kondo resonance is well formed) on the surface of Cu(111).

Chapter 4

Scattering Theory of Quantum Mirages

4.1 Elliptical Quantum Corral Mirages

In the Kondo effect a magnetic impurity in metallic bulk or on a metallic surface has its local moment screened by a cloud of conduction electrons, called the Kondo cloud, that forms in its vicinity[23]. Until recently, only bulk measurements were possible on Kondo systems, leaving isolated Kondo atoms and their scattering phase shifts unstudied. The atomic resolution of the STM now makes the study of single, isolated Kondo atoms possible [3, 10, 35]. Kondo adatoms are identified by a sharp (~ 10 meV wide) feature in the differential tunneling conductance (dI/dV) as a function of STM tip bias with respect to the surface of the material. The feature typically appears as a dip near the Fermi energy (E_F) in dI/dV, is localized to within

$\sim$ 10 Å of a Kondo impurity and is only observed at low temperatures ($\sim$ 4 K). If the temperature of the substrate becomes to high ($\sim$ 100 K), the correlations between the impurity spin and the conductions electrons are broken and the Kondo signature disappears.

Landmark STM experiments have recently discovered the remarkable fact that when a Kondo atom(Co, for example) is placed at one focus of a properly sized empty elliptical quantum corral built from Kondo adatoms, a "mirage" of the Kondo feature is cast to the opposite focus [3] more than 70 Å away. Since the Kondo effect arises from electron correlations, what does the Kondo feature at the unoccupied focus imply about local electron correlations there? An important feature of the mirage experiments is that they were done on the surface of Cu(111) which is known to have surfaces states which act as a 2-dimensional electron gas. The central result of this Letter is to present a theory of the Kondo mirage based on electrons in this surface state scattering to infinite order from all Kondo atoms–both the Kondo atoms that make up the walls of the corral and the Kondo atom that sits at the focus. The theory is valid for all arrangements of adatoms, whether arranged in a corral shape or any other arbitrary structure including "open" structures. Electron scattering on the surface can be directly related to the dI/dV of the STM measurements. Thus, by solving the electron scattering problem on the surface in the presence of impurities we can compute the STM conductance[2].

The basic Hamiltonian in the Kondo problem is given by

$$\hat{H} = \sum_{\mathbf{k}\sigma} \epsilon_k c^\dagger_{\mathbf{k}\sigma} c_{\mathbf{k}\sigma} + \frac{J}{N} \sum_{\mathbf{k},\mathbf{k}'\sigma\sigma'} \mathbf{S} \cdot \tau_{\sigma\sigma'} c^\dagger_{\mathbf{k}\sigma} c_{\mathbf{k}'\sigma'} \tag{4.1}$$

where ϵ_k is the dispersion relation (given by band structure calculations or experiment) of the conduction electrons, $c^\dagger_{\mathbf{k}\sigma}$ is an operator that creates an electron in the state $\mathbf{k}$ with spin σ and $c_{\mathbf{k}\sigma}$ destroys an electron in the state $\mathbf{k}$ with spin σ. This first term describes the energy of free conduction electrons. The second term describes spin-flip scattering processes where a conduction electron flips its spin and the impurity changes its spin in response during a scattering event. N is the number of sites in the lattice, J is the coupling constant, $\mathbf{S}$ represents the impurity spin and $\tau_{\sigma\sigma'}$ represents the conduction electron spin. It is well known that the Kondo effect occurs when $J > 0$ [23] and the low energy properties of this Hamiltonian are described by an effective Hamiltonian with $J \to \infty$ so that the conduction electrons become "locked" into an anti-aligned state with the impurity moment. Spin-flip process are thus frozen out. We do not attempt to solve this Hamiltonian, but assume that we are working in the low temperature regime where spin flips are frozen out as experiment suggests from the feature in dI/dV described in Refs[2-4].

In the Fermi liquid description of Kondo impurities below their Kondo temperature, T_K, the impurities may be characterized by a scattering phase shift that they impart to impinging electrons (quasi-particles) [30]. For $T << T_K$ Kondo impurities act as potential scatterers with all the many-body physics appearing as an energy scale in the (resonant) scattering phase shift[23, 30]. We apply our theory to experimental data to extract the phase shift with full energy dependence of a single Kondo atom, report its value and present calculations that show beautiful *quantitative* agreement with experiment. Our theory clarifies what the STM does and does not measure in mirage experiments regarding local correlations of electrons. In particular, our theory suggests that the mirage experiments do not probe local electron-electron correlations because the Kondo correlations only appear in the theory as an energy scale, T_K, in the scattering phase shift (or alternatively, in the density of states).

We emphasize that our theory is phenomenological in that we do not attempt to compute the tunneling conductance from first principles on top of an atom as was done in[34, 28]. Our theory is based on electron scattering which is by its nature asymptotic–an electron comes in, strikes a Kondo adatom, and leaves with a phase shift. Therefore, our theory only makes accurate quantitative predictions when the STM tip is more than 7 Å away laterally from a Kondo adatom on the surface. This is precisely the region where we can make accurate predictions about the quantum mirage with our theory. When the STM tip is within 7 Å laterally of an impurity there is accumulated screening charge and orbital density present that is not accounted for in our theory and thus the theory has no predictive power there.

When an STM tip is biased negatively with respect to the surface of a metal, such as Cu(111), electrons can tunnel from the tip onto the surface, creating a region of enhanced electron amplitude under the tip which travels outwards as a wave on the surface. Heller *et al.*[2] showed that because the Fermi wavelength of the surface state electrons on Cu(111) is much larger than the size of adatoms and because the adatoms are separated by a distance large compared to their size, it is permissible to use a multiple s-wave scattering expansion to calculate the electron amplitude on the surface. In this picture, the scattered electron wave, and therefore the STM signal, are determined by a single quantity: the s-wave phase shift of the scattered wave, $\delta_0(\epsilon)$, which will typically be complex. The imaginary part of the phase shift represents "absorption" (incoherent scattering of electrons) by the adatoms which tend to couple surface states to bulk states[2, 19, 18] resulting in a loss of electrons from the surface states.

To compute dI/dV from a scattering calculation, we follow the method of Heller *et al*[2]. For s-wave scattering from a single adatom in two dimensions, the wave function is [36],

$$\psi(\mathbf{r}) \rightarrow \phi(\mathbf{r}) + f\frac{e^{i(kr-\frac{\pi}{4})}}{\sqrt{r}} \ , \tag{4.2}$$

where the scattering amplitude, f, is $f = \frac{e^{2i\delta_0(\epsilon)}-1}{\sqrt{2\pi k}}$. $\phi(\mathbf{r})$ is the amplitude of the circular electron wave emanating from the STM tip. There is no angular dependence of f in the s-wave approximation. $k = \frac{2\pi}{\lambda}$, where λ, the wavelength of the electrons on Cu(111), is 29.5Å. $\epsilon(k) = \frac{\hbar^2 k^2}{2m^*}$ is known from the surface state electron dispersion relation of Cu(111) which has an effective mass of $m^* = 0.38 m_e$. Once $\delta_0(\epsilon)$ is determined, the surface scattering can be computed. In the limit of small bias voltages and low temperature[8],

$$\frac{\mathrm{dI}}{\mathrm{dV}} \propto \mathrm{LDOS}(\vec{r}, \epsilon) = \sum_{\nu} |\psi_\nu(\vec{r})|^2 \delta(E_\nu - \epsilon), \tag{4.3}$$

where ϵ is the energy determined by the bias voltage V and the Fermi energy E_F, via $\epsilon = \mathrm{E}_F + e\mathrm{V}$; ν labels the scattering eigenstates in the presence of the adatom. When several or many adatoms are present as in this paper, a multiple scattering approach [2] is used to compute $\mathrm{LDOS}(\vec{r}, \epsilon)$. By definition the LDOS is related to the Green's function by

$$\mathrm{LDOS}(\vec{r},\epsilon) = -\frac{1}{\pi}\mathrm{Im}[G_{\mathrm{ret}}(\vec{r},\epsilon)] \ , \tag{4.4}$$

where

$$G_{\mathrm{ret}} = G_0 + G_0 T G_0 \tag{4.5}$$

is the retarded Green's function and T is the T-matrix whose dimensions are N by N when there are N scatterers present. The T-matrix contains all the information about the physical positions of the scatters relative to each other and their corresponding phase shifts which could be different for each scatterer. $G_0(\vec{r},\epsilon)$, is the free electron's Green's function in two dimensions. Thus, dI/dV of the STM may be obtained by solving the scattering problem.

Our theory, then, involves the following approximations, assumptions and limitations: (i) The scattering of electrons from the adatoms is determined by a single parameter, the s-wave phase shift, and this must be determined from experiment or otherwise (ii) The internal degrees of freedom (spin) of the Kondo adatoms are frozen out at the temperature of the experiment ($\sim$ 4K) so we may use the results of Nozieres[30] to treat the Kondo atom as a potential scatterer with a phase shift (iii) The adatoms are far enough apart so that we may treat the electron propagation between them as free and that RKKY interactions are sufficiently weak so that the single-impurity Kondo physics is not altered (iv) The theory does not include any non-equilibrium effects and does not treat the charge density right at an atom correctly.

To make a direct comparison with experiment, we must obtain the phase shift of the Kondo adatoms. We do not have an *ab initio* calculation of the phase shift of a single Co adatom. Rather, we fit the resonant form of the phase shift, including inelasticity, and calculated the multiple scattering problem with this single atom data.

Since the on-atom electron orbital density is not accounted for in scattering theory, we used an on-atom fit (from experimental data of a single, isolated Co atom on Cu(111) at 4K) involving only a renormalization of the free-space Green's function and a change in the background phase shift to compute the STM signal on top of a Kondo adatom[34, 28]. This on-atom fit is not part of our theory, but only a means of setting a reference point between on-atom density not accounted for in our theory and the electron density anywhere more than 7 Å away from an atom on the surface which *is* accounted for properly in our theory. This fit in no way compromises our fundamental result that the mirage is due to resonantly scattering electrons from the Kondo atoms of the walls and focus. It is used only as a method to determine as accurately as possible the phase shift of the Co on Cu(111). Determining the phase shift this way from experimental data constitutes a measurement of the single Kondo atom phase shift. We find a good fit to the s-wave phase shift to be

$$\delta_0(\epsilon) = \delta_{bg} + i\delta'' + \tan^{-1}(\frac{\epsilon - \epsilon_0}{\Gamma/2}) \ , \tag{4.6}$$

where $\delta_{bg} = \frac{\pi}{4} \pm \frac{\pi}{10}$, $\delta'' = \frac{3}{2} \pm \frac{1}{4}$, $\Gamma = (9 \pm 1)$ meV and $\epsilon_0 = E_F$ -1 meV are determined by experiment. δ_{bg} is a background phase shift (possibly due to static charge screening at the impurity) that controls the resonant line shape of the adatom scattering cross-section. δ'' is a measure of the inelasticity in adatom scattering and controls the attenuation of the mirage at the empty focus. $\mathrm{Tan}^{-1}(\frac{\epsilon-\epsilon_0}{\Gamma/2})$ reflects resonant scattering due to the presence of Kondo physics. A similar form of phase shift has been derived by Ujsaghy *et al.* from a more microscopic point of view in [25]. The narrow spectral peak near E_F leads to resonant scattering Fermi surface electrons and sets the scale of the resonance in the phase shift. It is likely that both bulk and surface states are participating in the Kondo effect at an adatom, but the STM signal is dominated by the surface state Kondo effect in the regime of validity of our theory (> 7 Å away from adatom).

Applying the theory to elliptical corrals results in the images shown in Fig. 4.1 and Fig. 4.2. The agreement with experiment is excellent. Our calculation of the tunneling spectrum at the two foci is compared with experiment in Fig. 4.3. Note that the signal at the unoccupied focus is attenuated by approximately a factor of 8, both experimentally and theoretically. The calculated spectroscopy in Fig. 4.3 most clearly demonstrates that the Kondo mirage is due only to resonant scattering of electrons from the Co adatom at the opposite focus, even though the electrons are also resonantly scattering from the wall adatoms. (Calculations performed with $\delta = i\infty$ [2] instead of $\delta_0(\epsilon)$ for the wall atoms show the wall atoms' Kondo resonances play no essential role in the projection of the mirage to the empty focus. Experimentally the same result is found when the wall Co adatoms are replaced by CO [3].) Only certain sized ellipses will give a good mirage effect–those which have large surface state amplitude at the foci when the scattering problem is calculated–and this depends on the relative size of the ellipse and λ_F. Only then will there be appreciable surface state electron amplitude at the focal adatom to give a Kondo effect in the surface

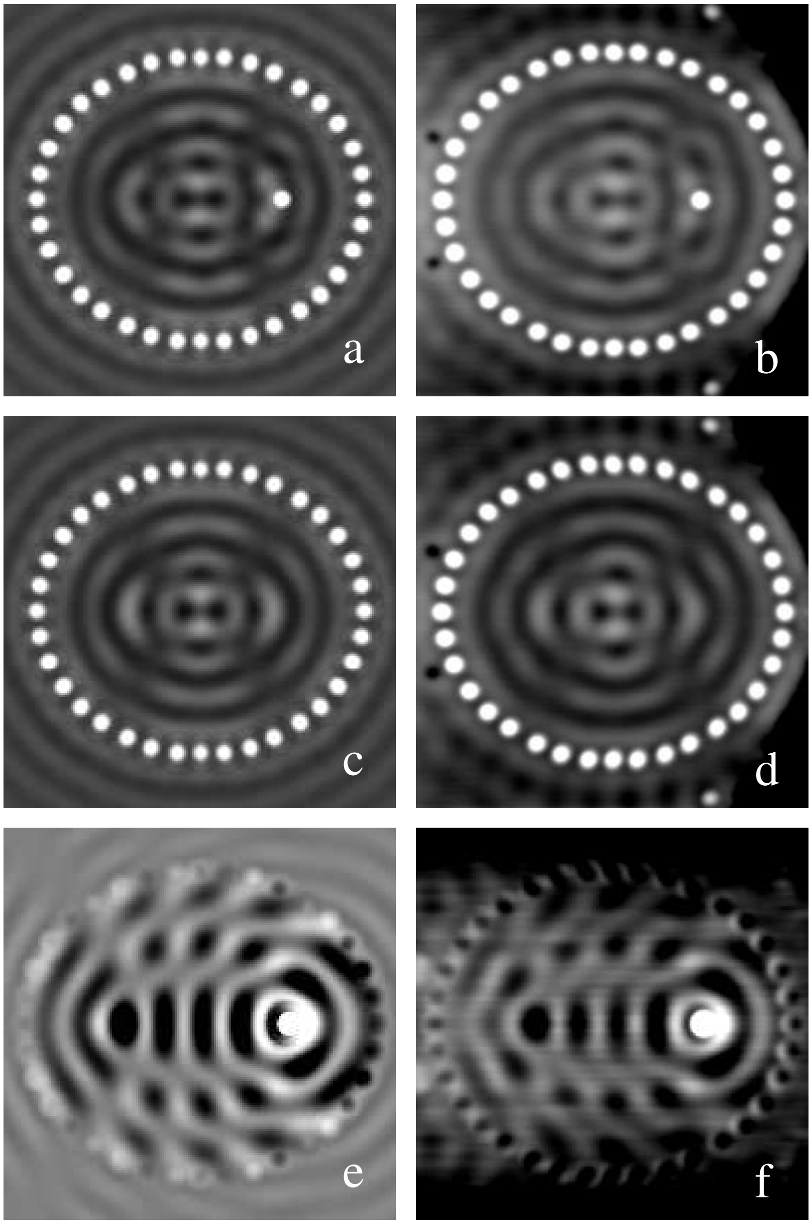

Figure 4.1: Topograph standing wave patterns of a Kondo corral. Using the scattering theory and phase shifts described in the text, these STM topograph images were computed using exact Co adatom positions on Cu(111) at 4 K. The agreement between theory (**a**, **c** and **e**) and experiment (**b**, **d** and **f**) is remarkable. All the experimental images have been symmetrized by adding the image to itself after being reflected about its major axis. Topographic images were calculated by numerically integrating the LDOS($\vec{r}, \epsilon$) over ϵ for $E_F \leq \epsilon \leq E_F + 10$ mV. This corresponds to the topographic images taken experimentally in **b** and **d** at a bias voltage of 10 mV. **e** is the difference of **a** and **c**. **f** is the difference of **b** and **d**.

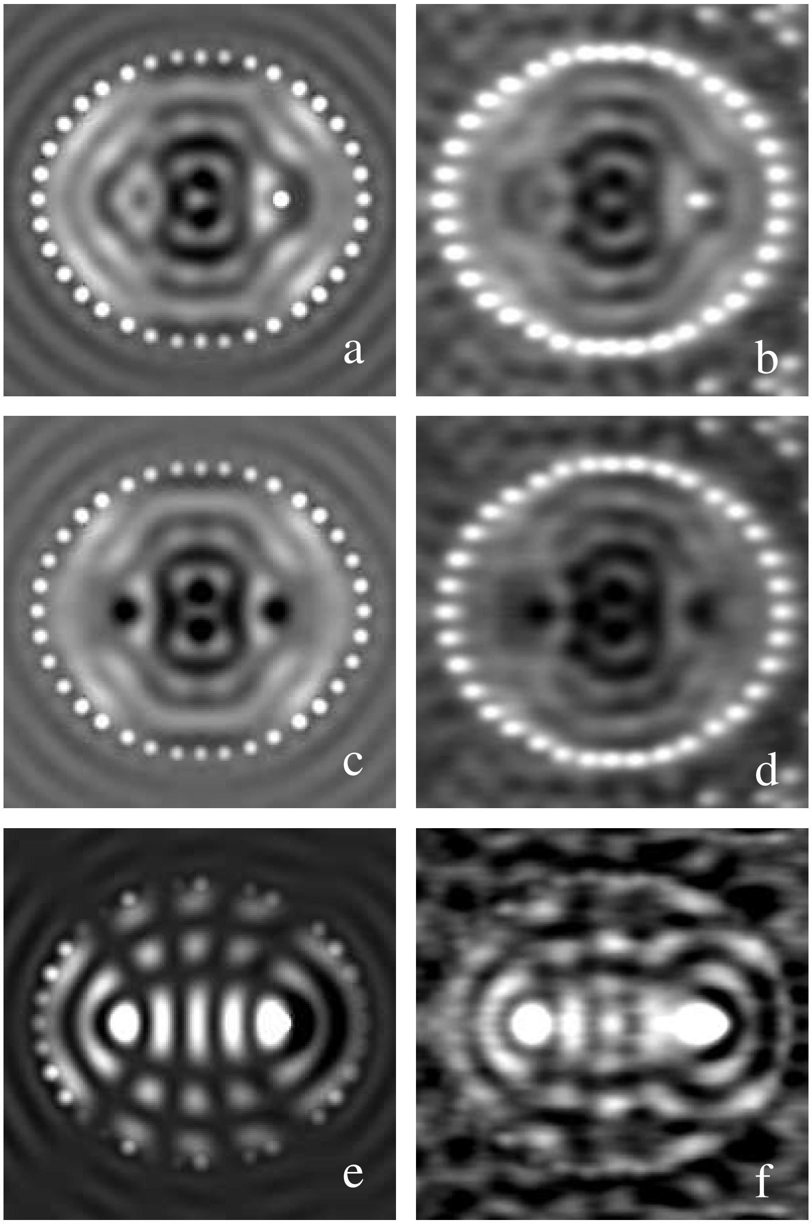

Figure 4.2: dI/dV Standing wave patterns of a Kondo corral. Same theory vs. experiment arrangement as in Fig. 4.1. dI/dV measurements were taken simultaneously with topographic images at a 10 meV bias. Note that **e** and **f** resemble an eigenstate of the ellipse. The ellipse was constructed to have large surface state amplitude at the two foci.

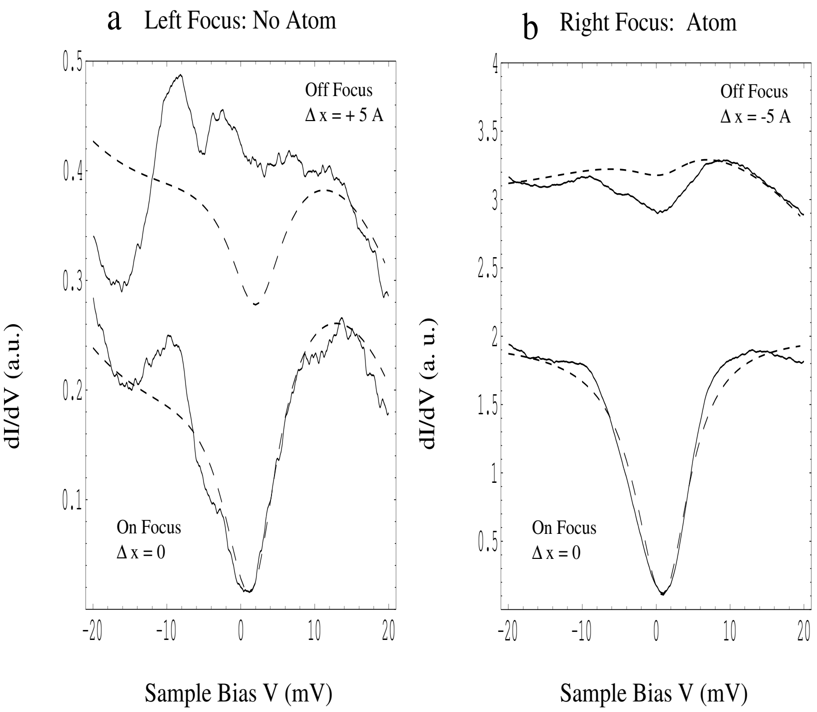

Figure 4.3: Tunneling into the focal atom and empty focus: The Mirage. Tunneling spectroscopy is calculated (dashed lines) with the scattering theory and phase shift given in the text at the empty focus **a**. Tunneling spectroscopy at the occupied focus is shown in **b**. A constant background slope has been removed from both the experimental data and the calculation. The attenuation of the mirage is determined by inelasticity in the scattering of electrons at the walls of the ellipse. The theoretical signal 5 Å away from the empty focus in **a** is lost in the noise of the experiment.

states of Cu(111). (The relative size of surface state amplitude at a given position in the ellipse also explains why the projection of the Kondo mirage is insensitive to whether the walls are Kondo (Co) or not (CO). Near the walls, this amplitude is small in ellipses that have peaked amplitude at the foci.) Our theory predicts that the Kondo mirage is not restricted to an ellipse or even a "closed" structure. Any time one can construct an arrangement of adatoms or other defects that lead to a build up of surface state electron amplitude at two locations within the electron's coherence length, a mirage can be projected.

In conclusion and returning to our original question of whether the mirage reveals any information about local correlation, we conclude that it does not. There is no explicit information about electron correlations in our theory, which gives remarkable agreement with experiment in reproducing the Kondo mirage and standing wave patterns in the elliptical corral. We are thus led to the conclusion that the mirage at the empty focus of the elliptical corral is not a result of electron correlations under the tip, but rather resonant scattering of electrons from the focal adatom and scattering (resonantly or not) from the adatoms of the walls of the corral. Intuitively this makes sense because the electrons tunneling out of the STM are unpolarized so it is not possible for the STM to give any direct information about electron spin correlations. The unpolarized STM only returns an average signal of spin up and spin down electrons tunneling into the surface.

4.2 "Kondo Lattice" Mirages

To date, only a few controlled STM studies have been reported on impurity-impurity interactions in Kondo systems. It was experimentally established by W. Chen *et al.*[37] that the formation (using the STM as an atom mover) of Co dimers on Au(111) leads to a loss of Kondo signal in the local density of states (LDOS) that would be present for an isolated Co atom[10, 11, 3, 38]. Later, V. Madhavan *et al.* experimentally found that the Kondo effect can persist at *some* (approximately 14%) Co atoms on Au(111) up to nearly a monolayer of "clustered" coverage[35]. In this section we apply the scattering theory of the previous section[12] to make contact with recent STM experiments in which Co atoms were positioned (using the STM) into a *lattice* on the Cu(111) surface[39]. The experiments of Ref. [39] were motivated by the the possibility of observing "Kondo Lattice" physics in STM experiments. A periodic array of Kondo atoms may lead to additional collective effects beyond the single-impurity Kondo effect [40] with a variety of possible ground states depending on the details of the system[41].

The lattices built by Manoharan *et al.* consisted of 18-36 Co atoms arranged on the Cu(111) surface in a triangular or square lattice pattern with a vacancy left in the center of the lattice[39]. They studied square lattice constants of 9.18, 12.7, 17.8, 25.1, 30.6 and 34.2 Å and triangular lattice constants of 8.83, 10.2 and 13.5 Å. See Fig. 4.4. These lattice constants should be compared with the Fermi wavelength of the surface state electrons of Cu(111) (29.5 Å) since this is the scale on which the

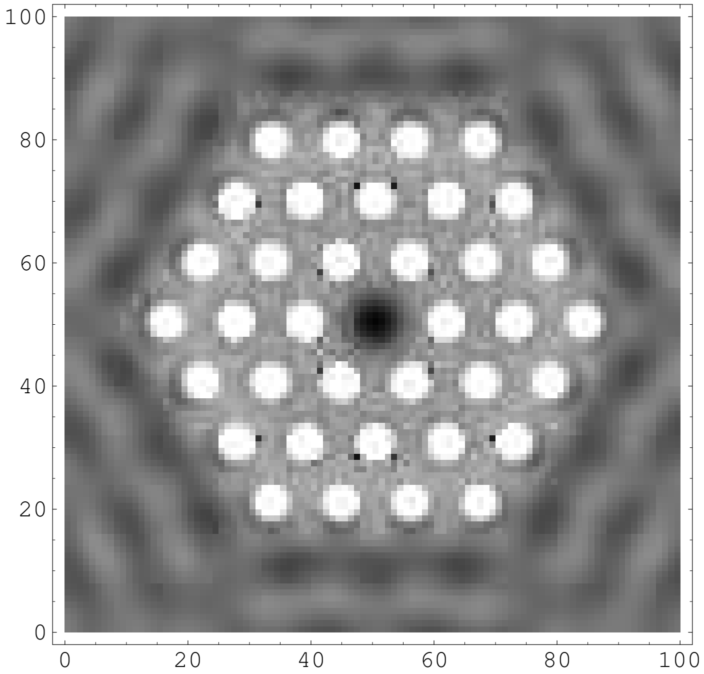

Figure 4.4: dI/dV map of triangular lattice of 36 Co atoms on Cu(111). The lattice constant is $\lambda_F/2 \approx 15$ Å. The axis labels are plotting artifacts and have no physical meaning.

spin polarization of the Fermi sea[1] should change sign[23].

The experiment is done by comparing the STM spectrum above a Co atom of the lattice with the spectrum above a Co atom on an otherwise clean surface. If there is a new energy scale associated with the lattice of Kondo atoms (there is "Kondo Lattice" physics present) this should appear in the width of the zero bias anomaly[11, 12]. The vacancy in the center of the Co lattice provides a crucial "second window" into the physics of the lattice because the STM signal in the vacancy may be compared directly with a recently developed scattering theory[12] for Co on

---

[1] Implicit in their study is the assumption that the Kondo physics is dominated by the surface state electrons rather than the bulk electrons. Recent experimental studies[38] suggest that this assumption is probably not correct.

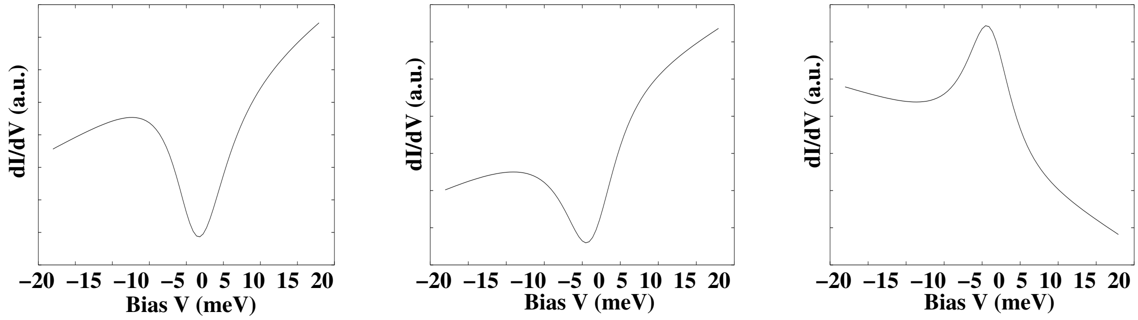

8.83 Angstroms 10.2 Angstroms 13.5 Angstroms

Figure 4.5: dI/dV spectra in the vacancy of selected triangular lattices. Lattice constants are given below each spectra. Energies are in units of meV and run from -20 meV to 20 meV. y-axis is in arbitrary units. The line shape and width are the important features. Parameters are the same as those used for the original “mirage” experiments[12].

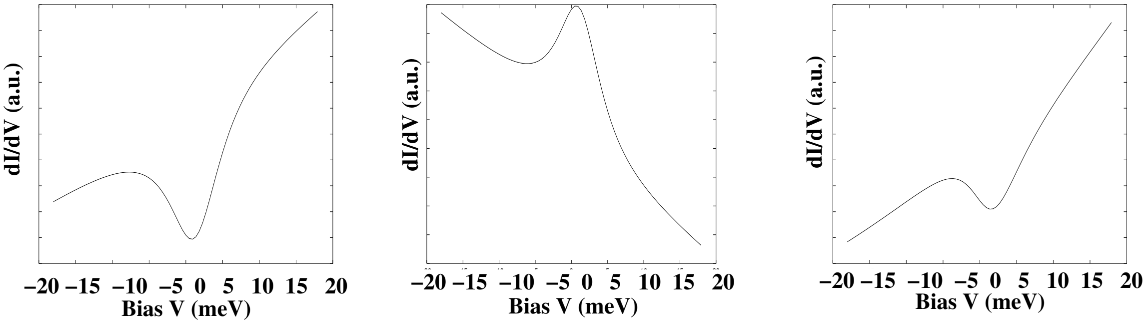

9.18 Angstroms 12.7 Angstroms 17.8 Angstroms

Figure 4.6: dI/dV spectra in the vacancy of smaller square lattices. Lattice constants are given below each spectra. Energies are in units of meV and run from -20 meV to 20 meV. y-axis is in arbitrary units. The line shape and width are the important features. Parameters are the same as those used for the original “mirage” experiments[12].

Cu(111) below the Kondo temperature. See Fig. 4.5, Fig. 4.6 and Fig. 4.6. The scattering theory assumes a single-impurity Kondo effect at each of the impurities. If the scattering theory with single Co atom parameters predicts the right dI/dV curves as well as the correct topographic images of the lattices then one can conclude the STM has not detected any evidence of “Kondo Lattice” physics in the structures.

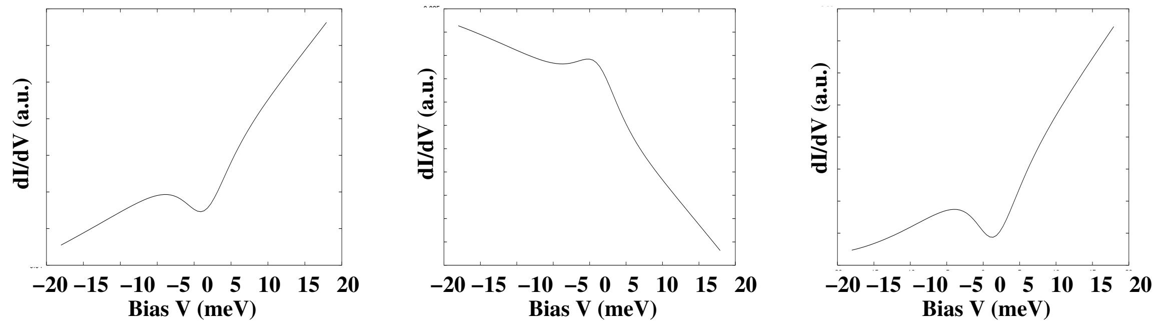

25.1 Angstroms 30.6 Angstroms 34.3 Angstroms

Figure 4.7: dI/dV spectra in the vacancy of larger square lattices. Lattice constants are given below each spectra. Axis same as above.

In the experiments both square and triangular lattices were built to allow for possible frustration effects that could occur at a given lattice spacing in a triangular lattice that would not be present in a square lattice of the same lattice constant. For example, suppose that impurity (cobalt) spin-spin correlations were established in the lattice that favored anti-alignment in nearest neighbors. In a square lattice, this could be achieved. However, in a triangular lattice, this would lead to frustration and could destroy collective lattice effects. The STM-built "Kondo Lattices" of Manoharan *et al.* were thus studied in two complementary ways: Correlation effects we searched for (i) on the top of Co atoms and (ii) in the central vacancy of the lattice as a function of both impurity (cobalt) concentration and lattice symmetry (square or triangular). The vacancy in the lattice allows for a possible "mirage" effect to be seen. If the impurity-impurity interactions are appreciable, then as the surface density of Co atoms increases from very low concentrations and drives the lattice toward a spin glass phase, one would expect a suppression[41] of the Kondo temperature, T_K, which would show up as a narrowing of the zero bias feature in the tunneling spectrum on top of a Co atom [28, 25, 29]. A change in the effective Kondo temperature of the system would show up in both the on atom and vacancy spectrum. However, due to limitations of our scattering theory[12] it can only be directly applied to the vacancy of the lattice.

When we apply our scattering theory to the experiments of Ref. [39] we find no signature of deviations from the single-impurity tunneling spectrum. This means that the STM supplies no evidence for a correlated state across the lattice. We speculate that this may be due to a relatively high density of electrons that can screen the impurity (Co) atoms. In the surface state alone, the electron density is 1 $e^-/160$ Å^{-2} so that one would expect to need a lattice constant at least as small as $\sim$12 Å^2. Which is about the limit of how close the Co atoms can be placed without the surface charge disturbances caused by the Co atoms overlapping each other. Although the 12 Å distance corresponds to the smaller lattice constants of Ref. [39], there are still the electrons in the bulk states which keep the electron density high at the impurity sites[38].

4.3 Related Work and Recent Developments

Recently there have been several important developments in the study of quantum corrals, especially related to the recent mirage experiments. While our scattering theory explains all of the observed features of quantum corrals, including the mirage experiments, it is phenomenological. A full understanding of the surface

---

[2] It should be emphasized that Kondo Lattice physics is expected to occur in systems with a small number of electrons per lattice site, typically order one[40, 41].

state response to magnetic impurities requires more detailed studies of single impurities: Experimentally with spin resolved STM and theoretically with first principle and many-body calculations. It is necessary to go beyond the single-particle theory to accurately calculate quantities such as spin-spin correlation functions of impurities in quantum corrals or details of the Kondo effect itself. Some of these studies have already been undertaken and we briefly describe them below.

4.3.1 Experimental

Since the mirage experiments, there have been few experimental studies specific to corrals reported, however, Kliewer and collaborators [4] have studied the effect of the modification of surface state electron density by corrals on the spectroscopy of Mn on Ag(111). Most STM studies have focused on the Kondo effect from the impurities themselves. Chen *et al.* [37] reported the disappearance of the Kondo resonance for Co dimers on Au(111). Jamneala *et al.* [42] carried out a systematic study of 3-d elements on Au(111). Odom *et al.* [43] reported Kondo effect from Co *clusters* adsorbed on single wall metallic nanotubes[3]. Madhavan *et al.* [35] studied Co on Au(111) as a function of impurity coverage from isolated impurities up to one monolayer. Nagoaka *et al.* [45] looked at the temperature dependence of the broadening of the Kondo resonance of Ti on Ag(100). Schneider *et al.* [21] measured the scattering phase shift from isolated Co atoms on Ag(111) and Knorr *et al.* [7] have studied the role of surface and bulk state contributions to the Kondo effect for Co on

---

[3] The Kondo effect generated by a ferromagnetic cluster turns out to have several interesting and nontrivial new features compared to a single impurity ([44]).

Cu(100) and Cu(111).

4.3.2 Theoretical

On the theoretical side, much more work has focused on the quantum mirage in corrals rather than on the single impurities. Agam and Schiller [46] and Porras *et al.* [47] and Weissmann and Bonadeo [48] have also developed theories for the quantum mirage based on a single-particle picture. More recently, Aligia [49] has developed a many-body theory of the quantum mirage. Chiappe and Aligia [50] and Correa *et al.* [51] have undertaken studies of the interaction between two magnetic impurities in a quantum corral. A model of interactions between two impurities in states confined to the surface of a sphere was studied by Hallberg *et al.* [52]. A recent renormalization group study carried out by Cornagli and Balseiro [53] for Kondo impurities in nanoscale systems also makes contact with the mirage experiments.

While there are now several theories addressing the physics of the mirage, we feel the least addressed question is that of the relative role of surface and bulk states in the formation of the Kondo effect at a single impurity. Many theories tend to neglect the bulk states and treat the quantum corral as a confined 2-d system. We believe theory should now move beyond this and include the role of both surface states and bulk states in Kondo resonance. It remains clear, however, that the mirage effect is dominated by a Kondo effect that *involves* the surface state electrons because the phase shift, Eq. (4.6), demands it.

Chapter 5

Kondo Effect from Ferromagnetic Nanoparticles

5.1 Introduction

Kondo physics[23] has seen a revival in recent years due to an exciting series of new experiments on mesoscopic[54, 55, 56, 57] and nanoscale[10, 11, 42, 3, 58, 43, 59] systems that has enabled a more thorough and controlled study of the basic problem of a local moment interacting with a sea of conduction electrons. It is now possible, for example in quantum dots, to tune the Kondo temperature, T_K, with externally applied gate voltages[54, 55, 56, 57, 58] or, with the scanning tunneling microscope (STM), to study the Kondo effect at single magnetic impurities on metallic surfaces[10, 11, 42, 3]. The superb spatial resolution of the STM permits unprecedented direct local spectroscopic detail of Kondo impurities.

Recent low temperature($\sim$ 4 K) STM experiments[43, 59] have probed the spectroscopy of isolated nanometer and sub-nanometer ferromagnetic (Co) clusters on metallic single walled carbon nanotubes[1]. The tunneling spectrum of these small ferromagnetic clusters exhibited several interesting features–most notably Kondo effect in sub-nanometer diameter clusters and well resolved discrete level spacing in nanometer size clusters. Both sub-nanometer and nanometer size clusters exhibited a Coulomb charging gap in the spectrum near zero bias. The Kondo effect in the sub-nanometer size clusters appeared in the spectrum as a Fano-like sharp *peak*[2] [25]with a half-width $\sim$ 15 meV ($T_K \sim$ 80 K) at 4 K. This peak was not present at 100 K, presumably due to thermal destruction of the Kondo resonance.

The goal of this paper is to present a theoretical framework to study the spin-flip scattering of conduction electrons from finite size ferromagnetic clusters adsorbed on metallic surfaces. In particular, we are interested in understanding some of the *size-dependent features* observed in the tunneling spectrum. We focus on how the Kondo Effect, the level spacing and the level widths depend on the size of the cluster.

Cluster ferromagnetism may be described by two alternate models: (i) In the experiments of Odom *et al.*[43, 59] magnetism of the cluster is most likely *itinerant* in nature as bulk Co is an itinerant band ferromagnet. The basic physics of itinerant

---

[1] As far as we are aware, no STM experiments on metallic nanotubes supported on metallic substrates have shown evidence of Luttinger-Liquid effects in the tunneling spectrum, perhaps due to charge screening by the substrate. We therefore neglect electron-electron interactions in our model of the nanotube conduction electrons. (Transport measurements on ropes of SWNT supported on an insulating substrate have, however, shown Luttinger-Liquid behavior: M. Bockrath *et al.*, Nature, **397**, 598 (1999).)

[2] In the experiments with magnetic atoms adsorbed on metallic surfaces like those described in Ref[10, 3] a dip-like feature was typically observed rather than a peak. The dI/dV vs. V line shape depends sensitively on the details of the impurity–conduction electron coupling and STM tip location. For a discussion see: M. Plihal and J.W. Gadzuk, Phys. Rev. B **63** 085404 (2001); A. Schiller and S. Hershfield, Phys. Rev. B **61**, 9036(2000) and Ref.[25].

clusters is captured in the model of Refs.[60, 61] (see Sec. 5.2). (ii) In some other cases, however, including the case of many semiconducting ferromagnets [62] and rare earth materials, ferromagnetism is better described in terms of *local moments* that couple ferromagnetically or antiferromagnetically to the cluster conduction electrons (holes). This motivated us to introduce another exactly solvable model, where d-electrons produce highly localized magnetic moments. While the excitation spectrum of the two models turns out to be very similar, the way they couple to the metallic substrate is rather different. The most appropriate model to use in a given physical situation depends on the material that composes the nanoparticle and whether it is more appropriate to think of the magnetism of the particle as due to localized moments or itinerant electrons that, although free to move about, are nevertheless polarized strongly enough to give a net spin to the cluster.

We make several assumptions during our computations: We assume the clusters to have between, say, eight and forty atoms and that they are large enough that bulk properties, such as the magnetization per atom, are not changed substantially due to their finite size. Furthermore, we assume that the single particle states on the island are of extended character, and therefore the single particle level spacing decreases as $\sim 1/N_A$ with an increasing number of cluster atoms, N_A. We also assume that the ferromagnetic spin splitting Δ_s of the extended states on the island is much larger than the single particle level spacing and is approximately independent of the size of the cluster. Thus the total spin of the cluster is rather large and is roughly proportional to $\sim N_A \gg 1$.

Depending on the strength of the electron tunneling between the metal and the cluster we may distinguish two regimes: weak and strong. For weak tunneling we derive an effective Kondo Hamiltonian in second order perturbation theory in the tunneling. In this regime we find that at very low energy scales the cluster behaves most similarly to a quantum dot with a single unpaired electron. However, ferromagnetic interactions induce a large spin on the cluster and at the same time *reduce* the value of the effective exchange coupling between the spin of the cluster and the electrons in the metal.

The sign of the exchange coupling depends on the specific details of the band structure on the nanoparticle. For a Co cluster, in particular, the itinerant model gives a tendency for *antiferromagnetic* coupling, and possibly produces a Kondo effect. However, the Kondo temperature T_K, decreases very fast with increasing cluster sizes, and therefore the Kondo effect can be observed only for very small clusters.

The effective couplings we obtain, J^{eff}, turn out to be in general $M \times M$ matrices describing spin-flip scattering among the M conduction band orbital modes that couple to the cluster (M=4 for metallic nanotubes[63]). Therefore we expect that a series of Kondo effects takes place at Kondo temperatures corresponding to the antiferromagnetic eigenvalues of J^{eff}. The total spin of the impurity, S_T gets successively screened at each Kondo temperature as the temperature is lowered: $S_T \to S_T - 1/2 \to S_T - 1 \ldots$. For a nanotube this compensation can never be complete[26] for any spin greater than 2 since there are only four channels available for screening[63]. The degeneracy of the remaining unscreened spin will ultimately be lifted by magnetic anisotropy induced by spin-orbit coupling[64, 65, 66].

To make closer contact with the experiments of Odom *et al.*[43, 59] we compute the STM tunneling spectrum using the itinerant model. The simultaneous observation of the Coulomb gap and the discrete levels, whose widths almost equal the level spacing, suggest that the clusters investigated are in the intermediate tunneling regime. Nevertheless, carrying out perturbative calculations in the weak tunneling limit, we are able to reproduce the essential features of the STM spectrum *above* the the Coulomb charging energy. We find that small fluctuations in the charging energies can give rise to very asymmetrical STM spectra.

From the STM spectra of the clusters at higher voltages, we can crudely estimate the Kondo temperature, T_K, of a small Co cluster of the size that exhibited a Kondo effect in Ref. [43, 59]. However, our estimates tend to give a T_K that is too small. We find that typical mesoscopic fluctuations in the charging energies of a ferromagnetic cluster can considerably increase the Kondo temperature, however, they do not account for the difference between our theoretical estimates and the experimentally observed T_K [43, 59]. Nevertheless, the fact that some small Co clusters exhibit Kondo effect while others do not, indicates that these mesoscopic fluctuations may indeed play an important role in determining T_K: Since T_K depends exponentially on J^{eff}, relatively small changes in the latter can induce large variations of T_K.

This paper is organized as follows. In Sec. 5.2 we introduce the itinerant model of nanoscale ferromagnets. In Sec. 5.3 we study the spin-flip scattering of conduction electrons from an itinerant cluster using second order perturbation theory in the cluster-substrate tunneling, and we derive a general expression for the matrix of Kondo couplings, J^{eff}. In Sec. 5.4 we make contact to the experiments of Odom *et al.*[43, 59] by calculating in a simple approximation the STM tunneling spectrum of a ferromagnetic Co cluster on a metallic substrate in the limit of weak tunneling. In Sec. 5.5 we introduce a new local moment model for ferromagnetism and show how to compute the effective interaction J^{eff} in this case. In Sec. 5.6 we discuss in detail the connection between our work and recent experiments. Finally, in Sec. 5.7 we present our conclusions.

5.2 Itinerant Ferromagnetic Cluster Model

An itinerant mean field model of a magnetic nanoparticle was first proposed by Canali and MacDonald[60] and later extended by Kleff *et al.*[61] to explain the dense spectrum in tunneling measurements of nanometer size Co particles[67, 68]. The basic Hamiltonian is

$$\hat{H}_{\mathrm{cluster}} = \sum_{j,\sigma} \epsilon_j c^\dagger_{j\sigma} c_{j\sigma} - \frac{1}{2}\frac{U}{N_A}\vec{S}\cdot\vec{S} + \frac{E_C}{2}(\hat{N} - n_g)^2 \tag{5.1}$$

where $c^\dagger_{j\sigma}$ ($c_{j\sigma}$) creates (destroys) an electron with spin σ at the j^{th} energy level of the cluster with kinetic energy ϵ_j (See Fig. 5.1). The first term in Eq. (5.1) represents the kinetic energy of the hybridized s, p and d-band electrons. The parameter $U > 0$ is the effective ferromagnetic exchange interaction on the cluster, N_A is the number of atoms that constitute the cluster, and

$$\vec{S} = \sum_j \frac{1}{2} \sum_{\alpha,\alpha'} c^\dagger_{j\alpha} \vec{\sigma}_{\alpha\alpha'} c_{j\alpha'} \tag{5.2}$$

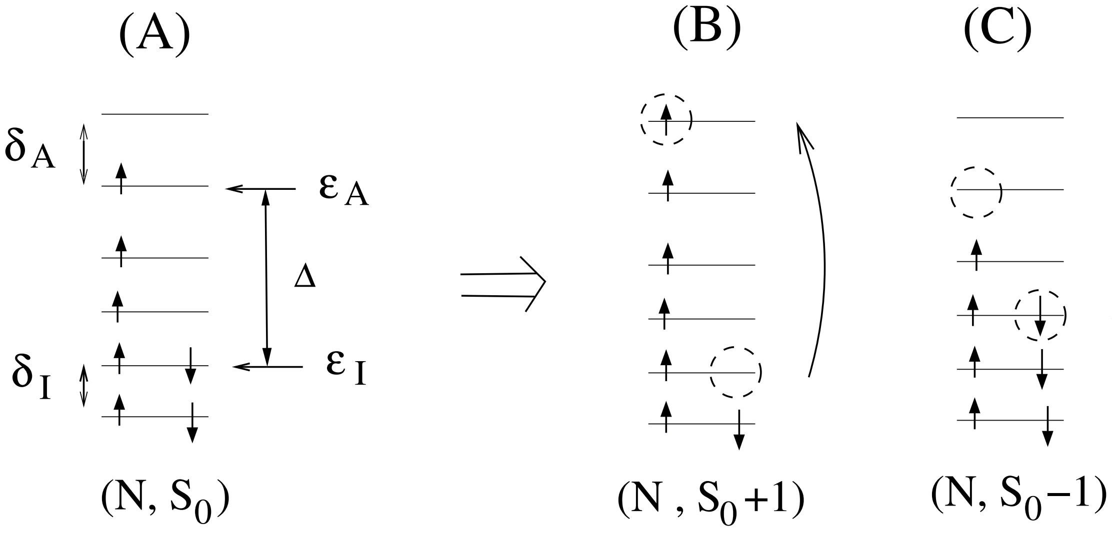

Figure 5.1: Spin excitations of a ferromagnetic nanoparticle. For the precise definition of $\epsilon_{A/I}$, $\delta_{A/I}$, and Δ_s see text. Fig. A: The fully porarized ground state. Figs. B and C: Lowest lying particle-hole excitations having energy $\sim \delta_{A/I}$.

is the total spin of the cluster. The second term in Eq. (5.1) corresponds to ferromagnetic exchange on the cluster: It gives rise to a spontaneous polarization of the cluster by making spin alignment of different levels energetically favorable. Finally the last term describes the charging of the cluster with E_C the Coulomb charging energy, $\hat{N} = \sum_{j,\sigma} \hat{n}_{j\sigma}$ the total number of electrons on the cluster, and n_g a dimensionless gate voltage that determines the number of electrons in the ground state[3].

Throughout this paper we are neglecting fluctuations in the level spacing. In a *real* nanoparticle, the level spacing between the j^{th} and $j+1^{th}$ energy level can be written as $\delta_j = \langle \delta_j \rangle + \eta_j$, where $\langle \delta_j \rangle$ is the level spacing corresponding to the bulk energy-dependent density of states, $\langle \delta_j \rangle \sim 1/\varrho(\epsilon_j)$, and η_j ($\langle \eta_j \rangle$=0) is a fluctuating

---

[3] In a semiconductor quantum dots[54, 56] and nanotube quantum dots[58] n_g can be tuned by a variable external gate voltage, thereby controlling the equilibrium number of electrons on the dot (cluster). For a ferromagnetic cluster adsorbed on a metallic surface, n_g is set by the chemistry of the cluster-metal interface and can not be freely changed in an experiment.

part due to shape irregularities in the nanoparticle. In this paper we take $\eta_j \equiv 0$, corresponding to an infinitely strong level repulsion.

The advantage of this model is that S^z, S^2 and n_j are conserved quantities and therefore the Hamiltonian in Eq. (5.1) can be diagonalized exactly. In the more general situation a magnetic anisotropy term should be added to the Hamiltonian. Nevertheless, for the experimentally investigated clusters this anisotropy is estimated to be much less then the width of the Kondo resonance observed, and therefore it can be neglected[4].

The ground state can be explicitly constructed:[61]

$$|S_0, S^z = S_0\rangle_G^N = \prod_{j=1}^{n_\uparrow} c_{j\uparrow}^\dagger \prod_{j=1}^{n_\downarrow} c_{j\downarrow}^\dagger |vac\rangle \tag{5.3}$$

with S_0 and N the spin and particle number in the ground state. The remaining states within the ground state multiplet may be explicitly constructed using the lowering operator:

$$|S_0, S^z\rangle_G^N = \sqrt{\frac{(S_0 + S^z)!}{(2S_0)!(S_0 - S^z)!}} (S^-)^{(S_0 - S^z)} |S_0, S_0\rangle_G^N. \tag{5.4}$$

In itinerant ferromagnets there is an approximate rigid band splitting between spin up and spin down electron density of states[69]. Throughout this paper, we will assume that our clusters are large enough that the band splitting energy, Δ_s, is well approximated by the bulk value of the specific material we are considering. In our model Δ_s can be defined as the energy difference between the highest occupied

---

[4] The itinerant model presented has a $(2S_0 + 1)$-fold degeneracy. In a real ferromagnetic cluster there will be anisotropy which, in the simplest case, will appear as a uniaxial anistropy[61]. For Co, the anistropy energy can be estimated to be of the order[61] .01-.1 meV $\approx$ .1-1.0 K which is safely below the experimental temperature range of 4-100 K[43] so we ignore it.

spin up level, ϵ_A, and the highest occupied spin down level, ϵ_I:

$$\Delta_s \equiv \epsilon_A - \epsilon_I \ ,$$

and from band structure calculations it is known to be typically of the order of a few electron volts[69] (see Fig. 5.1). It can be determined by demanding that the ground state of the ferromagnetic cluster be stable to fluctuations of energy level occupations with constant particle number, and is related to the interaction parameter U as[60]

$$U = \frac{N_A}{S_0}\Delta_s + d_0 \ , \tag{5.5}$$

where d_0 is a small quantity that scales as $1/N_A$, while the first term is roughly independent of the cluster size, since $S_0 \sim N_A$. Using Eq. (5.5), one can estimate the energy cost of a particle-hole excitation (see Fig. 5.1B,C). This turns out to be of the order of the level spacing ($\propto 1/N_A$) (and *not* the exchange splitting Δ_s):

$$\delta E(S_0 \pm 1, N) \equiv \min\{E_{\text{excited}}(S_0 \pm 1, N) - E_G\} \sim \delta_A, \delta_I \ , \tag{5.6}$$

where E_G denotes the ground state energy, and δ_A (δ_I) is the level spacing near ϵ_A (ϵ_I). If U is large enough to fully polarize the cluster, the energy scales outlined above may change[5].

The minimum cost of adding a particle or a hole to the cluster can be defined as,

$$\delta E_{\pm,\sigma} \equiv \min\{E(N \pm 1, S_0 + \sigma/2) - E_G\}, \tag{5.7}$$

---

[5] This definition is only appropriate for a partially polarized conduction band. If U is large enough to fully polarize the bands a more appropriate definition could be the energy difference of the highest occupied spin up level and that of the lowest *empty* spin down level. In this case the particle-hole excitation energy can clearly be substantially larger than the single particle level spacing and be of the order of the band splitting.

where the minimum is over all possible excited states. To determine $\delta E_{\pm,\sigma}$ we consider processes like those in Fig. 5.2. These energies can be estimated as

$$\delta E_{+,\uparrow} \approx \bar{\epsilon} + E_C^+ + \left(\delta_A - \frac{1}{2}\frac{S_0}{N_A}d_0 - \frac{3}{8}\frac{\Delta_s}{S_0}\right) , \tag{5.8}$$

$$\delta E_{+,\downarrow} \approx \bar{\epsilon} + E_C^+ + \left(\delta_I + \frac{1}{2}\frac{S_0}{N_A}d_0 + \frac{1}{8}\frac{\Delta_s}{S_0}\right) , \tag{5.9}$$

$$\delta E_{-,\uparrow} \approx \bar{\epsilon} + E_C^- - \left(\frac{1}{2}\frac{S_0}{N_A}d_0 + \frac{3}{8}\frac{\Delta_s}{S_0}\right) , \tag{5.10}$$

$$\delta E_{-,\downarrow} \approx \bar{\epsilon} + E_C^- + \left(\frac{1}{2}\frac{S_0}{N_A}d_0 + \frac{1}{8}\frac{\Delta_s}{S_0}\right) , \tag{5.11}$$

where the corrections scale as $O(1/N_A^2)$, and $E_C^\pm$ denote the charging energies in the limit of vanishing ferromagnetic coupling and an infinitely dense single particle spectrum:

$$E_C^\pm \equiv E_C(\frac{1}{2} \pm (N - n_g)) . \tag{5.12}$$

The parameter $\bar{\epsilon} \equiv (\epsilon_A + \epsilon_I)/2$ in Eq. (5.8) can be absorbed into the definition of n_g, and we will set it to zero in what follows.

The last terms in Eqs. (5.8-5.11), proportional to Δ_s/S_0, are specific to the mean field model discussed here and have little physical meaning. Their effect can be fully taken into account by renormalizing the ‘chemical potential’ $\bar{\epsilon}$ and the mesoscopic parameter d_0, and they therefore do not modify our results.

Using a stability analysis similar to the previous one it is a trivial matter to show that typically

$$\delta E_{\pm,\sigma} \sim E_C/2 . \tag{5.13}$$

For later purposes it is also useful to have excitation energies of particles and holes added to *any* level defined, $\delta E^j_{\pm,\sigma}(N \pm 1, S_0 + \sigma/2)$. For example, increasing

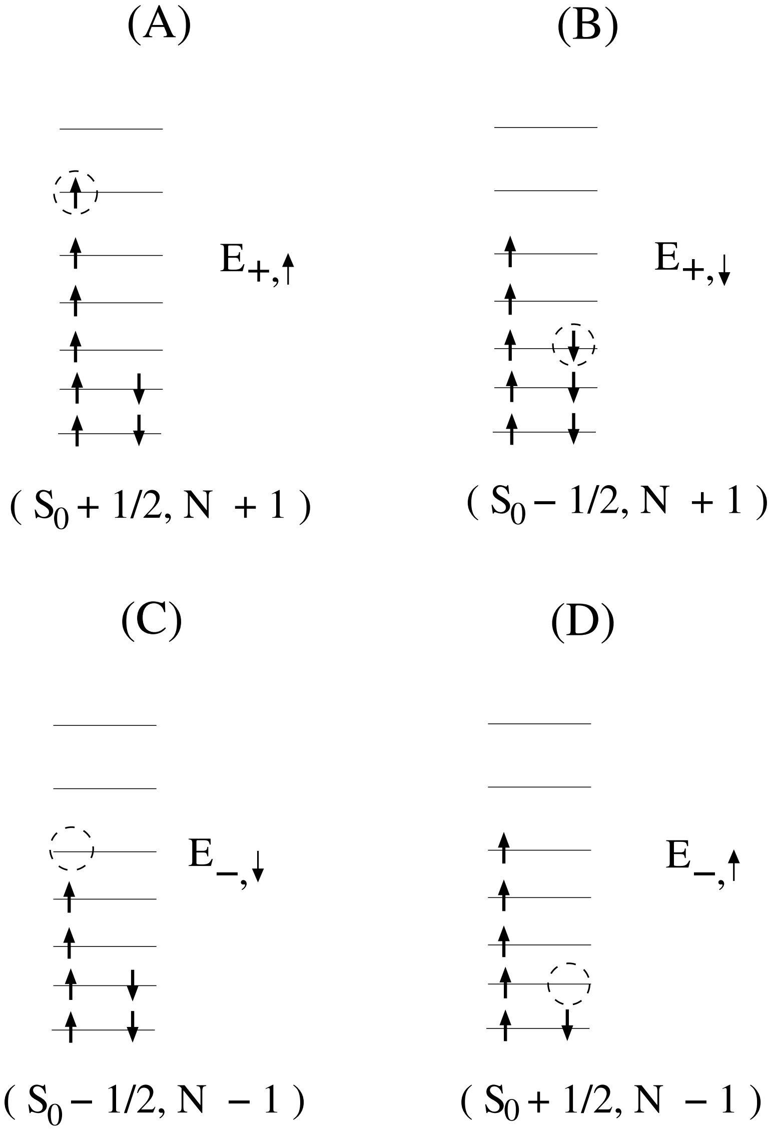

Figure 5.2: Charging excitations of a ferromagnetic particle. Circles indicate particles added to (removed from) the ground state. Fig. A (B): Lowest energy state for adding a majority (minority) electron to the cluster. Fig. C (D): Lowest energy state for adding a majority (minority) hole to the cluster.

the total spin by adding an electron to the j^{th} unoccupied level rather than the one immediately above ϵ_A gives,

$$\delta E^j_{+,\uparrow} \equiv \epsilon_j - (\epsilon_A + \delta_A) + \delta E_{+,\uparrow}\ . \tag{5.14}$$

Removing an electron from level j below ϵ_I so that the total spin increases gives

$$\delta E^j_{-,\uparrow} \equiv \epsilon_I - \epsilon_j + \delta E_{-,\uparrow}\ . \tag{5.15}$$

It is important to point out that in our model all effects of mesoscopic fluctuations have been put into the quantities E_C, d_0 and n_g. All other quantities of the itinerant model are specified by the bulk band structure and the number of atoms, N_A, in a given nanocluster.

5.3 Weak Tunneling between a Ferromagnetic Cluster and a Metal

5.3.1 General Expression

A finite size ferromagnetic cluster can scatter electrons between different orbital channels in the substrate and flip their spin while doing so. If the spin-orbit coupling is sufficiently weak then $SU(2)$ symmetry in the spin sector implies that the low-energy effective interaction between the cluster spin and the electrons takes the form (apart from a potential scattering term):

$$\hat{H}^{\text{eff}}_{\text{Kondo}} = \frac{1}{2}\sum_{k,k'} J^{\mu\nu}\vec{S}\cdot a^{\dagger}_{\mu k\alpha}\vec{\sigma}_{\alpha\alpha'}a_{\nu k'\alpha'} \tag{5.16}$$

where $J^{\mu\nu}$ is a Hermitian matrix of spin-flip exchange couplings among the various orbital channels, indexed by μ and ν. (In a one-dimensional system, such as a carbon nanotube, μ labels left-going and right-going modes of different symmetries. In an isotropic two or three dimensional host μ labels angular momenta about the cluster.) The total spin of the cluster is $\hat{S}$ and the $a^{\dagger}_{\mu k\alpha}$ ($a_{\mu k\alpha}$) are creation (annihilation) operators for conduction electrons of the metal in orbital channel μ, wavenumber k and spin α. A finite size cluster in an isotropic host will generally scatter electrons among all orbital channels, but in practice $J^{\mu\nu}$ can be truncated to include a finite number of channels, the largest angular momentum being $l \sim \frac{L}{\lambda_F}$ where L is the size of the cluster and λ_F is the Fermi wavelength of the conduction electrons.

In the limit of weak tunneling, $J^{\mu\nu}$ can be calculated in second order perturbation theory in the tunneling. The Hamiltonian we consider is $\hat{H} = \hat{H}_0 + \hat{V}$, where $\hat{H}_0 = \hat{H}_{\text{metal}} + \hat{H}_{\text{cluster}}$ and where $\hat{H}_{\text{metal}} = \sum_{\mu,k,\sigma} \epsilon_{\mu,k} a^{\dagger}_{\mu k\sigma} a_{\mu k\sigma}$ is the Hamiltonian of the free conduction electrons of the metal and

$$\hat{V} = \sum_{\mu,\sigma,j,k} (V^{j,k}_{\mu} c^{\dagger}_{j\sigma} a_{\mu k\sigma} + h.c.) \ , \tag{5.17}$$

where

$$V^{j,k}_{\mu} \equiv \sum_{n=1}^{N_p} V_n \varphi^{*}_{j}(\vec{R}_n) \psi_{\mu,k}(\vec{R}_n) \ , \tag{5.18}$$

and N_p is the number of points of electrical contact between the cluster and the metal. The $\varphi_j(\vec{R}_n)$ are the wave functions of the j^{th} levels on the cluster at the points of contact $\vec{R}_n$ and the $\psi_{\mu,k}(\vec{R}_n)$ are the wave functions of the metal at $\vec{R}_n$. The tunneling amplitude V_n can be estimated with a knowledge of the wave functions near the cluster-metal contact points and the work functions of the cluster and the metal.

We can determine $J^{\mu\nu}$ by equating

$$\langle f|\hat{H}^{\rm eff}_{\rm Kondo}|i\rangle = \sum_n \frac{\langle f|\hat{V}|n\rangle\langle n|\hat{V}|i\rangle}{E_i - E_n}\ , \tag{5.19}$$

where $|i\rangle = |S_0, S^z\rangle_G^N|\nu, k_i, \sigma\rangle$ and $|f\rangle = |S_0, S^{z'}\rangle_G^N|\mu, k_f, \sigma'\rangle$ denote the initial and final states with energies E_i and E_f, respectively, and $|n\rangle$ stands for all possible intermediate states with energy E_n, $H_0|n\rangle = E_n|n\rangle$. Here $|\nu, k, \sigma\rangle$ denotes the Fermi sea with an additional electron in the νth channel with momentum k and spin σ.

The easiest way to determine $J^{\mu\nu}$ is to focus on purely spin-flip process to which potential scattering does not contribute, and choose $S^z = S_0, \sigma =\downarrow$ and $S^{z'} = S_0 - 1, \sigma' =\uparrow$, giving $\langle f|\hat{H}^{\rm eff}_{\rm Kondo}|i\rangle = \frac{1}{2}\sqrt{2S_0}J^{\mu\nu}$. The RHS of Eq. (5.19) is evaluated by summing over both states with an extra particle and states with an extra hole in the intermediate state (See Fig. 5.3). After a rather straightforward computation we find that $J^{\mu\nu}$ is given by the sum of three contributions:

$$J^{\mu\nu} = J_d^{\mu\nu} + J_s^{\mu\nu} + J_e^{\mu\nu}\ . \tag{5.20}$$

The couplings $J_d^{\mu\nu}$ and $J_e^{\mu\nu}$ describe the contributions from tunneling processes involving doubly occupied and empty single particle levels:

$$J_d^{\mu\nu} = -\frac{1}{S_0 + 1/2}\sum_{j\le I} V_\mu^{j,k_f\,*} V_\nu^{j,k_i}\left(\frac{1}{\delta E_{-,\uparrow} + \epsilon_I - \epsilon_j} - \frac{1}{\delta E_{-,\downarrow} + \Delta_s + \epsilon_I - \epsilon_j}\right) \tag{5.21}$$

$$J_e^{\mu\nu} = -\frac{1}{S_0 + 1/2}\sum_{j> A} V_\mu^{j,k_f\,*} V_\nu^{j,k_i}\left(\frac{1}{\delta E_{+,\uparrow} - \epsilon_{A+1} + \epsilon_j} - \frac{1}{\delta E_{+,\downarrow} + \Delta_s - \epsilon_{A+1} + \epsilon_j}\right), \tag{5.22}$$

and the incoming and outgoing electrons were put at the Fermi energy. Since $\Delta_s \gg \delta E_{\pm,\sigma}$ both contributions are *ferromagnetic*, *i.e.*, all eigenvalues of $J_d^{\mu\nu} + J_e^{\mu\nu}$ are

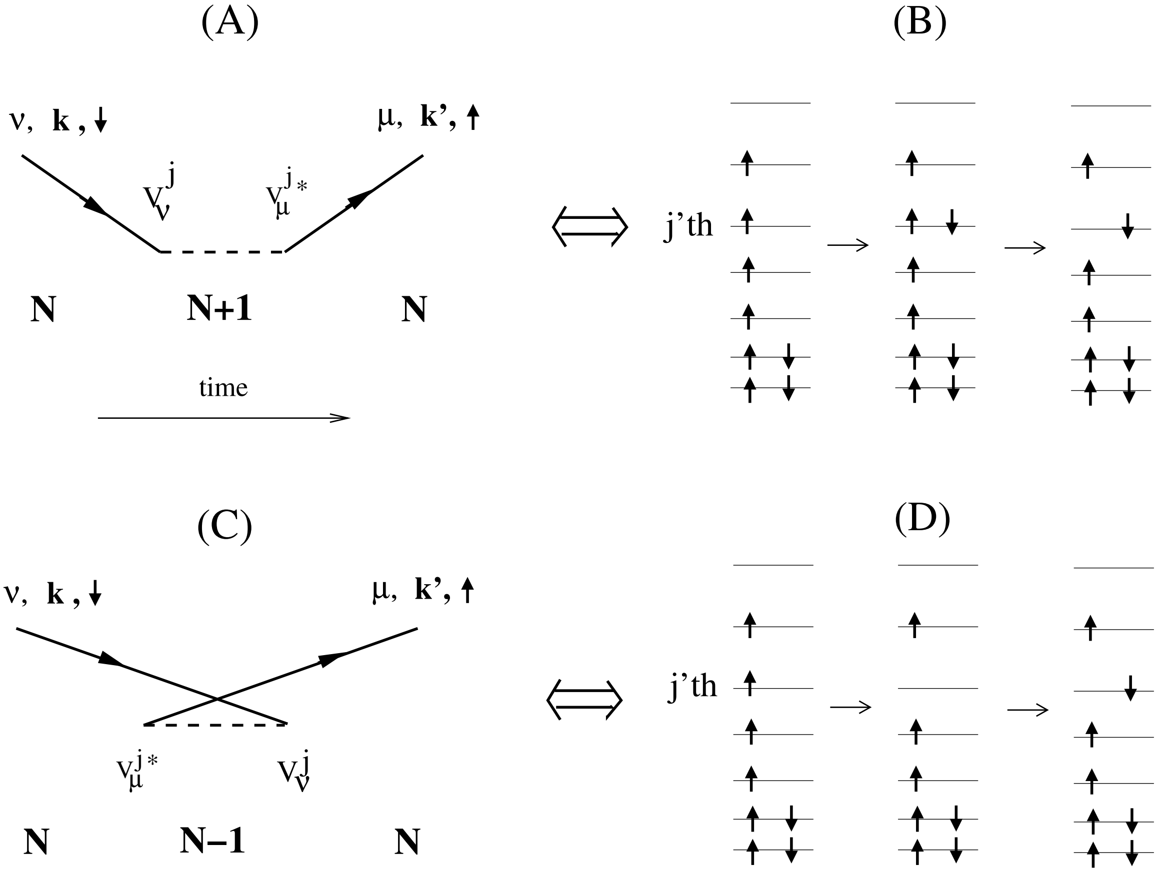

Figure 5.3: Kondo scattering from a ferromagnetic cluster. Figs. A and C: Time ordered diagrams in second order perturbation generating the single particle contribution Eq. (5.23) to the effective exchange $J^{\mu\nu}$. Continuous lines represent the incoming and outgoing electrons while dashed lines denote the intermediate excited state of the nanoparticle. In A an electron in state $|\nu, k, \downarrow>$ hops on the cluster onto level j and another electron leaves the cluster from level j with outgoing state $|\mu, k', \uparrow>$. In C first an electron hops out from level j into state $|\mu, k', \uparrow>$ and then the incoming electron hops onto level j. Level occupation changes are shown in D.

negative. To see this let us first neglect the k-dependence of the $V_\mu^{j,k}$'s. Then the matrices $J_a^{\mu\nu}$ $(a = e, d)$ can be expressed as a sum: $J_a^{\mu\nu} = \sum_j P_j^{\mu\nu}$. Each of these terms is obviously negative semidefinite, *i.e.* for any vector a^μ the product $a_\mu^* P_j^{\mu\nu} a_\nu$ is negative or zero. As a consequence, $J_e^{\mu\nu}$ and $J_d^{\mu\nu}$ are also negative semidefinite, *i.e.*, in a diagonal basis all their eigenvalues are negative or zero. This simple proof can readily be extended for k-dependent $V_\mu^{j,k}$'s.

The physical reason that the doubly occupied and empty single particle states give rise to a ferromagnetic contribution to $J^{\mu\nu}$ is that in the intermediate state in second order perturbation theory an electron (hole) that hops onto the island with spin parallel to that of the cluster has smaller energy than than an electron (hole) with opposite spin orientation, due to the ferromagnetic exchange *on* the cluster. Therefore an electron (hole) on the substrate with spin parallel to that of the cluster can lower its kinetic energy more efficiently through hopping to the empty (doubly occupied) states. This is reflected by the smaller energy denominator in Eqs. (5.21) and (5.22).

Singly occupied levels, on the other hand, give an *antiferromagnetic* contribution to $J^{\mu\nu}$:

$$J_s^{\mu\nu} = \frac{1}{S_0} \sum_{j=I+1}^{A} V_\mu^{j,k_f *} V_\nu^{j,k_i} \left(\frac{1}{\delta E_{+,\downarrow} - \epsilon_{I+1} + \epsilon_j} + \frac{1}{\delta E_{-,\downarrow} + \epsilon_A - \epsilon_j} \right), \tag{5.23}$$

with $J_s^{\mu\nu}$ having only non-negative eigenvalues[6]. This is a result of the Pauli principle, because only electrons (holes) in states with spin antiparallel to that of the cluster may hop onto singly occupied levels in second order perturbation theory, and thereby

---

[6] An alternative proof was given independently for the special case of a 2 × 2 $J^{\mu\nu}$ in Ref. [70].

reduce their kinetic energy.

Eqs. (5.21), (5.22), and (5.23) constitute one of the central results of the paper. They describe how $J^{\mu\nu}$ depends on the density of states of the singly occupied levels on the cluster, the excitation energies to the $N \pm 1$ manifold of states and the tunneling amplitudes to the various levels of the cluster.

In general, there is a competition among the three terms of Eq. (5.20), and thus the sign of eigenvalues of $J^{\mu\nu}$ depends on the specific structure of the single particle density of states on the cluster, and other mesoscopic parameters such as $\delta E_{\pm,\sigma}$. In the *absence* of ferromagnetic interactions on the cluster, $U = 0$, however, the ferromagnetic contributions $J_e^{\mu\nu}$ and $J_d^{\mu\nu}$ identically vanish, and the effective interaction is always antiferromagnetic, provided there is an odd number of electrons on the cluster.

The itinerant model has been used independently in Ref. [70] to describe spin $S = 1$ metallic nanoclusters with similar results. In that case the ferromagnetic interaction is weak, $U < \delta$, the island is far from a ferromagnetic unstability, and the $S = 1$ ground state of the island results rather from two single particle states of the island having energies accidentally closer than $U < \delta$. Then the ferromagnetic contribution of the doubly occupied and unoccupied levels is usually negligible, and the effective exchange interaction is dominated by the antiferromagnetic contributions of the singly occupied levels[70].

The off-diagonal elements of $J^{\mu\nu}$ are a sum of random numbers since the $\varphi_j^*(\vec{R}_n)\psi_{\mu,k}(\vec{R}_n)$ of Eq. (5.18) have random phase for different j and μ's. Therefore the size of the off-diagonal elements of $J^{\mu\nu}$ will be down by a factor of $\sim \sqrt{\frac{1}{2S_0}} \sim \sqrt{\frac{\langle\delta_{A,I}\rangle}{\Delta_s}}$ compared to the diagonal ones with $\mu = \nu$, and the matrix $J^{\mu\nu}$ will be dominated by the diagonal elements if the number of scattering channels M is much less than $2S_0$.

5.3.2 Weak Tunneling at a Single Point of Contact

It is instructive and also useful to specialize the results of Sec. 5.3A to the important case of a ferromagnetic cluster that makes contact with a metallic substrate in only a single point. Then we can choose a basis where $J^{\mu\nu}$ consists of a single non-zero element as all but one conduction channel will decouple from the cluster (that is, a linear combination of the host orbital modes can be found such that only one orbital mode in the new basis has non-zero amplitude at the impurity location). With the origin taken as the single point of contact, $V_\mu^{j,k}$ of Eq. (5.18) reduces to $V_j \equiv V\varphi_j^*(0)\psi_k(0)$. Eq. (5.23), *e.g.*, then becomes

$$J_s = \sum_j \frac{|V_j|^2}{S_0}\left(\frac{1}{\delta E_{+,\downarrow} - \epsilon_{I+1} + \epsilon_j} + \frac{1}{\delta E_{-,\downarrow} + \epsilon_A - \epsilon_j}\right). \tag{5.24}$$

In the limit $\Delta_s, \delta E_{\pm,\sigma} \gg \delta$ Eqs. (5.22), (5.21), and (5.23) can be approximately evaluated by assuming that the tunneling matrix amplitudes do not vary too much from level to level, and replacing the sums by integrals. For J_s, *e.g.*, we obtain:

$$J_s \approx \frac{\langle|V_j|^2\rangle_j}{S_0}\int_0^{\Delta_s} d\xi\,\varrho(\epsilon_I + \xi)\left(\frac{1}{\delta E_{+,\downarrow} + \xi} + \frac{1}{\delta E_{-,\downarrow} + \Delta_s - \xi}\right), \tag{5.25}$$

with $\varrho(\epsilon)$ the single particle density of states on the cluster, and $\langle|V_j|^2\rangle_j$ the average hybridization strength. The ferromagnetic couplings J_d and J_e can be expressed by similar integrals. For $S_0 \gg 1/2$ these integrals can be combined in a straightforward calculation where the integrand $\frac{1}{\delta E_{\pm,\sigma}+\xi}$ is separated into the two regions $\xi \gg \delta E_{\pm,\sigma}$ and $\xi \ll \delta E_{\pm,\sigma}$ and then approximated in each region. We obtain the following estimate for the effective exchange coupling valid when $\delta E_{\pm,\sigma} \gg \delta$:

$$J^{\text{eff}} \sim \frac{\langle |V_j|^2\rangle}{S_0}\left[P\int_{-\infty}^{\infty}\frac{\Delta_s \varrho(\xi)d\xi}{(\xi-\epsilon_I)(\epsilon_A-\xi)} - \varrho(\epsilon_I)\ln\left(\frac{\delta E_{+,\downarrow}}{\delta E_{-,\uparrow}}\right) + \varrho(\epsilon_A)\ln\left(\frac{\delta E_{+,\uparrow}}{\delta E_{-,\downarrow}}\right)\right]. \quad (5.26)$$

This simple expression is one of the central results of this work. Eq. (5.26) describes the dependence of J^{eff} on the *particular details of the density of states* of an itinerant ferromagnetic nanocluster. The first term involves a principal value integral (denoted by P) over energy and clearly shows that whenever $\epsilon_I < \xi < \epsilon_A$ the contribution to J^{eff} is antiferromagnetic; otherwise it is ferromagnetic, *i.e.* electron and hole excitations in the singly occupied states give rise to an antiferromagnetic coupling while electron (hole) excitations of the empty (doubly occupied) states give rise to a ferromagnetic contribution. The last two terms of Eq. (5.26) are *mesoscopic fluctuations* that depend on the specific charging energies of the nanocluster and the density of states at the top of the minority and majority bands. Other mesoscopic fluctuations come from variations in the tunneling matrix elements and in the level spacing, which are ignored in our model. These mesoscopic corrections become more pronounced for smaller cluster sizes and lead to strong fluctuations around J^{eff}.

For Co, the single particle density of states has a maximum within the spin-polarized part of the spectrum, $\epsilon_I < \xi < \epsilon_A$, resulting in a J^{eff} that tends to be *antiferromagnetic*. Numerical evaluation of Eq. (5.26) using the actual density of states for Cobalt [69] shows that the ferromagnetic contributions to J^{eff} from J_d and J_e reduce the dominant antiferromagnetic contribution from J_s by roughly 50-

60 percent. Fluctuations of $\delta E_{\pm,\sigma}$ in small clusters by a factor of 2 can lead to sample to sample fluctuations of $\sim$10% in J^{eff} for Co. This ultimately leads to large fluctuations in the Kondo temperature, T_K, from cluster to cluster, since J^{eff} appears in the exponent of the expression for T_K.

Eq. (5.26) also describes how J^{eff} scales with cluster size. From the normalization of the cluster wave functions we find $\langle |V_j| \rangle^2 \sim \frac{1}{N_A}$. Assuming that the magnetization of the cluster per atom is determined by microscopic mechanisms and thus $U \sim \Delta_s$ does not depend on the cluster size, both $S_0 \propto N_A$ and $\varrho \propto N_A$. This results in a fast decrease of J^{eff} with increasing cluster size (spin), $J^{\text{eff}} \propto \frac{1}{N_A} \propto \frac{1}{S_0}$, and therefore an exponentially suppressed T_K. Note that this suppression in T_K *depends only on the level structure* of the ferromagnetic nanocluster, not on any interference effects which may come from several points of contact[71].

It is useful at this point to mention what would happen if $U \ll \delta_{I,A}$ and we had an odd number of electrons on the cluster. There is then only one singly occupied level on the cluster, the sums in Eqs. (5.21) and (5.22) vanish, and the sum in Eq. (5.23) reduces to just two terms. As a result, for the spin 1/2 cluster, $J^{\text{eff}}_{1/2} \propto \frac{\langle |V_j| \rangle^2}{E_C} \propto \frac{1}{N_A^{1-\alpha}}$ with $\alpha > 0$ since $E_C \propto 1/N_A^{\alpha}$. Thus, for sufficiently large N_A, J^{eff} for the ferromagnetic cluster ($U \gg \delta_{I,A}$) will scale to zero faster with N_A than for the non-magnetic cluster. In Sec. 5.4.2 and in the conclusions, we will comment on what this means for the scaling of the Kondo temperature with the number of atoms in such a cluster.

5.3.3 Weak Tunneling at Several Points of Contact

For tunneling at several points of contact we again turn to Eqs. (5.20-5.23). In this case, $J^{\mu\nu}$ is necessarily a matrix reflecting the scattering of electrons in more than one orbital channel. As Eq. (5.18) shows, there will be significant random fluctuations in the matrix elements $J^{\mu\nu}$ from the $\varphi_j(\vec{R}_n)$ as cluster size is changed. For N_p points of contact there are a maximum of N_p orbital channels that will be scattered. However, if N_p is large, the number of orbital channels that are scattered may be much smaller. The largest angular momentum (orbital) channel scattered being $l \sim \frac{L}{\lambda_F}$, the matrix $J^{\mu\nu}$ is approximately of size $\sim l^2 \times l^2$ for a cluster in bulk or $\sim l \times l$ for a cluster in contact with a two-dimensional electron gas. For a nanotube at most 4 orbital channels can scatter low energy electrons[63].

As we discussed earlier in this case, in principle at least, one may observe a series of Kondo effects. The cluster displays an under-screened Kondo effect, where the spin of the impurity is large and several channels with different coupling constants try to screen it. The channel with the largest coupling to the impurity screens half a spin first and ceases to interact with the impurity. Then the channel with the largest coupling from the remaining channels screens half a spin and so on. In practice, however, the various Kondo temperatures are exponentially separated, and the very small Kondo temperatures are likely to be much smaller then the spin-anisotropy energy of the cluster. Therefore in a realistic situation one can only observe one, or possibly two Kondo effects[72].

5.4 STM Tunneling Spectra and Kondo Effect

5.4.1 STM Tunneling Spectra of Ferromagnetic Clusters

In the simplest model of STM spectra the tip is treated as a point source of electrons and the resulting signal is proportional to the local density of states (LDOS) at the tunneling position $\vec{r}$,[73]

$$\frac{dI}{dV}(\vec{r},V) \propto LDOS(\vec{r},\omega=eV) \equiv -\frac{1}{\pi}\mathrm{Im}[G^R(\vec{r},\omega=eV)]. \tag{5.27}$$

Here $G^R(\vec{r},\omega)$ is the retarded Green's function of the substrate below the tip, and V is the voltage difference between the STM tip and the substrate. Below we consider only tunneling directly into the cluster, ignoring any Fano-type interference effects[7] [25].

Let us first focus on the high-energy part of the spectrum at $\omega > T_K$, where the Kondo-type strong correlations are negligible. Using standard manipulations we can express the retarded Green's function as

$$\begin{aligned} G^R(\vec{r},\omega) \approx \frac{1}{N_G}\sum_{G,E,E'} \Bigg(& \langle G|\hat{\varphi}(\vec{r})|E\rangle \left(\frac{1}{(\omega-(\hat{E}-E_G)) - M^R(\omega)}\right)_{EE'} \langle E'|\hat{\varphi}^\dagger(\vec{r})|G\rangle \\ & + \langle G|\hat{\varphi}^\dagger(\vec{r})|E\rangle \left(\frac{1}{(\omega+(\hat{E}-E_G)) - M^R(\omega)}\right)_{EE'} \langle E'|\hat{\varphi}(\vec{r})|G\rangle \Bigg), \end{aligned} \tag{5.28}$$

where now $|E\rangle$ denotes excited states of the system in the *absence* of tunneling, *i.e.* $|E\rangle$ is a direct product of the excited states of the isolated cluster and the excited

---

[7] In the experiments with magnetic atoms adsorbed on metallic surfaces like those described in Ref[10, 3] a dip-like feature was typically observed rather than a peak. The dI/dV vs. V line shape depends sensitively on the details of the impurity–conduction electron coupling and STM tip location. For a discussion see: M. Plihal and J.W. Gadzuk, Phys. Rev. B **63** 085404/1 (2001); A. Schiller and S. Hershfield, Phys. Rev. B **61**, 9036(2000) and Ref.[25].

states of the isolated substrate and $\hat{E} = \delta_{E,E'}E$. The operator $\hat{\varphi}^\dagger(\vec{r})$ ($\hat{\varphi}(\vec{r})$) creates (annihilates) an electron at position $\vec{r}$ on the cluster. We average over the ground state multiplet $|G\rangle$ with degeneracy $N_G = 2S_0+1$, and M^R is the generalized retarded self-energy matrix.

Assuming that $\Gamma_0^j \equiv 2\pi\varrho_0 \sum_\mu |V_\mu^j|^2 < \min\{\delta E_{\pm,\sigma}, \delta_A, \delta_I\}$, we can do perturbation theory in the tunneling. In this case the ground state $|G\rangle$ can be approximated in leading order by the product of the independent ground states of the cluster and the metal, and the summation over the excited states $|E\rangle$ turns into a sum over the states $|E^j_{\pm,\sigma}\rangle$ defined in Sec. 5.2 (see Fig. 5.2). With these assumptions the retarded self-energy $M^R(\omega)$ is approximately diagonal in E and E'

$$M^R(\omega)_{EE'} \approx \text{real part} - i\delta_{EE'}\pi \sum_n \delta(\omega - E_n)|\langle n|\hat{V}|E\rangle|^2 \,, \tag{5.29}$$

where summation is carried out over all possible intermediate states $|n\rangle$ and $\hat{V}$ is given by Eq. (5.17). The real part of the self-energy produces only a slight shift of the levels, and it can be neglected. The imaginary part, on the other hand, describes the broadening of the spectrum.

Within these approximations the STM spectrum can be expressed as:

$$\frac{dI}{dV} \propto \sum_{j,\sigma,\pm} |\varphi_j(\vec{r})|^2 \frac{\Gamma^j_{\pm,\sigma}}{(\omega \mp \delta E^j_{\pm,\sigma})^2 + (\Gamma^j_{\pm,\sigma}/2)^2} \tag{5.30}$$

where $\Gamma^j_{\pm,\sigma}$ is the total decay rate of the excited state with excitation energy $\delta E^j_{\pm,\sigma}$.

Eq.(5.30) assumes that no two states of the cluster in the same spin sector are closer to each other than Γ_0. Otherwise they may produce Fano-type resonances due to the interference between electrons (or holes) that tunnel through these states.

For our mean field models with maximum level repulsion, however, this condition is always satisfied if $\Gamma_0 < \delta_I, \delta_A$. Also, if the ground-state energy difference for the cluster with N and $N \pm 1$ electrons on it (or with spin S_0 and $S_0 \pm 1$) is too small compared to Γ_0 the initial state will not have a definite electron number (or spin) and our computation breaks down.

For $\delta E^j_{\pm,\sigma} > \delta_{A,I}$ we find that the decay rate $\Gamma^j_{\pm,\sigma}$ is typically larger than the single particle tunneling rate $\sim \Gamma^j_0$. This can be understood as follows: Assuming that the STM-cluster voltage is already large enough to overcome the Coulomb blockade, an energy $\sim E_C/2$ is transfered to the cluster as an electron or hole hops onto the cluster from the STM tip. The extra charge carrier then tunnels into the leads. However, for $\delta E^j_{\pm,\sigma} > \delta_{A,I}$ the island can be left behind in a state that contains electron-hole excitations. Assuming for the sake of simplicity that $\Gamma^j_0 = \Gamma_0$ is independent of the single particle state index j we obtain the result that the width of a given level is proportional to the number of ways it can decay: $\Gamma^j_{\pm,\sigma} \approx N^{(j,\pm,\sigma)}_{\text{decay}} \Gamma_0$, where $N^{(j,\pm,\sigma)}_{\text{decay}}$ is the number of island states with N electrons whose energy $E(N) - E_G < \delta E^j_{\pm,\sigma}$ and which are accessible by the addition (or subtraction) of just one electron from the state corresponding to $\delta E^j_{\pm,\sigma}$. There is no simple expression for the $N^{(j,\pm,\sigma)}_{\text{decay}}$'s; they depend sensitively on the level j, N_A, E_C and the *fluctuating* mesoscopic parameters d_0 and n_g, and we have to determine them for each set of parameters and each level separately.

Within the mean field model we are using and to leading order in the tunneling $\hat{V}$ the number of decay channels of the state with energy $E^j_{\pm,\sigma}$ does not depend

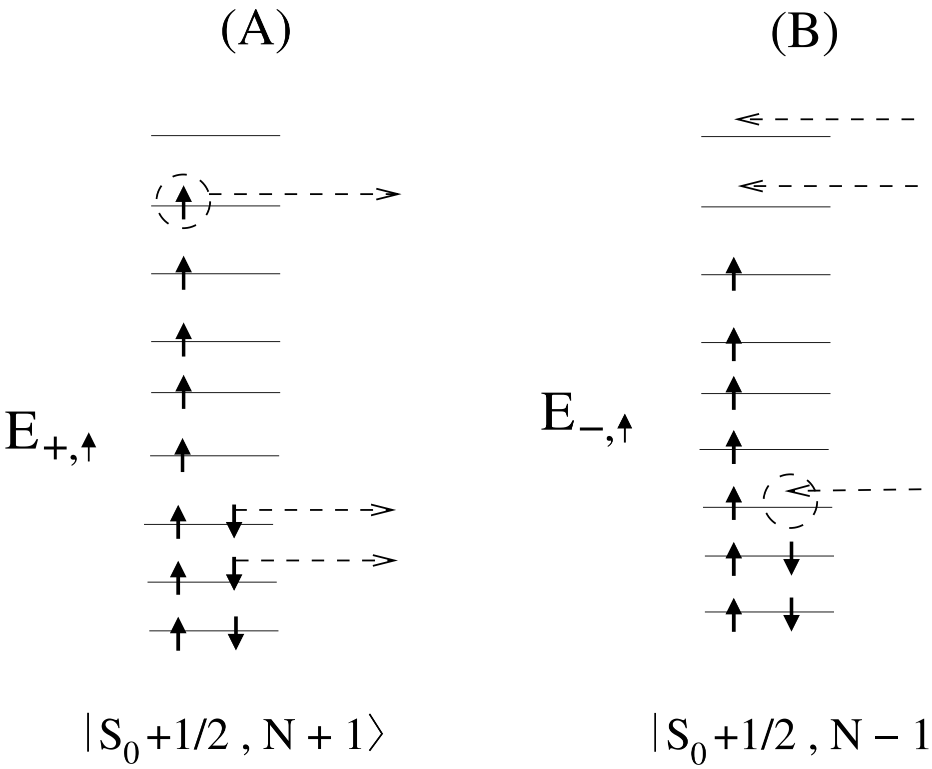

Figure 5.4: The dashed lines represent possible decay channels for the states $|E_{+,\uparrow}\rangle (N+1$ electrons) and $|E_{-,\uparrow}\rangle$ ($N-1$ electrons) to lower energy states with N electrons. In an actual decay, only one of processes indicated by the dashed lines would occur.

on j. This is an artifact of the mean field approximation: In higher orders of the tunneling (virtual tunneling processes) or in the presence of electron-electron interactions on the island (which may also change level occupations) excited states with larger energies generally have a larger decay amplitude. Examples of decay processes for a given excited state are shown in Fig. 5.4.

According to Eq. (5.30), the weakly coupled cluster spectrum is simply a series of Lorentzian peaks centered at the particle and hole addition energies determined by Eq. (5.1), Eq. (5.5) and the actual band structure of Co [69] with a weight modulated by a random amplitude $|\varphi_j(\vec{r})|^2$. In our calculation (See Fig. 5.5) of the

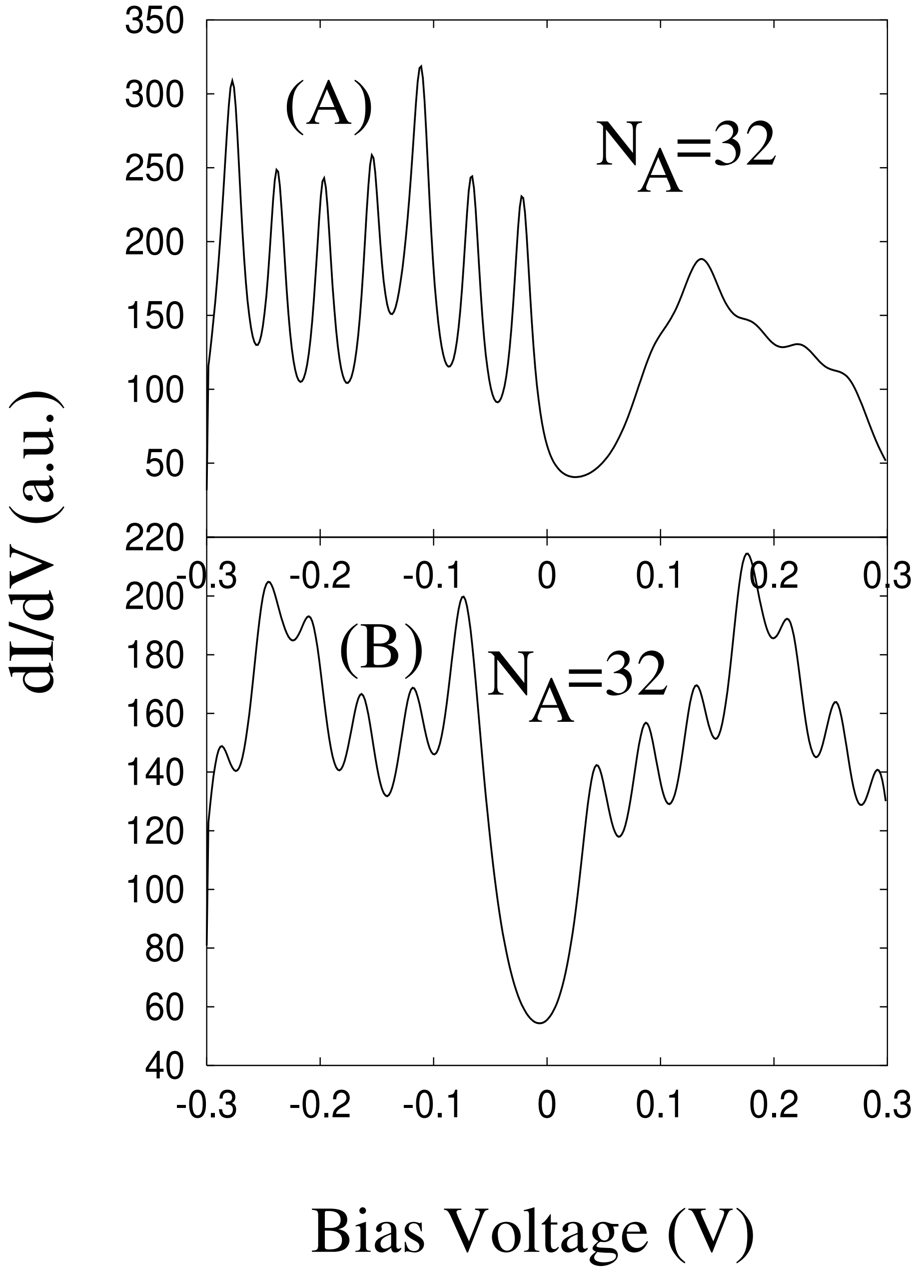

Figure 5.5: Calculated STM spectra of nanometer-size ferromagnetic clusters with parameters $N_A = 32$, $E_C^+ = .01\text{eV}$, $E_C^- = .08\text{eV}$, $\Gamma_0 = .02\text{eV}$, and $\mu = 0$ at 4 K (see main text). We took $\Gamma_0^j = 2\pi|V_j|^2\varrho_0 \approx \Gamma_0$, independent of j, and $|\varphi(\vec{r})|^2 = const$ in Eq. (5.30). In Fig. A we set $d_0 = .07\text{eV}$ while in Fig. B $d_0 = -.05\text{eV}$. The difference between the two cases demonstrates the sensitivity to mesoscopic parameters.

STM tunneling conductance we ignore (i) the amplitude modulation, (ii) fluctuations in the level spacing of the cluster beyond that given by band structure calculations[69] (as we discussed in Sec. 5.2) and (iii) fluctuations in the hybridization $\Gamma_0^j \approx \Gamma_0$. These effects could be included with some effort, but they would not be expected to change our conclusions.

In principle, contributions from phonon scattering or electron-electron interactions also contribute to the relaxation rate $\Gamma^j_{\pm,\sigma}$; however, in the experiments of Ref. [43, 59] these can probably be neglected with respect to the single particle relaxation channel considered here.

To compute the tunneling spectrum of an actual cluster with N_A atoms we generated a discrete set of levels ϵ_j with a level spacing corresponding to the single particle density of states in Co[69]. As discussed above, the non-uniform density of states is important to obtain a predominantly antiferromagnetic coupling, but is also important to obtain a stable ground state with a partially polarized band. The STM spectrum for low bias voltages is governed by the level structure near ϵ_A and ϵ_I since these are the only states probed in an STM measurement at low voltage bias. The majority and minority level spacing at these energies can be estimated from band structure calculations as δ_A=5.55 eV/N_A, δ_I=1.43 eV/N_A and $S_0 = 0.855 N_A$[69]. For Co, $\Delta_s = \epsilon_A - \epsilon_I \approx 2\text{eV}$.

For the sake of simplicity we set $\bar{\epsilon} = (\epsilon_I + \epsilon_A)/2 = 0$ in our computations, effectively absorbing it into n_g. This corresponds to a specific choice of contact potential between the lead and the cluster, and does not influence the overall features of the spectrum.

Eq. (5.30) assumes the cluster is in its ground state before the electron from the STM tunnels into it. Thus, in the numerical calculation it is important to ensure that the parameters of the model give a ground state with definite S_0 and N. Using Eq. (5.1) and Eq. (5.5) and keeping track of the $1/N_A$ corrections which are all put into d_0, one can derive the conditions for stability of the ground state, which we assume to have $N_s \approx 1.71 N_A$ singly occupied levels. By considering the fluctuations in the ground state spin shown in Fig. 5.1B and C one can show that to guarantee stability, d_0 must satisfy the conditions:

$$-\frac{N_A}{S_0}\delta_I < d_0 < \frac{N_A}{(S_0+1)}\left(\delta_A - \frac{\Delta_s}{S_0}\right) . \tag{5.31}$$

For Co this simplifies to $-1.67\frac{eV}{N_A} < d_0 < 3.21\frac{eV}{.855N_A+1}$. Similar conditions can easily be derived for the quantities E_C^+ and E_C^- by considering fluctuations to the $N \pm 1$ manifold of states like those in Fig. 5.2 and requiring $\delta E_{\pm,\sigma} > 0$. For our model applied to Co we obtain $E_C^+ > -1.0\frac{eV}{N_A}$ and $E_C^- > 2.48\frac{eV}{N_A}$.

A calculation of the tunneling spectrum of a ferromagnetic cluster with $N_A = 32$ atoms and a corresponding spin $S_0 = 27$ is shown in Fig. 5.5. For the computations we used the parameters $E_C^+ = .01\mathrm{eV}$, $E_C^- = .08\mathrm{eV}$ and $\Gamma_0 = .02\mathrm{eV}$ in both figures. Then once d_0 is given all the $\delta E^j_{\pm,\sigma}$ are determined via relations similar to Eq. (5.8). The quantity $N^{(j,\pm,\sigma)}_{\mathrm{decay}}$ is computed numerically. In Fig. 5.5A $d_0 = .07\mathrm{eV}$, and the ground state is close to being unstable against the lowest lying state within the (N, S_0+1) subspace, while in Fig. 5.5B $d_0 = -0.05$ eV, and the ground state is close to the lowest lying state within the (N, S_0-1) subspace.

In the spectrum in Fig. 5.5A there is a series of sharp peaks at negative bias (electrons are removed from the cluster) while the spectrum at positive bias (electrons are added to the cluster) is rather smooth. These features correspond very well with asymmetrical features seen in some spectra of Ref. [43, 59]. On the other hand, the lower spectra of Fig. 5.5B has less contrast between positive and negative biases. The only parameter that has been changed between the two spectra is d_0 of Eq. (5.5). Different values of d_0 lead to different values of the number of decay channels $N_{\text{decay}}^{(j,\pm,\sigma)}$ for positive and negative bias, and hence lead to different widths of the peaks in dI/dV. This calculation shows how mesoscopic fluctuations may make a significant qualitative difference in the spectra of two clusters with the same N_A, E_C and n_g. For real clusters mesoscopic fluctuations in E_C and n_g are also expected for fixed N_A and these will also lead to qualitative changes in the spectra.

A careful comparison of our calculated spectra corresponding to the first few charging peaks with the experimental spectra shows that at voltage biases up to $\approx \pm E_C$ our calculations are in agreement with experiment, however at larger biases, eV$>$ E_C (when *two* additional electrons (or holes) could be added to the cluster at the same time), the experimental spectra show additional structure, not present in our calculations, presumably due to many-body and/or non-equilibrium excitations left out of our simple model.

As we will see in the next section, for the cluster size of Fig. 5.5 the estimated Kondo temperature is significantly below the experimental temperature, and no Kondo peak appears at zero bias.

5.4.2 Estimating the Kondo Temperature

It is obvious that Eq. (5.30) does not include Kondo correlations and therefore does not produce a Kondo peak in the spectrum. However, it is generally true that when the Kondo effect is present, it produces a peak of width $\sim T_K$ at the Fermi level with relative weight $\sim \frac{T_K}{\Gamma_0}$ due to the approximate unitary scattering, provided the temperature is less than T_K, $T < T_K$[23, 30].

In order to estimate T_K and its dependence on cluster size, we will use the results of Sec. 5.3.2 for a cluster contacting the substrate in only a single point of contact. There are several reasons why we believe this may be a reasonable assumption to make for Co nanoclusters on metallic nanotubes.[43, 59] First of all, the ratio of broadening Γ of energy levels on the cluster compared to their separation $\sim \delta_{A,I}$ is experimentally found to be almost independent of the cluster size. Since $\delta_{A,I} \sim 1/N_A$ and $\Gamma \sim N_P/N_A$ (N_P is the number of points of contact), this indicates that the number of effective tunneling points is approximately constant for the clusters investigated in the measurements[8]. In fact, since the diameter of the clusters (.5-1 nm) of Odom *et al.* [43, 59] are comparable to the diameter of a nanotube there is appreciable curvature at the cluster-nanotube interface, and it is quite possible that the cluster touches the surface of the nanotube only at a few points. Since the tunneling amplitude is exponentially sensitive to the tunneling distance, it is also possible that only one or two of these points dominates the conductance between the cluster and the

---

[8] Using the experimentally observed level widths of the Co clusters on nanotubes[43] and the density of states of a metallic nanotube[63] we estimate the bare hopping element (overlap integral) in a tight binding model from an atom of the nanotube to the nearest Co cluster atom to be ~3-4 eV. This is comparable to the overlap integral of the nearest neighbor C-C overlap integral in nanotubes: 2.5 eV[63]

nanotube, resulting effectively in a coupling in the form of a single point of contact.

The standard expression for the Kondo temperature in the Kondo model is given by[23]

$$T_K = D\sqrt{J^{\text{eff}}\varrho_0}e^{-1/J^{\text{eff}}\varrho_0} \tag{5.32}$$

where D is the bandwidth of the conduction electrons of the metallic host and ϱ_0 is the density of states of the host at the impurity site. For a ferromagnetic cluster, however, this formula is incorrect, since the Kondo Hamiltonian provides an appropriate description of the cluster dynamics only below the characteristic energy of inelastic excitations, $E_{\text{inel}} \equiv \min\{E_C, \delta_{A,I}\}$. As shown for example in the two-level system model,[74] above this energy scale fluctuations to various excited states destroy the coherent spin processes leading to the Kondo effect, and in the renormalization group approach in the regime above E_{inel} the Kondo coupling remains unrenormalized. Therefore, for a single point of contact we estimate the Kondo temperature as

$$T_K \sim \min\{E_C, \delta_{A,I}\}\sqrt{J^{\text{eff}}\varrho_0}e^{-1/J^{\text{eff}}\varrho_0}, \tag{5.33}$$

where we replaced the bandwidth D of the conduction electrons by the energy gap for inelastic processes on the cluster, $D \to \min\{E_C, \delta_{A,I}\}$. Eq. (5.33) is only of logarithmic accuracy. In general, T_K contains an overall prefactor that incorporates corrections from higher excited states as well as possible mesoscopic fluctuation effects. This prefactor is usually of the order of unity, however in some cases it can be quite large and considerably increase the Kondo temperature[75].

In principle, the quantities E_C and $\delta_{A,I}$ can be obtained directly from the

STM spectra, and $J^{\text{eff}}\varrho_0$ can also be related to the spectra via the width of the energy levels of the cluster. Recalling $\Gamma_0^j = 2\pi|V^j|^2\varrho_0$ we can write

$$J^{\text{eff}}\varrho_0 \approx \frac{\Gamma_0}{2\pi S_0}\left[P\int_{-\infty}^{\infty}\frac{\Delta_s\varrho(\xi)d\xi}{(\xi-\epsilon_I)(\epsilon_A-\xi)} - \varrho(\epsilon_I)\ln\left(\frac{\delta E_{+,\downarrow}}{\delta E_{-,\uparrow}}\right) + \varrho(\epsilon_A)\ln\left(\frac{\delta E_{+,\uparrow}}{\delta E_{-,\downarrow}}\right)\right], \quad (5.34)$$

where we have used Eq. (5.26) and taken $|V^j|^2 \rightarrow \langle|V_j|^2\rangle$. Recall that $\varrho(\epsilon) \propto N_A$.

As is evident from Eq. (5.30), the actual level width of cluster excited states observed in experiment is $\Gamma^j = N_{\text{decay}}\Gamma_0^j$, where N_{decay} is the number of energetically allowed decays for a particular excited state in the $N \pm 1$ manifold as described in Sec. 5.4A. According to our model STM spectra calculations (Sec. 5.4A) (which computes $N_{\text{decay}}^{(j,\pm,\sigma)}$ numerically) N_{decay} is typically 1-3 for clusters with 7-30 atoms. As the most favorable case for obtaining an experimentally consistent T_K, we take N_{decay}=1 in our estimates.

To obtain an estimate of the Kondo temperature for Co atoms adsorbed on nanotubes we used the experimental data of Ref. [43, 59]. For a cluster experimentally estimated to have $N_A = 8$ atoms, the value $\Gamma \sim 0.24$eV and $E_C \sim .36$eV can be directly determined from the experimental STM spectrum of cluster. Unfortunately, the level spacing $\delta_{I,A}$ cannot be determined directly from the STM spectra for these small clusters, but can we estimate them by rescaling the level spacing measured at larger clusters, giving $\delta_I \sim 0.24$ eV.

Assuming that the spin splitting takes its bulk value, $\Delta_s \sim 2$eV we can then estimate T_K using Eqs. (5.34) and (5.33). We numerically evaluated both the integral in Eq. (5.26) as well as the discrete sums in Eqs. (5.21-5.23) using the actual Co density of states[69] (assuming a single point of electrical contact). Neglecting the mesoscopic fluctuations in $\delta E_{\pm,\sigma}$, the integral and the discrete sum were found to be within 10% of each other for N_A =8, 16 and 32. The Kondo temperature estimated this way for $N_A = 8$, $T_K \sim 0.16$ K turned out to be about a factor 500 smaller than the experimentally observed Kondo temperature, $T_K^{\mathrm{exp}} \sim 80$ K. (We obtain a value of $J^{\mathrm{eff}} \varrho_0 = .12$ for N_A =8. This would need to be increased by a factor of ~ 2.5 to reach agreement with experiment.) Mesoscopic fluctuations of $E_{\pm,\sigma}$ may increase (or decrease) J^{eff} by $\sim 10\%$. Furthermore, our integrals (and sums) were evaluated with the assumption that V_j is independent of energy. This is not strictly true and will lead to additional fluctuations in J^{eff}. These mesoscopic fluctuation effects typically change the value of J^{eff} altogether by $10 - 15\%$. It seems unlikely such fluctuations could bring the theoretical estimate of T_K into the experimentally observed range. Thus, there is a discrepancy between experiment and theory. There may be several explanations for this disagreement that we discuss in detail in Sec. 5.6 of the paper.

Eq. (5.34), on the other hand, is in qualitative agreement with the experiments in that it predicts an extremely rapid decrease of T_K with increasing cluster size. Since for a single point of contact $\Gamma_0 \sim 1/N_A$, $S_0 \sim N_A$, and $\varrho(\xi) \sim N_A$, the dimensionless exchange coupling scales as $J^{\mathrm{eff}} \varrho_0 \sim 1/N_A$. We also verified numerically that the scaling $J^{\mathrm{eff}} \propto \frac{1}{N_A}$ of Eq. (5.26) is maintained for the discreet sum in Eqs. (5.22-5.23).

Note that if one were to assume multiple contacts between the cluster and substrate, while keeping the decay rate fixed, then one would obtain smaller values for the typical tunneling matrix element $V_{\mu}^{j,k}$ and, hence, a lower Kondo temperature.

As we found in Sec. 5.3.2, the dimensionless coupling constant for a non-magnetic cluster, $J^{\text{eff}}_{1/2}\varrho_0 \sim 1/N_A^{1-\alpha}$, so that the Kondo temperature is suppressed less rapidly with increasing N_A. In this sense, the large spin of a ferromagnetic cluster does not "help" the Kondo effect in anyway.

5.5 Local Moment Clusters

5.5.1 Local moment mean field model

In many magnetic materials it is more appropriate to think of a localized d- or f-level (as in the Anderson Model) than to think of strongly hybridized s, p and d bands. These local moments may couple to each-other ferromagnetically and produce ferromagnetism.

For small enough magnetic clusters with large enough Curie temperature, at low enough temperature the local moments form a large and rigid ferromagnetic spin, S_d, that couples to the extended states (a 'conduction band') of s- and p-character. The simplest Hamiltonian that one can conceive to describe this situation reads

$$\hat{H}_{\text{cluster}} = \sum_{j,\sigma} \epsilon_j c^\dagger_{j\sigma} c_{j\sigma} + \frac{J}{N_A} \hat{S}_c \cdot \hat{S}_d + \frac{E_C}{2} (\hat{N} - n_g)^2, \tag{5.35}$$

with $\hat{S}_c$ and $\hat{S}_d$ the total spin of the extended states and the local moments, respectively. A justification of Eq. (5.35) is given in Appendix C. Similar to the itinerant model, the first term describes the kinetic energy of the extended electron states, and the third term accounts for the finite charging energy of the cluster. The second term of Eq. (5.35) describes the exchange interaction between the local moments and the extended states and tends to polarize the latter. We assume in what follows that the total spin of the conduction electrons is much smaller than that of the localized electrons. The exchange J is typically antiferromagnetic, $J > 0$, and the conduction electrons are polarized opposite to d-electrons[76].

The local moment model has S_T, S_T^z (the total spin and its z-component), $\{n_j\}$, S_d, and S_c as conserved quantum numbers, and can thus be diagonalized exactly. The ground state is given by

$$|S_T, S_T^z\rangle^N_{S_c,S_d} = \sum_{S_c^z, S_d^z; S_c^z + S_d^z = S_T^z} \langle S_c, S_d; S_c^z, S_d^z | S_T, S_T^z\rangle |S_c, S_d; S_c^z, S_d^z\rangle^N \ , \tag{5.36}$$

where $|S_c, S_d; S_c^z, S_d^z\rangle^N = |S_d, S_d^z\rangle |S_c, S_c^z\rangle^N$ and $S_T = S_d - S_c$ if $J > 0$. The state $|S_c, S_c\rangle^N$ can be computed from Eq. (5.3) with S_c replacing S_0 everywhere, and $|S_c, S_c^z\rangle^N$ is computed from Eq. (5.4) with S_c replacing S_0 and S_c^z replacing S^z.

Stability of the ground state implies the relation

$$J = \frac{N_A}{(S_d + 1)} \Delta_s + O(1/N_A) \ , \tag{5.37}$$

where Δ_s is now the band splitting of the conduction band.

Considering the type of particle-hole excitations shown in Fig. 5.1 and using Eq. (5.37), one finds that the excitation spectrum is very similar to that of the itinerant model. In particular, we find that for charge fluctuations $\delta E_{\pm,\sigma} \sim E_C/2$, and spin fluctuations have a gap $\sim \delta_A, \delta_I$.

5.5.2 Computation of the exchange coupling

The coupling constants $\tilde{J}^{\mu\nu}$ of the local moment model depend on the sign of the exchange coupling, J, of Eq. (5.35). Let us first focus on the case $J > 0$ and

$S_d > S_c$. For the local moment model, $\langle f|\hat{H}^{\rm eff}_{\rm Kondo}|i\rangle = \frac{1}{2}\sqrt{2S_T}\tilde{J}^{\mu\nu}$. To evaluate the RHS of Eq. (5.19) we must again evaluate contributions from the conduction electron states with double, single and no occupation:

$$\tilde{J}^{\mu\nu} = \tilde{J}^{\mu\nu}_d + \tilde{J}^{\mu\nu}_s + \tilde{J}^{\mu\nu}_e \; . \tag{5.38}$$

For the sake of simplicity, let us consider the contribution of singly occupied levels, $\tilde{J}^{\mu\nu}_s$. Various matrix elements of the type ${}^{N+1}_{j}\langle S_T + 1/2, S_T - 1/2|c^\dagger_{j\downarrow}|S_T, S_T\rangle^N$ arise in course of the evaluation of $\tilde{J}^{\mu\nu}$, and in contrast to the itinerant cluster model, the intermediate states of the local moment model (with $J > 0$ and $S_d > S_c$) have an *increase* in total spin on the cluster in this case. To evaluate ${}^{N+1}_{j}\langle S_T + 1/2, S_T - 1/2|c^\dagger_{j\downarrow}|S_T, S_T\rangle^N$ we first expand $|S_T, S_T\rangle^N_{S_c,S_d}$ and $|S_T + 1/2, S_T - 1/2\rangle^{N+1}_{S_c-1/2,S_d}$ using Eq. (5.36) to obtain

$$\begin{aligned} &{}^{N+1}_{j}\langle S_T + 1/2, S_T - 1/2|c^\dagger_{j\downarrow}|S_T, S_T\rangle^N = \\ &\qquad \sum_{S^z_c=-S_c}^{S_c} \langle S_c, S_d; S^z_c, S_T - S^z_c|S_T, S_T\rangle \\ &\qquad \langle S_c - 1/2, S_d; S^z_c - 1/2, S_T - S^z_c|S_T + 1/2, S_T - 1/2\rangle \\ &\qquad\qquad {}^{N+1}_{j}\langle S_c - 1/2, S^z_c - 1/2|c^\dagger_{j\downarrow}|S_c, S^z_c\rangle^N . \end{aligned} \tag{5.39}$$

What remains to be computed in Eq. (5.39) is the matrix element ${}^{N+1}_{j}\langle S_c - 1/2, S^z_c - 1/2|c^\dagger_{j\downarrow}|S_c, S^z_c\rangle^N$. To determine this, we use the states of Eq. (5.4) with S_c replacing S_0. The overlap is computed by first directly evaluating ${}^{N+1}_{j}\langle S_c - 1/2, S_c - 1/2|c^\dagger_{j\downarrow}|S_c, S_c\rangle^N$ and then applying the Wigner-Eckhart Theorem for general S^z_c. This yields ${}^{N+1}_{j}\langle S_c - 1/2, S^z_c - 1/2|c^\dagger_{j\downarrow}|S_c, S^z_c\rangle^N = \sqrt{\frac{S_c + S^z_c}{2S_c}}$. This can then be substituted into Eq. 5.39 which finally gives

$$\begin{aligned}
&{}_j^{N+1}\langle S_T+1/2, S_T-1/2|c_{j\downarrow}^{\dagger}|S_T, S_T\rangle^N \\
&\quad = \sum_{S_c^z=-S_c}^{S_c}\sqrt{\frac{S_c+S_c^z}{2S_c}}\langle S_c, S_d; S_c^z, S_T-S_c^z|S_T, S_T\rangle \\
&\quad\langle S_c-1/2, S_d; S_c^z-1/2, S_T-S_c^z|S_T+1/2, S_T-1/2\rangle\ . \qquad (5.40)
\end{aligned}$$

The results of the evaluation of all the matrix elements on the right hand side of Eq. (5.19) for the local moment model as well as the expression equivalent to Eq. (5.20) are somewhat lengthy so we relegated them to Appendix D. We evaluated them numerically for $S_T = S_d - S_c$ (antiferromagnetic J and $S_d > S_c$) and found that the single particle contribution to the final exchange coupling differs in an overall sign from the itinerant model result of Sec. 5.3, and it is ferromagnetic. On the other hand, if J is ferromagnetic, then $S_T = S_d + S_c$ and the matrix elements above agree in sign with those of Sec. 5.3.

This can qualitatively be understood as follows: Suppose the total spin, S_T, of the cluster points upward. Then by assumption $S_d > S_c$ the spin of the d-levels, S_d, also points up. If the internal interaction, J, between S_d and S_c is antiferromagnetic, delocalized electrons of the cluster with spin down will partially screen the local spin, S_d, so that the singly occupied states tend to have have spin down. A substrate conduction electron that hops on a singly occupied state must have, therefore, spin up that is parallel to the total spin, resulting in a ferromagnetic contribution to the effective interaction between the total cluster spin and the substrate. On the other hand, due to the antiferromagnetic interaction with the local spin, hopping to empty states with spin down have an energy smaller than those with spin up (parallel to the total spin), and give rise to an antiferromagnetic contribution to the effective interaction between the cluster spin and the substrate. The case $J < 0$ can be understood along the same lines.

Similar to the itinerant case, the signs of $\tilde{J}_d^{\mu\nu}$ and $\tilde{J}_e^{\mu\nu}$ are always opposite to that of $\tilde{J}_s^{\mu\nu}$ regardless of the sign of J. Therefore, there is in general a competition between these terms, and the sign of the final coupling depends on specific band structure features.

For an antiferromagnetic coupling, $J > 0$, in the limit where $\Delta_s, E_C \gg \delta$, and $S_c, S_d, S_T \gg 1$ we can obtain the following simple estimate for a single point of contact, analogous to Eq. (5.34):

$$\tilde{J}^{\text{eff}} \varrho_0 \sim -\frac{\langle |V_j|^2 \rangle}{S_T} \left[P \int_{-\infty}^{\infty} \frac{\Delta_s \varrho(\xi) d\xi}{(\xi - \epsilon_I)(\epsilon_A - \xi)} - \varrho(\epsilon_I) \ln\left(\frac{\delta E_{+,\uparrow}}{\delta E_{-,\downarrow}} \right) + \varrho(\epsilon_A) \ln\left(\frac{\delta E_{+,\downarrow}}{\delta E_{-,\uparrow}} \right) \right] . \tag{5.41}$$

The sign of the effective coupling depends on the sign of $S_c - S_d$ (here given for $S_c - S_d < 0$). For completeness, we also give the expression for $J < 0$, which does not depend on the relative size of S_c and S_d (note changes in mesoscopic fluctuations and overall sign):

$$\tilde{J}^{\text{eff}} \varrho_0 \sim \frac{\langle |V_j|^2 \rangle}{S_T} \left[P \int_{-\infty}^{\infty} \frac{\Delta_s \varrho(\xi) d\xi}{(\xi - \epsilon_I)(\epsilon_A - \xi)} - \varrho(\epsilon_I) \ln\left(\frac{\delta E_{+,\downarrow}}{\delta E_{-,\uparrow}} \right) + \varrho(\epsilon_A) \ln\left(\frac{\delta E_{+,\uparrow}}{\delta E_{-,\downarrow}} \right) \right] . \tag{5.42}$$

These expressions are particularly interesting: However large the constituent spins (S_c, S_d) of the cluster are, the cluster may still have a large effective coupling $\tilde{J}^{\text{eff}}$ if the coupling J between S_d and S_c is antiferromagnetic $(J > 0)$ and the total spin is sufficiently small. In most cases $S_c < S_d$, therefore $\tilde{J}^{\text{eff}}$ is ferromagnetic and no

Kondo effect develops. For $S_c > S_d$, however, $\tilde{J}^{\text{eff}}$ changes sign (still assuming $J > 0$) and becomes antiferromagnetic. In this case a Kondo effect occurs with an effective coupling proportional to $\sim 1/S_T$.

It should be pointed out that the results described above are valid only in the weak tunneling limit. In the strong tunneling limit, the relative signs of $\tilde{J}^{\text{eff}}$ and J are switched. For example, when the "internal" interaction $J > 0$ and the cluster is in the *strong* tunneling regime one cannot distinguish the cluster wave functions from those of the host. Thus, the $\tilde{J}^{\text{eff}}$ would have the same sign as J. Therefore we expect in this case J_{eff} to change sign as one gradually increases the tunneling between the cluster and the substrate. We have not studied in detail how this transition would occur.

5.6 Discussion

This work grew out of an effort to better understand the experiments of Odom *et al.*[43, 59] in which Kondo effect was observed at low temperatures ~5 K for sub-nanometer Co particles adsorbed on metallic carbon nanotubes. Our model correctly predicts a Kondo temperature that decreases quickly with increasing cluster size, however our numerical estimates of T_K tend to be too small by a factor of ~500 for a cluster with N_A=8.

There may be several explanations for our low estimate of T_K.

(a) Mesoscopic fluctuations in Eq. (5.26) can eventually increase the effective Kondo coupling and thus bring T_K close to its experimental value. However, since the sign of the mesoscopic fluctuations is random, this interpretation would appear to contradict the experiments in which a significant fraction of small Co clusters produced a Kondo effect. In addition to fluctuations in the various charging energies, the tunneling parameters V_j and the level positions ϵ_j also fluctuate from cluster to cluster. These additional fluctuations were neglected in Eq. (5.26), since their contributions decrease with increasing cluster size. For small clusters, however, they may produce important additional fluctuations in J^{eff}.

(b) It appears furthermore that the experiments were performed close to the mixed valence regime as the width of the levels is comparable to the Coulomb charging gap. The effective Kondo Hamiltonian we derived in second order perturbation theory may not adequately predict T_K in that case. In general, approaching the mixed valence regime the Kondo temperature becomes larger than expected by the naive Kondo model calculation, the Coulomb gap shrinks, and the Kondo resonance gradually merges with the high-energy part of the spectrum.

(c) It could be possible that some of the Co atoms in the cluster are not strongly attached to the others, and in the STM spectrum one observes the signal of these individual atoms. This explanation is, however, very unlikely in our opinion, because the Co atoms show a very strong tendency to cluster formation, and moreover the Kondo resonance is observed rather uniformly over the surface of clusters which are supported on nanotubes.

(d) In our analysis, we assumed that the anisotropy energy is smaller than the Kondo temperature, and therefore neglected it. However, it is conceivable that very small clusters have a considerably larger anisotropy than our estimates based on experiments on large clusters[67, 68]. According to the STM measurements,[43, 59] Co clusters in the nanotube experiments tend to have 'pancake-shape' and the relative position of the Co atoms is probably strongly modified with respect to the bulk due to the presence of the substrate. Although the value of spin-orbit interaction on Cobalt is not particularly large, it is still possible, that the highly anisotropic shape of the cluster and the deformed bonds generate an anisotropy, that is larger or comparable to the observed Kondo temperature, $T_K \sim 70K$. The effect of anisotropy on the behavior of the grain is rather complex, and we shall discuss it in a subsequent publication [77]. We would like to mention, however, two important results that may be relevant to the experiments. Large spin anisotropy is usually unfavorable to the Kondo effect: In most cases it leads to an Ising-like behavior with exponentially suppressed effective Kondo couplings, and gives rise to a dramatic decrease of T_K. However, for very small grains with a half-integer total spin and an almost perfect *planar* anisotropy, it can result in an effective strongly anisotropic Kondo coupling that is considerably *larger* than the couplings in Eq. (5.34). We find that for the smallest grains in Ref. [43, 59] strong planar anisotropy could give rise to a T_K in the experimental range.

(e) Another possible source of error is our assumption that the calculated bulk density of states can be used for a small cluster. If the peak in the density of singly occupied states is shifted significantly from the energy value shown in Ref. [69], the value of J^{eff} might be increased. It is also possible that many-body corrections, omitted from our mean field model, could increase the value of J^{eff} sufficiently to account for the discrepancy with the experimental T_K.

It is interesting to compare the results for ferromagnetic Co clusters with nonmagnetic Ag clusters studied on single wall metallic nanotubes[43, 59]. The Ag clusters showed no Coulomb gap or discrete level spacing in the STM spectrum. This suggests that the Ag clusters were not in the weak tunneling regime where valence fluctuations can be ignored, and where an effective Kondo Hamiltonian can be derived for a particle with an odd number of electrons. (Indeed, if the coupling to the substrate is sufficiently large, the mean number electrons on the cluster may be far from an integer, and the distinction between even and odd becomes meaningless.) Our analysis suggests that a Kondo effect can occur for a particle of a non-magnetic metal, with odd electron number, if the coupling to the nanotube is in an appropriate intermediate regime.

It is also interesting to compare the results for Co particles on nanotubes with measurements of several Co particles on a highly-oriented pyrolytic graphite (HOPG) sheet reported in Ref. [43, 59]. The STM measurements did not show apparent single particle levels in the latter case. Assuming that the coupling to a nanotube and graphite were not too different, this could be explained by a higher density of states on the HOPG surface[78]. (Recall that for 1 nm Co clusters on nanotubes, the level broadening was roughly equal to the level spacing. Thus the levels may be broadened beyond resolution on the HOPG surface.) The STM measurements typically show a minimum in the dI/dV spectrum near zero bias, when tunneling into the Co cluster on HOPG, but the width of the feature is relatively large. When fit to a Fano formula for a Kondo resonance, the authors of Ref. [43, 59] obtained values of T_K of order 700 K even for clusters as large as 1 nm in diameter. Since it was not possible to raise the temperature enough to observe a temperature effect on the tunneling feature, however, supporting evidence for existence of a Kondo effect could not be obtained from this source. We note that STM measurements for tunneling directly into the HOPG substrate also show a mininum at zero bias.

Differences in the coupling of Co clusters to a nanotube or graphite surface may also play a role in the observed spectral differences. Theoretical and experimental studies of STM images of graphite surfaces have indicated that there is an asymmetry in the local density of states at nearest neighbor atoms[79, 80]. This difference may also play a role in the interpretation of the spectra of Co on HOPG. Finally, it is possible that the matrix element for coupling between the cluster and the nanotube is reduced relative to the coupling to graphite due to the curvature of the nanotube.

5.7 Conclusions

In this paper we have studied electron scattering from ferromagnetic clusters on a metallic substrate. We studied two cluster models. The first model describes itinerant ferromagnetism [60] and is probably appropriate for the description of experiments such as those of Odom *et al.*[43, 59] on Co clusters. We also proposed another solvable cluster model, where spins on the d-levels are treated as *localized* entities. This latter model may be more appropriate for nanoscale rare earth ferromagnets or semiconducting ferromagnets such as GaMnAs, though in both cases spin-orbit interaction plays an important role and leads to strong spin-anisotropy effects.

We derived a general expression for the Kondo couplings $J^{\mu\nu}$ for both ferromagnetic cluster models. The sign of the obtained coupling depends in both models on the details of the band structure. For the itinerant model, virtual tunneling onto the singly occupied levels on the cluster induces an antiferromagnetic exchange interaction, while doubly occupied and unoccupied levels generate a ferromagnetic contribution to the exchange coupling.

We have shown that for Co clusters the itinerant model leads to *dominantly antiferromagnetic coupling* between the cluster spin and the conduction electron spins. However, fluctuations to doubly occupied and empty states give a large ferromagnetic contribution to the exchange coupling that reduce it to roughly half its original value, and thus cannot be neglected. (As we discussed in Sec. 5.3, for the non-ferromagnetic spin $S = 1$ islands studied in Ref. [70] these ferromagnetic contributions are small.)

The exchange coupling $J^{\mu\nu}$ involves various scattering channels. Therefore, in principle, the cluster could produce a series of Kondo effects where the spin of the cluster is gradually screened[72].

It is important to emphasize that in the regime of weak electron tunneling between the metallic substrate and the cluster, ferromagnetism has no special role in producing the Kondo effect as we have emphasized in Sec. 5.4.2. In fact, our calculation shows that ferromagnetism tends to *suppress* the Kondo temperature with increasing N_A more so than for the case of a non-ferromagnetic cluster. Besides the "strength" of the ferromagnetism, U,the Kondo scale is also affected by the density of states on the cluster and finite charging energy, as well as the cluster-metal conductance.

The weak tunneling analysis we performed is only appropriate if the conductance between the cluster and the metal lead is smaller than the quantum conductance. Increasing the number of tunneling points leads to an increase in the cluster-metal conductance. Once this conductance becomes larger than the quantum conductance, the effective charging energy is renormalized to a value close to zero, and a perturbative computation in $\hat{V}$ breaks down. In this regime extended states on the cluster are strongly hybridized with those in the metal, and can be viewed as part of the extended states in the metal.

In the regime of strong electron tunneling between the substrate and cluster, it is not clear whether the itinerant model is able to produce a Kondo effect. On the other hand, our local moment cluster model gives a natural description of the strong tunneling regime. In the local moment model the localized d-electron spins can be viewed as a magnetic cluster embedded in the metallic host. This model has been analyzed in detail in Ref. [71]. In our local moment model, antiferromagnetic exchange ($J > 0$ in Eq. (5.35)) between the local moments and the conduction electrons produces a Kondo effect in the strong tunneling regime, though, the Kondo temperature decreases very fast with increasing cluster size. We have also argued that within the local moment model, the effective coupling between the electrons in the substrate and the cluster spin must change sign as one gradually increases the tunneling between the cluster and the substrate.

Both the itinerant and local moment calculations show that the Kondo coupling is *inversely* proportional to the *total spin* S_T of a ferromagnetic cluster, which in turn, is proportional to the size of the cluster[9]. The Kondo effect is due to quantum fluctuations of the cluster spin, and these are suppressed as $1/S_T$ for large ferromagnetic clusters. Thus T_K goes to zero *exponentially* with increasing cluster size.

To make stronger contact with the experiments of Ref. [43, 59] on Co clusters on a carbon nanotube, we also calculated the STM spectra of a ferromagnetic cluster as described in Sec. 5.4A. We found that mesoscopic fluctuations in the charging energies may give rise to interesting qualitative changes and asymmetries in the STM spectrum. It is possible, for example, that the positively and negatively charged states of the cluster have very different decay rates and therefore the positive (negative) voltage side of the spectrum shows discrete levels while the negative (positive) voltage side displays a continuum spectrum.

We can use the model parameters extracted from the high energy part of the STM spectra to make an estimate of T_K and predict how it scales with cluster size. Our results agree with the experiments in that they produce a rapid decrease of T_K thereby rendering the Kondo effect impossible to observe in larger clusters. However, the Kondo temperature we find is already too small by a factor of ~ 500 compared to the T_K observed for a small cluster of ~ 8 atoms. In Sec. 5.6 we have enumerated a number of effects which might raise T_K relative to the predictions of our simple model which may be a possible explanation for the discrepancy between theory and experiment. We remark that by neglecting the ferromagnetic contributions to the

---

[9] We assumed that the magnetization per atom on the cluster is independent of the size of the cluster.

exchange coupling one would obtain a T_K that is larger by a factor of $\sim 10^3$. Thus the ferromagnetic contributions to the effective coupling are essential and cannot be neglected.

Many open questions remain regarding the physics of small ferromagnetic clusters. Among them are: (i) Accurate estimates of the net spin of 5-50 atom clusters supported on a substrate. (ii) Magnetic anistropy energies in clusters this size. (iii) The nature of non-equilibrium and other many body effects. We believe that the STM is a crucial tool for gathering cluster-specific data for ferromagnetic nanoparticles and will undoubtedly reveal even more intriguing physics of these tiny systems in the years to come.

Chapter 6

Introduction to the Diluted Magnetic Semiconductor $Ga_{1-x}Mn_xAs$

6.1 Brief Review of Central Experimental Results

Semiconductors have been the subject of intense research for decades due to their technological uses in electronic devices. Recently there has been a surge of interest in diluted magnetic semiconductors[81] (DMS)[1] because of their potential use in spin-based computation[83, 84] or "spintronic" devices. In particular, $Ga_{1-x}Mn_xAs$ has been shown to be ferromagnetic (at least for $0.03 < x < 0.07$, at sufficiently low temperatures) and to have a bulk Curie temperature as high as $T_c \sim 110$ K[62].

---

[1] Diluted refers to the fact that in materials like $Ga_{1-x}Mn_xAs$, a III-V semiconductor, the magnetic ions (Mn) only occupy a fraction of the available lattice sites. Earlier diluted magnetic semiconductor compounds were often based on II-VI materials such as CdTe and ZnSe. See Ref. [82] for reviews.

Diluted ferromagnetic semiconductors are very difficult materials to produce because magnetic ions (such as Mn) are often insoluble in the semiconducting host. The breakthrough in fabrication has been the ability in recent years to grow such materials by molecular beam epitaxy[85]. The technique involves nonequilibrium growth conditions. The properties of GaMnAs, such as the magnetization and Curie temperature, depend on the details of the annealing protocol[86]. In order to obtain the highest possible Curie temperature and magnetization, there is an optimal annealing time and temperature[87]. For $\mathrm{Ga}_{1-x}\mathrm{Mn}_x\mathrm{As}$ with $x \approx 0.05$ the optimal anneal is about 2 hours at 250^o C. (The sample itself is grown near or at 250^o C; the relatively low temperature is required to prevent the Mn from diffusing out of Ga lattice sites.)

Creating diluted magnetic semiconductors from a III-V semiconductor like GaAs has has a number of advantages over the older II-VI compounds[2]. Namely, GaAs is already used in many common electronic and optoelectronic devices (such as cellular phones (microwave transistors) and compact disks (semiconductor lasers) to name a couple) so there is potential to use the magnetism of a material like $\mathrm{Ga}_{1-x}\mathrm{Mn}_x\mathrm{As}$ in already existing devices, or at least with minimal modification.

In $\mathrm{Ga}_{1-x}\mathrm{Mn}_x\mathrm{As}$ the Mn ions are believed to be in the Mn^{2+} configuration corresponding to a half-filled d shell with spin $S = 5/2$ [89, 90, 91]. When Mn substitutes for a group III element like Ga, it gives a hole to the lattice. So both magnetism and doping are achieved at once. The doping, it turns out, is necessary for the ferromagnetism of $\mathrm{Ga}_{1-x}\mathrm{Mn}_x\mathrm{As}$. When Mn is substituted into a II-VI material, no doping occurs, and those materials are often antiferromagnetic. Where these

---

[2] For a condensed summary of early experimental data on $\mathrm{Ga}_{1-x}\mathrm{Mn}_x\mathrm{As}$ see Ref. [88].

doped holes go in $\mathrm{Ga}_{1-x}\mathrm{Mn}_x\mathrm{As}$ has become a subject of interest[3]. Several recent experiments[92, 93, 94] suggest the formation of an impurity band in the material at low ($x < 0.03$) concentrations of Mn, but at higher concentrations the impurity band must merge with the valance band.

The hole concentration of $\mathrm{Ga}_{1-x}\mathrm{Mn}_x\mathrm{As}$ is typically determined by Hall measurements, but lack of saturation of the magnetization in fields as high as 27 Tesla[95] have complicated its determination. Recent electrochemical capacitance-voltage profiling measurements have indicated that the actual hole concentration may be a factor of 5 or so larger than determined by Hall measurements[96]. The hole concentration is crucial to determine because many quantities depend sensitively on its value, as we will show in the next two chapters. In our calculations to follow, we typically assume a hole fraction of $f = 0.1 - 0.3$. Holes trapped at As antisite defects (As substituted for Ga) and Mn interstitials are generally thought to be responsible for the compensation. As of the writing of this thesis, it has become increasingly apparent that the details of different types of defects (interstitial Mn, $\mathrm{Mn_I}$, As antisites, $\mathrm{As_{Ga}}$, antiferromagnetically ordered pairs, $\mathrm{Mn_I} - \mathrm{Mn_{Ga}}$, etc.) in the material play an important role in the physics[97, 98, 87, 99]. Understanding the effect of these defects on the basic physics is a very active area of research.

Related to the issue of hole states are the two experimentally observed T=0 transitions as a function of x: (1) A metal-insulator transition and (2) a ferromagnetic to paramagnetic phase transition. Both of these transitions occur around

---

[3] Also how *many* holes there are is of interest. Depending on how the hole concentration is measured there may be as much as 90% compensation. (For every 100 Mn there are only 10-30 holes given to the lattice.)

$x \approx 0.03$, but it appears that ferromagnetism sets in (as a function of x) before metallic behavior[92, 93, 94]. Which side of the metal-insulator transition one is interested in determines the best theoretical approach to use to study the material.

6.2 Theoretical Approaches to $\mathrm{Ga}_{1-x}\mathrm{Mn}_x\mathrm{As}$

There are two physically important limits to understand, the dilute (insulating) and the metallic limit. In this thesis, the dilute limit corresponds to $x \approx 0.01$ and transport is characterized by hopping conduction and an impurity band. The metallic limit corresponds to $x \approx 0.05$ and the sample behaves for the most part as a metal (there is a Fermi sea of nearly free charge carriers) indicating that transport is dominated by the valence band. From the point of view of the theorist, the important difference between the two limits is the Hamiltonian one takes as the starting point. Typically in the dilute limit, some type of atomic-like or tight-binding approach is used while in the metallic limit a partially filled valence band (a Fermi sea) is taken as a starting point. Each approach has some advantages and some drawbacks. Below we emphasize the important features of each. Meanfield and Monte Carlo calculations are a staple for both limits.

6.2.1 Dilute Limit

In the dilute limit ($x \approx 0.01$) a reasonable starting point is to assume an atomic-like description for the holes[100] (doped in by the Mn)[4]. The hole wavefunc-

---

[4] For a review of this approach see R. N. Bhatt *et al.*, J. Superconductivity INM **15**, 71 (2002).

tions tend to be concentrated around the Mn ions because they are oppositely charged (at least for substitutional Mn which carry a -1 charge). Conduction is dominated by holes hopping from Mn to Mn. When the Mn concentration (and hence the hole concentration) becomes sufficiently large, there is appreciable overlap between the wavefunction tails of the holes centered on different Mn sites and an impurity band forms[101]. In this limit, then, the positional disorder of the substitutional Mn impurities is very important and affects many observable quantities, such as the Curie temperature, the shape and magnitude of the magnetization curve, the resistivity and the spin-wave spectrum[102]. While the interstitial Mn are thought not to participate in the magnetism, they are believed to be very important in clustering substitutional Mn during growth and therefore correlating the disorder[99]. In the dilute limit, the charged centers (Mn and other defects) are not well screened (compared to the metallic limit) and play an important role in the physics as well.

In chapter 7 we discuss our approach to the dilute limit which includes for the first time the effects of spin-orbit coupling in the hydrogenic-like states of a hole about a Mn impurity. This leads to a d-wave component of the wavefunction of a bound hole around a Mn ion and results in direction-dependent hopping parameters of an effective Hamiltonian that we derive. We show by means of a mean-field calculation that this direction-dependent hopping, coupled with positional disorder in the Mn ion locations produces a strong anisotropy in the magnetization. We also calculate the density of states and find a well-formed impurity band and a Fermi energy that sits at the mobility edge for reasonable sample parameters.

6.2.2 Metallic Limit

By contrast, in the metallic limit ($x \approx 0.05$) many of the holes are in the valence band and behave essentially as free particles[5]. The screening of the charged Mn and other defects is much more effective and can sometimes be neglected. One approach to take is to neglect disorder altogether by coarse graining the ions[103] into an effective field. Much progress can be made this way and many of the results are quite general (because they do not depend on disorder). However, it turns out that many features of the data require that the disorder be properly taken into account and nearly all current research on GaMnAs takes this point of view.

In chapter 8 we present results from our study of the metallic limit in which we keep the disorder in the system but assume the holes are free and reside in the valence band. As in chapter 7 we keep the effects of spin-orbit coupling in the GaAs host band structure and calculate the interaction kernel between two Mn ions a distance R away from each other within the Baldereschi-Lipari spherical approximation. We use the fact that the holes behave as spin-3/2 objects rather than the usual spin-1/2 objects familiar for metals. Using this kernel, we carry out a Monte Carlo study of the magnetization, susceptibility, Curie temperature and distribution of angles the individual Mn ion spins make with the net magnetization direction. We study how these quantities depend on Mn positional disorder and hole fraction, f.

---

[5] For a review of this approach see J. König *et al.* in Electronic Structure and Magnetism of Complex Materials, edited by D.J. Singh and D.A. Papaconstantopoulos (Springer Verlag 2002).

Chapter 7

Effective Hamiltonian for $Ga_{1-x}Mn_xAs$ in the Dilute Limit

7.1 The Effective Hamiltonian

In this chapter we focus on one of the most studied magnetic semiconductors, $Ga_{1-x}Mn_xAs$, with a maximum bulk Curie temperature $T_C \approx 110$K [62], though most of our calculations carry over to other p-doped III-V magnetic semiconductors[104]. In $Ga_{1-x}Mn_xAs$ substitutional Mn^{2+} play a fundamental role: They provide local spin $S = 5/2$ moments, and they also dope holes into the valence band[89]. Since the Mn^{2+} ions are negatively charged compared to Ga^{3+}, in the very dilute limit they bind these holes, forming an acceptor level with a binding energy of about $E_b \approx 112$meV [89]. As the Mn concentration increases, these acceptor states start to overlap and form an impurity band, which for even larger Mn concentrations merges with the valence band. Though the actual concentration at which the impurity band disappears is not known, according to optical conductivity measurements[94], this impurity band seems to persist at least up to nominal Mn concentrations of about $x \approx 0.05$. ARPES data[92, 93] and the fact that even "metallic" samples feature a resistivity upturn at low temperature[88] and seem to be on the localized side of the transition, suggest that for smaller concentrations (and maybe even for relatively large nominal concentrations) one may be able to describe $\mathrm{Ga}_{1-x}\mathrm{Mn}_x\mathrm{As}$ in terms of an impurity band [101].

In $\mathrm{Ga}_{1-x}\mathrm{Mn}_x\mathrm{As}$ the Coulomb potential created by the Mn ions is by far the largest energy scale in the problem [99], but spin-orbit coupling in the hole band is also quite large compared to the exchange coupling between the holes and the Mn spins[89].

Fortunately, in the dilute limit Coulomb scattering on the Mn ions can be handled non-perturbatively. We can therefore attempt to derive a many-body Hamiltonian in this limit that captures spin-orbit effects, treats the large Coulomb interaction non-perturbatively, and also incorporates the exchange coupling between the local moments and the holes. As we mentioned above, the model we construct is very general and appropriate for describing other p-doped III-V semiconductors as well, and a slightly modified version of it can be used for p-doped II-VI magnetic semiconductors [104].

The top of the valence band in $\mathrm{Ga}_{1-x}\mathrm{Mn}_x\mathrm{As}$ can be described in terms of spin $j = 3/2$ holes [105]. Ignoring for the moment the exchange interaction between the Mn spin and the holes, in the so-called spherical approximation, the motion of the holes in the Coulomb potential of an Mn ion is described by the following Hamiltonian[106],

$$H_0 = \frac{\gamma}{2m}\Big(p^2 - \mu \sum_{\alpha,\beta} J_{\alpha\beta} p_{\alpha\beta}\Big) - \frac{e^2}{\epsilon\ r} + V_{cc}(r)\ , \tag{7.1}$$

where $\gamma \approx 7.65$ is a mass renormalization parameter, m is the free electron mass, $\mu \approx 0.77$ is the strength of the effective spin-orbit coupling, $\epsilon \approx 10$ is the dielectric constant of GaAs, and V_{cc} is the so-called central cell correction [107]. The spin-orbit coupling term in Eq. (7.1) couples the momentum tensor of the holes $p_{\alpha\beta} = p_\alpha p_\beta - \delta_{\alpha\beta}\ p^2/3$ to their quadrupolar momentum, $J_{\alpha\beta} = (j_\alpha j_\beta + j_\beta j_\alpha)/2 - \delta_{\alpha\beta}\ j(j+1)/3$.

The bound states of H_0 (without the central cell correction) have been studied in detail in the seminal paper of Baldereschi and Lipari [106]. Due to the spherical symmetry, the total momentum, $\vec{F} \equiv \vec{L} + \vec{j}$, is a conserved quantity, where $\vec{L}$ is the orbital angular momentum. The ground state of H_0 is a four-fold degenerate $F = 3/2$ multiplet that contains a substantial d-wave contribution in the case of GaAs due to the strong spin-orbit coupling. In Fig. 7.1 we illustrate the importance of this d-wave component by presenting the spatial dependence of the hole polarization, $\vec{j}(\mathbf{r})$, for the state $|F = 3/2, F_z = 3/2\rangle$ which we calculated directly from the Baldereschi-Lipari wave functions with the central cell correction. (See Appendix F for exact expressions of the hole polarization and see Appendix E for details of the variational calculation of the Baldereschi-Lipari wave functions.) The direction of the induced hole polarization has a strong angular dependence due to the d-wave component.

In the dilute limit, for most purposes, we can restrict ourselves to this four-

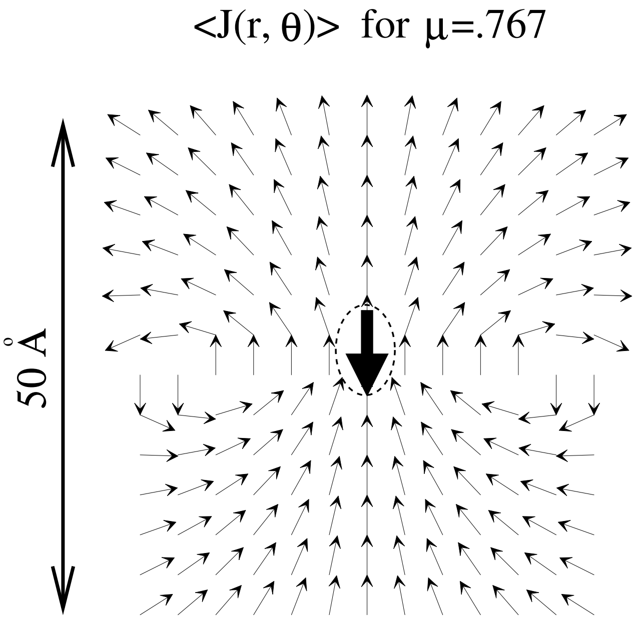

Figure 7.1: Polarization of a bound hole in the state $|F = 3/2, F_z = 3/2\rangle$ in $\mathrm{Ga}_{1-\mathrm{x}}\mathrm{Mn}_{\mathrm{x}}\mathrm{As}$ around a Mn ion (dark arrow pointing downwards represents the Mn S=5/2 spin). Only the direction of the polarization is indicated. The magnitude falls off on a scale ~ 10 Å.

fold degenerate $F = 3/2$ acceptor level. In the presence of a Mn spin the fourfold degeneracy of the state is lifted due to the exchange interaction between the Mn spin $\vec{S}$ at the origin:

$$H_{\mathrm{exch}} = G\vec{S} \cdot \vec{F} \ , \tag{7.2}$$

where the exchange coupling, $G \approx 5$ meV, can directly be determined by infrared spectroscopy[89]. Thus, in this limit, we can think of the charge carriers in $\mathrm{Ga}_{1-x}\mathrm{Mn}_x\mathrm{As}$ as spin $F = 3/2$ holes hopping between Mn sites and exchange coupled to the localized Mn spins. However, because of the large d-wave component of the Baldereschi-Lipari wave function, we expect the hopping of these carriers to be strongly spin-direction dependent. This expectation is born out by our microscopic calculations below.

To determine the numerical values of the parameters of our model we carried out a variational study of the molecular orbitals for a pair of Mn ions [104, 108]. (See Appendix G for details.) For the case where both the Mn-Mn bond and the quantization axis of F are parallel to the z-axis, F_z is conserved and the spectrum of the lowest lying levels can be fully characterized by the following Hamiltonian:

$$\begin{aligned}\hat{H}^{\text{eff}}_{\text{Mn}-\text{Mn}} &= \sum_{\nu} t_\nu(R)\left(c^\dagger_{1,\nu}c_{2,\nu} + \text{h.c.}\right) \\ &+ \sum_{\substack{i=1,2\\ \nu}} \left(K(R)\,\left(\nu^2 - \frac{5}{4}\right) + E(R)\right)\, c^\dagger_{i,\nu}c_{i,\nu} \\ &+ G\sum_{\substack{i=1,2\\ \mu,\nu}} \vec{S}_i\cdot\left(c^\dagger_{i,\mu}\vec{F}_{\mu\nu}\, c_{i,\nu}\right)\ . \end{aligned} \tag{7.3}$$

Here $c^\dagger_{i,\nu}$ creates a hole at the acceptor level $|F = 3/2, F_z = \nu\rangle$ at position i ($i = 1, 2$). By time reversal symmetry, the hopping parameters satisfy $t_{3/2} = t_{-3/2}$ and $t_{1/2} = t_{-1/2}$. All parameters depend only on the distance R between the two Mn sites. The R-dependence of the four independent couplings is shown in Fig. 7.2. The most obvious effect of the spin-orbit coupling is that the hopping parameters $t_{3/2}$ and $t_{1/2}$ substantially differ from each-other; Holes that have their spin aligned with the Mn-Mn bond are more mobile.

As indicated by the arrows, at the typical Mn-Mn distance for $x = 0.01$, K and $t_{1/2}$ can be entirely neglected compared to the energy shift E and the hopping $t_{3/2}$. Therefore, in many cases it is enough to keep the latter two terms only in the effective Hamiltonian.

Having determined the effective Hamiltonian for a pair of Mn ions, we can proceed and approximate the Hamiltonian for a given set of positions $\{\mathbf{R}_i\}$ of the Mn

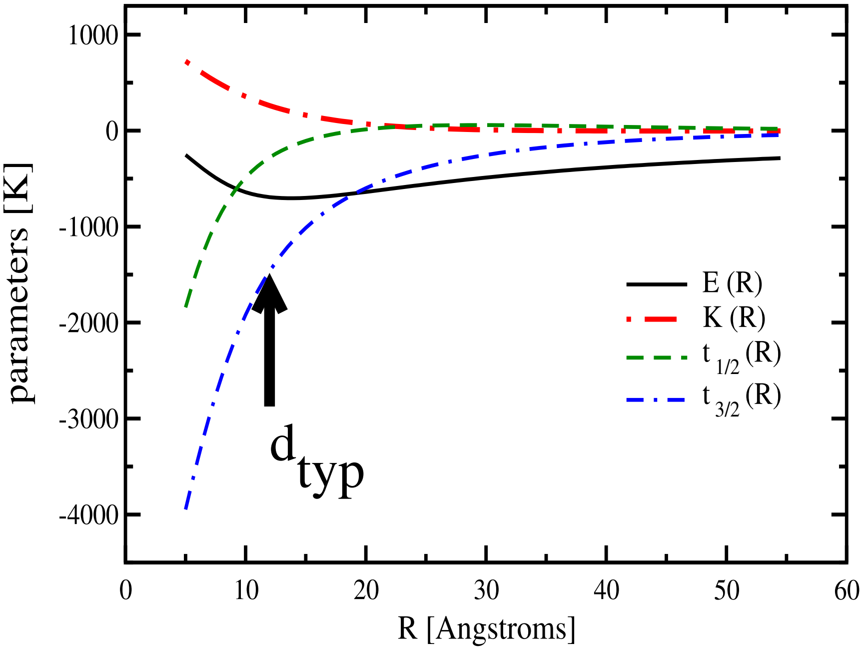

Figure 7.2: Parameters of the two-impurity Hamiltonian Eq. (7.3) obtained from the variational study of two Mn ions. The arrows indicate the typical Mn-Mn distance, d_{typ}, for $x = 0.01$ Mn concentration.

ions as:

$$\begin{aligned}\hat{H} &= \sum_{(i,j)} c^{\dagger}_{i,\mu} t^{\mu\nu}_{ij} c_{j,\nu} + \sum_{i} c^{\dagger}_{i,\mu} \left(K^{\mu\nu}_{i} + E_i\,\delta^{\mu\nu}\right) c_{i,\nu} \\ &+ G \sum_{i,\mu,\nu} \vec{S}_i \cdot (c^{\dagger}_{i,\mu} \vec{F}_{\mu\nu}\, c_{i,\nu})\ . \end{aligned} \tag{7.4}$$

The Hopping matrix $t^{\mu\nu}_{ij}$ above can be obtained by rotating the z-axis along the bond direction $\vec{n}_{ij}$, $\mathbf{t}_{ij} = \mathbf{D}(\vec{n}_{ij})\hat{\mathbf{t}}(R_{ij})\mathbf{D}^{\dagger}(\vec{n}_{ij})$, where $\mathbf{D}(\vec{n}_{ij})$ is a spin 3/2 rotation matrix, and $\hat{\mathbf{t}}(R)$ denotes the diagonal matrix $diag\left(t_{3/2}(R),\ t_{1/2}(R),\ t_{1/2}(R),\ t_{3/2}(R)\right)$. The anisotropy term, $\mathbf{K}_i$, and the energy shift E_i are given by $\mathbf{K}_i = \frac{1}{2}\sum_{j\neq i} K(R_{ij})\ ((\vec{n}_{ij} \cdot \vec{F})^2 - \frac{5}{4})$ and $E_i = \frac{1}{2}\sum_{j\neq i} E(R_{ij})$, respectively.

So far we have neglected the interaction between holes. In the localized phase, however, this interaction may play an important role. In general, the Coulomb interaction between holes on different Mn sites has a very complicated form [104], though for large separations the interaction takes on a much simpler form. Fortunately, the dominant interaction term is the *on site* hole-hole interaction term. Within the spherical approximation this interaction can be simply expressed as (See Appendix H for details):

$$\hat{H}_{\mathrm{int}} = \frac{U_N}{2} \sum_i : \hat{N}_i^2 : + \frac{U_F}{2} \sum_i : \hat{\vec{F}}_i^{\,2} : , \tag{7.5}$$

where $\hat{N}_i = \sum_\nu c^\dagger_{i,\nu} c_{i,\nu}$, $\hat{\vec{F}}_i = \sum_{\mu,\nu} c^\dagger_{i,\mu} \vec{F}_{\mu\nu} c_{i,\nu}$, and : ... : denotes normal ordering. We estimated the constants appearing in Eq. (7.5) by evaluating exchange integrals as $U_N = 2600$ K and a Hund's rule coupling $U_F = -51$ K.

Eqs. (7.4) and (7.5), together with the microscopic parameters of Fig. 7.2, constitute our central results. They provide a well controlled theoretical framework that is able to capture the most important aspects of dilute magnetic semiconductors such as the localization phase transition, random anisotropy, disorder effects, and frustrated ferromagnetism. Postponing much of our detailed analysis to a longer publication, here we only demonstrate the power of this model on a few examples. Parameters for other materials will be presented elsewhere [104].

7.2 Mean Field Study of Effective Hamiltonian

To get a better understanding of the model we first computed the ground state of four Mn atoms at a separation of $\sim 15\mathring{A}$ due to the interaction mediated by a single hole on the cluster. We treated the Mn spins classically and used the simple mean field approximation of Ref. [101]. We considered only configurations where the

Mn ions were positioned on a slightly distorted tetrahedron with three edges of length $a = 15\mathring{A}$ and three edges of length b (see Fig. 7.3). In all cases, in the ground state, the Mn spins are relatively collinear apart from a slight tilt of the order of $5 - 10^o$. However, the spatial position of the Mn ions generates a strong anisotropy. Thus, the energy depends strongly on the directional orientation of the net spin relative to the underlying lattice. To demonstrate this we calculated the ground state energy as a function of the Mn spin direction (assuming full alignment). For a perfectly regular tetrahedron this anisotropy is rather small, less then 0.5K. However, the anisotropy increases with the ratio b/a, and for $b/a = 1.2$ it can be as large as 20K/Mn. In other words, random positions of the Mn ions induce a *random anisotropy* term that, depending on the disorder, is much larger than the bulk anisotropy, which is of the order of 1 K. Thus disorder and spin-orbit coupling together can induce a large random anisotropy energy that can easily be comparable to T_C. These findings are in good agreement with earlier results obtained in the metallic limit [109].

Finally, let us discuss some of the results we obtained for a finite system of $\mathrm{Ga_{1-x}Mn_xAs}$ of linear sizes $L = 10a_{\mathrm{lat}}$ and $L = 13a_{\mathrm{lat}}$ (with $a_{\mathrm{lat}} = 5.65\mathring{A}$, the size of the conventional unit cell) and active Mn concentration $x_{\mathrm{active}} = 0.01$, using the above-described mean field techniques at zero temperature. In the calculations presented below, we have not included the effects of Eq. (7.5). We have to emphasize that x_{active} can be substantially less then the nominal Mn concentration, x, which also includes inactive Mn sites [98, 96], and therefore these calculations may be relevant even for systems with larger nominal Mn concentration. The concentration of holes is

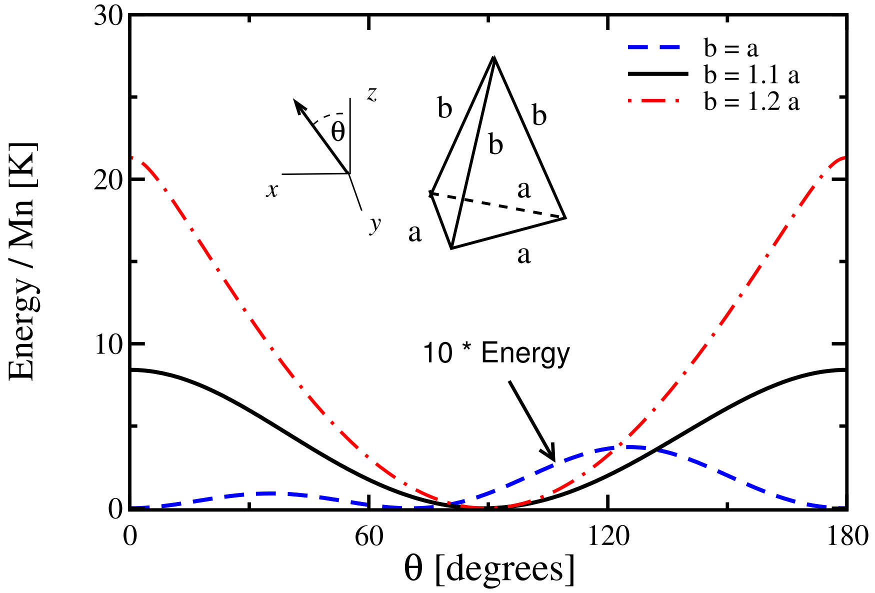

Figure 7.3: Anisotropy induced by the distortion of a regular Mn tetrahedron in the presence of a single hole. The Mn-Mn distances are $a = 15\mathring{A}$ and $b = 15\mathring{A}$, $b = 16.5\mathring{A}$, and $b = 18\mathring{A}$, respectively. Note that the distortion generated anisotropy can be almost two orders of magnitude larger than the undistorted anisotropy, which is of the order of about 1K.

also reduced compared to x due to strong compensation effects. In these calculations we assumed that the number of holes is reduced by a factor of $f = 0.3$ compared to the number of Mn ions.

To take into account correlations induced between interstitial Mn ions during the experimental growth process, we introduced a screened Coulomb repulsion between the Mn ions and let them relax for some time t_{relax} using classical $T = 0$ Monte Carlo simulations. For very large t_{relax} we found that the Mn ions form a regular bcc lattice with some point defects. The data we present here are for intermediate relaxation times, where there is still a lot of disorder in the system.

Once we fixed the Mn positions in a given instance, we solved the mean

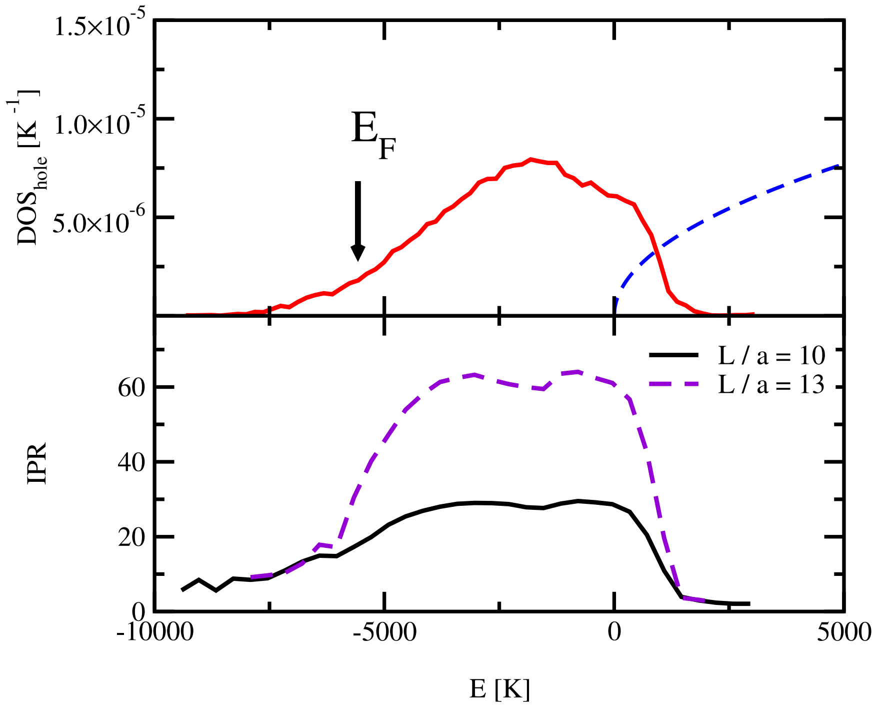

Figure 7.4: Top: Computed hole density of states for an $L = 10a$ lattice. We used $x = 0.01$ and $f = 0.3$. For comparison, we also show the density of states of the valence band (dashed line). The Fermi energy is ≈ -6500 K. Bottom: The inverse participations ratio for $L = 10a_{\text{lat}}$ and $L = 13a_{\text{lat}}$. States in the tails are localized while states in the middle of the impurity band seem to be delocalized. States in the valence band side tail probably mix with the band and are delocalized in reality.

field equations derived from (7.4) self-consistently [101]. In our calculations we used periodic boundary conditions and implemented a short distance cutoff in the hopping parameters of Eq. (7.4) which corresponds to about 8 neighbors for each Mn. The use of this cut-off is justified by the observation that our molecular orbit calculations are only appropriate for "nearest neighbor" ion pairs, and in reality, holes cannot hop directly over the first "shell" of ions. In course of the calculations we started from a configuration with fully aligned classical Mn spins, $\vec{\Omega}_i \equiv \vec{S}/S$, and then let the system relax to the nearest metastable state. Similar to the metallic case [109], we find a ferromagnetic state with a largely reduced magnetization, $|\langle\vec{\Omega}_i\rangle| \approx 0.4$ for $L = 10a_{\mathrm{lat}}$. We find that this reduction is largely due to spin-orbit coupling, and that the cosine of the angle θ between the spins and the ground state magnetization has a broad distribution similar to the metallic case [109].

The density of states is shown in Fig. 7.4 (as a comparison, we also plotted the approximate density of states for the hole band). The half-width of the impurity band is about 0.2 eV at this density, which therefore slightly overlaps with the bulk density of states of the holes. However, comparison with the valence hole density of states suggests that at this concentration a well-formed impurity band may still be present, and it might even persist up to higher concentrations. Indeed, as mentioned in the introduction, this scenario seems to be supported by many experiments[94, 92, 93].

The impurity band has a tail of localized states that reaches somewhat inside the band gap. These localized states can be identified by computing the inverse participations ratio, IPR= $\left[\sum_i\left(\sum_\alpha|\psi_{i\alpha}|^2\right)^2\right]^{-1}$ for various system sizes (see Fig. 7.4). This tail gradually disappears when we introduce correlations between the Mn ions which tend to form regular structures [104]. In agreement with ARPES data[92], we also find that the chemical potential lies deep ($\sim 0.5\,\mathrm{eV}$) inside the gap, in the vicinity of the mobility edge, a regime where our model is probably more reliable. This raises the interesting possibility that the localization phase transition in $\mathrm{Ga}_{1-x}\mathrm{Mn}_x\mathrm{As}$ could happen inside the impurity band and that the ferromagnetic phase for smaller Mn concentrations is governed by localized hole states [99, 110].

We emphasize that, though our calculations are based on microscopic model calculations, they are certainly only approximate, and more realistic band structure calculations would be needed to give a quantitative answer concerning the role of the impurity band. Also, though the spherical approximation we used is able to reproduce rather well the spectrum of a single acceptor, it might overestimate the effect of spin-orbit coupling.

In summary, based on microscopic calculations we constructed a many-body Hamiltonian that is appropriate for describing $\mathrm{Ga}_{1-x}\mathrm{Mn}_x\mathrm{As}$ in the dilute limit. We find that the hopping of the carriers is strongly correlated with their spin, $F = 3/2$. This spin-dependent hopping is absolutely crucial for capturing spin-orbit coupling induced random anisotropy terms, the lifetime of the magnon exitations, or even to capture the universality class of the localization phase transition correctly. Our calculations suggest the presence of an impurity band for $x_{\text{active}} = 0.01$ Mn concentration.

Chapter 8

Effects of Positional Disorder and Spin-orbit Coupling in Optimally Doped $\mathrm{Ga}_{1-x}\mathrm{Mn}_x\mathrm{As}$

8.1 Effective Impurity-Impurity Interaction

Optimal doping in $\mathrm{Ga}_{1-x}\mathrm{Mn}_x\mathrm{As}$ ($x \approx 0.05$) is the doping level that results in the highest observed bulk Curie temperature, $T_C \approx 110$ K[62, 86]. For these concentrations it is believed that the Fermi energy lies within the valence bands (in contrast to the case that we discussed in the previous chapter for $x \approx 0.01$ in which the Fermi energy is thought to lie an impurity band)[93]. For this chapter, we will take this as a given and assume moreover that *all* (assuming, of course, there is still the compensation of 70-90% that we mentioned before) of the holes occupy valence band states. We will also assume that the individual Mn ions can be treated as a perturbation on this Fermi sea of holes. Because of compensation effects, the number of holes is actually less than the number of Mn, so we are not strictly in the single impurity limit discussed in Chapter 3 of this thesis. However, making this assumption allows us to explore some of the effects of spin-orbit coupling on the magnetization and other quantities to be discussed below as a function of hole concentration and Mn positional disorder. We still expect our results to qualitatively apply to $\mathrm{Ga}_{1-x}\mathrm{Mn}_x\mathrm{As}$.

The main effect of the strong host spin-orbit coupling is to couple spin-1/2 holes to the p-like states of the top of valence band at the Γ point in the Brillouin zone to form spin-3/2 (denoted by J) particles that move through the material. It has recently been pointed out[109] that the strong spin-orbit coupling in the valence band of $\mathrm{Ga}_{1-x}\mathrm{Mn}_x\mathrm{As}$ results in highly anisotropic spin-spin interactions (within the Baldereschi-Lipari spherical approximation) that generally lead to orientational frustration. We re-derive and extend this result below.

The full Hamiltonian is $H = H_{\mathrm{sp}} + H_{\mathrm{int}}$ where

$$H_{\mathrm{sp}} = \frac{\gamma_1}{2m}\left(p^2 - \nu \sum_{\alpha,\beta} J_{\alpha\beta} p_{\alpha\beta}\right) , \tag{8.1}$$

is the Baldereschi-Lipari spherical Hamiltonian[106] and

$$H_{\mathrm{int}}(\mathbf{R}) = G\mathbf{S}\cdot\mathbf{J}(\mathbf{R}) , \tag{8.2}$$

is the coupling of the Mn spin, $\mathbf{S}$, with the valence hole density, $\mathbf{J}(\mathbf{R})$, at the location of the Mn ion, $\mathbf{R}$. Here $G > 0$, so the coupling is antiferromagnetic. We have used the convention that $J_{\alpha\beta} = \frac{1}{2}(J_\alpha J_\beta + J_\beta J_\alpha) - \frac{1}{3}\delta_{\alpha\beta}\mathrm{Tr}\{J_\alpha J_\beta\}$ (likewise for the linear momentum tensor $p_{\alpha\beta}$) and $\nu = (6\gamma_3 + 4\gamma_2)/5\gamma_1 \approx 0.77$ for GaAs[106]. The various γ_i are the so-called Luttinger parameters[105] that characterize the band structure of a given semiconductor. The terms left out when H_{sp} is taken to describe the band structure are those terms that contain only the strict symmetry of the crystal; only those terms that are fully rotationally invariant are kept in H_{sp}. Thus, there is no explicit reference to the underlying lattice structure (information about it is still encoded in ν through the Luttinger parameters) in Eq. (8.1) which contains a spin-orbit like term. It is the effect of this spin-orbit term that we will focus on in the remainder of this chapter.

H_{sp} can be diagonalized in the chiral basis:

$$\hat{H}_{\mathrm{sp}} = \sum_{\mathbf{k},\mu} \frac{k^2}{2m_\mu} c^\dagger_{\mathbf{k}\mu} c_{\mathbf{k}\mu} \, , \tag{8.3}$$

where $c^\dagger_{\mathbf{k}\mu}$ denotes the creation operator of a hole with wavevector $\mathbf{k}$ and spin projection μ along $\hat{\mathbf{k}}$. Diagonalizing $\hat{H}_{\mathrm{sp}}$, however, produces a strongly momentum dependent carrier-impurity interaction:

$$\hat{H}_{\mathrm{int}} = \frac{G}{V} \sum_{\mathbf{k},\mathbf{k}'} \sum_{\alpha,\mu,\mu'} S^\alpha c^\dagger_{\mathbf{k}\mu} J^\alpha_{\mu\mu'}(\hat{\mathbf{k}}, \hat{\mathbf{k}}') c_{\mathbf{k}'\mu'} e^{-i(\mathbf{k}-\mathbf{k}')\mathbf{R}} \, . \tag{8.4}$$

Here $J^\alpha_{\mu\mu'}(\hat{\mathbf{k}}, \hat{\mathbf{k}}') \equiv \sum_{j,j'} D^\dagger_{\mu j}(\hat{\mathbf{k}}) J^\alpha_{jj'} D_{j'\mu'}(\hat{\mathbf{k}}')$ where $D(\hat{\mathbf{k}})$ is the spin 3/2 rotation matrix and V is the volume of the sample. The rotation matricies are defined by the operator $\hat{U} = e^{-i\frac{\hat{j}^z\phi}{\hbar}} e^{-i\frac{\hat{j}^y\theta}{\hbar}}$ and the matrix element $D_{j\mu}(\hat{\mathbf{k}}) = \langle j|\hat{U}(\hat{\mathbf{k}})|\mu\rangle$. Fig. 8.1 illustrates the rotation.

Using Eq. (8.4) one can calculate the effective interaction between two Mn impurities by second order perturbation theory. The result is a Hamiltonian of the

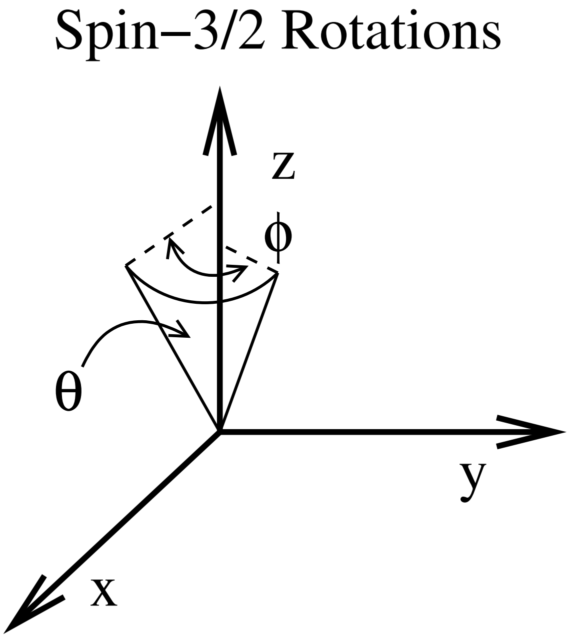

Figure 8.1: Spin 3/2 rotations. The rotations used to transform a general state $\mathbf{k}$ to lie along the z-axis where its effective mass and energy are determined.

form

$$H_{\text{eff}} = -K_{\text{par}}(R)\mathbf{S}_{\mathbf{1}}^{||} \cdot \mathbf{S}_{\mathbf{2}}^{||} - K_{\text{perp}}(R)\mathbf{S}_{\mathbf{1}}^{\perp} \cdot \mathbf{S}_{\mathbf{2}}^{\perp} \ , \tag{8.5}$$

where $R = |\mathbf{R_1} - \mathbf{R_2}|$ and $\mathbf{S_i}$ is the Mn spin at position $\mathbf{R_i}$.

The first order correction to the H_{sp} eigenstates are given by

$$|\mathbf{k},\mu\rangle' = |\mathbf{k},\mu\rangle_0 - \frac{G}{V}\sum_{\alpha,\mathbf{k}',\mu'} \frac{J^{\alpha}_{\mu\mu'}(\hat{\mathbf{k}},\hat{\mathbf{k}'})S^{\alpha}}{\epsilon_{\mathbf{k}'\mu'} - \epsilon_{\mathbf{k}\mu}} |\mathbf{k}',\mu'\rangle_0 \ , \tag{8.6}$$

where $|\mathbf{k},\mu\rangle_0 = c^{\dagger}_{\mathbf{k}\mu}|FS\rangle$ and the sum is over all *unoccupied* states. The quantity we wish to calculate is

$$\langle H_{\text{int}}\rangle = \sum_{\substack{\mathbf{k},\mu \\ \epsilon_{\mathbf{k}\mu}}}{}' \langle \mathbf{k},\mu|H_{\text{int}}|\mathbf{k},\mu\rangle' \ . \tag{8.7}$$

Dropping a piece of the energy independent of relative spin orientations, and including the energy of the spin at the origin in the field of the spin at $\mathbf{R}$ which leads to an overall factor of 2, we find

$$H_{\mathrm{RKKY}} = -2\left(\frac{G}{V}\right)^2 \sum_{\alpha\beta} \mathbf{S}^{\alpha}_{\mathbf{R}}\mathbf{S}^{\beta}_{\mathbf{0}} \sum_{\substack{\mathbf{k},\mu \\ \mathbf{k}'\mu'}} \frac{1}{\epsilon_{\mathbf{k}'\mu'} - \epsilon_{\mathbf{k}\mu}} \left(e^{i(\mathbf{k}'-\mathbf{k})\mathbf{R}} J^{\beta}_{\mu\mu'} J^{\alpha}_{\mu'\mu} + c.c.\right) \ , \tag{8.8}$$

which can be rewritten as

$$H_{\mathrm{RKKY}} = -\sum_{\alpha\beta} S^{\alpha}(\mathbf{R}) K^{\alpha\beta}(\mathbf{R}) S^{\beta}(0) \ . \tag{8.9}$$

It can be shown that only the terms with $\alpha = \beta$ are nonzero which then gives Eq. (8.5). Converting the sums to integrals and assuming a parabolic dispersion, we can write

$$\begin{aligned} K^{\alpha\alpha}(\mathbf{R}) \;&=\; 2G^2 \sum_{\mu\mu'} \int_0^{k_{F,\mu}} \frac{k^2 dk}{2\pi^2} \int_{k'_{F,\mu}}^{\infty} \frac{k'^2 dk'}{2\pi^2} \frac{1}{\frac{k'^2}{2m_{\mu'}} - \frac{k^2}{2m_{\mu}}} \\ &\quad \times \langle |J^{\alpha}_{\mu\mu'}(\theta,\theta',\phi,\phi')|^2 \, 2\cos(kR\cos(\theta) - k'R\cos(\theta'))\rangle_{\theta,\theta',\phi,\phi'} \ , \end{aligned} \tag{8.10}$$

where we have taken the angle θ (θ') to be the angle that $\hat{\mathbf{k}}$ ($\hat{\mathbf{k}'}$) makes with the z-axis, ϕ (ϕ') the angle of rotation about the z-axis as measured from the x-axis (See Fig. 8.1) and the brackets denote the angular average over the angles θ, θ', ϕ and ϕ'. Making the substitutions $k \to \sqrt{2m_{\mu}\epsilon_F}k$ and $k' \to \sqrt{2m_{\mu'}\epsilon_F}q$ yields the expression

$$K^{\alpha\alpha}(\mathbf{R}) = 8\,\epsilon_F \sum_{\mu,\mu'} g_{\mu} g_{\mu'} \int_0^1 dk \int_1^{\infty} dq \frac{q^2k^2}{q^2-k^2} I^{\alpha}_{\mu\mu'}(k_{F,\mu}kR, k_{F,\mu'}qR) \ , \tag{8.11}$$

where

$$I^{\alpha}_{\mu\mu'}(k_{F,\mu}kR, k_{F,\mu'}qR) = \langle |J^{\alpha}_{\mu\mu'}(\theta,\theta',\phi,\phi')|^2 \, 2\cos(k_{F,\mu}kR\cos(\theta) - k_{F,\mu'}qR\cos(\theta'))\rangle_{\theta,\theta',\phi,\phi'} \ . \tag{8.12}$$

Here we have used $g_{\mu} = G\varrho_{\mu} = G\frac{m_{\mu}^{3/2}}{\sqrt{2}\pi^2}\epsilon_F^{1/2}$.

To evaluate $K^{\alpha\alpha}(\mathbf{R})$ we first evaluate $I^{\alpha}_{\mu\mu'}(k_{F,\mu}kR, k_{F,\mu'}qR)$ by doing the angular integrals. We will illustrate the calculation by example. We determine the heavy hole contribution to the z-component (parallel component) of the exchange coupling. The expression is evaluated by first doing the ϕ and ϕ' integrals. Heavy holes have spin projection $\pm 3/2$ along the axis of propagation. The heavy hole contribution is

$$I^z_{hh} = I^z_{11} + I^z_{14} + I^z_{41} + I^z_{44} \ . \tag{8.13}$$

Since the ϕ integrals can be done separately we can define a quantity

$$A^z_{\mu\mu'} \equiv \langle |J^z_{\mu\mu'}(\theta, \theta', \phi, \phi')|^2 \rangle_{\phi,\phi'} \ , \tag{8.14}$$

then

$$A^z_{hh} = A^z_{11} + A^z_{14} + A^z_{41} + A^z_{44} = \frac{9}{16}(1 + \cos^2(\theta) + \cos^2(\theta') + 5\cos^2(\theta)\cos^2(\theta')) \ . \tag{8.15}$$

The integral over θ and θ' remains to be done:

$$\begin{aligned} I^z_{hh}(k_{F,h}kR, k_{F,h}qR) = \langle &\frac{9}{16}(1 + \cos^2(\theta) + \cos^2(\theta') + 5\cos^2(\theta)\cos^2(\theta')) \\ &\times 2\cos(k_{F,h}kR\cos(\theta) - k_{F,h}qR\cos(\theta'))\rangle_{\theta,\theta'} \ , \end{aligned} \tag{8.16}$$

which evaluates to (setting $r = k_{F,h}R$),

$$\begin{aligned} I^z_{hh}(rk, rq) = \frac{9}{10}\frac{\sin(kr)}{kr}\frac{\sin(qr)}{qr} + \frac{45}{2}&\left(\frac{\cos(kr)}{k^2r^2} - \frac{\sin(kr)}{k^3r^3} + \frac{3}{5}\frac{\sin(kr)}{kr}\right) \\ &\times\left(\frac{\cos(qr)}{q^2r^2} - \frac{\sin(qr)}{q^3r^3} + \frac{3}{5}\frac{\sin(qr)}{qr}\right) , \end{aligned} \tag{8.17}$$

so that

$$I^z_{hh}(rk, rq) = \frac{9}{10}\frac{F(k)F(q)}{kq} + \frac{45}{2}\frac{G(k)G(q)}{kq} \ , \tag{8.18}$$

where F and G have the obvious definitions. We are thus led to evaluate integrals of the form

$$\int_0^1 dk \int_1^\infty dq \frac{qk}{q^2-k^2} F(k)F(q) \ . \tag{8.19}$$

We show in Appendix I that for F and G of the form that will appear in the evaluation of Eq. (8.11),

$$\begin{aligned}&\int_0^1 dk \int_1^\infty dq \frac{qk}{q^2-k^2} F(k)F(q) \\ &\qquad = \frac{\pi}{2} i \int_0^1 dkk \left[F^+(k)^2 - F^-(k)^2 + F(k) \mathrm{lim}_{\mathrm{q}\to 0} \left\{ \frac{2q^2}{q^2-k^2} F^+(q) \right\} \right] \ ,\end{aligned} \tag{8.20}$$

which we can use to do all the q integrals. Returning to the evaluation of $K^{zz}(\mathbf{R})$, we have the heavy hole contribution,

$$\begin{aligned} K^{zz}_{h,h}(\mathbf{R}) &= 8\,\epsilon_F g_h^2 \int_0^1 dk \int_1^\infty dq \frac{q^2k^2}{q^2-k^2} I^\alpha_{hh}(k_{F,h}kR, k_{F,h}qR) \\ &= 8\,\epsilon_F g_h^2 \int_0^1 dk \int_1^\infty dq \frac{1}{q^2-k^2} \left[\frac{9}{10} kqF(k)F(q) + \frac{45}{2} kqG(k)G(q) \right] \ , \end{aligned} \tag{8.21}$$

for which the q integral can be evaluated by using the identity, Eq. (8.20). Applying this formula, we obtain (upon making the substitution $a = k_{F,h}R$)

$$\begin{aligned} K^{zz}_{h,h}(\mathbf{R}) = 4\pi\,\epsilon_F g_h^2 \int_0^1 dk \Bigg[&\frac{9}{20} \frac{k\sin(2ka)}{a^2} + \frac{45}{2} \Bigg(\frac{\cos(ka)}{a^5k^2} + \frac{3\cos(2ka)}{5a^3} - \frac{3\cos(2ka)}{a^5k^2} \\ &- \frac{\sin(ka)}{a^6k^3} + \frac{3\sin(ka)}{5a^4k} + \frac{\sin(2ka)}{2a^6k^3} - \frac{11\sin(2ka)}{10a^4k} + \frac{9\sin(2ka)}{50a^2} \Bigg) \Bigg] \\ \equiv 4\pi\,\epsilon_F g_h^2\, C^{\text{heavy}}_{\text{para}}(a) \ . \end{aligned} \tag{8.22}$$

The remaining parts of the kernel are given in Appendix J. See Fig. 8.2 for the spatial dependence of various parts of the kernel.

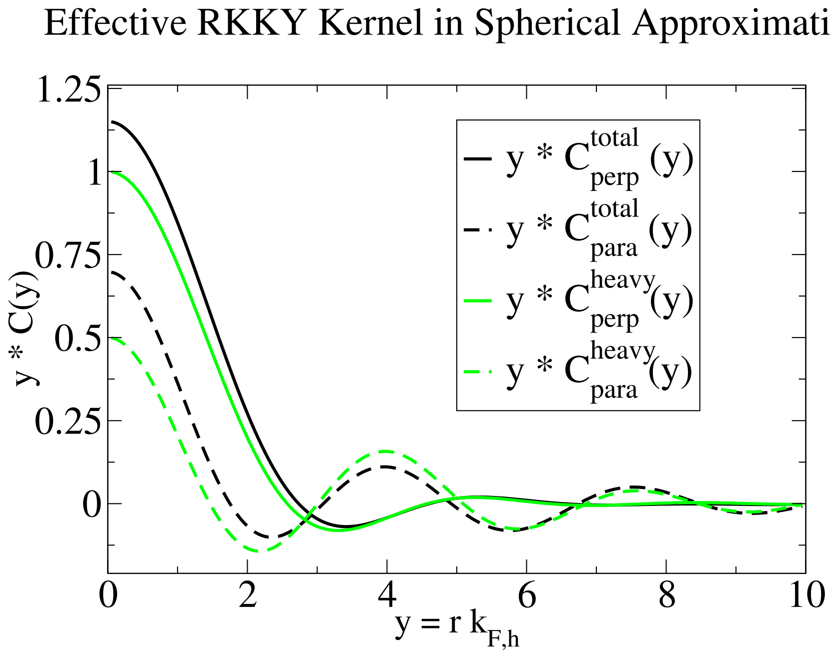

Figure 8.2: Effective RKKY Kernel in the Spherical Approximation. At the typical Mn-Mn separation, d$^{\text{typ}}$ ≈11Å the the kernel is very sensitive to the value of the hole concentration, which lies in the range $f = 0.10 - 0.25$ relative to the Mn concentration. This corresponds to y$^{\text{typ}}{}_{f=0.10}$ = d$^{\text{typ}}k_F^{f=0.10}$=1.6 and y$^{\text{typ}}{}_{f=0.25}$ = d$^{\text{typ}}k_F^{f=0.25}$=2.2. In both cases the perpendicular part of the kernel dominates and is ferromagnetic. However, for $f = 0.10$ the parallel component is ferromagnetic while for $f = 0.25$ the parallel component is antiferromagnetic. The effect of this also be seen by looking at the distribution of ground state angles in Figs. 8.12 and 8.13. The relative size of K_{perp} and K_{para} means that spins prefer to ferromagnetically align perpendicular to the axis joining them. In general this leads to frustration and noncollinear magnetism. Shown are the curves for (i) Heavy hole sector only and (ii) Both heavy and light hole sectors (total). The C are given by Eq. (8.22) and the expressions in Appendix J.

8.2 Monte Carlo Study of the Optimal Doping Limit

In order to investigate several physical properties of Ga$_{1-x}$Mn$_x$As we carried out classical Monte Carlo calculations in the spin degrees of freedom. We studied the effect of the kernel in Eq. (8.5) and Fig. 8.2 on the magnetization, the susceptibility, and the distribution of individual spin angles relative to the total magnetization

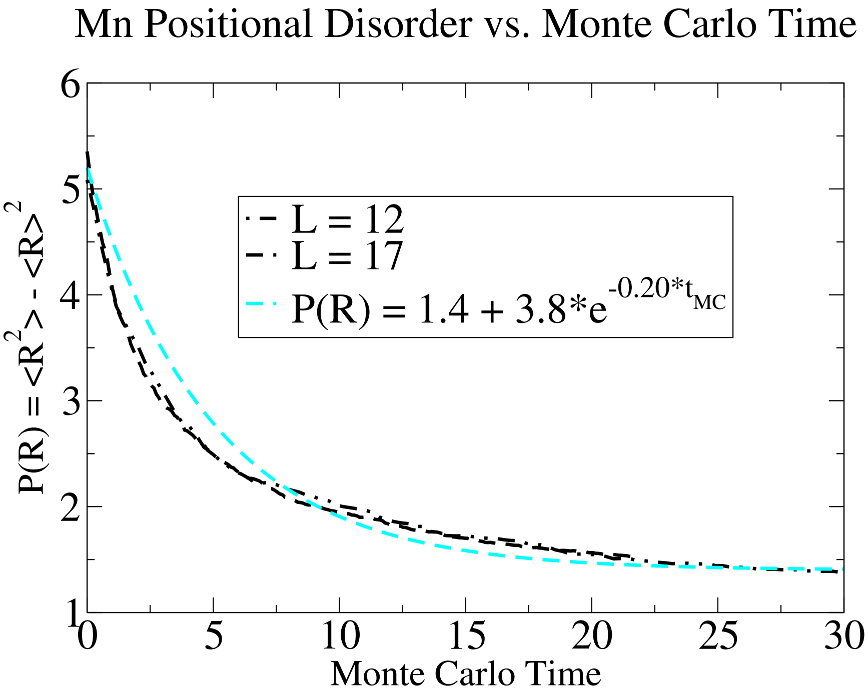

Figure 8.3: Lattice disorder vs. Monte Carlo time. Two samples sizes are considered– one with L=12 FCC unit cells and one with L=17 FCC unit cells. The disorder is quantified by Eq. (8.23) which is computed as a function of Monte Carlo time. Initially, the Mn ions are placed randomly on an FCC lattice. The Mn ions are taken to interact with each other via a screened Coulomb interaction. Ion moves are randomly proposed and accepted according to the Metropolis algorithm. In the limit of large Monte Carlo time a BCC lattice tends to form with a few defects. Note that the disorder as a function of Monte Carlo time is independent of system size, as it should be. The exponential is "fit" for later comparison with the Monte Carlo time dependence of disorder on other quantities like the magnetization and susceptibility.

direction as a function of temperature, hole concentration (for fixed Mn concentration, $x = 0.05$) and Mn positional disorder.

Before we study the interactions of the spins, we first fix the positions of the Mn ions. We can control the amount of disorder in the system by allowing the ions to interact with each other and to move to new locations in order to minimize the energy of the overall configuration of ions. In all of our calculations, we began with a random orientation of Mn ions on an $L \times L \times L$ FCC lattice (the Mn are constrained to always remain on an FCC lattice) with probability $x = 0.05$. Each realization was constrained to have the *same* number of Mn. We took $L = 10, 12, 14$ and 17 for finite-size scaling studies. In order to simulate sample growth conditions, we allow the Mn to interact with each other through a screened Coulomb interaction and to hop from site to site. The randomly proposed hops are accepted according to the Metropolis Algorithm.

We have found that when the Mn are allowed to hop for long times, they tend to form a BCC lattice. The amount of disorder in the lattice can be quantified by

$$P(R_{ij}) \equiv \langle R_{ij}^2 \rangle - \langle R_{ij} \rangle^2 \ , \tag{8.23}$$

where R_{ij} is the distance between neighbors. (Neighbors are defined to be Mn ions within some cut-off distance which results in approximately 5-10 neighbors/ion.) Fig. 8.3 illustrates how this quantity behaves as a function of Monte Carlo time (the number of proposed ion moves divided by the number of ions in the lattice) for two different size lattices. Note that the curves are essentially identical and independent of system size, as they should be.

In all of the simulations to be described below the Mn spins were replaced by their classical angular variables (which should be a reasonable approximation for the $S = 5/2$ Mn), $\mathbf{S} \rightarrow S\mathbf{\Omega}$. To take account of the finite mean free path $l \approx 7$Å of the valence holes[111], we used an exponential cutoff for the RKKY interaction: $K\mathrm{para/perp}(\mathbf{R}) \rightarrow K\mathrm{para/perp}(\mathbf{R})e^{-R/l}$.

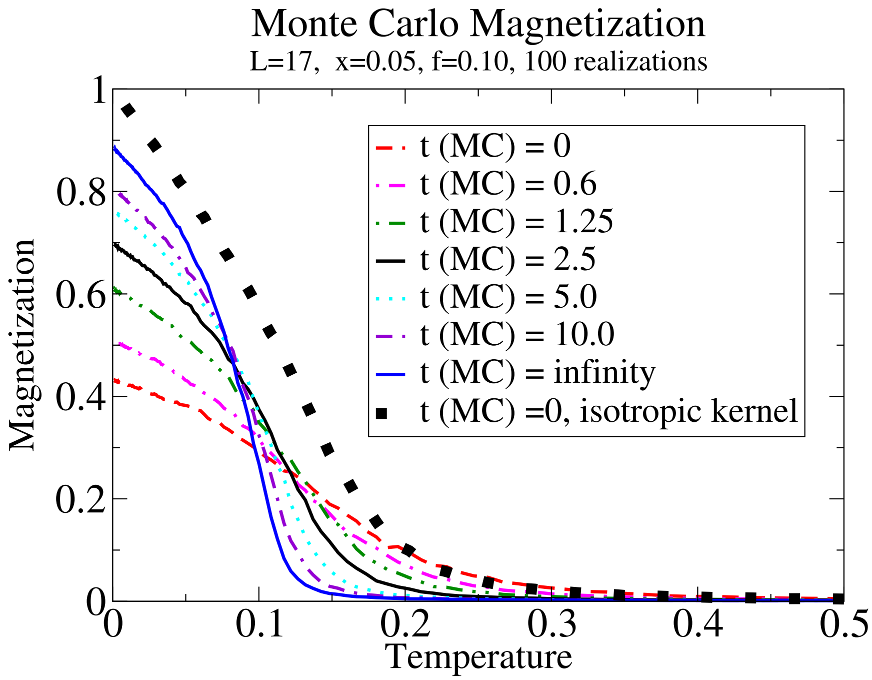

Figure 8.4: Magnetization curves are shown for the hole fraction $f = 0.10$ as a function of Monte Carlo time. Note that for large disorder the curves are quite linear over a wide temperature range while for smaller disorder they move over to a much more “meanfield” like shape. The zero temperature magnetization increases smoothly as the disorder in the Mn positions decreases. Temperature is measured in units of $4\pi\epsilon_F g_h^2$, where $g_h = G\varrho_h$ with ϱ_h the heavy-hole density of states at the Fermi energy. Note that the isotropic kernel results in nearly full polarization for the completely disordered sample demonstrating the the reduction of the magnetization is due to frustration effects from to the anisotropic kernel given in Eq. (8.5) and Fig. 8.2 and not from the antiferromagnetic part of the RKKY kernel.

8.2.1 Magnetization

In Figs. 8.4 and 8.5 we show the magnetization $M \equiv |\langle\Omega_i\rangle|$, for different amounts of disordered (measured by Monte Carlo time and Fig. 8.3), as a function of temperature for two different hole fractions, f. A spontaneous magnetization develops at low temperatures. For small Monte Carlo times (large disorder) the transition between the paramagnetic and magnetic phases takes place rather smoothly, and

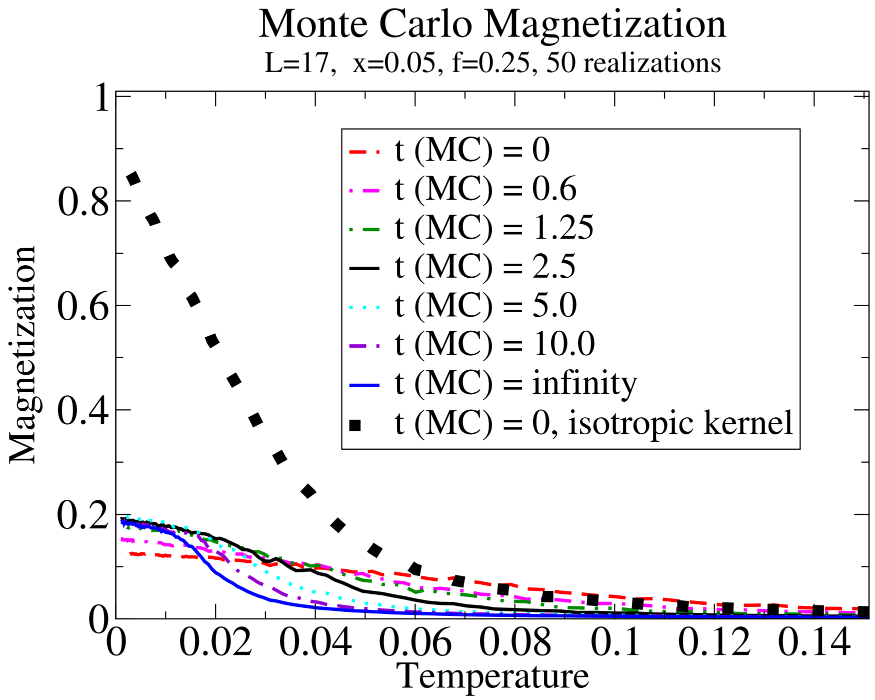

Figure 8.5: Magnetization curves are shown for the hole fraction $f = 0.25$ as a function of Monte Carlo time. Note the difference in temperature scale from Fig. 8.4. For large disorder the curves are quite linear over a large temperature range while for smaller disorder they move over to a much more "meanfield" like shape. The zero temperature magnetization rises sharply as the disorder in the Mn positions decreases and then tends to saturate. Temperature is measured in units of $4\pi\epsilon_F g_h^2$, where $g_h = G\varrho_h$ with ϱ_h the heavy-hole density of states at the Fermi energy. The averaged (isotropic) kernel results in a substantial increase in zero temperature magnetization, but it still only saturates to about 90% of its full value due to appreciable *antiferromagnetic* interactions at this hole fraction.

then the magnetization increases approximately linearly with decreasing temperature, qualitatively similar to many experiments[88, 87]. Both properties are characteristic of strongly disordered magnets[100]. The spontaneous magnetization, however, tends to a value at $T = 0$ that is much *smaller* than that of a fully polarized ferromagnet. On the other hand, for larger Monte Carlo times (smaller disorder) the curves behave more meanfield-like, also similar to experiments[87] in which the samples were "op-

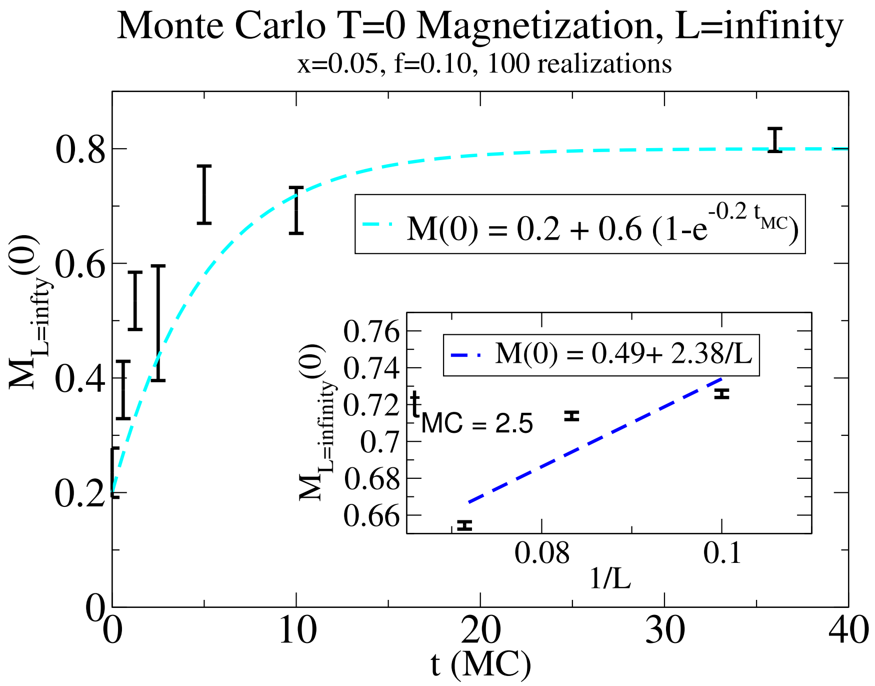

Figure 8.6: Finite size scaling, $f = 0.10$. By using finite size scaling (see figure inset) we determine the infinite system magnetization at zero temperature as a function of Monte Carlo time (disorder). Depending on disorder the infinite system magnetization varies between 20% and 80%. Note that the magnetization increases montonically with Monte Carlo time, with a time scale that is roughly the same as the disorder changes. (See Fig. 8.3.) The dashed curves are a guide to the eye.

timally" annealed. Note that the simulations with $f = 0.25$ show a much stronger reduction of the zero temperature magnetization relative to the case of $f = 0.10$. We will show in Section 8.2.3 that this is due to a much larger degree of noncollinearity of the magnetism for $f = 0.25$ relative to $f = 0.10$ by measuring the distribution of angles of individual Mn spins relative to the total magnetization direction. The origin of the noncollinearity depends on the hole concentration as we discuss below: for $f = 0.10$ the reductions is due entirely to the special form of the anisotropic spin-spin interaction given in Eq. (8.5) and has nothing to do with the RKKY oscillations of

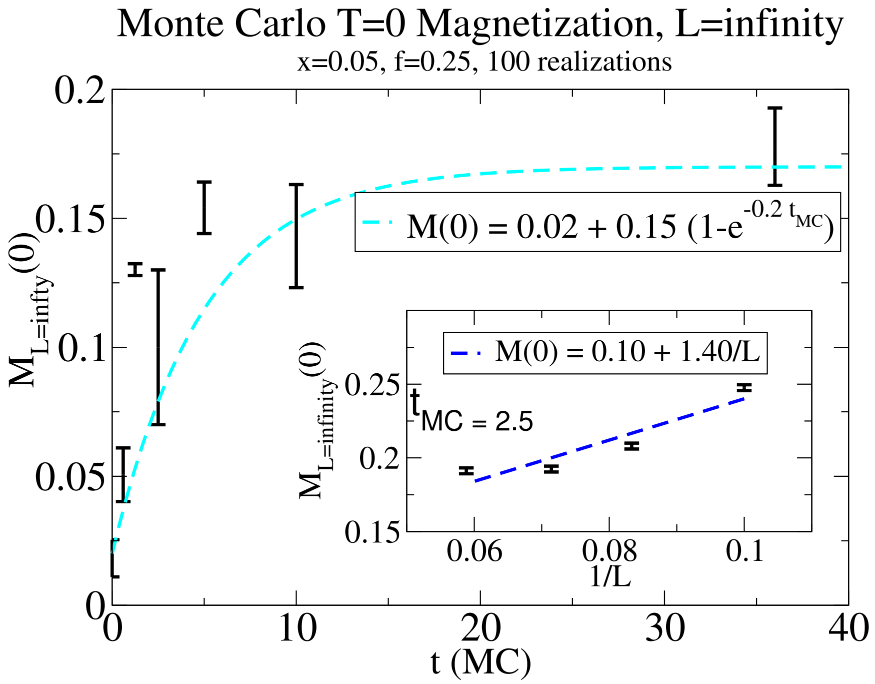

Figure 8.7: Finite size scaling, $f = 0.25$. By using finite size scaling (see figure inset) we determine the infinite system magnetization at zero temperature as a function of Monte Carlo time (disorder). Depending on disorder the infinite system magnetization varies between nearly zero and 17%. Note that the magnetization increases montonically with Monte Carlo time, with a time scale that is roughly the same as the disorder changes. (See Fig. 8.3.) The dashed curves are a guide to the eye.

the Mn-Mn interaction, while for $f = 0.25$ the reduction is much larger and *is* due to both the anistropy *and the antiferromagnetic part of the RKKY coupling.* To demonstrate this, we repeated the simulations by replacing the interaction in Eq. (8.5) by its angular average for both $f = 0.10$ and $f = 0.25$ as shown in Figs. 8.4 and 8.5. The magnetization for $f = 0.10$ saturates to its maximum value and almost all Mn spins are fully polarized, while for $f = 0.25$ there is still about a 10% reduction from full magnetization with the isotropic kernel showing the antiferromagnetic part of the RKKY kernel is playing an important role in the reduction of zero temperature magnetization. This can also be understood from Fig. 8.2 which shows that for $f = 0.10$ the parallel component of the kernel is ferromagnetic for typical Mn-Mn separations, while for $f = 0.25$ it is antiferromagnetic.

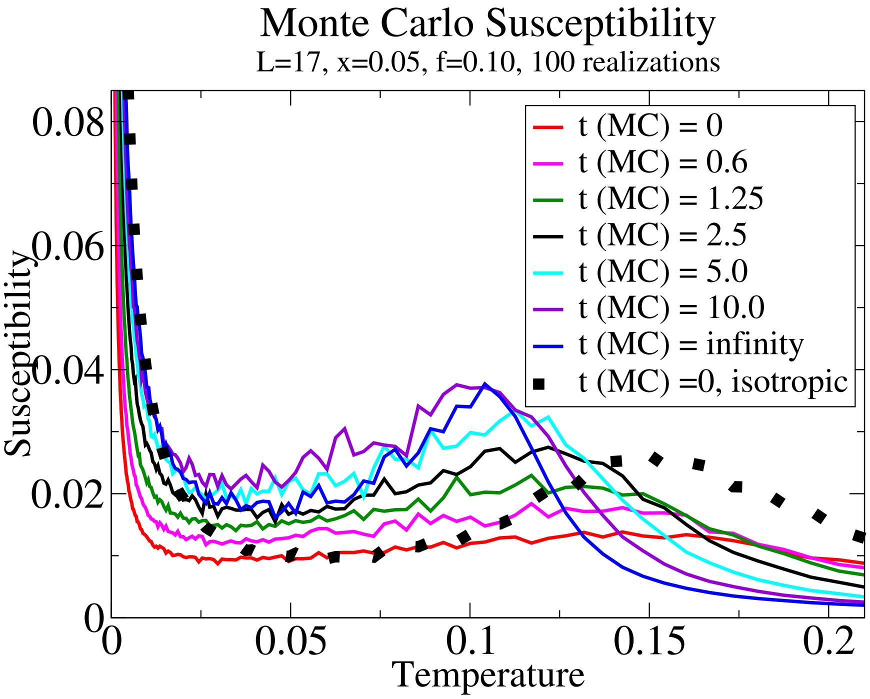

Figure 8.8: Magnetic susceptibility for $f = 0.10$ is shown for various amounts of disorder. The peak in the susceptibility becomes more pronounced as disorder decreases. It is unclear what the low temperature divergence is due to. Perhaps glassy physics is responsible. The istropic kernel has a peak at nearly the same position as the anistropic kernel for full disorder indicating that T_C is determined only by the average value of the kernel.

8.2.2 Susceptibility

In Figs. 8.8 and 8.9 we show the susceptibility,

$$\chi(T) = \frac{1}{T}\left(\langle M(T)^2\rangle - \langle M(T)\rangle^2\right) \ , \tag{8.24}$$

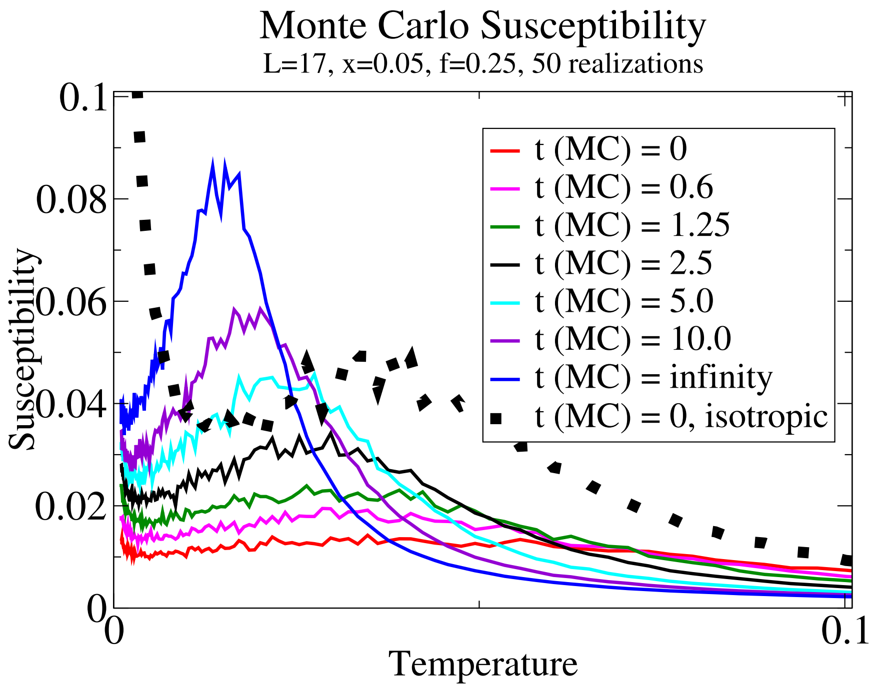

Figure 8.9: Magnetic susceptibility for $f = 0.25$ is shown for various amounts of disorder. Note that the response near T_C is about the same as for $f = 0.10$ except for the zero temperature divergence. By looking at the peak location, one can determine where the critical temperature is. The Curie temperature is nearly an order of magnitude smaller for $f = 0.25$ compared to $f = 0.10$. The istropic kernel has a peak at somewhat lower temperatures compared to the anistropic kernel for full disorder indicating that antiferromagnetic interactions may play an important role in determining T_C for $f = 0.25$.

expressed in units of $(4\pi\epsilon_F g_h^2)^{-1}$. Note that for both hole fractions the peak in the susceptibility becomes better defined as the sample becomes more ordered.

From the position of the peak in the susceptibility, we can determine the dependence of the Curie temperature, T_C, on the disorder and hole concentration in the infinite system limit by using finite size scaling. Figs. 8.10 and 8.11 shows that T_C tends to be enhanced with more disorder and tends to be nearly an order of magnitude larger for $f = 0.10$ compared to $f = 0.25$.

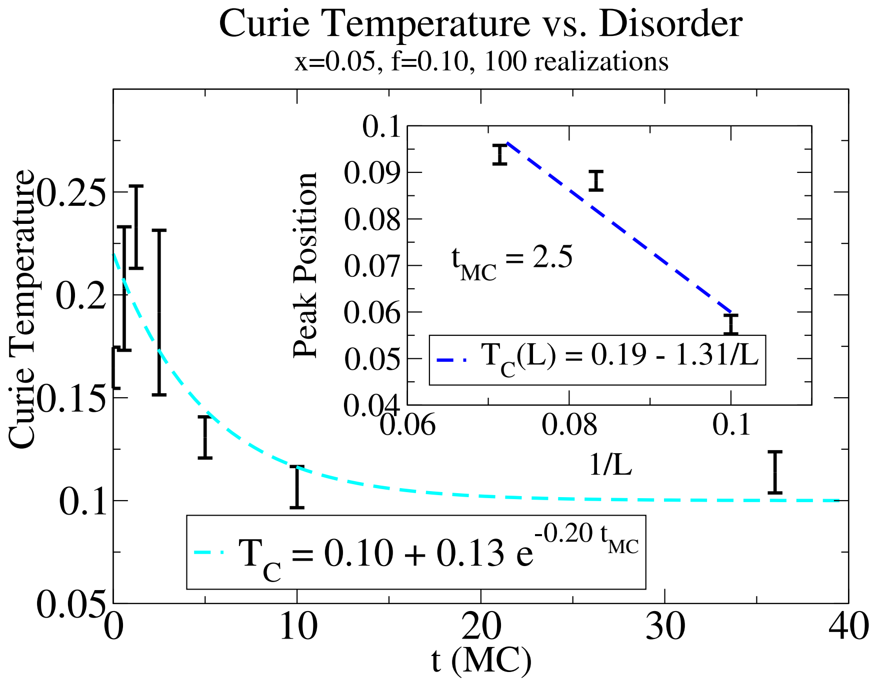

Figure 8.10: Dependence of T_C on Monte Carlo time $f = 0.10$. Curie temperature is expressed in units of $(4\pi\epsilon_F g_h^2)^{-1}$. The Curie temperature actually drops with order, so it is favorable to have some disorder in the material to achieve the highest Curie temperatures. However, as Figs. 8.4 and 8.5 show, higher Curie temperatures tend to come at the cost of lower zero temperature magnetization for fixed hole and Mn concentration. The Curie temperatures for $f = 0.10$ are almost an order or magnitude larger than for $f = 0.25$.

8.2.3 Noncollinearity of Ground State Magnetization

More information about the ground state properties can be determined by looking at the distribution of $\cos\theta = \mathbf{\Omega_i} \cdot \mathbf{n}$, where $\mathbf{n}$ is the unit vector parallel to the ground state magnetization and $\mathbf{\Omega_i}$ is the unit vector parallel to the 1^{th} spin. Without spatial anisotropy induced by the spin-orbit coupling, $P(\cos\theta) = \delta(\cos\theta - 1)$, at zero temperature since the spins would be fully aligned. As shown in Figs. 8.12 and 8.13 this is not the case once the anisotropic interaction of Eq. 8.5 is used instead of the familiar istropic RKKY form. With the anisotropic interaction one sees a

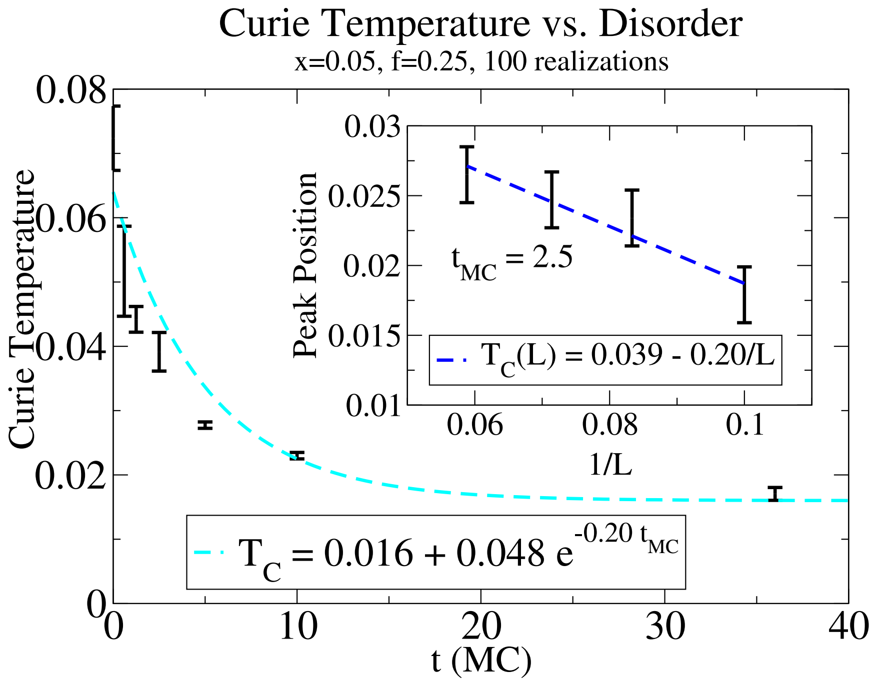

Figure 8.11: Dependence of T_C on Monte Carlo time $f = 0.25$. Curie temperature is expressed in units of $(4\pi\epsilon_F g_h^2)^{-1}$. The Curie temperature actually drops with order, so it is favorable to have some disorder in the material to achieve the highest Curie temperatures. However, as Figs. 8.4 and 8.5 show, higher Curie temperatures tend to come at the cost of lower zero temperature magnetization for fixed hole and Mn concentration.The Curie temperatures for $f = 0.10$ are almost an order or magnitude larger than for $f = 0.25$.

broadened distribution associated with the reduced (relative to the isotropic case) zero temperature magnetization seen in Figs. 8.4 and 8.5.

Clearly there is a large difference in the ground state spin distribution for different values of hole concentration, f. For larger concentrations, $f = 0.25$, the distribution is much broader than for smaller concentrations, $f = 0.10$, corresponding to many more spins *antiparallel* to the magnetization direction. This can be understood by considering where one sits on the kernel shown in Fig. 8.2. For $f = 0.10$, at the typical Mn-Mn distance, the parallel component of the kernel is *ferromagnetic* while

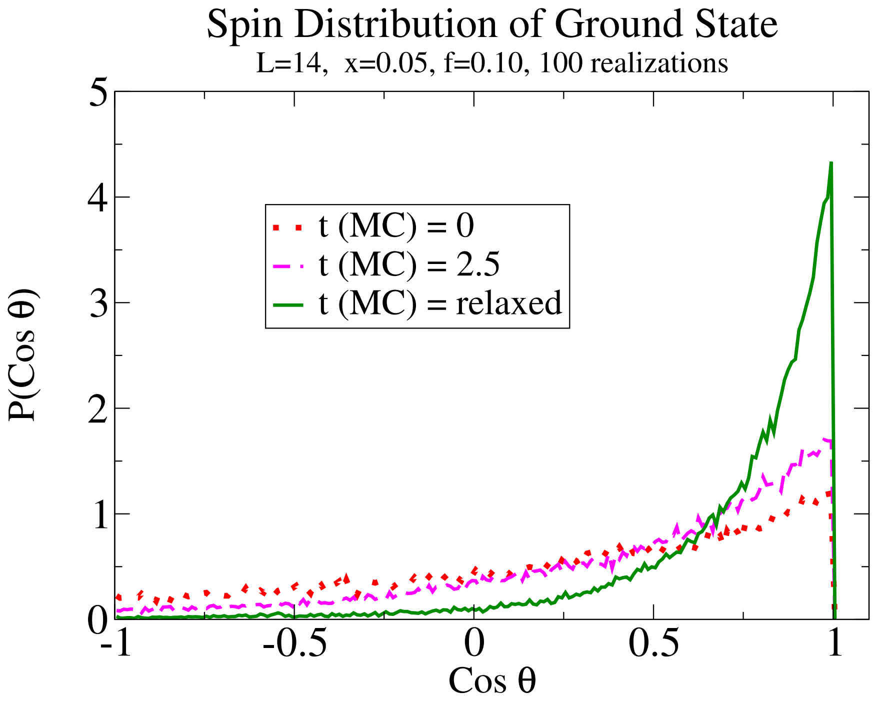

Figure 8.12: Ground state spin distribution for $f = 0.10$. The degree of noncollinear magnetism is measured by the width of the distribution of the cos of the angles individual Mn spins make with the direction of the net magnetization vector, $\mathbf{n}$: $\cos\theta_i = \mathbf{\Omega_i} \cdot \mathbf{n}$. When all spins are aligned, $P(\cos\theta) = \delta(1 - \cos\theta)$. Clearly, the more ordered the positions of the Mn ions, the more peaked the distribution becomes. This explains the smooth monotonic increase in the zero temperature magnetization with Monte Carlo time shown in Fig. 8.4. For this hole concentration the parallel part of the kernel shown in Fig. 8.2 is *ferromagnetic* at typical Mn-Mn separations.

for $f = 0.25$ the parallel component of the kernel is *antiferromagnetic.*

8.3 Conclusions

There are several messages that can be taken away from the calculations presented in this chapter of the thesis. Namely, that spin-orbit effects play an important role in the physics of GaMnAs at "optimal" doping, $x \approx 0.05$ and should be included in any realistic study. The main effect of strong spin-orbit coupling in the

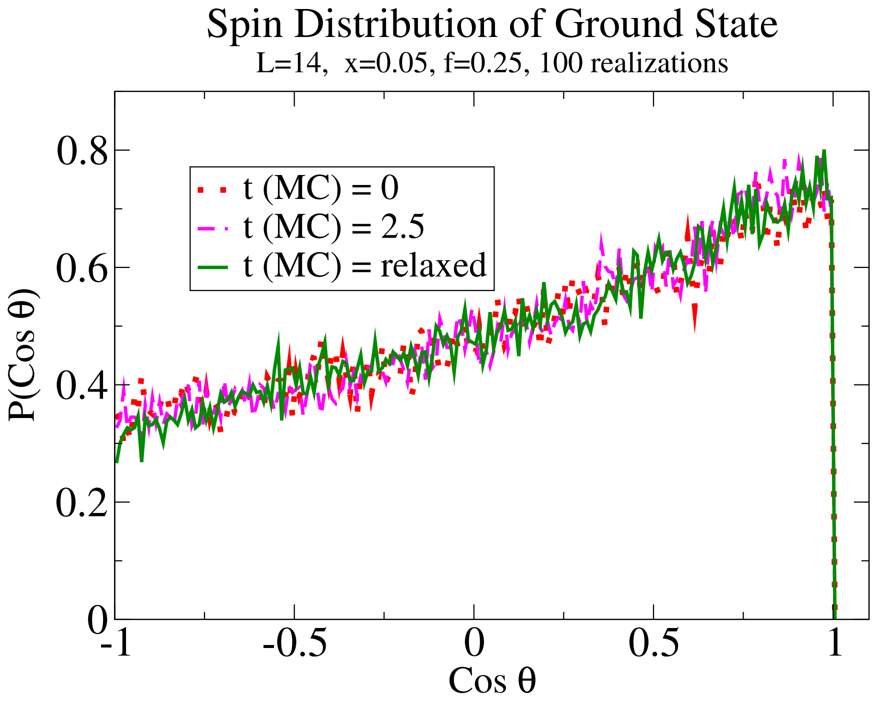

Figure 8.13: Ground state spin distribution for $f = 0.25$. The degree of noncollinear magnetism is measured by the width of the distribution of the cos of the angles individual Mn spins make with the direction of the net magnetization vector, $\mathbf{n}$: $\cos\theta_i = \mathbf{\Omega_i} \cdot \mathbf{n}$. When all spins are aligned, $P(\cos\theta) = \delta(1 - \cos\theta)$. Note that in contrast to Fig. 8.12 there is almost no change in the distribution with Monte Carlo time. This explains the apparent "saturation" in the zero temperature magnetization shown in Fig. 8.5; there is an initial increase due to the enhanced order for short Monte Carlo times, but there is no "tightening" of the spin distribution at later times to give a further increase in M(0). Note also that this distribution is much broader than the corresponding one for $f = 0.10$ shown in Fig. 8.12 which explains the significantly lower values of the zero temperature magnetization relative to the case for $f = 0.10$. For this hole concentration the parallel part of the kernel shown in Fig. 8.2 is *antiferromagnetic* at typical Mn-Mn separations.

GaAs host is to make the holes taken an angular momentum value of $J = 3/2$ due to coupling of the bare spin-1/2 holes to the p-like states at the top of the valence band. However, within the Baldereschi-Lipari spherical Hamiltonian there is an effective spin-orbit interaction that results and this is what we are primarily investigating in this chapter.

The most striking direct consequence of this spin-orbit effect is that the effective Mn-Mn indirect exchange (RKKY) interaction becomes anisotropic, with a preference for ferromagnetic spin alignment *perpendicular* to the axis joining the two impurities. The parallel component turns out to depend very sensitively on the hole concentration for the experimentally relevant values. (See Fig. 8.2.) This kernel can be used to interpret the reduction of the zero temperature magnetization from its fully polarized value as a function of hole concentration at optimal doping. We find that the reduction of the zero temperature magnetization can be attributed entirely to frustrational effects only over a certain range of hole concentration, which lies on the more highly compensated side of the experimentally determined values. When the hole fraction is on the larger side of the experimental range, it appears that antiferromagnetic coupling in the RKKY kernel may also be responsible for the reduction of the zero temperature magnetization[1]. We emphasize that while the RKKY calculation is not fully justified (Mn concentration is much greater than free hole concentration), we believe that the qualitative results and trends should still apply to GaMnAs.

We used the RKKY kernel shown in Fig. 8.2 to carry out classical Monte Carlo calculations in the spin variables. We studied the magnetization, susceptibility and ground state spin distribution as a function of Mn positional disorder and hole concentrations. Positional disorder was studied by allowing Mn ions to interact via a screened Coulomb interaction and move according to a Metropolis algorithm.

---

[1] This is the same conclusion reached independently by Kennett and Bhatt (private communication) theoretically and by Yu *et al.* cond-mat/0303217 experimentally.

(We also used the Metropolis algorithm for the Mn spins.) Positional disorder was measured according to Eq. (8.23) and is shown in Fig. 8.3 as a function of Monte Carlo time. For hole fractions in the range $f = 0.10 - 0.25$ it appears that disorder is helpful in increasing the Curie temperature of the material as T_C tends to decrease with Monte Carlo time over these values of hole concentration. In order for the magnetization curves to display the characteristic linear behavior over a large range of temperatures[87], the material must be fairly disordered, corresponding to Monte Carlo times roughly less than 2.5. As the disorder is further reduced, the curves begin to take on a more “mean field” shape. (See Figs. 8.4 and 8.5.) Due to the frustrational effects of the anisotropic RKKY kernel, greater *order* results in larger zero temperature magnetization.

Chapter 9

Semiclassical Theory of Coherence and Decoherence

9.1 Summary

A general semiclassical approach to quantum systems with system-bath interactions is developed. We study system decoherence in detail using a coherent state semiclassical wavepacket method which avoids singularity issues arising in the usual Green's function approach. We discuss the general conditions under which it is approximately correct to discuss quantum decoherence in terms of a "dephasing" picture and we derive semiclassical expressions for the phase and phase distribution. Remarkably, an effective system wavefunction emerges which controls the decoherence, even after full ensemble averaging, which is equivalent to a density matrix formulation. We comment on the relation of our work to studies of Stern, Aharonov and Imry [Phys.

Rev. A **41**, 3436 (1990)].

9.2 Introduction

The challenge of understanding to what extent a quantum system can retain its coherence in the presence of interactions with other degrees of freedom has attracted much attention. Much of this attention is motivated by recent advances in mesoscopic[112, 113] and cold-atom experiments[114, 115] as well as keen interest in quantum computing, which depends crucially on quantum coherence[83, 84].

An essential ingredient in any discussion of coherence and decoherence is the identification of a "system" and a "bath" which interact with each other in such a way that a meaningful distinction can be made between the two. In the double slit experiment, for example, the electrons are taken as the system and the degrees of freedom in the slits (phonons or spins, for example) are taken as the bath. Because the experiment only involves detecting the interference pattern on a screen behind the slits, no direct measurement of the bath (i.e. the slit degrees of freedom) is made. (Since one has no knowledge of the state of the bath one must sum over all possible states of the bath, i.e. one "traces over the bath".) Only the system is directly observed. As is well known[116], if the bath detects the path of the particle no interference pattern will be seen; the particle has therefore decohered. On the other hand, if there is no or only partial detection of the path of the particle by the bath, some interference pattern will be seen with its intensity reflecting the degree of coherence of the particle[116]. We will later show how these familiar statements appear in a very transparent way in our semiclassical formalism.

The problem of a quantum system interacting with an environment has been addressed many times in the literature, e.g. [117, 118, 119]. The Feynman-Vernon influence functional approach is well known, although its usefulness beyond the context of harmonic baths has been an issue. The influence functional approach to more realistic systems has been advanced significantly by Makri and Thompson[120, 121], exploiting and developing coherent state methods with smooth kernels suitable for Monte Carlo sampling. However, the generality of their approach necessarily means some detailed insights and limiting cases are lost in the machinery, so to speak.

Another approach is to make a semiclassical approximation for the system-bath evolution. We describe such a formalism here, involving a semiclassical wavepacket description. Since a semiclassical approach is based on classical trajectories, we can present an intuitive picture of the criteria for coherence and decoherence in a coupled system-bath. One of the insights which emerges relates to recent discussions in the literature concerning the equivalence of a "bath overlap" picture of decoherence with a simpler "system dephasing" picture. (See Stern, Aharonov and Imry (SAI)[119, 122, 113] and Feynman and Vernon[117].) Indeed our main counterpoint here is the provocative work of SAI, so we briefly summarize their dephasing arguments in Sec. 9.3. (The challenging and subtle problem of the low temperature limit of electron dephasing in disordered conductors[123, 74, 124, 125] is left for future work.)

9.3 Dephasing Arguments of Stern, Aharonov and Imry

Recently SAI have argued[119, 122] that decoherence may be thought of as dephasing, i.e. that a quantum particle acquires a distribution of possible phases so that its phase is "randomized" and thereby loses coherence. SAI argue that decoherence due to shifting a bath into an orthogonal state and decoherence due to a particle acquiring a distribution of possible phases are equivalent. In this section we give the skeleton of their argument in their original notation to provide a background for our discussion that follows.

SAI consider a quantum particle (coordinate x) moving around both arms of an Aharonov-Bohm ring threaded by magnetic flux with a bath (coordinate η) that only interacts with the particle in the right arm as shown in Fig. 9.1. Particles moving around the left arm are assumed not to interact with the environment. The initial wavefunction is taken to be

$$\psi(t=0) = [l(x) + r(x)] \otimes \chi_0(\eta) \ , \tag{9.1}$$

and corresponds to the particle having just entered the ring region (near point A in Fig. 9.1), but not yet interacting with the bath. Here $l(x)$ ($r(x)$) is the initial particle wavefunction on the left (right) arm, assumed to be a wavepacket, and $\chi_0(\eta)$ is the initial state of the bath, assumed to be localized in the right arm. SAI then take a final wavefunction (near point B in Fig. 9.1)

$$\psi(\tau) = l(x,\tau) \otimes \chi_l(\eta) + r(x,\tau) \otimes \chi_r(\eta) \ , \tag{9.2}$$

where $\chi_l(\eta)$ ($\chi_r(\eta)$) is the state of the bath had the particle gone around the left (right) arm[1]. SAI distinguish between "dynamical" and "nondynamical" environments, which either do or do not involve non-trivial dynamics on their own, respectively. From Eq. (9.2), SAI obtain the result that the interference term is (taking the trace over the environment)

$$2\mathrm{Re}\left[l^*(x)r(x)\int d\eta\chi_l^*(\eta)\chi_r(\eta)\right] \ , \tag{9.3}$$

which allows one to interpret the reduction of the interference (loss of coherence) in terms of a reduction in the overlap of the bath states for the two paths around the ring[2]. SAI then argue that one can make the identification

$$\langle e^{i\hat{\phi}}\rangle = \int d\eta\,\chi_l^*(\eta)\chi_r(\eta) \ , \tag{9.4}$$

where $\langle e^{i\hat{\phi}}\rangle \equiv \langle\chi_0|e^{i\hat{\phi}}|\chi_0\rangle$ and where for nondynamical environments the phase angle ϕ is

$$\phi = -\int dt\,V[x(t)]/\hbar \ , \tag{9.5}$$

with $x(t)$ the classical trajectory of the particle around the right ring arm[3]. For the case of dynamical environments

$$\langle\chi_0|e^{i\hat{\phi}}|\chi_0\rangle = \langle\chi_0|\hat{T}e^{-\frac{i}{\hbar}\int_0^\tau dt'\,\hat{V}_I(t')}|\chi_0\rangle \ , \tag{9.6}$$

where $\hat{V}_I(t')=e^{i\hat{H}_\mathrm{b}t'/\hbar}\hat{V}e^{-i\hat{H}_\mathrm{b}t'/\hbar}$ is the potential in the interaction representation and $\hat{T}$ is the time ordering operator. A nondynamical environment is distinguished from

---

[1] This innocent looking final wavefunction actually neglects entangling on the right arm between the particle and the bath by writing the term $r(x,\tau_0)\otimes\chi_r(\eta)$ as a direct product which is not correct in general.

[2] One must also also be careful when interpreting the extrema of the interference term of Eq. (9.3) (as a function of magnetic field in the Ahronov-Bohm experiment, for example) as a measure of the coherence. The difference of the maximum and minimum of the interference term must be normalized by the direct terms to divide out Debye-Waller factors which reduce both the the direct terms above and the interference cross terms[126]. In general one must normalize the interference term by a flux dependent term to prevent "flux blocking" effects from being interpreted as decoherence.

[3] As SAI point out, what matters is the *relative* phase of the two arms of the Aharonov-Bohm ring. We are taking $V(x(t)) = 0$ in the left arm.

a dynamical one in that the interaction picture operator $\hat{V}_I(t')$ commutes with itself at different times in the nondynamical case. For a dynamical environment it is not generally possible[119, 127] to write down a simple relationship such as that expressed in Eq. (9.5). However, for a nondynamical environment,

$$\langle e^{i\hat{\phi}}\rangle = \int d\phi P(\phi) e^{i\phi} \,, \tag{9.7}$$

where $P(\phi) \equiv |\chi_0(\eta(\phi))|^2 \frac{d\eta}{d\phi}$.

The central result of the work of SAI is the equivalence expressed in Eq. (9.4) which states that the reduction of Eq. (9.3) can be viewed as either the shifting of the bath states for the two paths around the ring (due to the interactions in the right arm of the ring) or as the particle on the interacting arm being subject to an uncertain potential resulting in an uncertain phase shift and hence a reduction in $\langle e^{i\hat{\phi}}\rangle$.

Certainly the nondynamical bath (realized, for example, in the case of a particle subject to classical random fields, as in a large, warm electromagnetic cavity) is more compelling for the pure dephasing argument; one has to work a little to extract an actual distribution of phases on the case of a dynamical bath, Eq. (9.6), so there the identification is more formal. In a sense this brings us all the way back to a path integral evaluation to achieve the influence functional; the influence functional can always be written as the exponential of an influence phase, which is one way of realizing Eq. (9.7). But then, at that level, *everything* is a sum over phase factors.

However, we are not really addressing one's tastes in this matter here; rather, there is another issue, having to do with disturbance of the *system*. The key approximation of SAI is the assumption that the interaction in the right arm is weak enough to neglect changes in the trajectory of the particle, while still allowing the bath to change in response to the presence of the particle. This approximation eliminates entangling on the upper arm (the overall wavefunction is, of course, still entangled) and results in the appearance of a direct product of bath states in the interference term, Eq. (9.3). This simplification is necessary to reach a "pure dephasing" expression. In the general situation, the trajectory of the particle is in fact altered in the interacting arm, which leads to entangling with the bath, a dephasing effect not included in the SAI picture.

9.4 Semiclassical theory of decoherence

We set out to construct a more general formal context for decoherence, with the goal of reaching a useful and intuitive physical picture, free of the restriction that the system path is unperturbed. The most general formal structure for decoherence (e.g. influence functionals for general anharmonic baths) would not involve semiclassical approximations, and could claim formal exactness. However such formulations must necessarily miss the mark on the issue of "useful and intuitive". SAI have succeeded in giving a very intuitive foundation[119, 122], which we will show here is not completely general. They used certain semiclassical language, but not a formal semiclassical approach. By using a true semiclassical formulation, we will achieve both generality and intuitiveness at the same time. We will see that SAI's results fit nicely into an important limiting case of our more general approach.

It is useful to have a specific model in mind. The model of a two armed

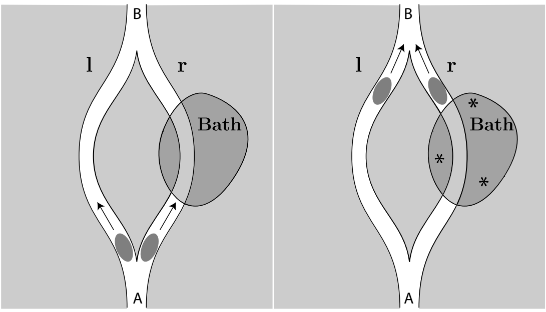

Figure 9.1: Intuitive picture for discussing decoherence. A wavepacket representing the "system" in a narrow waveguide is split coherently between two arms, one of which interacts with a "bath" of particles. Upon recombining on the other side, decoherence due to the system-bath interaction affects the interference (or lack of it) between the two arms.

device already introduced and used, for example, in the work of SAI serves that purpose well. In Fig. 9.1, a wavepacket representing the system is coherently split into two pieces, one of which later interacts with a bath. The degree of coherence can be checked experimentally by combining the packets (as in the Aharonov-Bohm experiments of Ref.[128]), although it is more general to check $M \equiv \mathrm{Tr}[\hat{\rho}_{\mathrm{red}}^2]$, where $\hat{\rho}_{\mathrm{red}}$ is the reduced density matrix for the system, after tracing over the bath variables.

An ambiguity in checking for interference fringes of the recombined beams is illustrated by supposing that there is a static potential maximum in the left arm but not the right, and no system-bath interaction in either arm. This will cause a time delay of the left wavepacket compared to the right, so no interference will result, even though the system is completely coherent. There are ways to avoid this, such as taking longer coherent wave trains initially for the system, but one must be careful, and other ambiguities can arise. The treatment of SAI assumes that the interaction with the bath is sufficiently weak that no changes occur to the interacting trajectory of the system to lowest order, so this issue does not arise.

On the other hand, M is simply 1 for a completely coherent system, and less than 1 if some decoherence has taken place. For example, suppose we have a system wavepacket broken into two nonoverlapping but coherent pieces, i.e. $\psi = 1/\sqrt{2}(\psi^l + \psi^r)$, with $\langle\psi^l|\psi^r\rangle = 0$ and $\langle\psi^l|\psi^l\rangle = \langle\psi^r|\psi^r\rangle = 1$. Then the density matrix, $\hat{\rho}$, is

$$\hat{\rho} = \frac{1}{2}\sum_{i,j} |\psi^i\rangle\langle\psi^j| \, , \tag{9.8}$$

with i and j taking on the values l and r. It is easily seen that $\mathrm{Tr}[\hat{\rho}] = \mathrm{Tr}[\hat{\rho}^2] = 1$, i.e. the system is completely coherent. However, if somehow the two parts l and r become completely decohered, (this in fact requires the action of more degrees of freedom) we loose the off diagonal elements of $\hat{\rho}$, getting

$$\bar{\hat{\rho}} = \frac{1}{2}\left(|\psi^l\rangle\langle\psi^l| + |\psi^r\rangle\langle\psi^r|\right) \, . \tag{9.9}$$

Now we have $\mathrm{Tr}[\bar{\hat{\rho}}] = 1$, but $\mathrm{Tr}[\bar{\hat{\rho}}^2] = 1/2$. This is not the end of decoherence for this system, if the left and right packets somehow undergo their own, “internal” decoherence. This “internal” decoherence will happen on a much longer time scale than the decoherence of the two initially coherent wavepackets because it is the *difference* in the interactions that each wavepacket experiences that determines the decoherence rate. This rate is almost always larger for two separated wavepackets than for a given wavepacket. All this is elementary, but it sets the stage for the more detailed work to follow.

9.4.1 Coherent States and Gaussian Wavepackets

Casting the system-bath interaction and the decoherence problem in terms of semiclassical wavepacket dynamics proves to be a useful and insightful exercise, and we proceed to set up the necessary tools. One may imagine a more traditional van Vleck semiclassical Green's function approach; however, this has the difficulty that caustic infinities abound in the van Vleck prefactors due ultimately to the failure of stationary phase in the limit of small action changes. For example, suppose we consider a harmonic oscillator and represent the n^{th} state, $|n\rangle$, semiclassically so that $\langle x|n\rangle$ has singularities at the classical turning points for energy E_n. Suppose now we displace $|n\rangle$ slightly in position; call this $|\tilde{n}\rangle$. The semiclassical projections onto all of the original basis states $\langle n|\tilde{n}\rangle$ are completely wrong for small displacements. All but one of the projections are incorrectly predicted to be 0, since their classical manifolds do not overlap, whereas the overlap with the undisplaced original state is nearly singular. The same displacement of the n^{th} harmonic oscillator state, expanded in terms of localized Gaussians, is quite accurate; it has no such difficulties. Essentially, this is an automatic way to keep track of a unifomization of the WKB result. Slight displacements of system or bath states is commonplace in the decoherence problem, so we avoid the caustic difficulties by starting with a wavepacket description, avoiding the singularities. We have called this the "oil on troubled waters" effect of using a wavepacket description[129].

We require a brief review of Gaussian wavepacket dynamics to set the stage for our approach to the decoherence problem. It is well known that the problem of the usual kinetic energy operator with a time dependent potential at most quadratic in the coordinates is exactly solvable, and is especially simple in the case of initial wavefunctions which are Gaussian; these remain exactly Gaussian wavepackets under the time evolution.

Before we continue, we note that our goals extend far beyond such quadratic systems; we will see that a semiclassical approximation permits the use of quadratic form dynamics in more general contexts. We make use of the so-called "thawed guassian approximation"[130, 131, 132] which employs the auxillary variables $\mathbf{Z}$ and $\mathbf{P_Z}$, whose dynamics are given by the equations below. The "thawed Gaussian approximation" allows one to approximate the potential *locally* as quadratic thus taking advantage of the exactness of Gaussian propagation on quadratic potentials.

In a multidimensional form, a general Gaussian wavepacket is given by

$$\begin{aligned}\psi(\mathbf{q},t) = \exp\{\frac{i}{\hbar}[(\mathbf{q}-\mathbf{q_t})^T \cdot \mathbf{A_t} \cdot (\mathbf{q}-\mathbf{q_t}) \\ +\mathbf{p_t} \cdot (\mathbf{q}-\mathbf{q_t}) + s_t]\} \ , \qquad (9.10)\end{aligned}$$

where $\mathbf{A}_t$ is an $N \times N$ matrix for N coordinates describing the stability of the center of the Gaussian wavepacket, and $\mathbf{q_t}$, $\mathbf{p_t}$ are N-dimensional vectors describing the position and momentum evolution of the center of the wavepacket. We have introduced the more conventional wavepacket notation $\mathbf{q_t} = \mathbf{q}(t)$, etc. Let the classical Hamiltonian, $\mathrm{H} = \mathrm{T} + \mathrm{V}$, have the usual Cartesian kinetic energy operator and a general time dependent potential V smooth at least up to quadratic order in the coordinates. The parameters of the Gaussian then obey[133, 134]

$$\frac{d}{dt}\mathbf{q_t} = \nabla_p \mathrm{H} \qquad (9.11)$$

$$\begin{aligned}
\frac{d}{dt}\mathbf{p_t} &= -\nabla_q \mathrm{H} && (9.12)\\
\mathbf{A_t} &= \frac{1}{2}\mathbf{P_Z}\cdot\mathbf{Z^{-1}} && (9.13)\\
\frac{d}{dt}\begin{pmatrix}\mathbf{P_Z}\\ \mathbf{Z}\end{pmatrix} &= \begin{pmatrix}\mathbf{0} & -\mathbf{V}''(t)\\ \mathbf{m^{-1}} & \mathbf{0}\end{pmatrix}\begin{pmatrix}\mathbf{P_Z}\\ \mathbf{Z}\end{pmatrix} && (9.14)\\
\dot{s}_t &= L_t + \frac{i\hbar}{2}\mathrm{Tr}[\dot{\mathbf{Z}}\cdot\mathbf{Z^{-1}}]\,, && (9.15)
\end{aligned}$$

where L_t is the usual classical Lagrangian. Integrating over time, we have

$$s_t = s_0 + S_t + \frac{i\hbar}{2}\mathrm{Tr}[\ln \mathbf{Z}]\,, \qquad (9.16)$$

where $\mathbf{V}''$ and $\mathbf{m^{-1}}$ are N-dimensional matrices of mixed second derivatives of the Hamiltonian with respect to position and momentum coordinates, respectively. That is,

$$[\mathbf{V}'']_{ij} = \frac{\partial^2 H}{\partial q_i \partial q_j}\,, \qquad (9.17)$$

and so forth. S_t is the usual classical action.

Eqs. (9.11-9.15) holds for a general time dependent V. We focus on the stability equations, Eq. (9.14), which admit the solution

$$\begin{pmatrix}\mathbf{P_{Z_t}}\\ \mathbf{Z_t}\end{pmatrix} = \mathbf{M}(t)\begin{pmatrix}\mathbf{P_{Z_0}}\\ \mathbf{Z_0}\end{pmatrix}\,, \qquad (9.18)$$

where

$$\mathbf{M}(t) = \hat{T}\, e^{\int^t \mathbf{K}(t')\, dt'}\,, \qquad (9.19)$$

and $\hat{T}$ denotes the time ordering operator, needed because

$$\mathbf{K}(t) = \begin{pmatrix}\mathbf{0} & -\mathbf{V}''(t)\\ \mathbf{m^{-1}} & \mathbf{0}\end{pmatrix} \qquad (9.20)$$

does not commute with itself (in general) at different times. $\mathbf{M}(t)$ is the usual classical stability matrix, where $\mathbf{M}_{11} = \partial p_t/\partial p_0$, etc.

9.4.2 Semiclassical approximation

Consider a narrow (in $\mathbf{q}$) Gaussian wavepacket centered on the classical position $\mathbf{q_0}$ and momentum $\mathbf{p_0}$. Assuming a reasonably smooth potential, let us expand around $\mathbf{q_0}$ up to quadratic terms, arguing that the tails of the Gaussian are negligible where the Taylor expansion starts to break down. We use this quadratic form to propagate the packet in the next time instant. Thus the Gaussian will propagate in the next instant according to Eqs. (9.11-9.15). If we agree to move the center of the Taylor expansion to the moving mean position of the wavepacket, $\mathbf{q_t}$, then Eqs. (9.11-9.15) will hold, since the potential is now, by construction, a time dependent quadratic form. However, the interpretation has changed–the position and momentum parameters $\mathbf{q_t}$ and $\mathbf{p_t}$ are now just exactly the usual classical trajectories on the *exact, anharmonic* potential, but the distortion of the *wavepacket is governed by the local quadratic expansion* of the potential–thus keeping the wavepacket Gaussian[130]. We illustrate the idea in Fig. 9.2.

In general this approximation breaks down after some time due to wavepacket spreading, but that time can be put off as long as we please as $\hbar \to 0$, since we can take a narrower wavepacket, with position and momentum uncertainties going as $\sqrt{\hbar}$. This delays the spreading by at least a factor $\sim 1/|\log \hbar|$ in time (for chaotic systems)[135, 136, 137, 138].

Since any quantum state (aside from spin states) can be built out of Gaus-

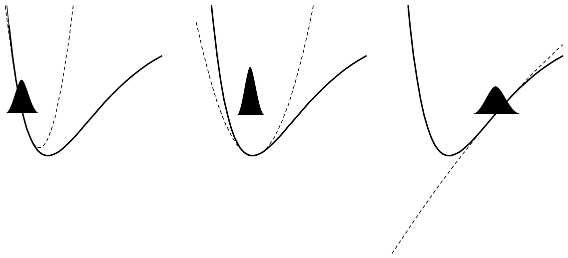

Figure 9.2: A Gaussian wavepacket in an anharmonic potential is approximately propagated by expanding the potential to quadratic order locally around the instantaneous center of the Gaussian.

sians, we have a full semiclassical approach, exact as $\hbar \to 0$. Each Gaussian is propagated with its own optimized time-dependent Hamiltonian.

The phase s_t of Eq. (9.16) is the usual action, taken along the guiding trajectory, modified by an extra term which takes the place of a Maslov phase. This term evolves smoothly in time and therefore is another advantage of a wavepacket approach as compared to the more troublesome eigenfunctions of Hermitian operators.

There are other approaches based on wavepackets which share the smoothing property, such as a full semiclassical coherent state propagator[139, 140, 141]. This differs from the above Gaussian wavepacket (GWP) method in that the propagator is optimized for both the initial Gaussian and a final Gaussian onto which it is projected. It is also the "natural" semiclassical approximation if one retains stationary phase as the defining idea while passing to a coherent state basis. The coherent state method is usually more accurate at the same value of $\hbar$ compared to GWP, but it suffers several complexities. Foremost among these is that complex classical trajectories come in, (albeit for real time) with their attendant analytical difficulties including Stokes lines. Therefore, we choose the GWP approach as a best compromise between accuracy and complexity. In the semiclassical limit, $\hbar \to 0$, there is no accuracy compromise.

9.4.3 Perturbation of Gaussian Wavepacket Dynamics

Perturbation theory may seem limited in scope at first glance, but we soon realize that strong interaction with many bath degrees of freedom leads to such rapid and near complete decoherence that an analysis of the strong system-bath coupling regime seems a little *post mortem.* We therefore focus our attention on the weak coupling limit.

In the setup in Fig. (9.1), we have a Hamiltonian given by

$$\hat{H} = \hat{H}_{\rm p} + \hat{H}_{\rm b} + \hat{V} \equiv \hat{H}_0 + \lambda \hat{V}_1 \ , \tag{9.21}$$

where $\hat{H}_{\rm p}$ ($\hat{H}_{\rm b}$) is the Hamiltonian of the particle (bath) and $\hat{V}$ is the coupling between them. Suppose we have solved the $\hat{H}_0 = \hat{H}_{\rm p} + \hat{H}_{\rm b}$ problem, and now we wish to include the effects of $\lambda \hat{V}_1$, the system-bath interaction. In accordance with perturbation theory, the first order effect is determined by the extra potential felt by the wavepacket as it travels over its old trajectory. Assuming this perturbation is smooth as a function of coordinates, we include only terms linear in the interaction strength, λ. We can include perturbations to quadratic order as well, at the cost of increased complexity, but we defer this for future work. A weak interaction with a bath will show up in two ways in the wavepacket given in Eq. (9.10): (1) Changes to the guiding trajectory, q_t

and p_t and (2) changes to the phase s_t.

Perturbation of the Guiding Trajectory

Let $\mathbf{q_0}(t)$ be the solution of the $\hat{H}_0$ problem for a particular trajectory. The first order perturbed solution we take to be $\mathbf{q}(t) = \mathbf{q_0}(t) + \lambda\delta\mathbf{q}(t)$, $\mathbf{p}(t) = \mathbf{p_0}(t) + \lambda\delta\mathbf{p}(t)$. By substituting this into Hamilton's equations, we find that $\delta\mathbf{q_t}, \delta\mathbf{p_t}$ obey

$$\frac{d}{dt}\begin{pmatrix} \delta\mathbf{p_t} \\ \delta\mathbf{q_t} \end{pmatrix} = \begin{pmatrix} \mathbf{0} & -\mathbf{V}''(t) \\ \mathbf{m^{-1}} & \mathbf{0} \end{pmatrix}\begin{pmatrix} \delta\mathbf{p_t} \\ \delta\mathbf{q_t} \end{pmatrix} + \begin{pmatrix} \mathbf{f}(t) \\ \mathbf{0} \end{pmatrix}, \tag{9.22}$$

where $f(t) = -V_1'(\mathbf{q_0}(t))$ is the time dependent forcing function. The solution is

$$\begin{pmatrix} \delta\mathbf{p_t} \\ \delta\mathbf{q_t} \end{pmatrix} = \mathbf{M}(t)\begin{pmatrix} \delta\mathbf{p_0} \\ \delta\mathbf{q_0} \end{pmatrix} + \mathbf{M}(t)\int_0^t \mathbf{M}(t')^{-1}\begin{pmatrix} \mathbf{f}(t') \\ \mathbf{0} \end{pmatrix} dt' \tag{9.23}$$

$$= \mathbf{M}(t)\int_0^t \mathbf{M}(t')^{-1}\begin{pmatrix} \mathbf{f}(t') \\ \mathbf{0} \end{pmatrix} dt', \tag{9.24}$$

since $\delta\mathbf{p_0} = \delta\mathbf{q_0} = \mathbf{0}$ in the present circumstances, with

$$\mathbf{M}(t)^{-1} = \hat{T}^\dagger \, e^{-\int^t \mathbf{K}(t')\, dt'}, \tag{9.25}$$

and $\hat{T}^\dagger$ forces the reverse order of times; i.e. earliest times to the left in the series expansion of $\mathbf{M}(t)^{-1}$. Note that $(d/dt)\mathbf{M}(t)^{-1} = \mathbf{M}(t)^{-1}\mathbf{K}(t)$. Thus, the perturbation of a general trajectory in classical mechanics generates a linearly forced oscillator problem. This is not surprising, since the small additional potential creates small new forces on the particle near its old trajectory.

Perturbation of the Phase

To see how the phase of the wavepacket changes under the perturbation, we examine

$$\begin{aligned}\delta s_t &= \delta S_t \\ &= \delta \int (T - V_0 - \lambda V_1)\ dt' \\ &= \delta \int (T - V_0)\ dt' - \delta \int \lambda V_1\ dt'\ . \end{aligned} \tag{9.26}$$

We see the change comes in two parts. The first is the change in the "old" action (it involves the old V_0) due to the new trajectory. Assuming the new one has not wandered too far, we have

$$\delta \int (T - V_0) dt' = \lambda\ p_t \delta q_t\ , \tag{9.27}$$

by the stationary principle of the action (the RHS of this equation is not zero since the perturbation causes a drift in final position, $\lambda \delta q_t$.) Thus, the wavepacket phase change, to first order, is

$$\begin{aligned}\phi_i &= \frac{\delta s_t}{\hbar} \\ &= \frac{1}{\hbar} \delta \int (T - V_0 - \lambda V_1)\ dt' \\ &= \lambda\ \frac{p_t \delta q_t}{\hbar}\ - \frac{\lambda}{\hbar} \int V_1(q_0(t'))\ dt'\ . \end{aligned} \tag{9.28}$$

9.4.4 Time-dependent Hartee approximation–a generalization of the perturbation approach

Suppose we have a Hamiltonian, $H = H_0(x) + H_0(y) + \lambda V(x,y)$. Within the perturbation theory just given, we note that a product of Gaussians in different degrees of freedom, e.g.

$$\psi(x,y) = g_1(x)g_2(y) \ , \tag{9.29}$$

will remain a product of the form

$$e^{-iHt/\hbar}\psi(x,y) = \psi(x,y,t) \approx g_1(x,t)g_2(y,t)e^{i\phi_t} \ , \tag{9.30}$$

where $g_{1,2}$ are still Gaussian, and ϕ_t is a phase. This suggests a generalization to the time-dependent Hartree approximation, first given in a time-dependent variational context in 1976[142]. The Hartree ansatz is simply that the individual wavepacket products remain in their product form through time; the optimal form and phase for the individual packets is determined by a time-dependent variational principle. The point was made in reference [142] that a great deal of correlation and (in modern language) entanglement is potentially contained in *superpositions* of such Hartree forms. The individual wavepackets evolve, as expected, in the mean fields of the other wavepackets. This generalizes the formalism thus far in this paper, in the sense that the key property of the equations to be derived depends on the *individual*, not global, separability of the wavepacket description, and not on the individual wavepackets being Gaussian. Thus, a TDH (time-dependent Hartree) form is suggested. This might have the advantage of accounting better for anharmonicities in the potentials, and for stronger than perturbative coupling. This is also a semiclassically correct procedure, for as $\hbar \to 0$ the Hartree ansatz is arbitrarily accurate for ever narrower initial wavefunctions. The formulation to follow applies to both perturbative and Hartree wavepacket approaches.

9.4.5 Decoherence

Assuming for a moment that the bath has a wavefunction (i.e. it is not described by a mixed density matrix, such as a thermal bath), it can generally be written in a basis $|\gamma\rangle$ as

$$\psi_{\text{bath}} = \sum_{\gamma} w_{\gamma} e^{i\xi_{\gamma}} |\gamma\rangle \ , \tag{9.31}$$

where w_γ are real, positive weights and the ξ_γ are the associated phases. The density matrix is,

$$\hat{\rho}_{\text{bath}} = \sum_{\gamma,\gamma'} w_{\gamma'} w_{\gamma} e^{i(\xi_{\gamma}-\xi_{\gamma'})} |\gamma\rangle\langle\gamma'| \ . \tag{9.32}$$

It is an interesting formal trick that the finite temperature density matrix, $\hat{\rho}_T$, can be obtained from Eq. (9.32) by treating the ξ_γ as random variables and then averaging over them,

$$\hat{\rho}_T = \sum_{\gamma} w_{\gamma}^2 |\gamma\rangle\langle\gamma| \ . \tag{9.33}$$

For a thermal bath, when the basis $|\gamma\rangle$ are eigenstates of the bath Hamiltonian, $w_\gamma^2 \propto e^{-\beta E_\gamma}$, where $\beta = 1/k_B T$, k_B is Boltzmann's constant and T is the temperature.

In other bases one has to show that a "diagonal" representation of the thermal density matrix is possible for some set of w_γ^2; this can always be done for coherent states. A simple semiclassical (high temperature) approximation for a bath with a (possibly anharmonic) Hamiltonian H in the coherent state representation $|\varphi\rangle$ is

$$\hat{\rho}_T = \frac{1}{Q} \int d^{2N}\varphi \ e^{-\beta\langle H\rangle_{\varphi}} |\varphi\rangle\langle\varphi| \ , \tag{9.34}$$

where $Q = \text{Tr}[\hat{\rho}_T]$ and $\langle H\rangle_\varphi = \langle\varphi|H|\varphi\rangle$.

Returning to the more general situation of a bath described by Eq. (9.31), we take the initial wavefunction of system and bath to be a product state[4]

$$|\Psi^{\{\xi\}}\rangle = \frac{1}{\sqrt{2}}\left(|g_0^l\rangle + |g_0^r\rangle\right)\sum_i w_i |G_{i0}\rangle e^{i\xi_i} \,, \tag{9.35}$$

with the intention of averaging over the random phases ξ_i later to obtain the finite temperature result, as in the discussion above. The states $|g_0^r\rangle$ and $|g_0^l\rangle$ are Gaussian wavepackets (coherent states) near the region A in Fig. 9.1. The states $|G_{i0}\rangle$ are multidimensional Gaussian wavepackets representing the bath states. We note again that this in no way implies the bath is harmonic. Under the dynamics, which includes interaction with the bath in the right arm, the wavefunction becomes, within the perturbation theory presented above,

$$|\Psi^{\{\xi\}}\rangle = \frac{1}{\sqrt{2}}\sum_i w_i \left(|g_{0t}^l\rangle|G_{it}^l\rangle + |g_{it}^r\rangle|G_{it}^r\rangle e^{i\phi_i}\right) e^{i\xi_i} \,, \tag{9.36}$$

where $|g_{it}^{r,(l)}\rangle$ is the wavepacket of the system particle moving in the right (left) arm at time t if the bath was in state $|G_{i0}\rangle$ initially. The state $|G_{it}^{r,(l)}\rangle$ is the perturbed wavepacket of the bath (according to Sec. III C 1) at time t for a particle moving in the right (left) arm where the bath was initially in state $|G_{i0}\rangle$. Note that since the particle in the left arm does not interact with the bath, $|G_{it}^l\rangle = |G_{it}^0\rangle$ and $|g_{it}^l\rangle = |g_{0t}^l\rangle$.

Several remarks are in order. First, we have split off the perturbative phase change

$$\phi_i \equiv \frac{\delta S_t}{\hbar} = \frac{\lambda}{\hbar}\left(p_t\delta q_t - \int V_1(q_0(t'))\,dt'\right) \,, \tag{9.37}$$

which applies only to the right arm and is different for each bath state i, since the

---

[4] One has to be careful with the form of the initial condition as it may affect the transient behaviors on time scales longer than the inverse frequency cut off of the bath[143].

trajectory the bath takes, and thus the interaction potential, depends upon the initial bath wavepacket. The initial bath wavepacket specifies the positions and momenta of all the particles in the bath, within the wavepacket uncertainty. Second, notice that the wavefunction involves a sum over products of Gaussian wavepackets in the system and bath variables. This is the exact form within the perturbation theory, since the forcing function $f(t) = -V_1'(t)$ only affects the positions and phase of each multidimensional Gaussian representing system and bath, but not the quadratic terms in the exponent (which could entangle the system and bath coordinates in individual Gaussian wavepackets). To be sure, the sum of such separable products (labeled by i) is, in general, highly correlated, and gives the exact wavefunction evolution in the semiclassical limit. The expressions Eq. (9.36) and Eq. (9.37) generalize and correct formulas Eq. (9.2) and Eq. (9.5) of SAI, in such a way that the convenient and intuitive form of products of system and bath wavefunctions appears, albeit in combinations which allow for quite general state changes and entanglements.

When obtaining the reduced density matrix corresponding to $|\Psi^{\{\xi\}}\rangle$, namely

$$\begin{aligned}\hat{\rho}_{\text{red}}^{\{\xi\}} &\equiv \text{Tr}_{\text{bath}}\left[\hat{\rho}_{\text{tot}}^{\{\xi\}}\right] \\ &= \text{Tr}_{\text{bath}}\left[\hat{\rho}^{rr,\{\xi\}} + \hat{\rho}^{rl,\{\xi\}} + \hat{\rho}^{lr,\{\xi\}} + \hat{\rho}^{ll,\{\xi\}}\right], \end{aligned} \tag{9.38}$$

where $\hat{\rho}_{\text{tot}} = |\Psi^{\{\xi\}}\rangle\langle\Psi^{\{\xi\}}|$. It is necessary only to examine the off diagonal cross terms, since they carry the information about the decoherence induced by the bath interaction. Carrying out the trace over the bath, we have

$$\hat{\rho}_{\text{red}}^{rl,\xi} = \frac{1}{2}\sum_{ij} |g_{it}^{r}\rangle\langle g_{0t}^{l}| w_i w_j e^{i\phi_i} e^{i\xi_i - i\xi_j} O_{ji}^{0r} \;, \tag{9.39}$$

where

$$O_{ji}^{0r} = \langle G_{jt}^0 | G_{it}^r \rangle \ , \tag{9.40}$$

with a similar expression for $\hat{\rho}_{\text{red}}^{lr,\xi}$. In deriving Eq. (9.39) we have used the approximate relation $\langle G_{jt}^0 | G_{it}^0 \rangle = \delta_{ij}$. The bath wavepacket $|G_{jt}^0\rangle$ has a superscript 0 to indicate that it is unperturbed from its trajectory if the system travels in the left arm. Eq. (9.39) is the appropriate reduced density matrix for a *completely coherent bath*; in order to simplify our expressions, we will average over the random phases, ξ. This would a apply to a bath which has been kicked into several states, or as we mentioned earlier, it can be thought of as a formal trick to obtain the finite temperature density matrix,

$$\hat{\rho}_{\text{red}}^{rl} = \frac{1}{2} \sum_i |g_{it}^r\rangle \langle g_{0t}^l | w_i^2 e^{i\phi_i} O_{ii}^{0r}. \tag{9.41}$$

Note that $|g_{0t}^l\rangle$ does not interact with the bath and therefore does not develop an index i depending on the bath state. When $\hat{\rho}_{red}$ is squared and traced over to obtain the decoherence measure $M \equiv \text{Tr}\,[\hat{\rho}_{\text{red}}^2]$, the terms $M_{\text{coh}} \equiv \text{Tr}\left[\hat{\rho}_{\text{red}}^{rl}\hat{\rho}_{\text{red}}^{lr} + \hat{\rho}_{\text{red}}^{lr}\hat{\rho}_{\text{red}}^{rl}\right]$ contain all the information on inter-arm coherence. These give

$$\begin{aligned} M_{\text{coh}} &= \frac{1}{4} \sum_{ij} \langle g_{jt}^r | g_{it}^r \rangle w_i^2 w_j^2 O_{jj}^{*0r} O_{ii}^{0r} e^{i\phi_i - i\phi_j} + \quad h.c. && (9.42) \\ &= \langle \psi^{\text{sys}} | \psi^{\text{sys}} \rangle \ , && (9.43) \end{aligned}$$

where

$$|\psi^{\text{sys}}\rangle = \frac{1}{\sqrt{2}} \sum_i w_i^2 O_{ii}^{0r} e^{i\phi_i} |g_{it}^r\rangle \ , \tag{9.44}$$

and M_{coh} encodes the inter-arm coherence information. Remarkably, $M_{\text{coh}}$is the self overlap of a (generally non-normalized) effective system wavefunction. The emergence of a wavefunction form is unexpected because we have already performed the ensemble average over random phases. We can check this result in the limit of no interaction with the bath: then, the overlap factors are all unity, the phases $\phi_i = 0$, and all the gaussians $|g^r_{it}\rangle$ are the same (normalized) unperturbed state $|g^r_{0t}\rangle$. Then,

$$|\psi^{\text{sys}}\rangle = \frac{1}{\sqrt{2}} \sum_i w_i^2 \; |g^r_{0t}\rangle = \frac{1}{\sqrt{2}} |g^r_{0t}\rangle \; , \tag{9.45}$$

implying $\langle \psi^{\text{sys}} | \psi^{\text{sys}} \rangle = M_{\text{coh}} = 1/2$, i.e. maximum coherence.

Eq. (9.42) is the central result of this section. It applies to any bath (harmonic or not) at finite temperature with weak system coupling and any number of degrees of freedom. As we mentioned earlier, it could also apply to a bath at zero temperature with a number of excitations (justifying the average over ξ).

Eq. (9.42) is composed of system wavepacket overlap factors $\langle g^r_{jt} | g^r_{it} \rangle$, bath overlap factors O^{0r}_{jj}, weighting factors (coming from the initial bath conditions) w_i^2, and finally phase factors $e^{i\phi_i}$. The phases ϕ_i are classical actions divided by $\hbar$. The "system wavefunction" overlap form, Eq. (9.44), is especially convenient for intuition and computation. Decoherence shows up as a reduction in the norm of the system wavefunction. This comes about from any or all of three factors: bath overlap decay, phase jitter, and system wavepacket displacement.

The are several more interesting facets of Eq. (9.42) deserving discussion. We will do this systematically, by considering important special cases which highlight aspects of this formula.

9.4.6 Special Cases of Decoherence

We begin our discussion of various limits by assuming that the system overlaps and possibly also the bath overlaps are near unity. This regime is indeed accessible, since the classical action perturbation term is $\phi_i = \frac{1}{\hbar}\delta S_t$, where δS_t is the action due to the perturbation along the unperturbed orbit. There is no doubt the action term can be large compared to 2π and vary widely, since the perturbing classical action can be large compared to $\hbar$.

At the same time, the wavepacket displacement can remain small compared to its width, in both position and momentum space. Classical action changes are always accompanied by corresponding areas or volumes in phase space; if one plots the manifolds of the perturbed system exactly, then a phase $\phi = 2\pi$ will be accompanied by a loop or area in phase space which is of this magnitude. However, the wavepacket width goes as $\sim \sqrt{\hbar}$, but the perturbing action increases as $\hbar^{-1}$. Therefore, for small enough perturbations and small enough $\hbar$, we can safely take the wavepacket overlaps to be 1, and focus on the phase terms.

Suppose that the system wavepackets $|g^r_{jt}\rangle$ are not displaced by the interaction with the bath, then we have

$$\langle g^r_{jt}|g^r_{it}\rangle \approx 1 \tag{9.46}$$

and Eq. (9.42) becomes

$$\begin{aligned} M_{\text{coh}} &= \frac{1}{4}\sum_{ij} w_i^2 w_j^2 O^{0r}_{ii} O^{0r*}_{jj} e^{i\phi_i - i\phi_j} + \quad h.c. \\ &= \frac{1}{2}\left|\sum_i w_i^2 O^{0r}_{ii} e^{i\phi_i}\right|^2 \equiv \frac{1}{2}|\mu|^2 \, . \end{aligned} \tag{9.47}$$

If we had not averaged over the ξ, we would have found that

$$\begin{aligned} \mu &= \sum_{ij} w_i w_j e^{i\phi_i} e^{i(\xi_i - \xi_j)} O^{0r}_{ji} \\ &= \int d\eta \, \chi_l^*(\eta) \chi_r(\eta) \ , \end{aligned} \tag{9.48}$$

which is just a simple bath overlap. This gives the interpretation of $M_{\rm coh}$ as one half the bath overlap squared, then averaged over different "runs", or realizations of the bath, which were encoded by the random phases ξ, i.e.

$$M_{\rm coh} = \frac{1}{2} < |\mu_\xi|^2 > \ . \tag{9.49}$$

From the system wavefunction viewpoint, we have (in the limit of Eq. (9.46)),

$$|\psi^{\rm sys}\rangle = \left(\frac{1}{\sqrt{2}} \sum_i w_i^2 O^{0r}_{ii} e^{i\phi_i} \right) |g_{0t}\rangle \ , \tag{9.50}$$

which lays the blame for decoherence entirely in the sum contained in the brackets. This can be reduced in magnitude by both bath overlap decay factors or by phase jitter.

Nondynamical bath

The "nondynamical" bath limit emerges by further setting $O^{0r}_{ii} = 1$, i.e. bath wavepackets undisplaced by the interaction, which would be the case indeed if the bath Hamiltonian commutes with the bath-particle interaction potential. Then,

$$|\psi^{\rm sys}\rangle = \left(\frac{1}{\sqrt{2}} \sum_i w_i^2 e^{i\phi_i} \right) |g_{0t}\rangle \ . \tag{9.51}$$

The reduction of the norm (corresponding to decoherence) is due entirely to phase jitter. In this case we have a compelling formula emerging, in the spirit of SAI,

$$\int d\eta\, \chi_l^*(\eta)\chi_r(\eta) = \sum_i w_i^2 e^{i\phi_i} \equiv < e^{i\phi_i} > , \qquad (9.52)$$

where the phase ϕ_i is imparted with probability w_i^2. ϕ_i is the phase acquired if the bath wavepacket is $|G_{i0}\rangle$ initially, and this happens with probability w_i^2, the probability weight of that wavepacket in the initial bath. This formula gives a more concrete picture of the nondynamical bath limit, and the origin of the phases which are averaged over: they are classical actions for the trajectory of the system-bath dynamics, divided by $\hbar$. In terms of $M_{\rm coh}$, we have

$$M_{\rm coh} = \frac{1}{2}| < e^{i\phi_i} > |^2 . \qquad (9.53)$$

The limit of a nondynamical bath can also be achieved (without the bath Hamiltonian commuting with the bath-particle interaction potential) by a high temperature bath whose wavepacket description involves mostly very excited coherent states. Such coherent states are robust against self overlap decay, unless large energy exchange is occurring. This kind of nondynamical bath corresponds to classical states of the radiation field in a large cavity with high enough temperature. It is well known that this situation is described quantum mechanically in terms of excited coherent states of the field oscillators. Such baths (or similarly, externally applied fields) tend not to contribute to decoherence *via* a bath overlap decay mechanism for weak coupling, but rather the sort of “dephasing” expressed by Eq. (9.52).

In the high temperature bath limit there is unitary evolution of the system, with an effective potential $V(x,t)$ acting on the system particle with coordinates x, as can be seen within either the perturbative or Hartree formulations: By assuming that the bath wavepackets are unshifted by the interaction $\lambda V(x,\eta)$, where η are the bath coordinates, there arises an effective x potential $V_i(x,t) = \lambda V(x,\eta_{it})$ or $V(x,t) = \lambda\langle G^0_{it}|\hat{V}(x)|G^0_{it}\rangle$ in the perturbative and Hartree formulations, respectively, for each realization i of the bath initial conditions. The ensemble average over different realizations of the field, (i.e. the average over distinct bath initial wavepackets $|G_{i0}\rangle$) which occurs in any real measurement involving a thermal bath becomes the agent of decoherence. Note that nondynamical baths do not guarantee that the system wavepackets are weakly displaced; see the next section.

The nature of bath decoherence is illustrated by considering a harmonic bath mode subject to a given forcing function, and separately subject to a fixed energy exchange. The overlap decay D of an arbitrary coherent state $|\alpha_0\rangle$, is defined as

$$D = |\langle\tilde{\alpha}_t|\alpha_t\rangle| \ , \tag{9.54}$$

where $|\tilde{\alpha}_t\rangle$ is that coherent state which resulted from the force acting on the initial $|\alpha_0\rangle$ for time t, and $|\alpha_t\rangle$ is the coherent state which evolves unperturbed from the initial $|\alpha_0\rangle$. D is given by

$$D = e^{-|a_t|^2/2} \ , \tag{9.55}$$

where

$$a_t = e^{-i\omega t}(2m\omega\hbar)^{-\frac{1}{2}}\int_0^t f(t')e^{i\omega t'}dt' \ . \tag{9.56}$$

This equation shows that the amplitude and the frequency content of the force at the frequency of the oscillator are key to the displacement of the oscillator. Notice this result does not depend on the initial coherent state, which would seem to argue against our assertion that highly excited coherent states are more "classical". However, the maximum energy exchanged by the force goes as the square root of the initial expectation value of the energy, so the forcing, while it causes fixed wavepacket overlap reduction, is exchanging large amounts of energy for highly excited coherent states. When the system has only little energy to exchange, it is better to consider a fixed energy transfer, such as a one quantum process. The normalized state obtained by increasing the expectation of the number of quanta in a given coherent state $|\alpha_0\rangle$ by one is

$$|\tilde{\alpha}_0\rangle = \frac{1}{\sqrt{< E > /\hbar\omega + 1}} \hat{a}^\dagger |\alpha_0\rangle \ , \tag{9.57}$$

where $< E >= \langle \alpha_0 | H | \alpha_0 \rangle$. Then the relevant overlap decay is easily shown to be

$$\begin{aligned} D &= |\langle \tilde{\alpha}_0 | \alpha_0 \rangle| = \left(\frac{< E > -\hbar\omega/2}{< E >} \right)^{1/2} & (9.58) \\ &\propto 1 - \frac{\hbar\omega}{4 < E >} + \ldots \ . & (9.59) \end{aligned}$$

Thus, for a fixed energy exchange with the system, the decoherence is *weaker* at higher temperature, where the average energy is larger. A bath consisting of low frequency modes $\hbar\omega << kT$ (such as translational modes in a liquid) can be effectively nondynamical, again provided the systems does not exchange large amounts of energy with it. Another example is given by Stark perturbation of an atomic transition by an ambient and nonresonant thermal radiation field.

Dynamical Bath

More generally, we see from Eq. (9.47) that the decoherence (still assuming little system displacement) arises from two sources: phase decoherence and amplitude decoherence (due to $|O_{ii}^{0r}| < 1$). The latter is caused by the bath wavepackets becoming displaced by interaction with the system. In this case, it is less compelling to associate $\langle e^{i\phi_i}\rangle$ with $\sum\limits_i w_i^2 O_{ii}^{0r} e^{i\phi_i}$, since the overlap factors are not naturally written as integrals over phase factors, although one could always do this, however absent of physical motivation. This situation corresponds to SAI's dynamical bath. The present formulation shows a pure phase average picture for this case is somewhat forced. Bath wavepacket displacement (and in the next section, system wavepacket displacement) thus emerges as a restraint on a pure "dephasing" picture of decoherence.

The dynamical bath limit would be uninteresting if decoherence is always dominated by dephasing. But low temperature baths are prime suspects for overlap decay to dominate dephasing effects. For example, if there is just one bath coherent state, e.g. as in a $T = 0$ bath whose true ground state is describe well by a single multidimensional coherent state, the Eq. (9.42) becomes

$$M_{\text{coh}} = \frac{1}{2}|O_{11}^{0r}|^2 , \tag{9.60}$$

i.e. the decoherence is entirely caused by bath overlap decay. This is true even if the system wavepacket is strongly displaced, since the system wavepacket simply overlaps itself in Eq. (9.42) when there is but a single state in the sums. It is therefore possible to decohere from the zero temperature initial state or a given single coherent state of the bath, due to bath overlap decay; however, at zero temperature this requires degeneracies of the bath.

Here, it is especially clear that a phase average picture is not natural for a dynamical bath: in this case there is only one "quantum trajectory" so to speak, a single product wavepacket which describes the bath-system evolution in the right arm. Eq. (9.42) shows that the effect in this case is decoherence due to a displaced bath wavepacket.

9.4.7 System Overlap Decoherence

We now relax the artificial (though possible) condition that the system overlap terms are essentially 1, i.e. the system wavepackets can be significantly displaced by interacting with the bath. Here we leave the realm considered by SAI.

The concepts of a dynamical and nondynamical bath still apply; the question at hand now is the further role of system overlap decay in forming the coherence measure M_{coh}.

We assume a nondynamical bath to make the analysis simpler; this means that bath wavepacket self-overlaps are unity, and any decoherence can be blamed either on random phases (the dephasing limit) and/or on system overlap decay. We now investigate the relative importance of these two.

The relevant effective system wavefunction is then

$$|\psi^{\text{sys}}\rangle = \frac{1}{\sqrt{2}} \sum_i w_i^2 e^{i\phi_i} |g_{it}^r\rangle \tag{9.61}$$

The self overlap of this wavefunction is

$$M_{\mathrm{coh}} = \frac{1}{2}\sum_{ij} w_i^2 w_j^2 \; e^{i\phi_i - i\phi_j} \langle g_{jt}^r | g_{it}^r \rangle \tag{9.62}$$

The phase and overlap contributions are manifest. It is not possible to give a general rendition of the relative importance of phase and overlap contributions to this expression; this will depend on the system and bath under consideration. However, the diagonal terms always survive, even in the limit of strong kicking of the system wavepackets. (We remind the reader that even though our analysis was perturbative for the wavepacket displacements, in the sense of classical perturbation theory, the displacements can be strong in the quantum sense. "Strong" is measured by wavepacket overlap decay, which can be severe even while classical perturbations are correctly giving the wavepacket displacements). Restoring the bath overlap factors for a moment, for the diagonal terms we get

$$M_{\mathrm{coh}} = \frac{1}{2}\sum_{i} w_i^4 |O_{ii}^{0r}|^2 \leq \frac{1}{2}\sum_{i} w_i^4 \; . \tag{9.63}$$

Since $\sum\limits_i w_i^2 = 1$,

$$\sum_{i} w_i^4 \sim 1/N \; , \tag{9.64}$$

is an inverse participation ratio, where N is the number of participating quantum states describing the bath. When N is large, Eq. (9.64) predicts that M_{coh} will be vastly smaller than 1/2, effectively meaning the system is completely decohered in this limit. This is the limiting form in the strong system-kicking limit.

There remains a question, however: could the system overlap decay strongly as above without strong phase randomization, so that a pure dephasing picture would miss it? When one considers, for example, the harmonic model, the conclusion is soon reached that for finite temperature it is not easy to strongly displace the system wavepackets randomly without strong phase randomization.

9.5 Conclusions

In this paper, we have presented a semiclassical, wavepacket-based formalism for decoherence. We have limited ourselves to the case of a single system wavepacket split initially into two mutually coherent pieces, one of which interacts with a bath. This situation is well suited to discussion of the SAI approximation, which seeks to lay the blame for decoherence at the feet of random phases imparted to the system by the bath. In one limit, discussed in Sec.(9.4.6), this is exactly the case, when neither system nor bath wavepackets are significantly displaced by the interaction, but phases develop which decohere the system anyway (corresponding to SAI's "nondynamical" bath). In this case decoherence takes place without an appreciable exchange of energy. In another limit, discussed in Sec.(9.4.6), wherein system wavepackets are also barely perturbed but bath wavepackets are significantly displaced, one can still force a random phase picture, within the SAI identification embodied in Eq. (9.6), although the identification with an average over random phase factors is more of a mathematical equivalence than a physically motivated idea.

If, however, the system wavepacket is more strongly perturbed by the interaction, as in Sec.(9.4.7), a new decoherence mechanism sets in which does not fit into the SAI scheme at all. Such system disturbance is hardly rare or unlikely. Stronger perturbation of the system can occur with or without significant bath displacement. Finally, the relative importance of wavepacket displacement and phase randomization is $\hbar$ dependent, with smaller $\hbar$ favoring a dephasing mechanism.

One perhaps surprising and potentially very computationally and intuitively useful aspect of our formulation is the emergence of an effective system wavefunction, which measures the decoherence. Similar ideas have been introduced in the context of a stochastic Schrodinger equation [144].

The distinction we are making between phase randomization versus overlap decay has long been central within the context of spectroscopy of systems embedded in a bath (see, e.g. Ref. [145]). The concepts of "dephasing", "depopulation", and "pure dephasing" are traditional in spectroscopy. Within the context of exponential decay, the relation

$$\frac{1}{T_2} = \frac{1}{2T_1} + \frac{1}{T_2^*} \tag{9.65}$$

is legion, where T_2 is the dephasing time, T_1 is the depopulation time, and T_2^* is the pure dephasing time. The translation of concepts into the present discussion is: "dephasing" → "decoherence"; "pure dephasing" → "dephasing". The time T_2 is typically the time constant for decay of the initial wavefunction created by absorption of a photon, and is measured from the width of of an absorption line. (If we had introduced a tunnel coupling between the two arms of our model device, we could also have had a natural population decay-the probability of being in each arm. This is an interesting subject for future study).

It is important to mention the limitations of our theory. Since our theory has not included the Pauli exclusion principal it can not be straightforwardly applied to the electron dephasing problem; the Fermi sea and its additional phase-space constraints on available system decay states has not been properly incorporated. We have also neglected spin, but this can be included without much difficulty[123].

The approach we have taken to decoherence is not limited to the physical circumstances used here. The semiclassical wavepacket-perturbation approach should be applicable to wide variety of situations and physical observables, and we hope to pursue some of these in the near future.

Appendix A

Evaluation of STM Current

The following is adapted directly from Ref. [8].

$$M_{\mu\nu} = \frac{\hbar^2}{2m} \int d\vec{S} \cdot (\psi_\mu^* \vec{\nabla} \psi_\nu - \psi_\mu \vec{\nabla} \psi_\nu^*) \ . \tag{A.1}$$

The matrix elements $M_{\mu\nu}$ can be evaluated by expanding the the surface state wave function as

$$\psi_\nu = \frac{1}{\sqrt{\Omega_s}} \sum_G a_G e^{(\kappa^2 + |\vec{\kappa}_G|^2)^{1/2} z} e^{i\vec{\kappa}_G \cdot \vec{x}} \ , \tag{A.2}$$

where Ω_s is the volume of the sample, $\kappa = \sqrt{\frac{2mW}{\hbar^2}}$ and $\vec{\kappa}_G = \vec{k}_{||} + \vec{G}$. Here m is the mass of the electron, W the work function of the metal, $k_{||}$ the wave vector parallel to the surface and $\vec{G}$ is a reciprocal lattice vector.

The tip wavefunctions can be written in the s-wave approximation (point source of electrons) as

$$\psi_\mu = \frac{1}{\sqrt{\Omega_t}} \frac{c_t R e^{\kappa R}}{|\vec{r} - \vec{r}_0|} e^{-\kappa |\vec{r} - \vec{r}_0|} \ , \tag{A.3}$$

where R is the radius of the tip, $\vec{r}_0$ is the center of the tip, Ω_t is the volume of the tip and c_t is some prefactor. ψ_μ can then expanded in the same form as the surface states using

$$\frac{e^{-\kappa \vec{r}}}{\kappa \vec{r}} = \int d^2 q b(\vec{q}) e^{-(\kappa^2+q^2)^{1/2}|z|} e^{i\vec{q}\cdot\vec{x}} \tag{A.4}$$

and

$$b(\vec{q}) = (2\pi)^{-1}\kappa^{-2}(1+q^2/\kappa^2)^{-1/2} \ , \tag{A.5}$$

where z is the distance from the surface Plugging into the expression for $M_{\mu\nu}$ and evaluating term by term in G gives

$$M_{\mu\nu} = \frac{\hbar^2}{2m}\frac{4\pi}{\sqrt{\Omega_t}} R e^{\kappa R} \psi_\nu(\vec{r}_0) \ , \tag{A.6}$$

which yields a current

$$I = \frac{32\pi^3 e^2 V W^2 D_t(E_F) R^2 e^{2\kappa R}}{\hbar \kappa^4} \sum_\nu |\psi_\nu(\vec{r}_0)|^2 \delta(E_\nu - E_F) \ , \tag{A.7}$$

where $D_t(E_F)$ is the tip density of states and V is the tip-sample bias voltage.

Appendix B

Scattering Phase Shift from DOS

The following is adapted directly from Ref. [23].

In this Appendix we show how to relate the phase shift of an impurity, $\delta(\varepsilon)$, to the retarded Greens function, $\hat{G}$, and the impurity density of states.

As we showed in Chapter 2, Dyson's equation (Lippmann-Schwinger equation in the context of scattering theory) can be written

$$\hat{G} = \hat{G}_0 + \hat{G}_0 \hat{V} \hat{G} \ , \tag{B.1}$$

which can be expanded as

$$\begin{aligned} \hat{G} &= \hat{G}_0 + \hat{G}_0 \hat{V} G_0 + \hat{G}_0 \hat{V} \hat{G}_0 \hat{V} G_0 + \cdots \\ &= \hat{G}_0 + \hat{G}_0 (\hat{V} + \hat{V} \hat{G}_0 \hat{V} + \cdots) G_0 \ , \end{aligned} \tag{B.2}$$

where the terms in the parenthesis can be grouped into into a single object called the *t-matrix*. The *t-matrix* is defined by

$$\hat{T} = \hat{V} + \hat{V} \hat{G}_0 \hat{V} + \cdots \ . \tag{B.3}$$

It has the utility that once it is known, the Lippman-Schwinger equation reduces to

$$\hat{G} = \hat{G}_0 + \hat{G}_0 \hat{T} \hat{G}_0 \ , \tag{B.4}$$

which relates the full Greens function, $\hat{G}$, to the free Greens function, $\hat{G}_0$.

We assume a one-body Hamiltonian of the form

$$\hat{H} = \sum_{\mathbf{k},\sigma} \epsilon_{\mathbf{k}} c^{\dagger}_{\mathbf{k},\sigma} c_{\mathbf{k},\sigma} + \sum_{\mathbf{k},\mathbf{k}',\sigma} V_{\mathbf{k},\mathbf{k}'} c^{\dagger}_{\mathbf{k},\sigma} c_{\mathbf{k}',\sigma}, \tag{B.5}$$

which can be diagonalized exactly to yield

$$\hat{H} = \sum_{\alpha,\sigma} \epsilon_{\alpha} c^{\dagger}_{\alpha,\sigma} c_{\alpha,\sigma} \ , \tag{B.6}$$

where the creation and annihilation operators have obvious meaning. In the diagonal basis,

$$G_{\alpha,\alpha'}(\varepsilon) = \langle \alpha | \hat{G}(\varepsilon) | \alpha' \rangle = \frac{\delta_{\alpha\alpha'}}{\varepsilon - \varepsilon_{\alpha} + is} \ , \tag{B.7}$$

where s is a positive infinitesimal. The density of states can then be computed directly from the retarded Greens function,

$$\varrho(\varepsilon) = -\frac{1}{\pi} \mathrm{Im}\mathrm{Tr}[\hat{G}(\varepsilon)] \ . \tag{B.8}$$

Consider the case of a single impurity in a host. Then, to a good approximation, the density of states is just the sum of the two: $\varrho(\epsilon) = \varrho_0(\epsilon) + \varrho_{\mathrm{imp}}(\epsilon)$. Therefore, $\Delta\varrho(\epsilon) \equiv \varrho(\epsilon) - \varrho_0(\epsilon) = \varrho_{\mathrm{imp}}(\epsilon)$. Thus, we can write, using Eq. B.8,

$$\Delta\varrho(\epsilon) = -\frac{1}{\pi} \mathrm{Im}\mathrm{Tr}[\hat{G}(\varepsilon) - \hat{G}_0(\varepsilon)] \ . \tag{B.9}$$

The matrix identity $\mathrm{Tr}\ln\mathbf{A} = \ln\det\mathbf{A}$ generalizes, after using Eq. B.7 to

$$\mathrm{Tr}\hat{G}(\varepsilon) = -\frac{\partial}{\partial\varepsilon} \ln\det\hat{G}(\varepsilon) \ , \tag{B.10}$$

which allows us to re-express Eq. B.9 as

$$\Delta\varrho(\varepsilon) = \frac{1}{\pi}\mathrm{Im}\frac{\partial}{\partial\varepsilon}\ln\left(\det[\hat{G}(\varepsilon)\hat{G}_0(\varepsilon)^{-1}]\right) \ . \tag{B.11}$$

The Greens function can be solved as $\hat{G} = (1-\hat{G}_0\hat{V})^{-1}\hat{G}_0$ so that

$$\Delta\varrho(\varepsilon) = \frac{1}{\pi}\mathrm{Im}\frac{\partial}{\partial\varepsilon}\ln\left(\det[(1-\hat{G}_0\hat{V})^{-1}]\right) \ . \tag{B.12}$$

Since we are considering time independent potentials, $\hat{V}$ does not depend on the energy ε. Therefore, we can replace $(1-\hat{G}_0\hat{V})^{-1}$ by $\hat{V}(1-\hat{G}_0\hat{V})^{-1} = \hat{T}$ because the derivative acting on the term with V alone will give zero (recall det(AB)=det(A)det(B) and ln(ab)=ln(a) + ln(b)). Hence,

$$\Delta\varrho(\varepsilon) = \frac{1}{\pi}\mathrm{Im}\frac{\partial}{\partial\varepsilon}\ln\left(\det\hat{T}\right) \ . \tag{B.13}$$

The phase shift is defined as

$$\delta(\varepsilon) = \mathrm{arg}\det\hat{T}(\varepsilon) \ . \tag{B.14}$$

(When the *t-matrix* is expressed in position representation,

$$T(\varepsilon) = 2i(e^{2i\delta(\varepsilon)}-1)\delta(\mathbf{r_0}-\mathbf{r}'')\delta(\mathbf{r_0}-\mathbf{r}') \ ,$$

which can be checked explicitly to satisfy the relation, Eq. B.14 above.) Using the fact that the imaginary part of the ln is the argument,

$$\Delta\varrho(\epsilon) = \frac{1}{\pi}\frac{\partial\delta(\epsilon)}{\partial\epsilon}. \tag{B.15}$$

The phase shift and number of impurity states, n_{imp}, are thus determined by integrating over the density of states

$$n_{\mathrm{imp}} = \int_{-\infty}^{E_F}\Delta\varrho(\epsilon) = \frac{\delta(E_F)}{\pi} \ , \tag{B.16}$$

where we have taken $\delta(-\infty) = 0$ and E_F is the Fermi energy.

Appendix C

Derivation of Local Moment Model for Magnetic Nanoclusters

Consider N_A magnetic impurities embedded in close proximity in a metallic host. The Hamiltonian is $\hat{H} = \hat{H}_{\text{metal}} + \hat{H}_{\text{int}}$ where $\hat{H}_{\text{metal}} = \sum_{\mu,k,\sigma} \epsilon_{\mu,k} \hat{n}_{\mu k \sigma}$ describes the free conduction electrons and

$$\hat{H}_{\text{int}} = -\sum_{\vec{r},\vec{r}'} J_F(\vec{r},\vec{r}')\vec{S}_d(\vec{r}) \cdot \vec{S}_d(\vec{r}') + J \sum_{\vec{r}} \vec{S}_c(\vec{r}) \cdot \vec{S}_d(\vec{r}) \tag{C.1}$$

describes the direct interactions between the impurity d-levels and the interactions between the conduction electrons and the magnetic impurities. The first term in Eq. (C.1) describes the ferromagnetic interaction among the localized d-levels of the impurity atoms and the second term, $H_K \equiv J \sum_{\vec{r}} \vec{S}_c(\vec{r}) \cdot \vec{S}_d(\vec{r})$, describes Kondo scattering from these d-levels by the conduction electrons. $J_F(\vec{r},\vec{r}') > 0$ is the ferromagnetic exchange interaction between two localized d-levels and $J > 0$ is the bare Kondo exchange coupling between the d-levels and the conduction electrons. The conduction electron spin operator at position $\vec{r}$ is

$$\vec{S}_c(\vec{r}) = \frac{1}{2}\sum_{j,j'} \varphi_j^*(\vec{r})\varphi_{j'}(\vec{r}) c_{j\alpha}^\dagger \vec{\sigma}_{\alpha\alpha'} c_{j'\alpha'} \tag{C.2}$$

where $\varphi_j(\vec{r})$ is the wave function of conduction electrons with level index j at $\vec{r}$. The utility of Eq. (C.1) is two-fold: (i) It gives an expression for the important limiting case of a "cluster" which consists of just one impurity. In this limit, $\hat{H}_{\text{int}} = J\vec{S}_c(0) \cdot \vec{S}_d(0)$ which is just H_K for a single impurity. (ii) Eq. (C.1) can describe the limit of a cluster so strongly coupled to the metallic host that the conduction band conduction electrons of the cluster and those of the host cannot be distinguished. Thus, the character of the $\varphi_j(\vec{r})$ that appear in Eq (C.2) vary depending on the physical situation. For a single impurity, $\varphi_j(\vec{r})$ is the wave function of the host metal conduction electrons, for a cluster in the weak tunneling regime as described in Sec. 5.3 $\varphi_j(\vec{r})$ describes the conduction band wave functions of the ferromagnet or ferromagnetic semiconductor and for a cluster in the strong tunneling regime $\varphi_j(\vec{r})$ is a strong hybridization of the ferromagnetic conduction band electrons and the conduction electrons of the host metal.

To derive Eq. (5.35), we neglect anisotropy in the cluster magnetization formed by the localized d-levels. We further neglect spin-wave excitations to states of different total d-electron spin of the cluster. In a Heisenberg-type model one may estimate the cost for such an excitation as $E_{\text{spin-wave}} \sim J_F(ak)^2$ where a is the lattice spacing of the cluster's atoms and k is the largest wave vector of the spin wave allowed by the physical size of the cluster. If we take $J_F \sim 0.1$ eV, *e.g.*, then for a small cluster of size $L \sim 10$ Åwith lattice constant $a \sim 2.5$ Å, $k_{\text{min}} \sim \frac{\pi}{L}$ so that the minimum spin-wave energy $E^{\rm min}_{\rm spin-wave} \sim 60{\rm meV} \approx 600{\rm K}$. Below that energy scale spin waves can be therefore neglected and we can concentrate on the subspace where

$$\sum_{\vec{r}} \vec{S}_d(\vec{r}) = N_A S_d = S_d^{\rm max}. \tag{C.3}$$

Within the subspace of maximum total d-level spin, the d-level spin is a rigid spin which can only change its projection on the z-axis. The collective effect of the impurity d-levels is to give the cluster a net spin. It is this spin that conduction electrons will scatter from–either "directly" in the limit of strong tunneling between the cluster and metallic host or "indirectly" as described in Sec. 5.3 in the limit of weak tunneling. (In the limit of weak tunneling only conduction band electrons may hop on and off the cluster.) Within the $S_d = S_d^{\rm max}$ subspace,

$$\begin{aligned} \langle S_d, S_d'^z | \hat{H}_K | S_d, S_d^z \rangle &= \frac{J}{2} \sum_{\vec{r},j,j'} \varphi_j^*(\vec{r}) \varphi_{j'}(\vec{r}) c^\dagger_{j\alpha} \vec{\sigma}_{\alpha\alpha'} c_{j'\alpha} \langle S_d, S_d'^z | \vec{S}_d(\vec{r}) | S_d, S_d^z \rangle && \text{(C.4)} \\ &\approx \frac{J}{2} \sum_{\vec{r},j,j'} \varphi_j^*(\vec{r}) \varphi_{j'}(\vec{r}) c^\dagger_{j\alpha} \vec{\sigma}_{\alpha\alpha'} c_{j'\alpha} \frac{1}{N_A} \langle S_d, S_d'^z | \vec{S}_d | S_d, S_d^z \rangle . && \text{(C.5)} \end{aligned}$$

The sum over $\vec{r}$ can be estimated,

$$\sum_{\vec{r}} \varphi_j^*(\vec{r}) \varphi_{j'}(\vec{r}) = \begin{cases} 1 & j = j' \text{ (normalization)} \\ \sim \frac{1}{\sqrt{N_A}} & j \neq j' \text{ (random numbers)} \end{cases} \tag{C.6}$$

Neglecting the off-diagonal terms,

$$\begin{aligned} H_K &\approx \frac{J}{N_A} \frac{1}{2} \sum_j c^\dagger_{j\alpha} \vec{\sigma}_{\alpha\alpha'} c_{j'\alpha} \cdot \vec{S}_d && \text{(C.7)} \\ &= \frac{J}{N_A} \vec{S}_c \cdot \vec{S}_d \, . && \text{(C.8)} \end{aligned}$$

The full Hamiltonian is

$$H_{\rm cluster} = \sum_{j,\sigma} \epsilon_j \hat{n}_{j\sigma} + \frac{J}{N_A} \vec{S}_c \cdot \vec{S}_d + \frac{E_C}{2} (\sum_{j,\sigma} \hat{n}_{j\sigma} - n_g)^2 - \sum_{\vec{r},\vec{r}'} J_F(\vec{r},\vec{r}') \vec{S}_d(\vec{r}) \cdot \vec{S}_d(\vec{r}') \; , \tag{C.9}$$

where we have put in the Coulomb charging energy by hand. Recall that now the $c^{\dagger}_{j\sigma}$ refer to conduction band electrons, not s, p and d hybridized bands as in the itinerant model. The last term in C.9 is just an irrelevant shift in the total energy in the subspace $S_d = S_d^{\max}$ so we drop it. Thus, we arrive at

$$\hat{H}_{\text{cluster}} = \sum_{j,\sigma} \epsilon_j \hat{n}_{j\sigma} + \frac{J}{N_A} \vec{S}_c \cdot \vec{S}_d + \frac{E_C}{2} (\sum_{j,\sigma} \hat{n}_{j\sigma} - n_g)^2. \tag{C.10}$$

Appendix D

Matrix Elements and Kondo Couplings for Local Moment Models

In this Appendix, we include some more lengthy expressions not included in Sec. 5.5.2. To complete the evaluation the RHS of Eq. (5.19) for the local moment model described in Sec. 5.5.2 we need the matrix elements:

$$\begin{aligned} M_2 &\equiv {}^N\langle S_T, S_T-1|c_{j\uparrow}|S_T+1/2, S_T-1/2\rangle_j^{N+1} \\ &= -\sum_{S_c^z=-S_c}^{S_c}\sqrt{\frac{S_c-S_c^z}{2S_c}}\langle S_c, S_d; S_c^z, S_T-S_c^z-1|S_T, S_T-1\rangle \\ &\quad \langle S_c-1/2, S_d; S_c^z+1/2, S_T-S_c^z-1|S_T+1/2, S_T-1/2\rangle \qquad \text{(D.1)} \end{aligned}$$

$$\begin{aligned} M_3 &\equiv {}_j^{N-1}\langle S_T+1/2, S_T-1/2|c_{j\uparrow}|S_T, S_T\rangle^N \\ &= \sum_{S_c^z=-S_c}^{S_c}\sqrt{\frac{S_c+S_c^z}{2S_c}}\langle S_c, S_d; S_c^z, S_T-S_c^z|S_T, S_T\rangle \end{aligned}$$

$$\langle S_c - 1/2, S_d; S_c^z - 1/2, S_T - S_c^z | S_T + 1/2, S_T - 1/2\rangle \tag{D.2}$$

$$\begin{aligned} M_4 &\equiv {}^N\langle S_T, S_T - 1 | c^\dagger_{j\downarrow} | S_T + 1/2, S_T - 1/2\rangle_j^{N-1} \\ &= \sum_{S_c^z=-S_c}^{S_c} \sqrt{\frac{S_c - S_c^z}{2S_c}} \langle S_c, S_d; S_c^z, S_T - S_c^z - 1 | S_T, S_T - 1\rangle \\ &\quad \langle S_c - 1/2, S_d; S_c^z + 1/2, S_T - S_c^z - 1 | S_T + 1/2, S_T - 1/2\rangle. \end{aligned} \tag{D.3}$$

The matrix elements then directly yield the expression for the generalized Kondo couplings for the local moment model:

$$\tilde{J}_s^{\mu\nu} = \sqrt{\frac{2}{S_T}} \sum_{j=I+1}^{A} V_\mu^{j,k_f\,*} V_\nu^{j,k_i} \left(\frac{M_4 M_3}{\delta E_{-,\uparrow} + \epsilon_A - \epsilon_j} - \frac{M_2 M_1}{\delta E_{+,\uparrow} - \epsilon_{I+1} + \epsilon_j} \right), \tag{D.4}$$

where M_1 denotes the matrix element already given in Eq. (5.40). The products $M_4 M_3$ and $M_2 M_1$ can be evaluated directly:

$$\tilde{J}_s^{\mu\nu} = -\frac{1}{S_T + 1} \sum_{j=I+1}^{A} V_\mu^{j,k_f\,*} V_\nu^{j,k_i} \left(\frac{1}{\delta E_{-,\uparrow} + \epsilon_A - \epsilon_j} + \frac{1}{\delta E_{+,\uparrow} - \epsilon_{I+1} + \epsilon_j} \right), \tag{D.5}$$

giving a ferromagnetic contribution when $J > 0$. If $J < 0$ and $S_T = S_d + S_c$ ($\uparrow \to \downarrow$) one finds $-\frac{1}{S_T+1} \to \frac{1}{S_T}$ which agrees with Eq. (5.23) of the itinerant model with $S_T \to S_0$.

A calculation similar to the one that led to Eq. (D.4) and Eq. (D.5) then yields:

$$\tilde{J}_e^{\mu\nu} = \sum_{j>A} V_\mu^{j,k_f\,*} V_\nu^{j,k_i} \left(\frac{\frac{2}{2S_T+1}}{\delta E_{+,\downarrow} - \epsilon_{A+1} + \epsilon_j} - \frac{\frac{1}{S_T+1}\left(\frac{2S_c}{2S_c+1}\right)}{\delta E_{+,\uparrow} + \Delta_s - \epsilon_{A+1} + \epsilon_j} \right), \tag{D.6}$$

and from the doubly occupied states

$$\tilde{J}_d^{\mu\nu} = \sum_{j<=I} V_\mu^{j,k_f\,*} V_\nu^{j,k_i} \left(\frac{\frac{2}{2S_T+1}}{\delta E_{-,\downarrow} + \epsilon_I - \epsilon_j} - \frac{\frac{1}{S_T+1}\left(\frac{2S_c}{2S_c+1}\right)}{\delta E_{-,\uparrow} + \Delta_s + \epsilon_I - \epsilon_j} \right), \tag{D.7}$$

where we have agained assumed $J > 0$, giving $\tilde{J}_e^{\mu\nu} > 0$ and $\tilde{J}_d^{\mu\nu} > 0$ since $\delta E_{\pm,\sigma} \sim E_C/2$. In the limit of a single point of contact, one recovers an expression similar to

Eq. (5.26), Eq. (5.41), except with an overall sign difference when $J > 0$ (and the precise form of the mesoscopic fluctuations). In the case $J < 0$ (take ↑→↓ and ↓→↑) we have $\frac{2}{2S_T+1} \to -\frac{2}{2S_T+1}$ and $\frac{1}{S_T+1}\left(\frac{2S_c}{2S_c+1}\right) \to -\frac{1}{S_T}\left(\frac{2S_c}{2S_c+1}\right)$ which makes $\tilde{J}_e^{\mu\nu} < 0$ and $\tilde{J}_d^{\mu\nu} < 0$.

The reduced matrix elements[146] for the all the states of the local moment model are given below:

D.1 J>0

$$\begin{aligned}
{}_j^{N-1}\langle S_T + 1/2||c_j||S_T\rangle_d^N &= \sqrt{\frac{2S_c}{2S_c+1}}\sqrt{2S_T+2} \\
{}_j^{N-1}\langle S_T - 1/2||c_j||S_T\rangle_d^N &= \frac{2S_T}{\sqrt{2S_T+1}} \\
{}_j^{N+1}\langle S_T + 1/2||c_j^\dagger||S_T\rangle_s^N &= \frac{2S_T+1}{\sqrt{2S_T+2}} \\
{}_j^{N-1}\langle S_T + 1/2||c_j||S_T\rangle_s^N &= \sqrt{2S_T+2} \\
{}_j^{N+1}\langle S_T + 1/2||c_j^\dagger||S_T\rangle_e^N &= \frac{2S_T+1}{\sqrt{2S_T+2}}\sqrt{\frac{2S_c}{2S_c+1}} \\
{}_j^{N+1}\langle S_T - 1/2||c_j^\dagger||S_T\rangle_e^N &= \sqrt{2S_T+1}
\end{aligned}$$

D.2 J<0

$$ {}_j^{N-1}\langle S_T + 1/2||c_j||S_T\rangle_d^N = \frac{2S_T+2}{\sqrt{2S_T+1}} $$

$$
\begin{aligned}
{}_{j}^{N-1}\langle S_T - 1/2||c_j||S_T\rangle_d^N &= \sqrt{2S_T}\sqrt{\frac{2S_c}{2S_c+1}} \\
{}_{j}^{N+1}\langle S_T - 1/2||c_j^\dagger||S_T\rangle_s^N &= \frac{2S_T+1}{\sqrt{2S_T}} \\
{}_{j}^{N-1}\langle S_T - 1/2||c_j||S_T\rangle_s^N &= \sqrt{2S_T} \\
{}_{j}^{N+1}\langle S_T + 1/2||c_j^\dagger||S_T\rangle_e^N &= \sqrt{2S_T+1} \\
{}_{j}^{N+1}\langle S_T - 1/2||c_j^\dagger||S_T\rangle_e^N &= \frac{2S_T+1}{\sqrt{2S_T}}\sqrt{\frac{2S_c}{2S_c+1}}
\end{aligned}
$$

Appendix E

Variational Calculation of the Baldereschi-Lipari Wavefunctions

We start from the Hamiltonian Eq. (7.1), the spherical Hamiltonian with central cell correction $V_{cc} = -V_0 e^{-(\frac{r}{r_0})^2}$,

$$H_0 = \frac{\gamma}{2m}\Big(p^2 - \mu \sum_{\alpha,\beta} J_{\alpha\beta} p_{\alpha\beta}\Big) - \frac{e^2}{\epsilon\ r} + V_{cc}(r)\ , \tag{E.1}$$

where r_0 is a short distance cutoff and all other parameters are as given in Sec. 7. Eq. (E.1) can be non-dimensionalized by rescaling distance $r \to r/a_{\text{eff}}$ where

$$a_{\text{eff}} = \hbar^2 \epsilon \gamma_1 / e^2 m_0 \tag{E.2}$$

is the effective Bohr radius (note that with the central cell correction this is no longer a measure of the spatial extent of the wavefunction),

$$R_{\text{eff}} = e^4 m_0 / 2\hbar^2 \epsilon^2 \gamma_1 \tag{E.3}$$

Table E.1: Numerical values of various authors.

Author	ϵ	r_0	a_{eff}	R_{eff}	V_0	$\tilde{V}$	E^{us}_{gnd}	E^{auth}_{gnd}
Y&M	10	2.59 Å	40.3 Å	17.8 meV	2.5 eV	141	74 meV	124 meV
B&B	10.66	2.8 Å	42.98 Å	15.7 meV	2.7 eV	172	102 meV	112 meV
US	10.66	2.8 Å	42.98 Å	15.7 meV	3.0 eV	198	112 meV	-

is the effective Rydberg and then multiplying through by $2m_0 a^2_{\text{eff}}/\hbar^2\gamma_1$. We define

$$\tilde{V} \equiv \frac{2m_0 V_0 a^2_{\text{eff}}}{\hbar^2\gamma_1} . \tag{E.4}$$

Table E.1 list the parameters we used as well as those used by various authors for Mn in GaAs. All authors have used the values γ_1=7.65 and $\mu = .767$ for GaAs. The values for ϵ_0, r_0, V_0 and E^{auth}_{gnd} where taken from Refs.[110, 107] while a_{eff}, R_{eff} and $\tilde{V}$ are the values calculated from Eq. E.2, Eq. E.3 and Eq. E.4. E^{us}_{gnd} was calculated by the variational method described below. We used the numerical values of Ref.[107] but we shifted V_0 to obtain the accepted binding energy of 112 meV.

When $\mu \neq 0$ in Eq. E.1 the ground state of a hole bound to an acceptor is no longer an $L = 0$ state. The "spin-orbit" term will mix in some $L = 2$ part[106]. The ground state is no longer Hydrogenic and must be solved by numerical methods. The total angular momentum $\vec{F} = \vec{L} + \vec{J}$ is a constant of the motion with $\mu \neq 0$ and the ground state is $F = 3/2$. The wavefunction for the ground state can then be written

$$\begin{aligned} \phi_{F_z}(\vec{r}) &= f_0(r)|L = 0, J = 3/2, F = 3/2, Fz\rangle \qquad \text{(E.5)} \\ &+ g_0(r)|L = 2, J = 3/2, F = 3/2, Fz\rangle . \end{aligned}$$

By taking matrix elements of Eq. E.1 in Eq. E.5 one obtains the following set of integral equations to be solved for $f_0(r)$ and $g_0(r)$:

$$\begin{pmatrix} \frac{d^2}{dr^2} + \frac{2}{r}\frac{d}{dr} + \frac{2}{r} - \tilde{V}_{cc} + E_{gnd} & -\mu\left(\frac{d^2}{dr^2} + \frac{5}{r}\frac{d}{dr} + \frac{3}{r^2}\right) \\ -\mu\left(\frac{d^2}{dr^2} - \frac{1}{r}\frac{d}{dr}\right) & \frac{d^2}{dr^2} + \frac{2}{r}\frac{d}{dr} - \frac{6}{r^2} + \frac{2}{r} - \tilde{V}_{cc} + E_{gnd} \end{pmatrix} \begin{pmatrix} f_0(r) \\ g_0(r) \end{pmatrix} = 0 \; . \tag{E.6}$$

In order to solve Eq. E.6 we follow the variational solution of Ref. [106] by expanding

$$f_0(r) = \sum_{i=1}^{21} A_i f_i(r) \; , \tag{E.7}$$

and

$$g_0(r) = \sum_{i=1}^{21} B_i g_i(r) \; , \tag{E.8}$$

where the A_i and B_i are variational parameters to be determined and $f_i(r)$ and $g_i(r)$ are normalized but not orthogonal basis functions given by

$$f_i(r) = \frac{2\sqrt{2}(g^{i-1}\alpha)^{3/4}}{\sqrt[4]{\pi/2}} e^{-g^{i-1}\alpha r^2} \; , \tag{E.9}$$

and

$$g_i(r) = r\frac{4\sqrt{2}(g^{i-1}\alpha)^{5/4}}{\sqrt{3}\sqrt[4]{\pi/2}} e^{-g^{i-1}\alpha r^2} \; , \tag{E.10}$$

with $\alpha_i = g^{i-1}\alpha$ where we have taken α=1 $\times 10^{-2}$ so that α_{21}=5 $\times 10^5$ as in Ref. [106]. Eq. E.7 and Eq. E.8 are then substituted into Eq. E.6, which leads to a series of guassian integrals that make up a (21+21) × (21+21) matrix. Once the nonorthogonality of the basis set is taken into account the transformed (21+21) × (21+21) matrix can be diagonalized to find the weights A_i and B_i. (A matrix diagonalization gives the variational weights becuase the states are linear in the variational parameters.) Roughly this goes as follows. The energy of the system is given by

$$E = \frac{\psi_i^\dagger H_{ij} \psi_j}{\psi_i^\dagger S_{ij} \psi_j} \; , \tag{E.11}$$

where H is the Hamiltonian of Eq. E.1 in the basis $\psi = \{f_0, g_0\}$ given by Eq. E.7 and Eq. E.8 and S is the matrix of overlaps of the non-orthogonal basis functions. The $f_0(r)$ and $g_0(r)$ satisfy the normalization condition $\int_0^\infty r^2(f_0(r)^2 + g_0(r)^2)dr = 1$. We can write $S = O^\dagger \Lambda O$ where Λ is a diagonal matrix. Therefore $\psi_i^\dagger S_{ij} \psi_j = \psi_i^\dagger O_{ik}^\dagger \Lambda_{kk} O_{kj} \psi_j$ so that we can define $\tilde{\psi} = \sqrt{\Lambda} O \psi$. This gives

$$E = \frac{\tilde{\psi}^\dagger (\sqrt{\Lambda}^{-1} O H O^\dagger \sqrt{\Lambda}^{-1}) \tilde{\psi}}{\tilde{\psi}^\dagger \tilde{\psi}} \,, \tag{E.12}$$

which can then be diagonalized to give the eigenvalues and eigenvectors in the new basis. The eigenvectors in the original basis are then found from $\psi = \sqrt{\Lambda}^{-1} O^\dagger \tilde{\psi}$. This determines the wavefunctions for the ground state (and higher excited states, in principal).

Appendix F

Expressions for Angular Dependence of Induced Hole Polarization

With wavefunctions in hand (Appendix E), we can calculate quantities such as $\langle \vec{J}(r,\theta,\phi) \rangle$ which will show the effects of the anisotropy of the Baldereschi-Lipari wavefunctions due to the effective spin-orbit coupling. As an example, consider $\langle J_z(r,\theta,\phi) \rangle_{F_z=3/2}$. Expanding part of Eq. (E.5),

$$
\begin{aligned}
&|L=0, J=3/2, F=3/2, F_z=3/2\rangle = \\
&\qquad\qquad \langle L=0, Lz=0, J=3/2, J_z=3/2 | F=3/2, F_z=3/2\rangle \\
&\qquad\qquad \times |L=0, L_z=0\rangle |J=3/2, Jz=3/2\rangle \qquad \text{(F.1)}
\end{aligned}
$$

which simplifies to

$$|L=0, J=3/2, F=3/2, F_z=3/2\rangle = |0,0\rangle|3/2,3/2\rangle. \tag{F.2}$$

For the $L=2$ component of Eq. (E.5) there are more terms,

$$|L=2, J=3/2, F=3/2, F_z=3/2\rangle = \sum_{J_z+L_z=3/2} \langle 2, Lz, 3/2, J_z|3/2,3/2\rangle|2,L_z\rangle|3/2,Jz\rangle\ , \tag{F.3}$$

which becomes

$$|2,3/2,3/2,3/2\rangle = \sqrt{\frac{2}{5}}|2,2\rangle|3/2,-1/2\rangle - \sqrt{\frac{2}{5}}|2,1\rangle|3/2,1/2\rangle + \sqrt{\frac{1}{5}}|2,0\rangle|3/2,3/2\rangle\ . \tag{F.4}$$

Projecting into $\langle\theta,\phi|$, which turns the orbital part, L, into spherical harmonics, one finds for the full wavefunction

$$\begin{aligned}\phi_{F_z=3/2} &= \left(f_0(r)Y_{00} + \frac{g_0(r)}{\sqrt{5}}Y_{20}(\theta,\phi)\right)|3/2,3/2\rangle \\ &- g_0(r)\sqrt{\frac{2}{5}}Y_{21}(\theta,\phi)|3/2,1/2\rangle + g_0(r)\sqrt{\frac{2}{5}}Y_{22}(\theta,\phi)|3/2,-1/2\rangle\ .\end{aligned} \tag{F.5}$$

Taking the expectation value of J_z in this state gives,

$$\langle J_z(r,\theta,\phi)\rangle_{F_z=3/2} = \frac{3}{8\pi}\left[f_0(r)^2 + f_0(r)g_0(r)(3\cos^2(\theta)-1) + g_0(r)^2\cos^4(\theta)\right]\ , \tag{F.6}$$

after expressing the spherical harmonics interms of trigonometric functions. The same calculation can be repeated for the other components of $\vec{J}$ in different F_z states to obtain

$$\langle J_{||}(r,\theta,\phi)\rangle_{F_z=\pm3/2} = \pm\frac{3}{8\pi}\left[f_0(r)^2 + f_0(r)g_0(r)(3\cos^2(\theta)-1) + g_0(r)^2\cos^4(\theta)\right] \tag{F.7}$$

$$\langle J_{\perp}(r,\theta,\phi)\rangle_{F_z=\pm3/2} = \pm\frac{3}{4\pi}\left[(f_0(r) + \frac{g_0(r)}{2}(3\cos^2(\theta)-1))g_0(r) + g_0(r)^2\sin^2(\theta)\right]\sin(\theta)\cos(\theta) \tag{F.8}$$

$$\begin{aligned}\langle J_{||}(r,\theta,\phi)\rangle_{F_z=\pm 1/2} = \pm\frac{1}{8\pi}\Bigg[f_0(r)^2 \quad &- \quad f_0(r)g_0(r)(3\cos^2(\theta)-1) \\ &+ \quad \frac{g_0(r)^2}{8}(5+12\cos(2\theta)-9\cos(4\theta))\Bigg]\end{aligned} \tag{F.9}$$

$$\langle J_{\perp}(r,\theta,\phi)\rangle_{F_z=\pm 1/2} = \pm\frac{3}{4\pi}\left[(f_0(r) \quad - \quad \frac{g_0(r)}{2}(3\cos^2(\theta)-1))g_0(r)\right]\sin(\theta)\cos(\theta) \tag{F.10}$$

where $\|$ and $\perp$ is taken with respect to the z-axis.

Appendix G

Parameter Determination of Effective Hamiltonian

G.1 1-hole 2-ion Problem

The idea is to extract pair-wise interaction elements from the two impurity problem to put into a more general calculation that includes many impurities and then treat that problem in a mean field calculation.

We assume that we have two impurities separated by a distance z_0. We take the quantization axis, z, to be along the line joining the two impurities. In this case we have the Hamiltonian

$$H_0 = \frac{\gamma}{2m}\Big(p^2 - \mu \sum_{\alpha,\beta} J_{\alpha\beta} p_{\alpha\beta}\Big) + V_1(r) + V_2(r) \ , \tag{G.1}$$

where

$$V_i(r) = -\frac{e^2}{\epsilon\ |\vec{r} - \vec{r}_i|} + V_{cc}(|\vec{r} - \vec{r}_i|), \tag{G.2}$$

with $\vec{r}_1$ and $\vec{r}_2$ the locations of the two impurities. Here ϵ is the dielectric constant of the host ($\epsilon \approx 10$ for GaAs). We solve the problem in the subspace of $F = 3/2$ states centered on each impurity. The F_z subspaces decouple because of the azimuthal angular integration and can therefore be diagonalized separately:

$$S_{3/2} = \begin{array}{c c} & \begin{array}{cc} \pm 3/2, 1 & \pm 3/2, 2 \end{array} \\ \begin{array}{c} \pm 3/2, 1 \\ \pm 3/2, 2 \end{array} & \left(\begin{array}{cc} 1 & a \\ a & 1 \end{array} \right) \end{array}, \tag{G.3}$$

$$H_{3/2} = \begin{array}{c c} & \begin{array}{cc} \pm 3/2, 1 & \pm 3/2, 2 \end{array} \\ \begin{array}{c} \pm 3/2, 1 \\ \pm 3/2, 2 \end{array} & \left(\begin{array}{cc} E_{gnd} + e_1 & e_3 + aE_{gnd} \\ e_3 + aE_{gnd} & E_{gnd} + e_1 \end{array} \right) \end{array}, \tag{G.4}$$

for the $F_z = \pm 3/2$ subspace and

$$S_{1/2} = \begin{array}{c c} & \begin{array}{cc} \pm 1/2, 1 & \pm 1/2, 2 \end{array} \\ \begin{array}{c} \pm 1/2, 1 \\ \pm 1/2, 2 \end{array} & \left(\begin{array}{cc} 1 & b \\ b & 1 \end{array} \right) \end{array}, \tag{G.5}$$

$$H_{1/2} = \begin{array}{c c} & \begin{array}{cc} \pm 1/2, 1 & \pm 1/2, 2 \end{array} \\ \begin{array}{c} \pm 1/2, 1 \\ \pm 1/2, 2 \end{array} & \left(\begin{array}{cc} E_{gnd} + e_2 & e_4 + bE_{gnd} \\ e_4 + bE_{gnd} & E_{gnd} + e_2 \end{array} \right) \end{array}, \tag{G.6}$$

for the $F_z = \pm 1/2$ subspace. The parameters are the overlaps between the two holes at site 1 and site 2: $a = {}_{\pm 3/2}\langle 1|2\rangle_{\pm 3/2} = {}_{\pm 3/2}\langle 2|1\rangle_{\pm 3/2}$, $b = {}_{\pm 1/2}\langle 1|2\rangle_{\pm 1/2} = {}_{\pm 1/2}\langle 2|1\rangle_{\pm 1/2}$, $e_1 = {}_{\pm 3/2}\langle 1|V_2|1\rangle_{\pm 3/2} = {}_{\pm 3/2}\langle 2|V_1|2\rangle_{\pm 3/2}$, $e_2 = {}_{\pm 1/2}\langle 1|V_2|1\rangle_{\pm 1/2} = {}_{\pm 1/2}\langle 2|V_1|2\rangle_{\pm 1/2}$, $e_3 = {}_{\pm 3/2}\langle 1|V_2|2\rangle_{\pm 3/2} = {}_{\pm 3/2}\langle 1|V_1|2\rangle_{\pm 3/2} = {}_{\pm 3/2}\langle 2|V_1|1\rangle_{\pm 3/2} = {}_{\pm 3/2}\langle 2|V_2|1\rangle_{\pm 3/2}$, and $e_4 = {}_{\pm 1/2}\langle 1|V_2|2\rangle_{\pm 1/2} = {}_{\pm 1/2}\langle 1|V_1|2\rangle_{\pm 1/2} = {}_{\pm 1/2}\langle 2|V_1|1\rangle_{\pm 1/2} = {}_{\pm 1/2}\langle 2|V_2|1\rangle_{\pm 1/2}$. The explicit formulas for these quantities are given below. E_{gnd} is the ground state energy of the single bound hole as determined in Appendix E. Using Eq. E.5, expanding the angular parts in spherical harmonics and then rewriting the expressions in cylindrical coordinates, we have $r^2 = \rho^2 + z^2$, with ρ the radial coordinate. To simplify our expressions, we introduce the notation $f_0 = f_0(r)$ (same for g_0), $f_0(z_0) = f_0(\sqrt{\rho^2 + (z - z_0)^2})$ (same for g_0) and $r(z_0) = \sqrt{\rho^2 + (z - z_0)^2}$. Here z_0 is the distance between the two impurities and $V_1(z_0) = V_1(\sqrt{\rho^2 + (z - z_0)^2})$ is given by Eq. G.2.

$$a = 2\pi \int_0^\infty \rho d\rho \int_{-\infty}^{\infty} dz \Bigg[\frac{1}{4\pi} \left(f_0 + \frac{g_0}{2} \left(3\frac{z^2}{r^2} - 1 \right) \right) \left(f_0(z_0) + \frac{g_0(z_0)}{2} \left(3\frac{(z - z_0)^2}{r(z_0)^2} - 1 \right) \right) + \frac{3}{4\pi} g_0 g_0(z_0) \frac{\rho^2}{r^2 r(z_0)^2} \left(z(z - z_0) + \frac{1}{4}\rho^2 \right) \Bigg]$$

$$b = 2\pi \int_0^\infty \rho d\rho \int_{-\infty}^{\infty} dz \Bigg[\frac{1}{4\pi} \left(f_0 - \frac{g_0}{2} \left(3\frac{z^2}{r^2} - 1 \right) \right) \left(f_0(z_0) - \frac{g_0(z_0)}{2} \left(3\frac{(z - z_0)^2}{r(z_0)^2} - 1 \right) \right) + \frac{3}{4\pi} g_0 g_0(z_0) \frac{\rho^2}{r^2 r(z_0)^2} \left(z(z - z_0) + \frac{1}{4}\rho^2 \right) \Bigg]$$

$$e_1 = 2\pi \int_0^\infty \rho d\rho \int_{-\infty}^{\infty} dz V_1(z_0) \left[\frac{1}{4\pi} \left(f_0 + \frac{g_0}{2} \left(3\frac{z^2}{r^2} - 1 \right) \right)^2 + \frac{3}{4\pi} g_0^2 \frac{\rho^2}{r^4} \left(z^2 + \frac{1}{4}\rho^2 \right) \right]$$

$$e_2 = 2\pi \int_0^\infty \rho d\rho \int_{-\infty}^{\infty} dz V_1(z_0) \left[\frac{1}{4\pi} \left(f_0 - \frac{g_0}{2} \left(3\frac{z^2}{r^2} - 1 \right) \right)^2 + \frac{3}{4\pi} g_0^2 \frac{\rho^2}{r^4} \left(z^2 + \frac{1}{4}\rho^2 \right) \right]$$

$$e_3 = 2\pi \int_0^\infty \rho d\rho \int_{-\infty}^{\infty} dz V_1(z_0) \Bigg[\frac{1}{4\pi} \left(f_0 + \frac{g_0}{2} \left(3\frac{z^2}{r^2} - 1 \right) \right) \left(f_0(z_0) + \frac{g_0(z_0)}{2} \left(3\frac{(z - z_0)^2}{r(z_0)^2} - 1 \right) \right)$$

$$+\frac{3}{4\pi} g_0 g_0(z_0) \frac{\rho^2}{r^2 r(z_0)^2}\left(z(z-z_0)+\frac{1}{4}\rho^2\right)\Bigg]$$

$$e_4 = 2\pi \int_0^\infty \rho d\rho \int_{-\infty}^{\infty} dz V_1(z_0)\Bigg[\frac{1}{4\pi}\left(f_0 - \frac{g_0}{2}\left(3\frac{z^2}{r^2}-1\right)\right)\left(f_0(z_0) - \frac{g_0(z_0)}{2}\left(3\frac{(z-z_0)^2}{r(z_0)^2}-1\right)\right)$$
$$+\frac{3}{4\pi} g_0 g_0(z_0) \frac{\rho^2}{r^2 r(z_0)^2}\left(z(z-z_0)+\frac{1}{4}\rho^2\right)\Bigg] .$$

It should be kept in mind that a, b, and the four e_i all depend on the spin-orbit strength μ and separation distance z_0. We can solve the above problem as a function of distance by diagonalizing the Hamiltonian to find the eigenstates and the corresponding eigenenergies. We use these results to find the values of the parameters in the effective Hamiltonian below.

The effective Hamiltonian we consider for the 1-hole 2-ion problem is

$$\begin{aligned} H^{\text{eff}} &= t_{3/2}\left(c^\dagger_{3/2,1} c_{3/2,1} + c^\dagger_{-3/2,1} c_{-3/2,1}\right) + h.c. \\ &+ t_{1/2}\left(c^\dagger_{1/2,1} c_{1/2,1} + c^\dagger_{-1/2,1} c_{-1/2,1}\right) + h.c. \\ &+ k((F_z)^2 - 5/4)\sum_{F_z,i} n_{F_z,i} \\ &+ E\sum_{F_z,i} n_{F_z,i}. \end{aligned} \tag{G.7}$$

Using the same matrix conventions as before we have

$$H_{3/2} = \begin{array}{c c} & \begin{array}{cc} \pm3/2,1 & \pm3/2,2 \end{array} \\ \begin{array}{c} \pm3/2,1 \\ \pm3/2,2 \end{array} & \begin{pmatrix} E+k & t_{3/2} \\ t_3/2 & E+k \end{pmatrix} \end{array}, \tag{G.8}$$

for the $F_z = \pm 3/2$ subspace and

$$H_{1/2} = \begin{array}{c c} & \begin{array}{cc} \pm 1/2, 1 & \pm 1/2, 2 \end{array} \\ \begin{array}{c} \pm 1/2, 1 \\ \pm 1/2, 2 \end{array} & \left(\begin{array}{cc} E - k & t_{1/2} \\ t_{1/2} & E - k \end{array} \right) \end{array}, \tag{G.9}$$

for the $F_z = \pm 1/2$ subspace. By comparing the states and eigenvalues of H^{eff} to the real problem H, we can relate the parameters of the original model to those of the effective model. Equating the eigenvalues for the two systems for corresponding states gives

$$t_{3/2} = \frac{a e_1 - e_3}{a^2 - 1} \tag{G.10}$$

$$t_{1/2} = \frac{b e_2 - e_4}{b^2 - 1} \tag{G.11}$$

$$k = \frac{e_1 - b^2 e_1 + (a^2 - 1) e_2 - a e_3 + a b^2 e_3 + b e_4 - a^2 b e_4}{a(a^2 - 1)(b^2 - 1)} \tag{G.12}$$

$$E = E_{gnd} + \frac{1}{4}\left(\frac{e_3 - e_1}{a - 1} + \frac{e_3 + e_1}{a + 1} + \frac{e_4 - e_2}{b - 1} + \frac{e_4 + e_2}{b + 1} \right). \tag{G.13}$$

This completes the derivation of the effective Hamiltoninian for the two impurity problem. The effective parameters are plotted in Fig. G.1.

G.2 General Case

In the more general case, with three or more impurities, we need to know how to generalize the above Hamiltonian to the situation where the impurities do not

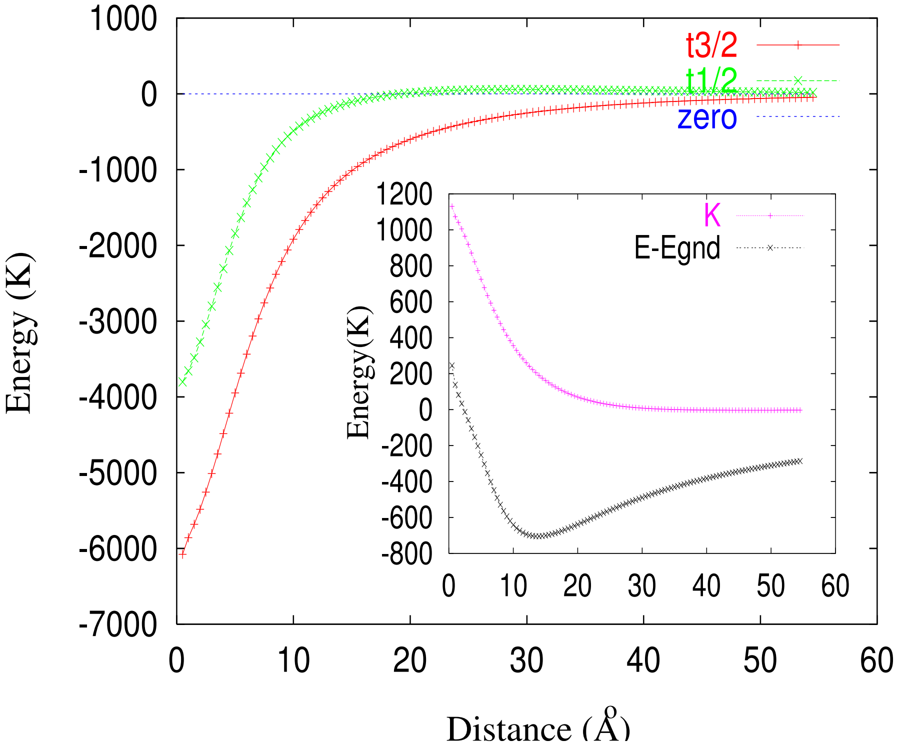

Figure G.1: The positional dependence of the Effective Hamiltonian parameters for Mn in GaAs. See also Fig. 7.2.

lie along the z-axis. When the impurities lie along the z-axis the hopping matrix is

$$\hat{t} = \begin{pmatrix} t_{3/2} & 0 & 0 & 0 \\ 0 & t_{1/2} & 0 & 0 \\ 0 & 0 & t_{1/2} & 0 \\ 0 & 0 & 0 & t_{3/2} \end{pmatrix} . \tag{G.14}$$

For hopping between 2 sites $|\alpha\rangle$ and $|\beta\rangle$ we should have

$$\sum_{\mathrm{allF_z}} \langle\alpha|\hat{t}|\beta\rangle = \sum_{\mathrm{allF_z}} \langle\alpha'|\hat{t}|\beta'\rangle \; , \tag{G.15}$$

where $|\alpha'\rangle$ and $|\beta'\rangle$ are the same distance from each other as $|\alpha\rangle$ and $|\beta\rangle$ but do not lie along the z-axis. It is an identity that $\langle\alpha|\hat{t}|\beta\rangle = \langle\alpha|U^\dagger(U\hat{t}U^\dagger)U|\beta\rangle$ where

$U = e^{-i\hat{F}_z\phi}e^{-i\hat{F}_y\theta}$. We can think of $|\beta'\rangle = U|\beta\rangle$, so that the $\tilde{\hat{t}} = U\hat{t}U^\dagger$. Inserting a complete set of states (z-basis) every where,

$$\tilde{\hat{t}} = \sum_{M',M,m'm} |M'\rangle\langle M'|e^{-i\hat{F}_y\theta}|m'\rangle e^{-iM'\phi}t_{m'm}e^{iM\phi}\langle m|e^{i\hat{F}_y\theta}|M\rangle\langle M| \, , \tag{G.16}$$

which means we must evaluate $\langle m|e^{i\hat{F}_y\theta}|M\rangle$. This can be done by expressing $J_y = (J_+ - J_-)/2i$ and then exponentiating. Performing the the matrix multiplications, this finally yields a Hermitian matrix with elements

$$\begin{aligned}
\tilde{t}_{11} &= \frac{1}{8}(3t_{1/2} + 5t_{3/2} - 3(t_{1/2} - t_{3/2})\cos(2\theta)) \\
\tilde{t}_{12} &= -\frac{\sqrt{3}}{4}e^{-i\phi}(t_{1/2} - t_{3/2})\sin(2\theta) \\
\tilde{t}_{13} &= -\frac{\sqrt{3}}{4}e^{-2i\phi}(t_{1/2} - t_{3/2})\sin^2(\theta) \\
\tilde{t}_{14} &= 0 \\
\tilde{t}_{22} &= \frac{1}{8}(5t_{1/2} + 3t_{3/2} + 3(t_{1/2} - t_{3/2})\cos(2\theta)) \\
\tilde{t}_{23} &= 0 \\
\tilde{t}_{24} &= \tilde{t}_{13} \\
\tilde{t}_{33} &= \tilde{t}_{22} \\
\tilde{t}_{34} &= -\tilde{t}_{12} \\
\tilde{t}_{44} &= \tilde{t}_{11} \, .
\end{aligned}$$

When there are two sites not along the z-axis the spin-splitting term generalizes to $k((\vec{n}_{ij} \cdot \vec{F})^2 - 5/4)$, where n_{ij} is a unit vector pointing along the axis joining the two impurities. In the diagonal basis we have

$$k(F_z^2-5/4)=\begin{pmatrix} k & 0 & 0 & 0 \\ 0 & -k & 0 & 0 \\ 0 & 0 & -k & 0 \\ 0 & 0 & 0 & k \end{pmatrix}. \tag{G.17}$$

Expanding $(\vec{n}_{ij}\cdot\vec{F})^2=(n_xF_x+n_yF_y+n_zF_z)^2$ with $n_x=\cos(\phi)\sin(\theta)$, $n_y=\sin(\phi)\sin(\theta)$ and $n_z=\cos(\theta)$, and expressing the F_x and F_y in terms of the raising and lowering operators gives for a general direction, we obtain the following matrix elements for the general case,

$$\begin{aligned}
k((\vec{n}_{ij}\cdot\vec{F})^2-5/4)_{11} &= \frac{1}{4}k(1+3\cos(2\theta)) \\
k((\vec{n}_{ij}\cdot\vec{F})^2-5/4)_{12} &= \sqrt{3}e^{-i\phi}k\cos(\theta)\sin(\theta) \\
k((\vec{n}_{ij}\cdot\vec{F})^2-5/4)_{13} &= \frac{\sqrt{3}}{2}e^{-2i\phi}k\sin^2(\theta) \\
k((\vec{n}_{ij}\cdot\vec{F})^2-5/4)_{14} &= 0 \\
k((\vec{n}_{ij}\cdot\vec{F})^2-5/4)_{22} &= -\frac{1}{4}k(1+3\cos(2\theta)) \\
k((\vec{n}_{ij}\cdot\vec{F})^2-5/4)_{23} &= 0 \\
k((\vec{n}_{ij}\cdot\vec{F})^2-5/4)_{24} &= k((\vec{n}_{ij}\cdot\vec{F})^2-5/4)_{13} \\
k((\vec{n}_{ij}\cdot\vec{F})^2-5/4)_{33} &= k((\vec{n}_{ij}\cdot\vec{F})^2-5/4)_{22} \\
k((\vec{n}_{ij}\cdot\vec{F})^2-5/4)_{34} &= -k((\vec{n}_{ij}\cdot\vec{F})^2-5/4)_{12} \\
k((\vec{n}_{ij}\cdot\vec{F})^2-5/4)_{44} &= k((\vec{n}_{ij}\cdot\vec{F})^2-5/4)_{11}\ .
\end{aligned}$$

Appendix H

Determination of hole-hole Interaction Strength

H.1 Derivation of on site interaction Hamiltonian

Here we only consider the on-site interaction of two holes. In second quantized form the interaction between two holes looks like

$$\hat{H}_{\mathrm{on-site}} = \frac{1}{2} \sum_{f_1,f_2,f_3,f_4} U_{f_1,f_2,f_3,f_4} c^{\dagger}_{f_1} c^{\dagger}_{f_2} c_{f_3} c_{f_4} \ , \tag{H.1}$$

where

$$U_{f_1,f_2;f_4,f_3} \equiv U_{f_1,f_2,f_3,f_4} = \langle f_1; f_2 | \hat{U}_{\mathrm{Coulomb}} | f_4; f_3 \rangle \ , \tag{H.2}$$

and where we have again restricted ourselves to the same $F = 3/2$ subspace. Thus, the f_i man take on the values ±3/2 and ±1/2. To evaluate the matrix element $U_{f_1,f_2;f_4,f_3}$ we insert unity in the form of of an integral over position and a sum over the values of J_z,

$$\sum_{\mu} \int d^3\vec{r}\, |\vec{r},\mu\rangle\langle\vec{r},\mu| = 1 \ , \tag{H.3}$$

so that

$$U_{f_1,f_2;f_4,f_3} = \sum_{\mu,\nu} \int d^3\vec{r} \int d^3\vec{r}'\, \phi^*_{\mu,f_1}(\vec{r})\phi_{\mu,f_4}(\vec{r}) \frac{e^2}{\epsilon|\vec{r}-\vec{r}'|} \phi^*_{\nu,f_2}(\vec{r}')\phi_{\nu,f_3}(\vec{r}') \ , \tag{H.4}$$

where we have already calculated the $\phi_{\mu,f_i}(\vec{r})$ with the variational calculation outlined in Appendix E and Appendix F. See Eq. (E.5) and Eqs. (F.3-F.5) for an illustration of how the angular dependence of $\phi_{\mu,f_i}(\vec{r})$ is obtained. A simple projection of $\langle J = 3/2, J_z = 1/2|$ into Eq. (F.5) picks out $\phi_{1/2,3/2}(\vec{r}) = -g_0(r)\sqrt{\frac{2}{5}}Y_{21}(\theta,\phi)$, for example.

Because of symmetry, Eq. (H.1) simplifies to $F = 0$ and $F = 2$ irreducible representations. One can verify by direct evaluation that the operator

$$\hat{D}_2 = c^\dagger_{1/2}c^\dagger_{3/2} \tag{H.5}$$

produces the state $|F = 2, F_z = 2\rangle$ when acting on the vacuum. The $F = 2$ states of lower F_z can then be produced by applying the lowering operator. They are

$$\hat{D}_1 = c^\dagger_{-1/2}c^\dagger_{3/2} \tag{H.6}$$

$$\hat{D}_0 = \frac{1}{\sqrt{2}}(c^\dagger_{-3/2}c^\dagger_{3/2} + c^\dagger_{-1/2}c^\dagger_{1/2}) \tag{H.7}$$

$$\hat{D}_{-1} = c^\dagger_{-3/2}c^\dagger_{1/2} \tag{H.8}$$

$$\hat{D}_{-2} = c^\dagger_{-3/2}c^\dagger_{-1/2} \ , \tag{H.9}$$

and likewise for the sole $F = 0$ operator,

$$\hat{S}_0 = \frac{1}{\sqrt{2}}(c^\dagger_{-1/2}c^\dagger_{1/2} - c^\dagger_{-3/2}c^\dagger_{3/2}) \ , \tag{H.10}$$

so the the Hamiltonian may be written in the form

$$\hat{H}_{\text{on-site}} = \frac{1}{2}U_D \sum_m \hat{D}_m \hat{D}_m^\dagger + \frac{1}{2}U_S \hat{S}_0 \hat{S}_0^\dagger \, . \tag{H.11}$$

One can then write projection operators (with indicies suppressed) as

$$\hat{P}_D = c^\dagger c^\dagger c c \frac{\vec{F}^2}{6} \, , \tag{H.12}$$

and

$$\hat{P}_S = c^\dagger c^\dagger c c \left(1 - \frac{\vec{F}^2}{6}\right) \, , \tag{H.13}$$

where $\vec{F} = \vec{F}_1 + \vec{F}_2$ is the total $\vec{F}$ of the two holes, so that

$$\frac{\vec{F}^2}{6} = \frac{5}{4} + \frac{\vec{F}_1 \cdot \vec{F}_2}{3} \, . \tag{H.14}$$

Hence, for any specified set of indicies

$$U_D \hat{P}_D + U_S \hat{P}_S = \left(\frac{5U_D - U_S}{4} + \frac{U_D - U_S}{3} \vec{F}_1 \cdot \vec{F}_2\right) c^\dagger c^\dagger c c \, , \tag{H.15}$$

where we can define

$$U_N \equiv \frac{5U_D - U_S}{4} \, , \tag{H.16}$$

and

$$U_F \equiv \frac{U_D - U_S}{3} \, , \tag{H.17}$$

to give a Hamiltonian of the form

$$\hat{H}_{\text{int}} = \frac{U_N}{2} \sum_i : \hat{N}_i : + \frac{U_F}{2} \sum_i : \vec{F}_i^{\,2} : \, , \tag{H.18}$$

where :...: denotes normal ordering and i is the site index. We have

$$\hat{N}_i = \sum_f c_{i,f}^\dagger c_{i,f} \, , \tag{H.19}$$

and

$$\hat{\vec{F}}_i = \sum_{f,f'} c^{\dagger}_{i,f} \vec{F}_{f,f'} c_{i,f'} \ . \tag{H.20}$$

By comparing the matrix elements of Eq. (H.11) to the matrix elements of Eq. (H.1), we can evaluate the U_D and U_S interms of the U_{f_1,f_2,f_3,f_4} which in turn allow us to evaluate the U_N and U_F of Eq. (H.18). Carrying out the evaluation, one obtains

$$U_D = 2\left(U_{3/2,1/2;3/2,1/2} - U_{3/2,1/2;1/2,3/2}\right) \tag{H.21}$$

$$U_S = 4\left(U_{1/2,-1/2;1/2,-1/2} - U_{1/2,-1/2;-1/2,1/2}\right) - U_D \ , \tag{H.22}$$

and therefore,

$$U_N = 3U_{3/2,1/2;3/2,1/2} - 3U_{3/2,1/2;1/2,3/2} - U_{1/2,-1/2;1/2,-1/2} + U_{1/2,-1/2;-1/2,1/2} \tag{H.23}$$

$$U_F = \frac{4}{3}\left(U_{3/2,1/2;3/2,1/2} - U_{3/2,1/2;1/2,3/2} - U_{1/2,-1/2;1/2,-1/2} + U_{1/2,-1/2;-1/2,1/2}\right) \ . \tag{H.24}$$

H.2 Evaluation of U_N and U_F

To obtain a numerical value of U_N and U_F we must determine the values $U_{3/2,1/2;3/2,1/2}$, $U_{3/2,1/2;1/2,3/2}$, $U_{1/2,-1/2;1/2,-1/2}$ and $U_{1/2,-1/2;-1/2,1/2}$ by evaluating the integrals in Eq. (H.4). These integrals depend on the radial wavefunctions that we evaluated variationally in Appendix E and are material specific. In order to evaluate the integrals in Eq. (H.4) the $\phi_{\mu,f_i}(\vec{r})$ must be decomposed into spherical harmonics. Various products of sperical harmonics will result in the integrand. The integrals are then hopeless to evaluate unless one makes use of the very important formula

$$\frac{1}{|\vec{r} - \vec{r}'|} = \frac{4\pi}{r_>} \sum_{l=0}^{\infty} \sum_{m=-l}^{l} \left(\frac{r_<}{r_>}\right)^l \frac{(-1)^m}{2l+1} Y_{lm}(\Omega) Y_{lm}(\Omega') \ , \tag{H.25}$$

where Ω (Ω') is the angle of $\vec{r}$ ($\vec{r}'$). With this formula, almost all of the integrals are zero. The few remaining integrals yield

$$U_{3/2,1/2;3/2,1/2} = \frac{e^2}{\epsilon a_{\text{eff}}} \int_0^\infty r^2 dr \int_0^\infty r'^2 dr' \frac{1}{r_>} \Big[(f_0(r)^2 + g_0(r)^2)(f_0(r')^2 + g_0(r')^2) - \frac{4}{25} \left(\frac{r_<}{r_>} \right)^2 f_0(r) g_0(r) f_0(r') g_0(r') \Big] \tag{H.26}$$

$$U_{3/2,1/2;1/2,3/2} = \frac{e^2}{\epsilon a_{\text{eff}}} \int_0^\infty r^2 dr \int_0^\infty r'^2 dr' \frac{8}{25} \frac{1}{r_>} \left(\frac{r_<}{r_>} \right)^2 f_0(r) g_0(r) f_0(r') g_0(r') \tag{H.27}$$

$$U_{1/2,-1/2;1/2,-1/2} = \frac{e^2}{\epsilon a_{\text{eff}}} \int_0^\infty r^2 dr \int_0^\infty r'^2 dr' \frac{1}{r_>} \Big[(f_0(r)^2 + g_0(r)^2)(f_0(r')^2 + g_0(r')^2) + \frac{4}{25} \left(\frac{r_<}{r_>} \right)^2 f_0(r) g_0(r) f_0(r') g_0(r') \Big] \tag{H.28}$$

$$U_{1/2,-1/2;-1/2,1/2} = 0 \ , \tag{H.29}$$

where

$$\frac{e^2}{\epsilon a_{\text{eff}}} = 31.6\text{meV} \ . \tag{H.30}$$

Inspection of the equations above reveals that only two integrals need to be evaluted numerically. When these integrals are evaluated, we obtain

$$U_N = 2570K \ , \tag{H.31}$$

and

$$U_F = -51K \ . \tag{H.32}$$

Appendix I

Evaluation of Singular RKKY Integrals for Spin 3/2 Particles

We establish the identity

$$\int_0^1 dk \int_1^\infty dq \frac{qk}{q^2-k^2} F(k)F(q) = \frac{\pi}{2} i \int_0^1 dkk \biggl[F^+(k)^2 - F^-(k)^2 \\ + F(k) \mathrm{lim}_{\mathrm{q}\to 0} \left\{ \frac{2q^2}{q^2-k^2} F^+(q) \right\} \biggr] \ . \tag{I.1}$$

We note that the functions $F(k)$ that appear in the evaluation of the RKKY kernal, Eq. (8.11), have two important properties that we will use in the derivation of Eq. (I.1): (i) $F(-k) = -F(k)$ and (ii) the *most singular* behavior of F as $k \to 0$ is $F(k) \sim k^{-2}$.

To do this we first prove that

$$I = \mathrm{lim}_{\delta\to 0} \int_{-1+i\delta}^{1+i\delta} dz \int_{-1}^{1} dq \frac{qz}{q^2-z^2} F(z)F(q) = 0 \ , \tag{I.2}$$

where δ is a positive infinitesimal quantity. Decomposing the integrand gives $\frac{q}{q^2-z^2} =$

$\frac{1}{2}\left(\frac{1}{q-z}+\frac{1}{q+z}\right)$. Let x be defined by $z = x + i\delta$. Then the integral can be rewritten as

$$\begin{aligned} I &= \int_{-1}^{1} dx \int_{-1}^{1} dq \frac{1}{2}\left[P\frac{1}{q-x} + P\frac{1}{q+x} + i\pi\delta(q-x) - i\pi\delta(q+x)\right] xF(x)F(q) \; , \\ &= \int_{-1}^{1} dx \int_{-1}^{1} dq \left[P\frac{q}{q^2-x^2} + i\frac{\pi}{2}\delta(q-x) - i\frac{\pi}{2}\delta(q+x)\right] xF(x)F(q) \; , \end{aligned}$$

where P denotes the principal part of the integral. The principal value integral over the first term is zero by symmetry. This can be see by making the change of variable $x \rightarrow q$ and $q \rightarrow x$ and noting that this part of the integrand changes sign. Next we look at the last two terms with delta functions. The integral over these terms evaluates to $i\frac{\pi}{2}(qF(q)F(q) - (-q)F(-q)F(q)) = 0$ since $F(-q) = -F(q)$. Thus, we have shown Eq. (I.2), $I = 0$.

We now return to the formula, Eq. (I.1). Using the fact that the integrand is even in both k and q and the result, Eq. (I.2) we can extend the region of integration to obtain

$$\int_0^1 dk \int_1^\infty dq \frac{qk}{q^2-k^2} F(k)F(q) = \lim_{\delta\rightarrow 0}\frac{1}{4}\int_{C_1} dz \int_{-\infty}^{\infty} dq zF(z)\frac{1}{2}\left(\frac{1}{q-z}+\frac{1}{q+z}\right)F(q) \; . \tag{I.3}$$

We now turn our attention to the integral

$$R = \int_{-\infty}^{\infty} dq \left(\frac{1}{q-k}+\frac{1}{q+k}\right)F(q) \; , \tag{I.4}$$

where we now extend the region of integration into the complex plain as shown in Fig. I.1. The function F is complexified: $F(q) = F^+(q) + F^-(q)$ where $F^+(q)$ $(F^+(q))$ is analytic in the upper (lower) half plane with the possible exception of the origin. For example, from Eq. (8.18), we have $F(q) = \frac{\sin(kr)}{r} = \frac{e^{ikr}}{2ir} - \frac{e^{-ikr}}{2ir}$. $G(q)$ from Eq. (8.18) would be decomposed in the same way term by term. The integral, R,

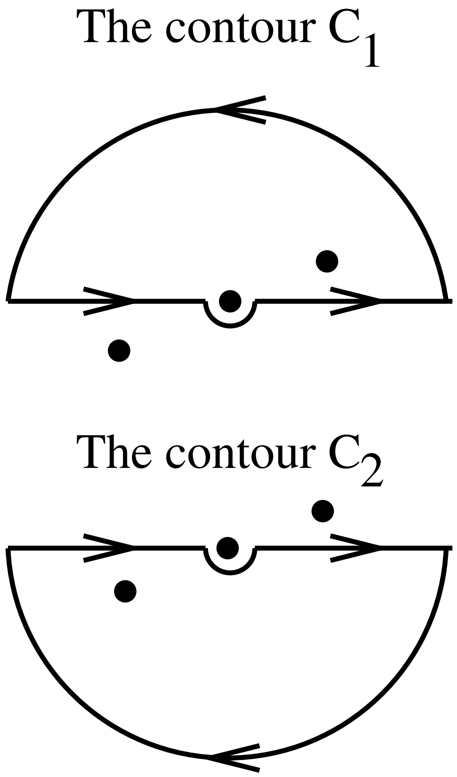

The contour C_1

The contour C_2

Figure I.1: The contours used in the evaluation of Eq. (I.5).

then becomes

$$R = \int_{C_1} \left(\frac{1}{q-k} + \frac{1}{q+k} \right) F(q)^+ + \int_{C_2} \left(\frac{1}{q-k} + \frac{1}{q+k} \right) F(q)^- \, , \qquad \text{(I.5)}$$

where the contours C_1 and C_2 are shown in Fig. I.1. Evaluation of the first integral gives $2\pi i \left[F^+(k) + \mathrm{Res}_{\mathrm{q}\to 0} \left\{ \frac{2q^2}{q^2-k^2} F^+(q) \right\} \right]$ and evaluation of the second integral gives $2\pi i(-1)F^-(-k)$. Using the fact that $(-1)F^-(-k) = F(k)^+$ we have the final result that

$$R = 2\pi i \left[2F^+(k) + \mathrm{Res}_{\mathrm{q}\to 0} \left\{ \frac{2q}{q^2-k^2} F^+(q) \right\} \right] \, . \qquad \text{(I.6)}$$

Since the worst singularity is $F \sim k^{-2}$ the residue term of Eq. (I.6) is either zero or just a constant in the most singular cases. For this special case,

$$\mathrm{Res}_{\mathrm{q}\to 0}\left\{\frac{2q}{q^2-k^2}F^+(q)\right\} = \lim_{\mathrm{q}\to 0}\left\{\frac{2q^2}{q^2-k^2}F^+(q)\right\} \ , \tag{I.7}$$

which is a convenient calculational tool. Thus,

$$\int_0^1 dk \int_1^\infty dq \frac{qk}{q^2-k^2}F(k)F(q) = \frac{1}{8}\int_{-1}^1 dkkF(k)2\pi i\left[2F^+(k) + \lim_{\mathrm{q}\to 0}\left\{\frac{2q^2}{q^2-k^2}F^+(q)\right\}\right] \ . \tag{I.8}$$

In the first term we can make the replacement under the integral $F^+(k) = \frac{1}{2}\left(F^+(k) + F^+(k-)\right]$ since $kF(k)$ is even. Recalling that $F(q) = F^+(q) + F^-(q)$ and $F^+(-k) = -F^-(k)$,

$$\begin{aligned}
&\int_0^1 dk \int_1^\infty \ dq \frac{qk}{q^2-k^2}F(k)F(q) \\
&\quad = \ \frac{1}{8}\int_{-1}^1 dkk2\pi i\left[F^+(k)^2 - F^-(k)^2 + F(k)\lim_{\mathrm{q}\to 0}\left\{\frac{2q^2}{q^2-k^2}F^+(q)\right\}\right] \\
&\quad = \ \frac{\pi}{2}i\int_0^1 dkk\left[F^+(k)^2 - F^-(k)^2 + F(k)\lim_{\mathrm{q}\to 0}\left\{\frac{2q^2}{q^2-k^2}F^+(q)\right\}\right] \ ,
\end{aligned} \tag{I.9}$$

which is just the indentity we wanted to establish.

Appendix J

Exact Expressions for the RKKY Kernel with SO Coupling

We give here the exact expressions for the RKKY kernel, Eq. (8.11). The z-component of the heavy hole contribution was already given in Eq. (8.22). Here we again use the notation $a = k_{F,h}R$ and $b = k_{F,l}R$.

$$\begin{aligned} K^{xx}_{h,h}(\mathbf{R}) = K^{yy}_{h,h}(\mathbf{R}) = 4\pi\,\epsilon_F g_h^2 \int_0^1 dk \frac{9}{2}\Bigg[& -\frac{\cos(ka)}{a^5k^2} - \frac{\cos(2ka)}{a^3} + \frac{\cos(2ka)}{a^5k^2} \\ & + \frac{\sin(ka)}{a^6k^3} - \frac{\sin(ka)}{a^4k} - \frac{\sin(2ka)}{2a^6k^3} + \frac{3\sin(2ka)}{2a^4k}\Bigg]\,. \end{aligned} \tag{J.1}$$

$$\begin{aligned} K^{zz}_{h,l}(\mathbf{R}) + K^{zz}_{l,h}(\mathbf{R}) \;=\; & 4\pi\,\epsilon_F g_h g_l \int_0^1 dk \Bigg[\frac{3}{2}\Bigg(-\frac{\cos(ka)\cos(kb)}{a^2b} + \frac{\cos(ka)\sin(ka)}{a^6k^3} \\ & + \frac{\cos(ka)\sin(ka)}{a^4k} + \frac{\cos(kb)\sin(ka)}{a^3bk} - \frac{\sin(2ka)}{2a^6k^3} - \frac{\sin(2ka)}{2a^4k} \\ & - \frac{\sin(kb)}{a^3bk} + \frac{\cos(ka)\sin(kb)}{a^3bk} + \frac{\sin(ka)\sin(kb)}{a^2b}\Bigg) \end{aligned}$$

$$\begin{aligned}
&+\frac{45}{2}\bigg(-\frac{\cos(ka)}{a^2b^3k^2}-\frac{\cos(kb)}{a^3b^2k^2}+\frac{\cos(ka)\cos(kb)}{a^2b^3k^2}+\frac{\cos(ka)\cos(kb)}{a^3b^2k^2}\\
&+\frac{\sin(ka)}{a^3b^3k^3}-\frac{\cos(kb)\sin(ka)}{a^3b^3k^3}+\frac{\cos(kb)\sin(ka)}{a^2b^2k}+\frac{\sin(kb)}{a^3b^3k^3}\\
&-\frac{\cos(ka)\sin(kb)}{a^3b^3k^3}+\frac{\cos(ka)\sin(kb)}{a^2b^2k}-\frac{\sin(ka)\sin(kb)}{a^2b^3k^2}-\frac{\sin(ka)\sin(kb)}{a^3b^2k^2}\bigg)\\
&+\frac{27}{2}\bigg(-\frac{\cos(ka)\cos(kb)}{ab^2}-\frac{\sin(ka)}{ab^3k}+\frac{\cos(kb)\sin(ka)}{ab^3k}+\frac{\cos(ka)\sin(kb)}{ab^3k}\\
&+\frac{\cos(kb)\sin(kb)}{b^6k^3}+\frac{\cos(kb)\sin(kb)}{b^4k}+\frac{\sin(ka)\sin(kb)}{ab^2}\\
&-\frac{\sin(2kb)}{2b^6k^3}-\frac{\sin(2kb)}{2b^4k}\bigg)\bigg]\,.
\end{aligned}\tag{J.2}$$

$$\begin{aligned}
K^{xx}_{h,l}(\mathbf{R})+K^{xx}_{l,h}(\mathbf{R}) &= K^{yy}_{h,l}(\mathbf{R})+K^{yy}_{l,h}(\mathbf{R})\\
&= 4\pi\,\epsilon_F g_h g_l\int_0^1 dk\bigg[\frac{3}{2}\bigg(-\frac{\cos(ka)\cos(kb)}{a^2b}+\frac{\cos(ka)\sin(ka)}{a^6k^3}\\
&\quad+\frac{\cos(ka)\sin(ka)}{a^4k}+\frac{\cos(kb)\sin(ka)}{a^3bk}-\frac{\sin(2ka)}{2a^6k^3}-\frac{\sin(2ka)}{2a^4k}\\
&\quad-\frac{\sin(kb)}{a^3bk}+\frac{\cos(ka)\sin(kb)}{a^3bk}+\frac{\sin(ka)\sin(kb)}{a^2b}\bigg)\\
&\quad+\frac{9}{2}\bigg(\frac{\cos(ka)}{a^2b^3k^2}+\frac{\cos(kb)}{a^3b^2k^2}+\frac{\cos(ka)\cos(kb)}{ab^2}-\frac{\cos(ka)\cos(kb)}{a^2b^3k^2}\\
&\quad-\frac{\cos(ka)\cos(kb)}{a^3b^2k^2}-\frac{\sin(ka)}{a^3b^3k^3}+\frac{\sin(ka)}{ab^3k}+\frac{\cos(kb)\sin(ka)}{a^3b^3k^3}\\
&\quad-\frac{\cos(kb)\sin(ka)}{ab^3k}-\frac{\cos(kb)\sin(ka)}{a^2b^2k}-\frac{\sin(kb)}{a^3b^3k^3}+\frac{\cos(ka)\sin(kb)}{a^3b^3k^3}\\
&\quad-\frac{\cos(ka)\sin(kb)}{ab^3k}-\frac{\cos(ka)\sin(kb)}{a^2b^2k}-\frac{\cos(kb)\sin(kb)}{b^6k^3}-\frac{\cos(kb)\sin(kb)}{b^4k}\\
&\quad-\frac{\sin(ka)\sin(kb)}{ab^2}+\frac{\sin(ka)\sin(kb)}{a^2b^3k^2}+\frac{\sin(ka)\sin(kb)}{a^3b^2k^2}\\
&\quad+\frac{\sin(2kb)}{2b^6k^3}+\frac{\sin(2kb)}{2b^4k}\bigg)\\
&\quad+3\bigg(\frac{k\cos(ka)\sin(ka)}{a^2}+\frac{k\cos(kb)\sin(ka)}{ab}-\frac{k\sin(2ka)}{2a^2}\\
&\quad+\frac{k\cos(ka)\sin(kb)}{ab}+\frac{k\cos(kb)\sin(kb)}{b^2}-\frac{k\sin(2kb)}{2b^2}\bigg)\bigg]\,.
\end{aligned}\tag{J.3}$$

$$
\begin{aligned}
K^{zz}_{l,l}(\mathbf{R}) &= 4\pi\,\epsilon_F g_l^2 \int_0^1 dk \Bigg[\frac{9\sin(2kb)}{20a^2} + \frac{45}{2}\Bigg(\frac{\cos(kb)}{a^5k^2} + \frac{\cos(2kb)}{15b^3} \\
&\quad - \frac{\cos(2kb)}{b^5k^2} - \frac{\sin(kb)}{b^6k^3} + \frac{\sin(kb)}{15b^4k} \\
&\quad + \frac{\sin(2kb)}{2b^6k^3} - \frac{17\sin(2kb)}{30b^4k} + \frac{k\sin(2kb)}{450b^2}\Bigg)\Bigg]\,. \qquad \text{(J.4)}
\end{aligned}
$$

$$
\begin{aligned}
K^{xx}_{l,l}(\mathbf{R}) &= K^{yy}_{l,l}(\mathbf{R}) \\
&= 4\pi\,\epsilon_F g_l^2 \int_0^1 dk \frac{9}{2}\Bigg[-\frac{\cos(kb)}{b^5k^2} + \frac{\cos(2kb)}{3b^3} + \frac{\cos(2kb)}{b^5k^2} + \frac{\sin(kb)}{b^6k^3} + \frac{\sin(kb)}{3b^4k} \\
&\quad - \frac{\sin(2kb)}{2b^6k^3} + \frac{\sin(2kb)}{6b^4k} + \frac{4k\sin(2kb)}{9b^2}\Bigg]\,. \qquad \text{(J.5)}
\end{aligned}
$$

Bibliography

[1] M. F. Crommie, C. P. Lutz, and D. M. Eigler, Science **262**, 218 (1993).

[2] E. J. Heller, M. F. Crommie, C. P. Lutz, and D. Eigler, Nature **369**, 464 (1994).

[3] H. C. Manoharan, C. P. Lutz, and D. M. Eigler, Nature **403**, 512 (2000).

[4] J. Kliewer, R. Berndt, and S. Crampin, Phys. Rev. Lett. **85**, 4936 (2000).

[5] S. D. Kevan and R. H. Gaylord, Phys. Rev. B **36**, 5809 (1987).

[6] Y. Hasegawa and P. Avouris, Phys. Rev. Lett. **71**, 1071 (1993).

[7] N. Knorr, M. A. Schneider, L. Diekhöner, P. Wahl, and K. Kern, Phys. Rev. Lett. **88**, 096804 (2002).

[8] J. Tersoff and D. R. Hamann, Phys. Rev. B **31**, 805 (1985).

[9] C. Bracher, M. Riza, and M. Klever, Phys. Rev. B **56**, 7704 (1997).

[10] J. Li, W.-D. Schneider, R. Berndt, and B. Delley, Phys. Rev. Lett. **80**, 2893 (1998).

[11] V. Madhavan, W. Chen, T. Jamneala, M. F. Crommie, and N. S. Wingreen, Science **280**, 567 (1998).

[12] G. A. Fiete, J. S. Hersch, E. J. Heller, H. C. Manoharan, C. P. Lutz, and D. M. Eigler, Phys. Rev. Lett. **86**, 2392 (2001).

[13] J. S. Hersch, *Scattering Resonances in the Extreme Quantum Limit*, Ph.D. thesis, Harvard University (1999).

[14] L. S. Rodberg and R. M. Thaler, *Introduction to the Quantum Theory of Scattering* (Academic, New York, 1967).

[15] M. F. Crommie, C. P. Lutz, and D. M. Eigler, Nature **363**, 524 (1993).

[16] S. Crampin and O. R. Bryant, Phys. Rev. B **54**, R17367 (1996).

[17] S. Chan, *Theories and Applications of Multiple Scattering of s-wave Scatterers*, Ph.D. thesis, Harvard University (1997).

[18] S. Crampin, M. H. Boon, and J. I. Inglesfield, Phys. Rev. Lett. **73**, 1015 (1994).

[19] G. Hormandinger and J. B. Pendry, Phys. Rev. B **50**, 18607 (1994).

[20] H. K. Harbury and W. Porod, Phys. Rev. B **53**, 15455 (1996).

[21] M. A. Schneider, L. Vitali, N. Knorr, and K. Kern, Phys. Rev. B **65**, 121406(R) (2002).

[22] L. Bürgi, O. Jeandupeux, H. Brune, and K. Kern, Phys. Rev. Lett. **82**, 4516 (1999).

[23] A. C. Hewson, *The Kondo Problem to Heavy Fermions* (Cambridge University Press, Cambridge, England, 1997).

[24] O. Újsághy, G. Zaránd, and A. Zawadowski, Solid State Comm. **117**, 167 (2001).

[25] O. Újásaghy, J. Kroha, L. Szunyogh, and A. Zawadowski, Phys. Rev. Lett. **85**, 2557 (2000).

[26] P. Nozieres and A. Blandin, J. de Phys. **41**, 193 (1980).

[27] P. W. Anderson, Phys. Rev. **124**, 41 (1961).

[28] A. Schiller and S. Hershfield, Phys. Rev. B **61**, 9036 (2000).

[29] M. Plihal and J. W. Gadzuk, Phys. Rev. B **63**, 085404 (2001).

[30] P. Nozieres, J. Low Temp. Phys. **17**, 31 (1974).

[31] J. Kondo, Prog. Theor. Phys. **32**, 37 (1964).

[32] J. R. Schrieffer and P. A. Wolf, Phys. Rev. **149**, 491 (1966).

[33] P. W. Anderson, J. Phys. C **3**, 2439 (1970).

[34] T. Kawasaka, H. Kasai, W. A. Dino, and A. Okiji, J. Appl. Phys. **86**, 6970 (1999).

[35] V. Madhavan, W. Chen, T. Jamneala, and M. F. Crommie, Phys. Rev. B **64**, 165412 (2001).

[36] L. D. Landau and E. M. Liftshitz, *Quantum Mechanics* (Butterworth-Heinmann, Oxford, 1997).

[37] W. Chen, T. Jamneala, V. Madhavan, and M. F. Crommie, Phys. Rev. B **60**, R8529 (1999).

[38] N. Korr, M. A. Schneider, L. Diekhöner, P. Wahl, and K. Kern, Phys. Rev. Lett. **88**, 096804 (2002).

[39] H. C. Manoharan, T. Yu, C. P. Lutz and D. M. Eigler, unpublished.

[40] H. Tsunetsugu, M. Sigrist, and K. Ueda, Rev. Mod. Phys. **69**, 809 (1997).

[41] G. Gruener and E. Babic, Physica B and C **86-88**, 850 (1977).

[42] T. Jamneala, V. Madhavan, W. Chen, and M. F. Crommie, Phys. Rev. B **61**, 9990 (2000).

[43] T. W. Odom, J.-L. Huang, C. L. Cheung, and C. M. Lieber, Science **290**, 1549 (2000).

[44] G. A. Fiete, G. Zarand, B. I. Halperin, and Y. Oreg, Phys. Rev. B **66**, 024431 (2002).

[45] K. Nagoaka, T. Jamneala, M. Grobis, and M. F. Crommie, Phys. Rev. Lett. **88**, 077205 (2002).

[46] O. Agam and A. Schiller, Phys. Rev. Lett. **86**, 484 (2001).

[47] D. Porras, J. Fernández-Rossier, and C. Tejedor, Phys. Rev. B **63**, 155406 (2001).

[48] M. Weissmann and H. Bonadeo, Physica E (Amsterdam) **10**, 44 (2001).

[49] A. A. Aligia, Phys. Rev. B **64**, 121102(R) (2001).

[50] G. Chiappe and A. A. Aligia, Phys. Rev. B **66**, 075421 (2002).

[51] A. Correa, K. Hallberg and C. A. Balseiro, eprint: cond-mat/0111441.

[52] K. Hallberg, A. A. Correa, and C. A. Balseiro, Phys. Rev. Lett. **88**, 066802 (2002).

[53] P. S. Cornaglia and C. A. Balseiro, Phys. Rev. B **66**, 115303 (2002).

[54] D. Goldhaber-Gordon, H. Shtrikman, D. Mahalu, D. Abusch-Magder, U. Meirav, and M. A. Kastner, Nature **391**, 156 (1998).

[55] D. Goldhaber-Gordon, J. Göres, M. A. Kastner, H. Shtrikman, D. Mahalu, and U. Meirav, Phys. Rev. Lett. **81**, 5225 (1998).

[56] S. Sasaki, S. D. Fraceschi, J. M. Elzerman, W. G. van der Wiel, M. Eto, S. Tarucha, and L. P. Kouwenhoven, Nature **405**, 764 (2000).

[57] W. van der Wiel, S. D. Fraceschi, T. Fujisawa, J. M. Elzerman, S. Tarucha, and L. P. Kouwenhoven, Science **289**, 2105 (2000).

[58] J. Nygard, D. H. Cobden, and P. E. Lindelof, Nature **408**, 342 (2000).

[59] T. W. Odom, *Electronic Properties of Single-walled Carbon Nanotubes*, Ph.D. thesis, Harvard University (2000).

[60] C. M. Canali and A. H. MacDonald, Phys. Rev. Lett. **85**, 5623 (2000).

[61] S. Kleff, J. von Delft, M. M. Deshmukh, and D. C. Ralph, Phys. Rev. B **64**, 220401 (2001).

[62] H. Ohno, Science **281**, 951 (1998).

[63] R. Saito, G. Dresselhaus, and M. S. Dresselhaus, *Physical Properties of Carbon Nanotubes* (Imperial College Press, London, 1998).

[64] O. Újsághy, A. Zawadowski, and B. L. Gyorffy, Phys. Rev. Lett. **76**, 2378 (1996).

[65] O. Újsághy and A. Zawadowski, Phys. Rev. B **57**, 11598 (1998).

[66] O. Újsághy and A. Zawadowski, Phys. Rev. B **57**, 11609 (1998).

[67] S. Guéron, M. M. Deshmukh, E. B. Myers, and D. C. Ralph, Phys. Rev. Lett. **83**, 4148 (1999).

[68] M. M. Deshmukh, S. Kleff, S. Guéron, E. Bonet, A. N. Pasupathy, J. von Delft, and D. C. Ralph, Phys. Rev. Lett. **87**, 226801 (2001).

[69] D. A. Papaconstantopoloulos, *Handbook of the Band Structure of Elemental Solids* (Plenum, New York, 1986).

[70] M. Pustilnik and L. I. Glazman, Phys. Rev. Lett. **87**, 216601 (2001).

[71] K. Levin and D. L. Mills, Phys. Rev. B **87**, 2354 (1974).

[72] W. van der Wiel, S. D. Francheschi, J. M. Elzerman, S. Tarucha, L. Kouwenhoven, J. Motohisa, F. Nakajima, and T. Fukui, Phys. Rev. Lett. **88**, 126803 (2002).

[73] J. Tersoff and D. R. Hammann, Phys. Rev. Lett. **50**, 1998 (1983).

[74] B. L. Altshuler, A. G. Aronov, and D. E. Khemlnitsky **15**, 7367 (1982).

[75] K. Yamada, K. Yoshida, and K. Hansawa, Prog. Theor. Phys. **71**, 450 (1984).

[76] F. J. Himpsel, J. E. Ortega, G. J. Mankey, and R. F. Willis, Adv. Phys. **47**, 511 (1998).

[77] G. A. Fiete and G. Zarand and B. I. Halperin , in preparation.

[78] P. R. Wallace, Phys. Rev. **71**, 622 (1947).

[79] D. Tomanek, S. G. Louie, H. J. Mamin, D. W. Abraham, R. E. Thomson, E. Ganz, and J. Clarke, Phys. Rev. B **35**, 7790 (1987).

[80] D. Tomanek and S. G. Louie, Phys. Rev. B **37**, 8327 (1988).

[81] For recent reviews see J. König *et al.* in Electronic Structure and Magnetism of Complex Materials, edited by D.J. Singh and D.A. Papaconstantopoulos (Springer Verlag 2002); R. N. Bhatt *et al.*, J. Superconductivity INM **15**, 71 (2002); T. Dietl, cond-mat/0201282.

[82] For reviews on the II-VI diluted magnetic semiconductors see N. B. Brandt and V. V. Mashalkov, Adv. Phys. **33**, 193 (1984); R. R. Galazka, J. Cryst. Growth **72**, 364 (1985); J. K. Furdyna, J. Vac. Sci. Technol. **A4**, 2002 (1986) and references therein.

[83] D. P. DiVincenzo, Science **270**, 255 (1995).

[84] M. A. Nielson and I. L. Chuang, *Quantum Computation and Quantum Information* (Cambridge University Press, Cambridge, UK, 2000).

[85] J. K. Furdyna, J. Appl. Phys. **64**, R29 (1988).

[86] H. Ohno, J. Magn. Magn. Mater. **200**, 110 (1999).

[87] S. J. Potashnik, K. C. Ku, S. H. Chun, J. J. Berry, N. Samarth, and P. Schiffer, Appl. Phys. Lett. **79**, 1495 (2001).

[88] A. V. Esch, L. V. Bockstal, J. D. Boeck, G. Verbanck, A. S. van Steenbergen, and P. J. Wellmann, Phys. Rev. B **56**, 13103 (1997).

[89] M. Linnarsson, E. Janzén, B. Monemar, M. Kleverman, and A. Thilderkvist, Phys. Rev. B **55**, 6938 (1997).

[90] J. Szczytko, A. Twardowski, K. Swiatek, M. Palczewska, M. Tanaka, T. Hayashi, and K. Ando, Phys. Rev. B **60**, 8304 (1999).

[91] J. Okabayashi, A. Kimura, O. Rader, T. Mizokawa, A. Fujimori, T. Hayashi, and M. Tanaka, Phys. Rev. B **58**, R4211 (1998).

[92] J. Okabayashi, A. Kimura, O. Rader, T. Mizokawa, A. Fujimori, T. Hayashi, and M. Tanaka, Phys. Rev. B **64**, 125304 (2001).

[93] H. Asklund, L. Ilver, J. Kanski, J. Sadowski, and R. Mathieu, Phys. Rev. B **66**, 115319 (2002).

[94] E. J. Singley, R. Kawakami, D. D. Awschalom, and D. N. Basov, Phys. Rev. Lett. **89**, 097203 (2002).

[95] H. Ohno, F. Matsukura, T. Omiya, and N. Akiba, J. Appl. Phys. **85**, 4277 (1999).

[96] K. M. Yu, W. Walukiewicz, T. Wojtowicz, W. L. Lim, X. Liu, Y. Sasaki, M. Dobrowolska, and J. K. Furdyna, Appl. Phys. Lett. **81**, 844 (2002).

[97] K. M. Yu, *et al.* cond-mat/0303217.

[98] K. M. Yu, W. Walukiewicz, T. Wojtowicz, I. Kuryliszn, X. Liu, S. Sasaki, and J. K. Furdyna, Phys. Rev. B **65**, 201303 (2002).

[99] C. Timm, F. Schäfer, and F. von Oppen, Phys. Rev. Lett. **89**, 137201 (2002).

[100] M. Berciu and R. N. Bhatt, Phys. Rev. Lett. **87**, 107203 (2001).

[101] M. P. Kennett, M. Berciu, and R. N. Bhatt, Phys. Rev. B **66**, 045207 (2002).

[102] M. Berciu and R. N. Bhatt, Phys. Rev. B **66**, 085207 (2002).

[103] J. König, H.-H. Lin, and A. H. MacDonald, Phys. Rev. Lett. **84**, 5628 (2000).

[104] G. Fiete, G. Zaránd and K. Damle (unpublished).

[105] W. Kohn and J. M. Luttinger, Phys. Rev. **98**, 915 (1955).

[106] A. Baldereschi and N. O. Lipari, Phys. Rev. B **62**, 2697 (1973).

[107] A. K. Bhattacharjee and C. B. á la Guillaume, Solid State Comm. **113**, 17 (2000).

[108] A. C. Durst, R. N. Bhatt, and P. A. Wolff, Phys. Rev. B **65**, 235205 (2002).

[109] G. Zaránd and B. Jankó, Phys. Rev. Lett. **89**, 047201 (2002).

[110] S.-R. Yang and A. H. MacDonald, e-print: http://xxx.lanl.gov/abs/cond-mat/0202021.

[111] S. v. M. H. Ohno, H. Munekata and L. L. Chang, Phys. Rev. Lett. **68**, 2664 (1992).

[112] L. L. Sohn, L. P. Kouwenhoven, and G. Schön, eds., *Mesoscopic Electron Transport* (Kluwer, Dordrecht, 1997).

[113] Y. Imry, *Introduction to Mesoscopic Physics* (Oxford University Press, New York, USA, 1997).

[114] M. Inguscio, S. Stringari, and C. Wieman, eds., *Bose-Einstein Condensation in Atomic Gases, Proceedings of the International School of Physics, Enrico Fermi, Course CXL* (International Organisations Services, Amsterdam, 1999).

[115] J. R. Anglin and W. Ketterle, Nature **416**, 211 (2002).

[116] R. P. Feynman, R. B. Leighton, and M. Sands, *The Feynman Lectures on Physics*, vol. III (Addison-Weslay, Massachusetts, USA, 1965).

[117] R. P. Feynman and F. L. Vernon, Ann. Phys. (N.Y.) **24**, 118 (1963).

[118] A. O. Caldeira and A. J. Leggett, Ann. Phys. (N.Y.) **149**, 374 (1983).

[119] A. Stern, Y. Aharonov, and Y. Imry, Phys. Rev. A **41**, 3436 (1990).

[120] N. Makri and K. Thompson, Chem. Phys. Lett. **291**, 101 (1998).

[121] K. Thompson and N. Makri, J. Chem. Phys. **110**, 1343 (1999).

[122] A. Stern, Y. Aharonov, and Y. Imry, in *Quantum Coherence in Mesoscopic Systems,*ed. by B. Kramer (Plenum Press, New York, USA, 1991).

[123] S. Chakravarty and A. Schmid **140**, 193 (1986).

[124] D. S. Golubev and A. Zaikin, Phys. Rev. B **59**, 9195 (1999).

[125] D. Cohen and Y. Imry, Phys. Rev. B **59**, 11143 (1999).

[126] Y. Imry, cond-mat/0202044 .

[127] D. Loss and K. Mullen, Phys. Rev. B **43**, 13252 (1991).

[128] A. Yacoby, M. Heiblum, D. Mahalu, and H. Shtrikman, Phys. Rev. Lett. **74**, 4047 (1995).

[129] E. J. Heller and S. Tomsovic, Physics Today **46**, 38 (1993).

[130] E. J. Heller, J. Chem. Phys. **62**, 1544 (1975).

[131] E. J. Heller, J. Chem. Phys. **65**, 4979 (1976).

[132] E. J. Heller, J. Chem. Phys. **67**, 3339 (1977).

[133] E. Heller, J. Chem. Phys. **62**, 1544 (1975).

[134] E. J. Heller, in *1989 NATO Les Houches Summer School on Chaos and Quantum Physics,*ed. by M-J. Giannoni, A.Voros, and J. Zinn-Justin (Elsevier, 1991).

[135] P. W. O'Connor, S. Tomsovic, and E. J. Heller, Physica D **55**, 340 (1992).

[136] P. W. O'Connor, S. Tomsovic, and E. J. Heller, J. Stat. Phys. **68**, 131 (1992).

[137] P. W. O'Connor, S. Tomsovic, and E. J. Heller, Chaos **2**, 105 (1992).

[138] M. A. Sepulveda, S. Tomsovic, and E. J. Heller, Phys. Rev. Lett. **69**, 402 (1992).

[139] Y. Weissman, J. of Phys. A (Mathematical and General) **16**, 2693 (1983).

[140] Y. Weissman, J. Chem. Phys. **76**, 4067 (1982).

[141] D. Huber, E. J. Heller, and R. G. Littlejohn, J. Chem. Phys. **89**, 2003 (1988).

[142] E. J. Heller, J. Chem. Phys. **64**, 63 (1976).

[143] V. Hakim and V. Ambegaokar, Phys. Rev. B **32**, 423 (1985).

[144] W. T. Strunz, L. Diósi, and N. Gisin, Phys. Rev. Lett. **66**, 4931 (1999).

[145] J. L. Skinner and D. Hsu, J. Phys. Chem. **90**, 4931 (1986).

[146] J. J. Sakurai, *Modern Quantum Mechanics Revised Edition* (Addison-Wesley, Massachusetts, 1994).